Aus dem Lehrstuhl für Physiologische Chemie
Institut der Ludwig-Maximilians-Universität München
Vorstand: Prof. Dr. Peter Becker

In Zusammenarbeit mit der
Klinik und Poliklinik für Strahlentherapie und Radioonkologie
Klinikum der Ludwig-Maximilians-Universität München
Direktor: Prof. Dr. Claus Belka

In Kollaboration mit Eisbach Bio GmbH

Targeting ALC1 for Synthetic Lethality in Cancer: A Superior Alternative to PARP Inhibitors

Dissertation
zum Erwerb des Doktorgrades der Naturwissenschaften
an der Medizinischen Fakultät der
Ludwig-Maximilians-Universität München

vorgelegt von
Katharina Arien Sahiri
aus
Zorneding

Jahr
2025

Mit Genehmigung der Medizinischen Fakultät
der Ludwig-Maximilians-Universität München

Betreuer:	Prof. Dr. Andreas G. Ladurner
Zweitgutachter:	Prof. Dr. Olivier Gires
Dekan:	Prof. Dr. med. Thomas Gudermann
Tag der mündlichen Prüfung:	16. Januar 2026

Table of content

Collaborative Research and Patent Contributions

This thesis was conducted as a collaborative effort between Eisbach Bio GmbH, the Department of Physiological Chemistry at the Ludwig-Maximilians-University of Munich (LMU) and the Clinic for Radiation Therapy and Radio oncology at the Ludwig-Maximilians-University of Munich (LMU), combining expertise from these institutions to address critical research questions in the development and characterization of small molecule inhibitors targeting ALC1. The research was supervised by Prof. Dr. Andreas Ladurner at the LMU, with significant contributions from Dr. Adrian Schomburg, CEO at Eisbach Bio and PD Dr. Anna Friedl from the Clinic for Radiation Therapy and Radiooncology at LMU, whose expertise greatly contributed to the success of this work.

The results of this thesis are reflected in several patents developed in collaboration with Eisbach Bio and filed through Zwicker Schnappauf & Partner Patentanwälte PartG mbB. These include "*Method to evaluate the capability of compounds on the trapping of proteins*" (Patent No. WO/2022/117781), authored by Sahiri, K., Blessing, C., Schomburg, A., and Ladurner, A., and "*Use of ALC1 inhibitors and synergy with PARPI*" (Patent No. WO/2023/213833), authored by Menzer, W. M., Sahiri, K., Schomburg, A., Ladurner, A., and Sennhenn, P.. Additional patents include "*Inhibitors for use in treating cancer by potentiating the effects of FDA-approved cancer drugs*" (Patent Nos. EP23205931.1, EP23207212.4, and EP24185254.0), authored by Menzer, W. M., Sahiri, K., and Schomburg, A., as well as "*ALC1 inhibitors ALC1i-1 and ALC1i-2 for use in treating pancreatic cancer by potentiating the effect of irinotecan*" (Patent No. EP23207219.9), authored by Menzer, W. M., Sahiri, K., Zhang, X., Schomburg, A., Ladurner, A., and Sieveke, J. These patents highlight the applied nature of the research and its potential for translational impact in cancer treatment.

Zusammenfassung:

Poly (ADP-ribose) Polymerase Inhibitoren (PARPi) zielen auf DNA-Reparaturmechanismen ab und führen in Tumorzellen mit defekter homologer Rekombination (HR) zu einer sogenannten synthetischen Letalität. Trotz ihres vielversprechenden Potenzials in der Krebstherapie gibt es Herausforderungen, vor allem durch die unspezifische Hemmung der PARP-Aktivität. Häufige Nebenwirkungen umfassen Resistenzen, unerwünschte Toxizität und die Störung wichtiger zellulärer Prozesse. Um diese Hürden zu überwinden, konzentriert sich die aktuelle Forschung darauf, neue Zielstrukturen zu finden, die eine präzisere und gezieltere Hemmung ermöglichen. Ein vielversprechender Ansatz ist ALC1 (Amplified in Liver Cancer 1), einen ATP-abhängiger Chromatin-Remodeler, der an DNA-Reparaturprozessen beteiligt ist. ALC1 wird durch Poly-ADP-Ribose (PAR) aktiviert und verändert die Zugänglichkeit von DNA-Schäden durch Nukleosomen-Verschiebung. Dies stellt eine potenzielle synthetisch letale Schwachstelle in Krebsarten mit homologer Rekombinationsdefizienz (HRD) dar.

Eisbach Bio GmbH hat ALC1-Inhibitoren (ALC1i) entwickelt, eine neue Klasse von synthetisch letalen Wirkstoffen, die darauf abzielen, ähnliche genetische Schwachstellen wie PARP-Inhibitoren anzugreifen, jedoch auf spezifischere Weise. In dieser Studie wurden ALC1i verwendet, um das therapeutische Potenzial von ALC1-Hemmung in der Krebsbehandlung zu untersuchen. In Zellkulturen führte ALC1-Hemmung zur Anhäufung von DNA-Schäden, veränderte die Dynamik von Reparaturproteinen an beschädigten DNA-Stellen und fixierte PARP1 auf Chromatin. Dies resultierte in einer synthetisch letalen Spezifität für Tumorzellen und folglich im Zelltod von HR-defizienten Zellen mit einer Selektivität von mehr als 20-fach. Weitere Analysen von Zelllinien unter ALC1i zeigten Sensitivität in Krebszellen, die über HRD hinausging. Auch in PARPi-resistenten Zellen blieb ALC1-Inhibition wirksam. Kombinationstherapien unter Einbeziehung von ALC1i zeigten synergistische Effekte mit verschiedenen zugelassenen Chemotherapeutika und experimentellen Wirkstoffen, einschließlich PARPi und Topoisomerase-1-inhibitoren (TOP1i). Im Xenotransplantat-Modell zeigte ALC1i hohe Wirksamkeit. Trotz der effektiven Bindung von PARP an Chromatin an DNA-Schadensstellen durch ALC1i gab es keine offensichtlichen Nebenwirkungen. Diese Beobachtung deutet darauf hin, dass die mit der PARP-Inhibition verbundene Toxizität eher mit der Beeinträchtigung zentraler zellulärer Mechanismen als mit dem Bindungsvorgang selbst verknüpft sein könnte. Die beobachtete synthetisch letale Spezifität für Tumorzellen, zusammen mit der nachgewiesenen Wirksamkeit in verschiedenen Krebskontexten, positioniert ALC1-Inhibition als vielversprechenden Kandidaten für weitere Entwicklung von neuen Medikamenten.

Abstract:

Poly(ADP-ribose) polymerase inhibitors (PARPi) have shown great potential in cancer treatment by selectively targeting DNA repair pathways and inducing synthetic lethality, leading to improved patient outcomes. However, their non-specific inhibition of PARP activity presents challenges such as drug resistance, undesirable toxicities, and disruption of crucial cellular housekeeping functions performed by PARP1. To address these challenges, there is a current focus on targeting new downstream targets that can offer more precise and targeted inhibition. Among the emerging candidates is ALC1 (Amplified in Liver Cancer 1), an ATP-dependent chromatin remodeler linked to DNA repair processes. The poly-ADP-ribose (PAR)-activated remodeler ALC1 impacts DNA lesion accessibility through nucleosome sliding and is a synthetic-lethal vulnerability in homologous recombination-deficient (HRD) cancers.

Eisbach Bio GmbH has developed ALC1 inhibitors (ALC1i), a new class of synthetic lethal medicines aiming to target the same genetic vulnerabilities as PARP inhibitors but in a more specific manner. In this thesis, inhibitors were employed to investigate the therapeutic potential of ALC1 inhibition in cancer treatment. In cellular contexts, ALC1i led to accumulation of DNA damage, changed DNA repair protein dynamics at DNA damage sites, and trapped PARPs on chromatin. This resulted in tumor-cell-specific synthetic lethality and, consequently, tumor cell death of HR-deficient over HR-proficient cells with a >20-fold selectivity. Further analysis of cell lines under ALC1i showed sensitivity in cancer cells extending beyond HRD. Importantly, ALC1 inhibition remained effective against PARP inhibitor-resistant cells. Combination treatments involving ALC1i showed synergistic effects with various approved chemotherapeutics and investigational agents, including PARPi. Moreover, when combined with Topoisomerase 1 inhibitors (TOP1i), like irinotecan, ALC1i showed high synergistic potential. In xenograft models, ALC1i have demonstrated great efficacy as a monotherapy, significantly reducing tumor growth. Despite the effective trapping of PARP on chromatin at DNA damage sites by ALC1i there were no apparent toxic side effects. This observation indicates that the toxicity associated with PARP inhibition may be linked more to its housekeeping functions rather than the process of trapping itself.

The outcomes of this study emphasize the prospective value of ALC1 inhibition as a novel and promising therapeutic approach in cancer treatment and personalized medicine. The observed tumor-cell-specific synthetic lethality, along with the demonstrated effectiveness in diverse cancer contexts, positions ALC1 inhibition as a noteworthy candidate for further exploration and development in the pursuit of advanced cancer therapies.

List of Figures

List of Supplementary Figures

List of Tables

List of Supplementary Tables

List of abbreviations

Definition	Abbreviation
Amplified in Liver Cancer 1	ALC1, CHD1L
Amplified in Liver Cancer 1 inhibitor	ALC1i
Alternative end joining	alt-EJ
Apurinic/apyrimidinic endonuclease 1	APE1
Ataxia-telangiectasia mutated	ATM
Ataxia telangiectasia mutated and Rad3-related	ATR
Area under the curve	AUC
Base excision repair	BER
Break-induced repair	BIR
Breast cancer gene	BRCA1, BRCA2
cell cycle checkpoint inhibitors	CCCi
Classical non-homologous end-joining	c-NHEJ
Cyclin-dependent kinase 1	CDK1
Chromodomain-Helicase-DNA-Binding Protein 1-Like	CHD1L
Checkpoint kinase	CHK
4′,6-diamidino-2-phenylindole	DAPI
DNA damage response	DDR
Dimethyl sulfoxide	DMSO
DNA-dependent protein kinase	DNA-PK
DNA-dependent protein kinase catalytic subunit	DNA-PKcs
Double-strand break	DSB
Double-strand break repair	DSBR
Double-stranded DNA	dsDNA
DNA structure-specific ends	DSE
DNA structure-specific ends	DSEs
Half maximal effective concentration	EC50
Epithelial-mesenchymal transition	EMT
Fluorescence-Activated Cell Sorting	FACS
Fetal bovine serum	FBS
Formalin-fixed paraffin-embedded	FFPE
Fibroblast growth factor	FGF
Fibroblast growth factor receptor	FGFR
Fluorescence resonance energy transfer	FRET
Genetically engineered mouse model	GEMM
Global genome nucleotide excision repair	GG-NER
Hepatocellular carcinoma	HCC
Holiday junctions	HJ
Homologous recombination	HR
Homologous recombination deficiency	HRD
Homologous recombination repair	HRR
Highest Single Agent	HSA
High -throughput-screen	HTS

Half-maximal inhibitory concentration	IC50
Immunofluorescence	IF
Ionizing radiation	IR
Knockout	KO
Live Cell Recruitment assay	LCI-assay
DNA ligase 3	LIG3
Loss of heterozygosity	LOH
Large-scale state transitions	LST
Microhomology-mediated end joining	MMEJ
Mismatch repair	MMR
Most Synergistic Area	MSA
Micro satellite instability	MSI
Micro satellite instability-high	MSI-H
Nicotinamide adenine dinucleotide	NAD
Nijmegen breakage syndrome protein 1	NBS1
Nucleotide excision repair	NER
Non-homologous end joining	NHEJ
NADPH oxidase	NOX
Nucleoside diphosphate linked moiety X hydrolase family members	NUDIX
Poly-ADP-Ribose	PAR
Poly (ADP-ribose) glycohydrolase	PARG
Poly (ADP-ribose) polymerase	PARP
Poly (ADP-ribose) polymerase inhibitor	PARPi
Phosphate Buffered Saline	PBS
Patient-derived organoid	PDO
Patient-derived xenograft	PDX
P-glycoprotein	P-gp
Phosphatidylinositol 3-kinase-related kinase	PIKK
Polynucleotide kinase 3′-phosphatase	PNKP
DNA Polymerase Theta	POLQ
DNA polymerase β	POLß
Pen Strep	PS
Reactive oxygen species	ROS
Replication Protein A	RPA
Receptor tyrosine kinase	RTK
Standard deviation	SD
Synthesis-dependent strand annealing	SDSA
Standard error of the mean	SEM
Small molecule inhibitor	SMI
Active metabolite of irinotecan	SN-38
Single nucleotide polymorphisms	SNP
Sulforhodamine B sodium salt	SRB
Single-strand break	SSB
Single-stranded DNA	ssDNA
Telomeric allelic imbalance	TAI

Terminal ADP-ribosyl glycohydrolase	TARD1
Trichloroacetic acid	TCA
Translational Controlled Tumor Protein	TCTP
Tyrosyl-DNA phosphodiesterase 1	TDP1
Tumor growth inhibition	TGI
Tail Moment	TM
Θ-mediated end joining	TMEJ
Topoisomerase 1	TOP1
topoisomerase 1 (TOP1) cleavage complex	TOP1cc
Topoisomerase 1 inhibitor	TOP1i
Topoisomerase 2	TOP2
Tri - adenosindiphosphat -ribose	Tri-ADP-ribose
Vascular endothelial growth factor	VEGF
Vascular endothelial growth factor receptor	VEGFR
WEE1 G2 Checkpoint Kinase	WEE1
X-Ray Repair Cross Complementing 1	XRCC1
Zero Interaction Potency	ZIP
Phosphorylated H2AX	γH2AX

1. Introduction

1.1. Exploring traditional and emerging approaches in cancer therapy

Cancer is a complex and diverse group of diseases that has long been a major challenge for medical science. Over the decades, various treatment strategies have been developed to combat its continuous spread. Classical methods such as surgery, radiation therapy, and chemotherapy, collectively known as classical cancer treatments, have emerged as cornerstones in the persistent search for effective treatments in the battle against this complex disease (Debela et al., 2021). These time-tested approaches have been fundamental in extending patient lifespans and mitigating symptoms. Even complete remission was achieved in a considerable number of cases. Nonetheless, conventional chemotherapies lack specificity and give rise to significant issues, such as side effects resulting from their unspecific toxicity or the development of drug resistance (Nurgali et al., 2018).

Immunotherapy has brought a groundbreaking shift to cancer treatment by utilizing the immune system to identify and eliminate malignant cells, reshaping the treatment landscape. Rather than directly attacking cancer cells like traditional approaches, immunotherapy focuses on strengthening and guiding the immune system's natural response to combat tumors. This innovative strategy has led to significant breakthroughs such as checkpoint inhibitors that activate immune cells, allowing them to better identify and combat cancerous cells (Yum et al., 2020). Immunotherapy offers the potential for longer-lasting responses and fewer side effects compared to traditional treatments.

Beyond the groundbreaking progress in immunotherapy, cancer treatment has seen significant advancements with the introduction of biologics and targeted therapy. Biologics, also known as biological therapies, involve using substances derived from living organisms or their components to selectively target molecules crucial for the proliferation and survival of cancer cells. These therapies can include monoclonal antibodies, cytokines, and vaccines designed to interfere with the cancer cells' signaling pathways or enhance the immune system's response (Papież & Krzyściak, 2021).

Similarly, targeted therapy uses precision medicine to find and target specific molecular changes in cancer cells. This approach improves treatment effectiveness and reduces harm to healthy tissues, leading to fewer side effects compared to traditional treatments. (Baudino, 2015). The introduction of biologics and targeted therapy marks a major shift in cancer treatment, making it more personalized by matching treatments to the specific characteristics of a patient's cancer.

1.2. Synthetic lethality: hitting the weak spot

Improved cancer treatment needs innovative strategies that target weaknesses in cancer cells while protecting healthy tissue. Among these strategies, the principle of synthetic lethality has emerged as a promising avenue. This approach takes advantage of the genetic and molecular abnormalities in cancer cells to deliver targeted treatment, effectively causing their destruction (Topatana et al., 2020). The fundamental concept of synthetic lethality, which originated from studies in model organisms like fruit flies and yeast, revolves around exploiting the interconnectedness of cellular pathways (Boone et al., 2007; Brough et al., 2011; Dobzhansky, 1946). The classical definition involves identifying genetic mutations or alterations in cancer cells that, in isolation, allow the cells to survive but become lethal when combined with another specific genetic alteration or when a particular pathway is blocked. This lethal interaction disrupts vital cellular processes necessary for growth and division, ultimately leading to cell death (O'Neil et al., 2017; Topatana et al., 2020).

The research by Akimov & Aittokallio, 2021 underscores the significance of considering factors beyond gene mutations as contributors to synthetic lethal interactions. These factors encompass protein and microRNA expression, pathway activation, microenvironmental shifts, and treatment responses. Traditionally, the term "synthetic lethality" has been associated with changes in cell viability rather than just the binary alive/dead outcome. To address this limitation, Akimov & Aittokallio, 2021 proposed an extended definition that involves the combined perturbation of multiple cellular components, resulting in changed phenotypes and decreased cell viability exceeding the sum of their individual effects. This redefined concept involves quantitative analysis of genetic interactions inspired by a synergy scoring approach used in drug combination screens. By linking observable phenotypes to gene mutations, this approach provides a more robust way to distinguish synthetic lethal interactions than relying solely on mutations. The principle of the extended definition of synthetic lethality is shown in Figure 1.

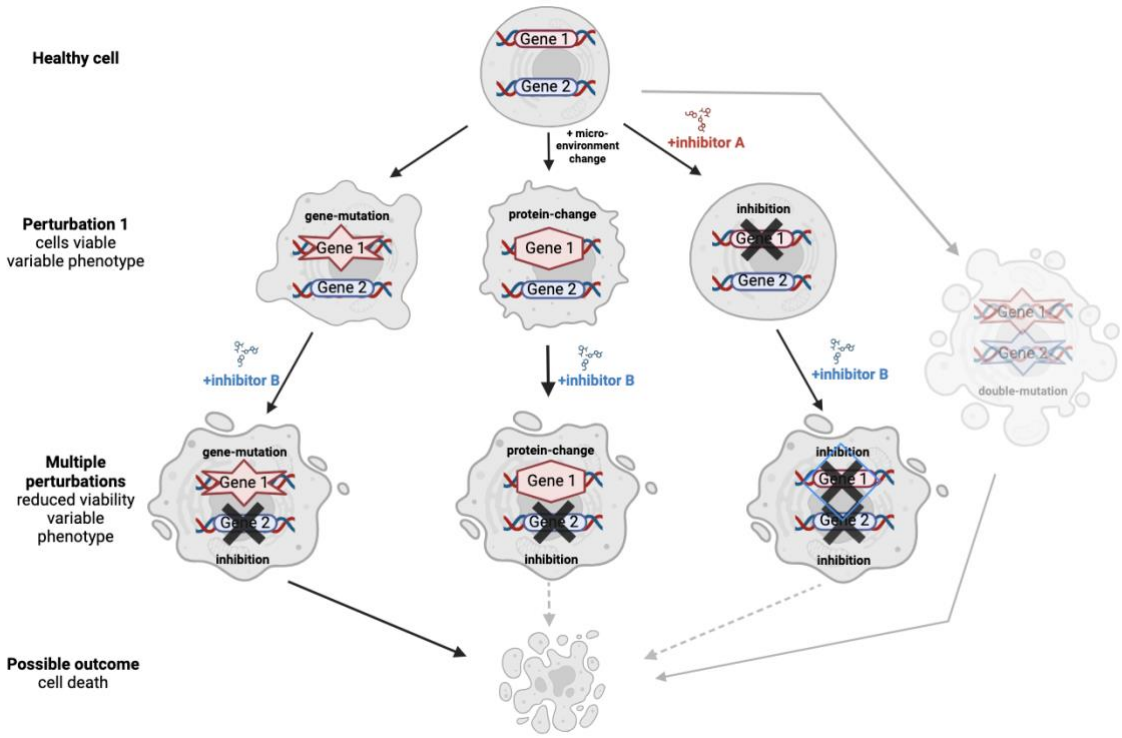

Figure 1: Principle for synthetic lethality

A mutation in gene 1 (red) in combination with inhibition of gene 2 (blue) (e.g., via inhibitor) leads to decreased cell viability, resulting in cell death (left path). Middle and right paths include factors beyond genetic alterations (e.g., protein and microRNA expression, pathway activation, microenvironmental shifts, etc.) (Akimov & Aittokallio, 2021). Perturbation 1 changes the cell phenotype; multiple perturbations additionally reduce cell viability. A double mutation (in gene 1 and gene 2) ultimately leads to cell death (right pathway) (created with Scientific Image and Illustration Software | BioRender).

A great example is the groundbreaking identification of synthetic lethal interactions involving deficiency in Poly (ADP-ribose) polymerase (PARP) and breast cancer genes 1 and 2 (BRCA1 and BRCA2) (Farmer et al., 2005). Many studies have shown the heightened susceptibility of BRCA-mutant cancer cells to inhibition of the DNA repair enzyme PARP. This has led to a new wave of research focused on treatments based on biomarkers and synthetic lethality for different types of cancer (Pilié et al., 2018).

Finding the weak spot, the cancer's specific genetic vulnerabilities ("Achilles heels"), is the key to personalized medicine, allowing a more dynamic and effective treatment for patients with fewer side effects.

1.3. The weak spot: targeting DNA damage response in cancer

DNA damage response (DDR) pathways are highly attractive as targets for synthetic lethality as they play a crucial role in maintaining genomic integrity. Cancer cells frequently harbor defects in DDR pathways, rendering them reliant on alternative mechanisms for survival. The principle of synthetic lethality exploits this vulnerability by identifying genes or proteins that, when inhibited in conjunction with compromised DDR, drive cancer cells to a state of lethality. The interplay of DNA repair processes, such as homologous recombination (HR) and base excision repair (BER), presents multiple opportunities for therapeutic intervention.

1.3.1. DNA damage response

DDR is a sophisticated network of cellular mechanisms that act as a guardian to preserve the integrity of genetic material. It becomes activated in response to various forms of damage, encompassing DNA breaks, modifications, and crosslinks, often arising from endogenous and exogenous sources such as replication stress or ionizing radiation (IR) (Friedberg et al., 2006; Saxena & Zou, 2022). The DDR orchestrates a spectrum of molecular processes by encompassing DNA repair, cell cycle checkpoints, and apoptosis (Giglia-Mari et al., 2010). This orchestration is essential for detecting, signaling, and repairing DNA damage, safeguarding genomic stability, avoiding mutation accumulation, and upholding cellular functionality. Understanding the complexities of the DNA damage response is crucial for uncovering how DNA repair works and has the potential to develop advanced cancer treatments. Important mediator- and effector proteins involved in the different DNA damage repair pathways are shown in Figure 2.

Repair pathway	NHEJ	HR	alt-NHEJ/ MMEJ	SSA	ICL repair	SSB repair	BER	TLS	NER	MMR
Source of DNA damage	IR, radiomimetics, topo II inhibitors	X-linking agents, replication inhibitors, anti-metabolites, topo I inhibitors			X-linking agents	IR, ROS, radiomimetics topo I inhibitors H2O2, alkylating agents	Alkylating agents	UV, alkylating agents	Alkylating agents, X-linkers	DNA pol proofreading errors
Damage sensors	Ku70/Ku80	MRN	PARP	MRN	FA core complex (FANCA, B, C,E, F, G, L and M)	PARP	DNA glycosylases, APE1	PCNA	XPC DDB2 CSA	MSH2, MSH3, MSH6, MLH1, PMS2
Signalling/ mediator proteins	DNAPK	ATM, ATR, MK2, CtIP, BRCA1/BARD1, BRCA2, PALB2, RPA		CtIP	FANCD1 [BRCA2] D2, I J [BRIP1] N [PALB2] O [RAD51C] P [SLX4]			RAD6 RAD18	XPA, XPF RPA	
Effector proteins	XRCC4 XLF LIG4 APLF Artemis PAXX WRN	RAD51 MUS81/EME1 SLX1/SLX4 RTEL1 BLM TOPOIII POLQ PARI RECQL5 FANCJ, BLM	XRCC1 LIG3, LIG1 CtIP POLQ	RAD52 others?	Shared with HR, TLS and NER.	XRCC1 PNKP POLBeta FEN1, TDP1 Aprataxin, LIG1, LIG3A	As SSB repair	REV1, POLH POLI, POLK.	XPG ERCC1 POLE POLD1 LIG1, LIG3	EXO1 POLD LIG1

Figure 2: DNA damage repair pathways and effector proteins

The DNA damage repair pathways are divided into double-strand break (DSB) repair (in blue) and single-strand break (SSB) repair (in red). Damage sensor, signaling, and effector proteins for the corresponding repair pathways are shown in this figure. Rational targets for DDR for future drug development are highlighted in red, including DNAPK, ATM, ATR, RAD51, PolQ, PARP and APE1. Repair pathways include non-homologous end-joining (NHEJ), homologous recombination (HR), alternative (Alt)- NHEJ or microhomology mediated end-joining (MMEJ), single-strand annealing (SSA), inter-strand crosslink (ICL) repair, single-strand break (SSB) repair, base excision repair (BER), tran-lesion synthesis (TLS), nucleotide excision repair (NER), mismatch repair (MMR) (figure from Brown et al., 2017).

In mammalian cells, DNA double-strand breaks (DSBs) can arise from various factors like replication fork stalling, physical stress, or exogenous factors like IR (Cannan & Pederson, 2015; Saxena & Zou, 2022). The response to DSBs via chromatin structure relies on a concept involving phosphorylated H2AX (γH2AX), which undergoes phosphorylation at serine 139 in response to IR or physiologically induced DSBs, where it accumulates, forms foci, and recruits other components of DDR (Scully & Xie, 2013). Two fundamental repair mechanisms can respond to two-ended DSBs: non-homologous end joining (NHEJ) and homologous recombination (HR). References suggest that NHEJ

can work in all phases of the cell cycle (X. Zhao et al., 2017) and is involved in the rapid ligation of DNA after minimal processing of DNA ends, including central factors like Ku70/80 and DNA-PKcs. HR is restricted to S and G2-phase (X. Zhao et al., 2017) and includes additional layers regulated by the cell cycle (Brown et al., 2017; Spies et al., 2021). The mechanisms of DSB repair are shown in Figure 3.

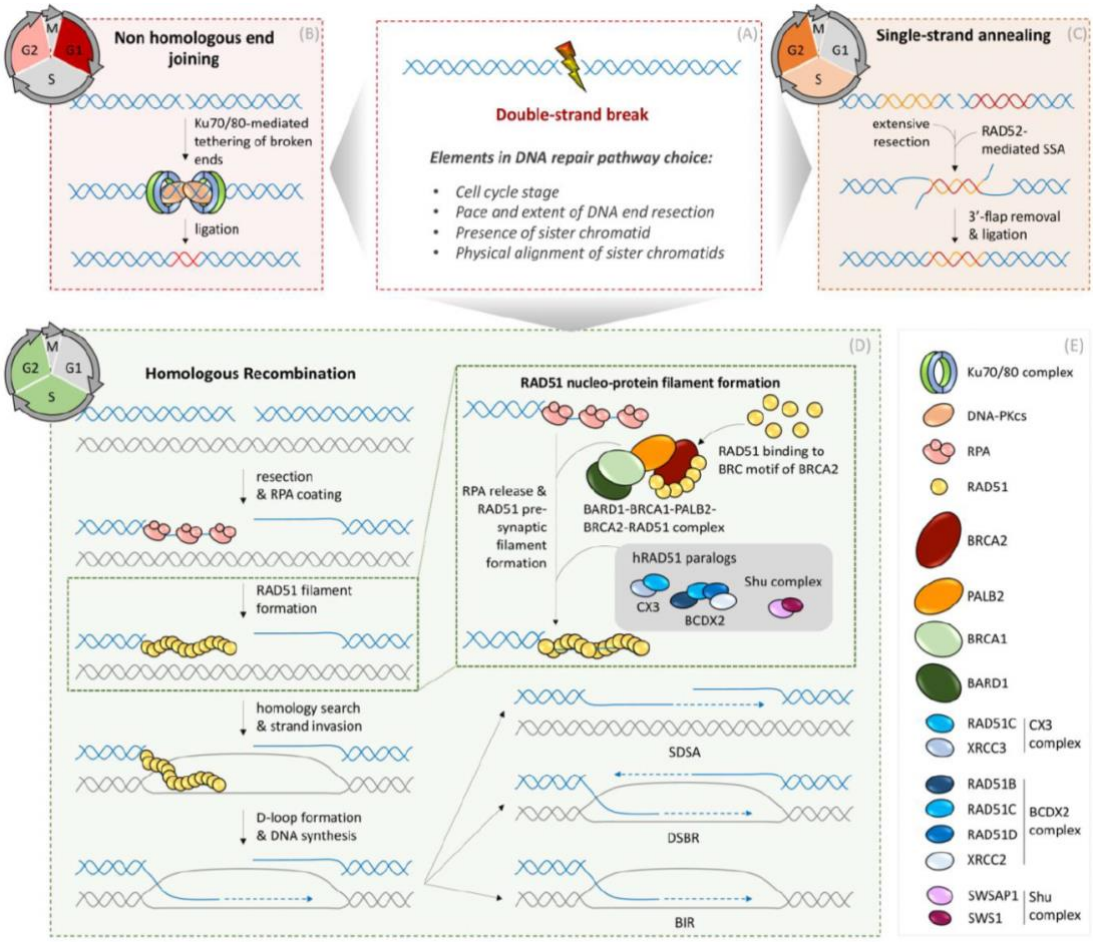

Figure 3: Mechanisms of DSB repair

DSB repair pathway choice (A) factors include cell cycle stage and chromatin shape. NHEJ (B) operates in the interphase. Central factors for NHEJ include Ku70/80 and DNA-PKcs. Single-strand annealing (SSA) (C) is used in S and G2 phase. RAD52 recombinase catalyzes the annealing of ssDNA. Repair through HR (D) needs the intact sister chromatid as a template to restore lost genetic information and therefore only takes place in S and G2 phase after DNA replication. 30 nucleotide ssDNA overhangs at the DSB ends are first bound by Protein A (RPA). Substitution of RPA by RAD51 is mediated by proteins like BRCA1, BRCA2, and PALB2 and RAD51 nucleo-protein-filaments are promoted by BRDX2, CX3, and Shu-complex. After homology search by stable RAD51 filaments and strand invasion, DNA repair synthesis is enabled. DSB repair results in either non-crossing over or crossing over products by resolving Holliday Junctions (HJ). Synthesis-dependent strand annealing (SDSA) results in non-crossing-over products.

Break-induced repair (BIR) occurs in case of a broken replication fork, where a second end of the DSB is unavailable. The intact sister chromatid is used as a template. Respective DNA repair enzymes are shown in (E) (figure from Spies et al., 2021).

The mechanism of HR repair is specifically required for the repair of one-ended DSBs primarily related to DNA replication (X. Li & Heyer, 2008). One-ended double-strand breaks (DSBs) can occur either from direct endonucleolytic activity at stalled forks or indirectly when the fork encounters a DNA nick. In repairing these one-sided DSBs, it appears that homologous recombination (HR) is the only pathway that reliably achieves effective and successful repair (X. Li & Heyer, 2008).

HR repair begins when the MRN complex (MRE11-RAD50-NBS1) identifies and binds to DSBs following DNA damage (Bian et al., 2019). Extensive ssDNA overhangs are generated by Exo1 together with BLM (Bloom Syndrome RecQ Like Helicase) and other helicases (Spies et al., 2021). Replication protein A (RPA complex) occupies 3´ends, which leads to secondary structures for an efficient HR. Dedicated mediators like BRCA2 and the BRCA1-BRD1 complex bind the ssDNA and RAD51 monomers to replace RPA with RAD51 (Cejka & Symington, 2021; Sung & Klein, 2006), leading to homology search. After invading the homologous DNA duplex, base-pairing with the complementary sequence on the sister chromatid is initiated. Homologous pairing and formation of a three-stranded DNA helix intermediate is facilitated by BRCA1-BARD1 together with RAD51 (Cejka & Symington, 2021; Sung & Klein, 2006). After base-pairing, RAD51-mediated ATP hydrolysis leads to the formation of a D-loop by the non-base-paired strand (Spies et al., 2021). RAD54 facilitates unloading of RAD51 to promote DNA repair synthesis. Then, a mechanism called gene conversion extends the invading strand using DNA from the sister chromatid as a template (Spies et al., 2021). During the D-loop extension in HR, DNA double-strand break repair (DSBR) can form a Holliday Junction, leading to crossover or non-crossover products. Alternatively, in the synthesis-dependent strand annealing (SDSA) pathway, the newly synthesized strand is displaced and anneals with the other DSB end, yielding non-crossover products (Nagaraju et al., 2006).

Alternative end joining (alt-EJ), also recognized as microhomology-mediated end joining (MMEJ), is thought to come into play when DSBs cannot be effectively repaired through c-NHEJ (Scully et al., 2019). This backup mechanism engages when c-NHEJ or HR encounters difficulties during DNA-end-processing during repair (Caracciolo et al., 2019; Iliakis et al., 2015). Alt-EJ involves minimal processing of DSB ends to expose short single-stranded microhomology sequences. When PARP1 outcompetes the Ku complex, a DSB sensor for c-NHEJ, it directs DSB repair towards alt-EJ (Robert et al., 2009; M.

Wang et al., 2006; Yang et al., 2018). Alt-EJ involves DNA polymerase Θ (POLQ), which inhibits HR via a RAD51-binding domain, and PolQ-helicase activity, promoting the displacement of RPA from resected double-strand-breaks. This displacement enables the annealing of DSBs and their subsequent joining (Ceccaldi, Liu, Amunugama, Hajdu, et al., 2015; Mateos-Gomez et al., 2017).

The trend for antitumor agents targeting mediators of DDR, based on the principle of synthetic lethality, has emerged in recent years, including developing inhibitors against PARP, WEE1 and POLQ (Brown et al., 2017). Small molecule inhibitors aimed at DDR proteins, like Ataxia telangiectasia mutated and Rad3-related (ATR) or ataxia-telangiectasia mutated (ATM) inhibitors, are making their way into clinical trials (Middleton et al., 2021; Priya et al., 2023).

One of the most successful targeted therapies for synthetic lethality with DDR are PARP inhibitors (PARPi). In cells with a deficiency in the HR repair pathway, like BRCA mutations, the repair pathway for DSBs is compromised. Inhibiting additional repair pathways dependent on PARP leads to an accumulation of DNA damage that the compromised BRCA-dependent repair pathway cannot effectively repair, ultimately causing the cancer cells to perish. This lethal interaction disrupts vital cellular processes necessary for growth and division, ultimately leading to cell death.

1.3.2. PARP enzymes, the essence of DDR

Poly (ADP-ribose) polymerase enzymes (PARPs), with PARP1 as a prominent representative, are multifaceted players in various molecular processes (Kanev et al., 2023). Their roles encompass DNA repair, DNA replication, transcriptional regulation, ribosome biogenesis, biomolecular condensate formation, and programmed cell death (D. Huang & Kraus, 2022; Leung, 2020), making them vital players in safeguarding the integrity of the cell's genetic material (Krishnakumar & Kraus, 2010; Schiewer & Knudsen, 2014).

Operating within diverse DNA repair pathways (Curtin, 2012; Rouleau et al., 2010), they are essential for the recognition of SSBs, the detection of DSBs, and an expanding range of DNA-based structures (Hu et al., 2014; Khodyreva & Lavrik, 2016; Langelier & Pascal, 2013; Sefer et al., 2022). Emerging research highlights PARP1's crucial role in DNA replication, including Okazaki fragment maturation, replication fork stability, and stress-induced fork restart. (Hanzlikova et al., 2018; Jackson & Moldovan, 2022).

Through their enzymatic activity, PARP enzymes (PARP1 & PARP2 in particular) catalyze the polymerization of ADP-ribose units through NAD+ on target proteins. (Chaudhuri & Nussenzweig, 2017; Demény & Virág, 2021). This alteration can influence protein function, cellular distribution, binding interactions, and overall stability. PARP1

triggers the production of PAR by linking an initial ADP-ribose molecule to amino acid residues on target proteins. (Leidecker et al., 2016; Martello et al., 2016; Pedrioli et al., 2018; Rack et al., 2020). PARylation causes chromatin to relax at the damaged site and serves as a molecular scaffold to help recruit PAR-binding proteins (Teloni & Altmeyer, 2016). This recruitment ensures efficient and accurate DNA repair, maintaining genomic integrity. Specific categories of DNA damage, notably DNA nicks and DSBs, provoke a substantial increase in the catalytic activity of PARP1 (Hassler & Ladurner, 2012; Konecny & Kristeleit, 2016). The mechanism of PARPs using NAD+ to generate and remove ADP-ribose is shown in Figure 4.

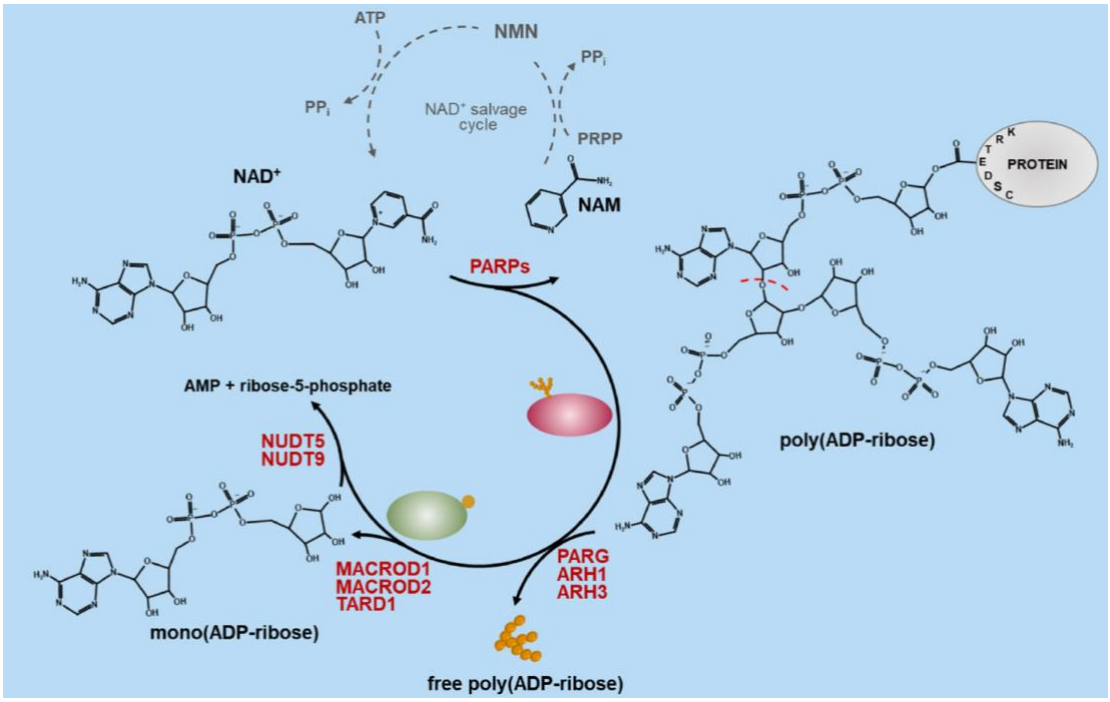

Figure 4: Mechanism of Mono- and poly-ADP-ribose generation

Via NAD+, proteins are ADP-ribosylated on glutamate, aspartate, or other residues by PARP. Nicotinamide (NAM) is back-converted into NAD+ in the phosphatidyl-ribosyl-pyrophosphate (PRPP) and NAD-salvage cycle under the consumption of ATP. Protein-bound poly-ADP-ribose is cleaved by the endo- / exo-glycohydrolases PARG and ADP-ribosylhydrolase 1 or 3 (ARH1/3), leading to depolymerization of these chains to mono-ADP-ribose units and freely diffusible polymers. Terminal ADP-ribosyl glycohydrolase (TARD1) or MacroD1/D2 remove the last unit of protein-bound PAR-chains or Protein-attached mono-ADP-ribose leading to free mono-ADP-ribose, which is hydrolyzed by nucleoside diphosphate linked moiety X hydrolase family members (NUDIX) to AMP and ribose-phosphate (figure from Demény & Virág, 2021).

The function of PARP1 in DNA repair was summarized by Kanev et al. (2023) and is visualized in Figure 5:

PARP1 is involved in classical non-homologous end joining (c-NHEJ) and homologous recombination (HR), though the exact molecular mechanism remains to be fully understood (Chaudhuri & Nussenzweig, 2017). Studies have demonstrated that PARP1 interacts with and adds PAR chains to the catalytic subunit of DNA-dependent protein kinase (DNA-PKcs), which is essential in classical non-homologous end joining (c-NHEJ). This interaction enhances DNA-PKcs kinase activity and directs subsequent events in the c-NHEJ pathway (Ruscetti et al., 1998; Spagnolo et al., 2012). Additionally, PAR facilitates the recruitment of the chromatin remodeler CHD2 (chromodomain helicase DNA binding protein 2), that positions Histon H3.3 near DNA breaks, facilitating chromatin expansion and the development of the c-NHEJ-complex (Luijsterburg et al., 2016).
As mentioned before, PARP1's crucial role in alt-EJ is highlighted when it outcompetes the Ku complex, thereby redirecting DSB repair towards alt-EJ (Robert et al., 2009; M. Wang et al., 2006; Yang et al., 2018). It facilitates recruitment of POLQ, that associates with annealed break-ends, extending them prior to the ligation-process (Mateos-Gómez et al., 2015; Wyatt et al., 2016) (Figure 5A). Ultimately, engagement of XRCC1-LIG3 facilitates to the closing of the breaks (Masani et al., 2016).
In the absence of HR, cells become increasingly dependent on the alt-EJ-repair pathway. Inhibiting POLQ disrupts DNA repair in these cells, particularly in tumors with BRCA1/2 deficiencies, leading to synthetic lethality (Ceccaldi, Liu, Amunugama, Hajdú, et al., 2015; Mateos-Gómez et al., 2015; Zatreanu et al., 2021).

Concerning HR, PARP1 has been observed to recruit subunits of the heterotrimeric MRN complex, which consists of Mre11, Rad50 and Nbs1, binding to DNA double-strand breaks (J.F. Haince et al., 2008). Furthermore, the ATM kinase has a site that binds to PAR, and this binding activates its function in repairing DNA damage (Aguilar-Quesada et al., 2007; J. F. Haince et al., 2007). PARP1 and PARylation help recruit BRCA1, which is essential for preparing DNA ends during repair through homologous recombination (M. Li & Yu, 2013). However, it's important to emphasize that all these mentioned proteins can be recruited through alternative mechanisms independent of PARP1. This suggests that their recruitment may not be solely dependent on PARP1 but rather facilitated by PARP1-induced chromatin relaxation near DNA breaks (Kanev et al., 2023).

In the realm of DNA repair, PARP1's most extensively studied role is in SSB-repair. Demonstrating high affinity, PARP1 promptly binds to SSBs, leading to PARylation near these breaks (Eustermann et al., 2015). Recognizing the PAR chains, X-ray repair cross-complementing 1 (XRCC1) serves as a scaffold for various enzymes involved in DNA-repair. These enzymes, including AP (aprataxin), PNKP (polynucleotide kinase 3′-phosphatase), POLB (DNA polymerase β), and LIG3 (DNA ligase 3), work together to process DNA ends, synthesize new DNA, and seal the breaks (Caldecott, 2019; Caldecott, 2022) (Figure 5D).

BER stands as a crucial DNA repair pathway responsible for replacing bases damaged by alkylation, deamination, or oxidation. (Beard et al., 2019). In the canonical BER process, a glycosylase enzyme eliminates the modified base, and the resulting abasic site undergoes processing aided by APE1, the apurinic/apyrimidinic endonuclease 1. POLB fills the single-base pair missing sections, and ligation is carried out through LIG1/LIG3 (Kim & Wilson, 2012). Although not traditionally classified as a BER protein, PARP1 speeds up the process by attaching to damaged DNA and bringing in other proteins, like POLB, XRCC1, and LIG3, to help fix the damage (Helleday, 2011) (Figure 5C).

Also, PARP1 helps remove DNA damage caused by topoisomerase 1 (TOP1) when it gets stuck on the DNA, which can happen during DNA copying, transcription, or when treated with certain cancer drugs like irinotecan (Pommier et al., 2014; Tubbs & Nussenzweig, 2017). Tyrosyl-DNA phosphodiesterase 1 (TDP1) cleaves TOP1ccs from DNA, which is facilitated by its interaction with the CAT domain of PARP1 (Das et al., 2014). Upon binding to PARP1, TDP1 undergoes PARylation, promoting its stability and enhancing its ability to bind and remove TOP1ccs. Subsequently, the PARP1-TDP1 complex recruits XRCC1 and its associated proteins to repair the SSBs generated during the removal of the cleavage complex (Das et al., 2014) (Figure 5 B).

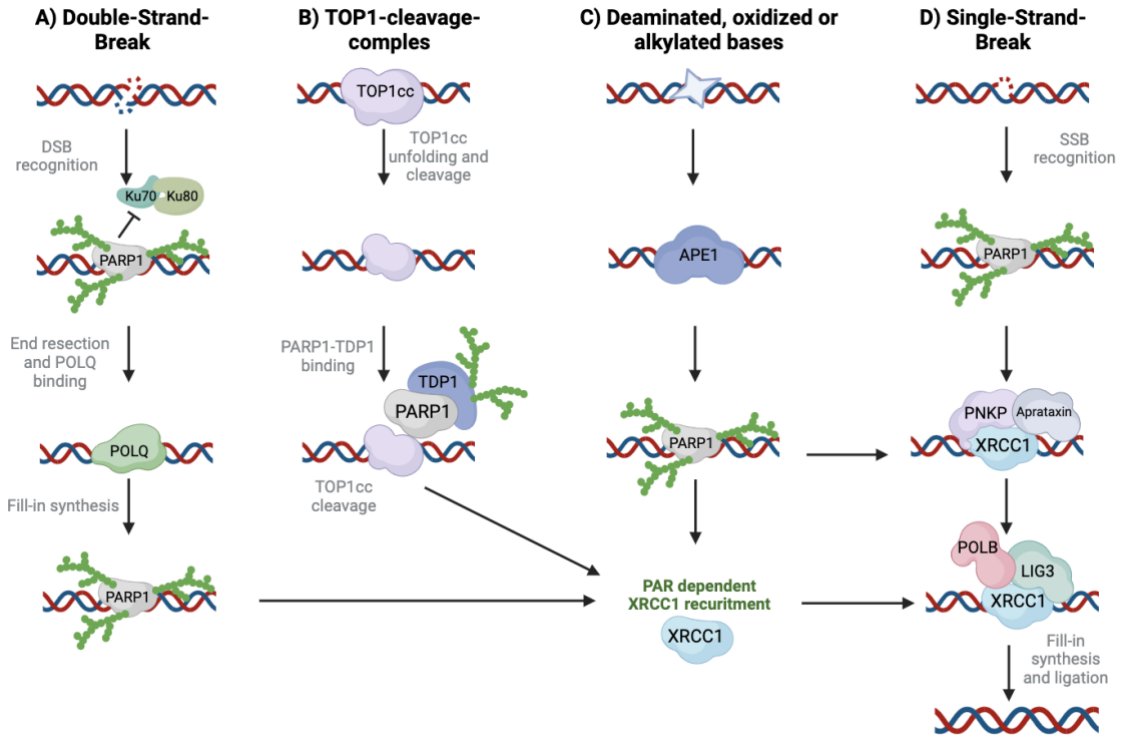

Figure 5: PARP1 plays pivotal roles in DNA repair pathways
(A) PARP1 competes with Ku, favoring POLQ-dependent alternative end joining (alt-EJ) over classical NHEJ. (B) PARP1 works with TDP1 to help cut the TOP1ccs, allowing the DNA to be repaired. (C) PARP1 attaches to the single-strand breaks that occur during the base excision repair process after APE1 has acted on the DNA. (D) Recognizing SSBs, PARP1 recruits XRCC1. XRCC1 helps process the broken DNA ends with the help of PNKP and AP, which then allows the DNA to be repaired and sealed by POLB and LIG3. (created using Scientific Image and Illustration Software | BioRender, modified from (Lord & Ashworth, 2017)

The recognition of PARPs involvement in DDR led to the development of targeted therapies, such as PARPi, holding promise in treating cancers with defective DNA repair mechanisms (Lord & Ashworth, 2017), thereby underscoring the clinical relevance of PARP enzymes in the context of DDR pathways.
PARPi have been established to selectively inhibit PARP1/2 and exploit a defect in the HR phenotype in BRCA1/2-deficient cells (Lord & Ashworth, 2017).

1.4. Homologous recombination deficiency and PARP inhibition

1.4.1. The principle of homologous recombination deficiency

Homologous recombination deficiency (HRD) has gained substantial clinical importance as an important concept in oncology. It can arise due to genetic alterations in essential genes important for HR (like BRCA1 or BRCA2), leading to impaired DNA DSB repair (Bonnet et al., 2022). Such a defect in DNA repair mechanisms can lead to genomic instability, increased susceptibility to DNA-damaging agents, and the accumulation of genetic alterations associated with cancer development and progression (Hanahan & Weinberg, 2011; Marquard et al., 2015). A compromised Homologous Recombination Repair pathway is often associated with various types of tumors, including breast, ovarian, prostate, and pancreatic cancers (Stewart et al., 2022). This vulnerability forms the foundation of synthetic lethality strategies, where inhibiting a compensatory pathway alongside a pre-existing DNA repair defect leads to extensive DNA damage accumulation and cell death. Exploiting synthetic lethality with HRD has advanced targeted therapies like PARP inhibitors (PARPi) (Lord & Ashworth, 2017), offering a novel approach to precision medicine in treating HRD-associated cancers.

1.4.2. PARP inhibitors for the treatment of HRD-cancers

In 2005, the synthetic lethality of PARP was initially observed in the context of BRCA mutations (Farmer et al., 2005). PARP inhibitors hamper alternative DNA repair pathways, leading to synthetic lethality in cancers with HR deficiencies (Bryant et al., 2005; Farmer et al., 2005; Pommier et al., 2016).

Small molecule inhibitors (SMIs) have been designed to specifically target these proteins that have become essential for the survival of specific cancer types. Numerous PARPi have been approved by the food FDA and are used in the clinic mainly to treat patients with ovarian or breast cancer. The six most common PARPi are shown in Figure 6.

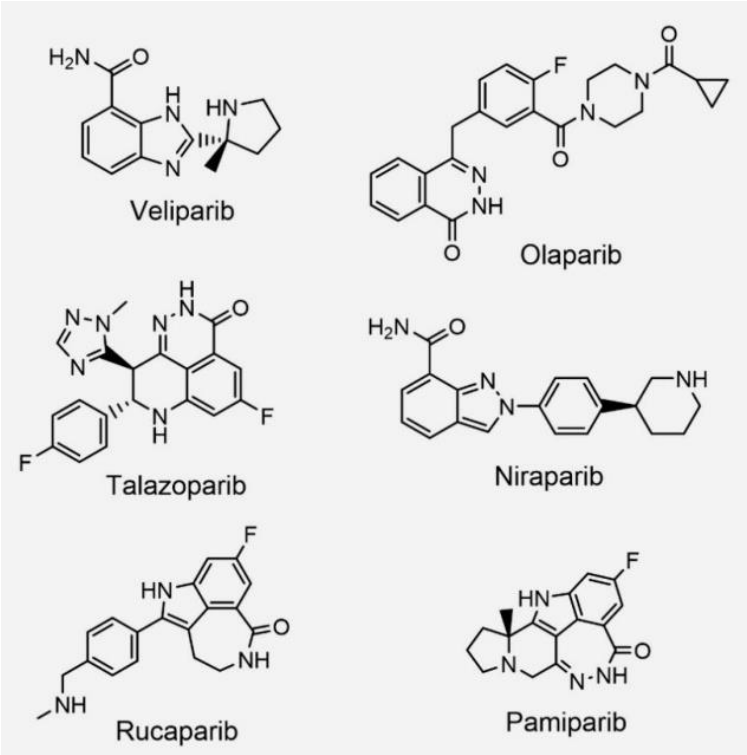

Figure 6: Most common PARPi, presented by (D.-H. Kim & Nam, 2022)

Various mechanisms underlying the inhibition of enzymatic activity by PARPi have been unveiled and are broadly categorized into two groups. One approach involves binding a PARPi to the enzyme's active site, hindering its enzymatic function. Alternatively, a PARPi can attach to the PARP-chromatin complex, capturing the enzyme in an inactive state on chromatin so-called protein-trapping. "PARP trapping" refers to the increased recruitment, association, or retention of enzymes on DNA damage sites in living cells (Shen et al., 2015; William Menzer et al., 2022). For instance, olaparib predominantly acts as an active site binder, whereas talazoparib exerts more potent trapping effects (Fan et al., 2020; Franzese et al., 2019; O'Cearbhaill, 2018).
The conventional understanding suggests that the cellular potency and toxicity of PARPi primarily arise from their ability to trap PARP enzymes on chromatin, thereby hindering DNA repair mechanisms (Hopkins et al., 2019).
The figure of Pommier et al. (2016) (Figure 7) describes the mechanism of PARP inhibition via protein-trapping in DDR: when an SSB occurs, PARP1 binds to the break and generates PAR-polymers, leading to auto-PARylation of itself, other proteins associated with chromatin and histones. This auto-PARylation helps loosen the chromatin to bring in repair proteins. Auto-PARylation lets PARP1 detach from the DNA, allowing it to interact with other repair factors organized by XRCC1.
The poly (ADP-ribose) glycohydrolase PARG removes PARylation, facilitating PARP1 reactivation. PARPi hinder NAD+ binding and PARylation, preventing PARP dissociation from the SSB. As a

result, unrepaired SSBs accumulate, and PARP trapping occurs. HR repair factors like BRCA1/2 and replication bypass pathways are required for cell survival to repair ensuing DSBs and the trapped PARP. PARP1 plays a role in the restoration of DNA structures termed "collapsed replication forks" featuring specific ends called DNA structure-specific ends (DSEs). Additionally, it contributes to the retraction and reinitiation of halted replication forks and the mending of double-strand-breaks (Pommier et al., 2016).

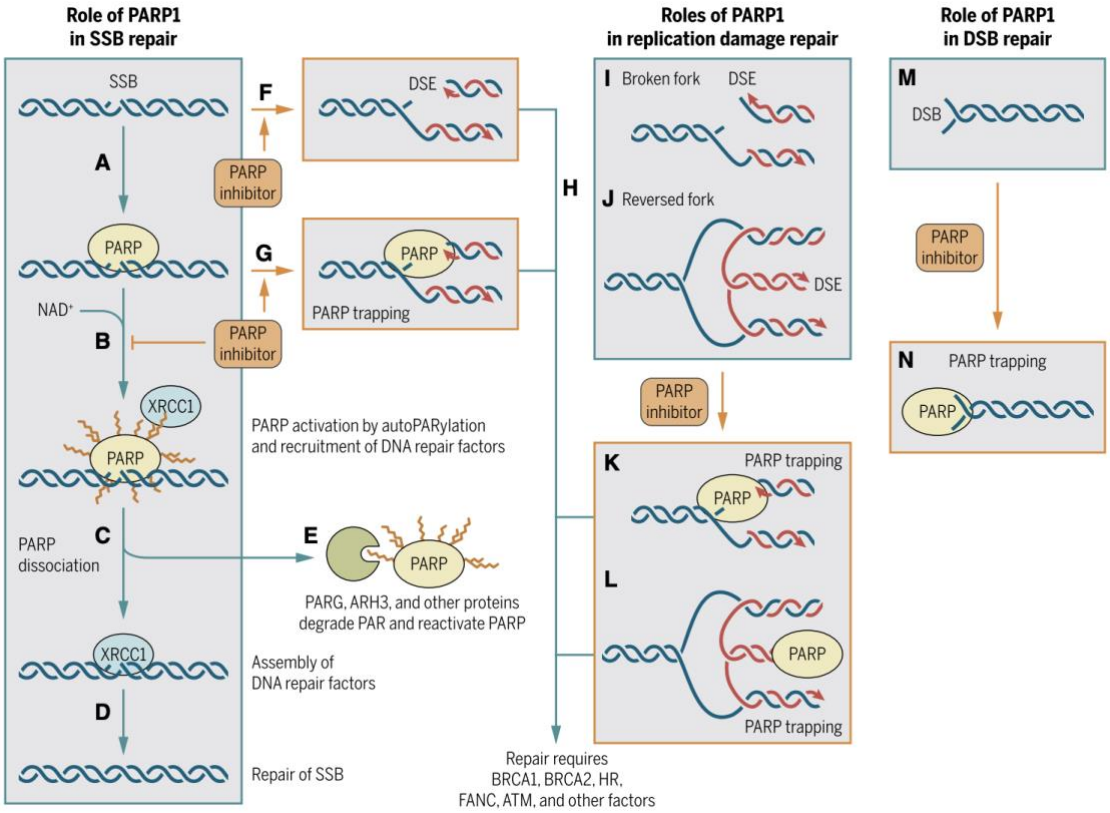

Figure 7: Effect of PARP inhibitors on PARP-dynamics in DDR

PARP1 binds to a SSB (shown in A), utilizes NAD+ (shown in B) to add PAR chains to itself (auto-PARylation) and to histones and proteins in the chromatin, helping to loosen the chromatin and bring in repair proteins. Auto-PARylation triggers PARP1 to dissociate from the DNA (shown in C), allowing other repair proteins to access the damage via XRCC1 (D). The glycohydrolase PARG (E) removes PARylation, allowing PARP1 reactivation. PARPi obstruct NAD+ binding and PARylation at the NAD+ site (see B), hintering PARP detachment from the single-strand-break. Unrepaired SSBs accumulate (F), and PARP trapping ensues (G). Cell survival necessitates other HR repair factors like BRCA1 and 2 and replication bypass pathways (H) to repair the ensuing DSBs and trapped PARP. PARP1 also helps to repair damaged forks with DNA structure-specific ends (DSEs) (I), restarts them (see J), and the repairs DNA double-strand breaks (M). PARPi effectively trap PARP at structure specific ends (shown in K and L) and breaks (N) (figure from Pommier et al., 2016).

Several enzymes involved in chromatin remodeling, histone modification, and other chromatin-related activities are recruited to DNA damage sites in a PAR-dependent context (Luijsterburg et al., 2016; Sellou et al., 2016; Timinszky et al., 2009). These enzymes lead to changes in chromatin compaction, suggesting their contribution to the regulation of DNA-repair processes. However, the mechanisms involved in releasing PARP1 and PARP2 from DNA lesions remain unclear. The specific impact of these chromatin-based procedures on the recruitment and release dynamics of PARP1 and PARP2 from DNA lesions requires further investigation. Thus, future studies are needed to elucidate the relationship between chromatin modifications and the dynamics of PARP1 and PARP2 at DNA damage sites (Blessing et al., 2020).

The importance of PARP trapping in the cytotoxic mechanism of PARPi appears to be context-dependent, as demonstrated by Murai, Zhang et al. (2014). They presented evidence challenging the notion that PARP trapping is the sole driver of the cytotoxic effects of PARP-inhibitors. They reported that while PARPi combinations with temozolomide demonstrated significant PARP trapping activity, the efficacy of these inhibitors in combination with other DNA-damaging agents like irinotecan or platinum seemed to be less dependent on PARP1 trapping. These and other findings highlight the need to reevaluate the underlying mechanisms contributing to the cellular toxicity of PARPi.

Selecting the appropriate PARPi is crucial, depending on how they function (trapping vs. catalytic inhibitor) and the patient's genetic background. Understanding and characterizing cancer cells with HRD is critical for studying the underlying mechanisms of this genomic alteration and developing targeted therapies. By identifying the distinctive vulnerabilities linked to HRD, clinicians can precisely identify individuals likely to respond well to treatments that target these specific weaknesses. This approach optimizes therapeutic outcomes while minimizing adverse effects.

1.4.3. HRD-characterization for patient selection

In recent years, extensive efforts have been made to identify and characterize cancer cells with HRD. Cell lines serve as invaluable models for investigating the molecular basis of HRD and evaluating novel therapeutic strategies. Comprehensive characterization of cancers with HRD involves assessing key genomic features, like mutations in HR-related genes, changes in DDR pathways, and genomic signatures associated with HRD. Additionally, functional assays can be employed to evaluate the cellular response to DNA-damaging agents and determine the sensitivity to targeted therapies (Stewart et al., 2022).

1.4.3.1. Analyzing genomic scars in HRD

Scoring HRD by measuring genomic scars and mutational signatures can help to predict sensitivity to potential targeted therapies for a better patient outcome in the clinic. A mutation in the DNA repair gene BRCA1/2 is well-known as a marker for HRD, making cancer cells more sensitive to DNA-damaging agents like platinum drugs (J. Zhang et al., 2016). The Myriad Genetics score to predict such sensitivity can be combined from three independent DNA-based measures of genomic instability looking at genomic single-nucleotide-polymorphisms (SNP) array data (see Figure 8):

- Telomeric allelic imbalance (TAI) (Birkbak et al., 2012); an analysis of the number of chromosomal sub-regions exhibiting allelic imbalance extended to the telomeres.
- Loss of heterozygosity (LOH), where one allele is lost at many sites of the genome by deletion or copy number variations (Abkevich et al., 2012).
- Large-scale transitions (LST) representing chromosomal breaks between adjacent regions of >10Mb (Popova et al., 2012).

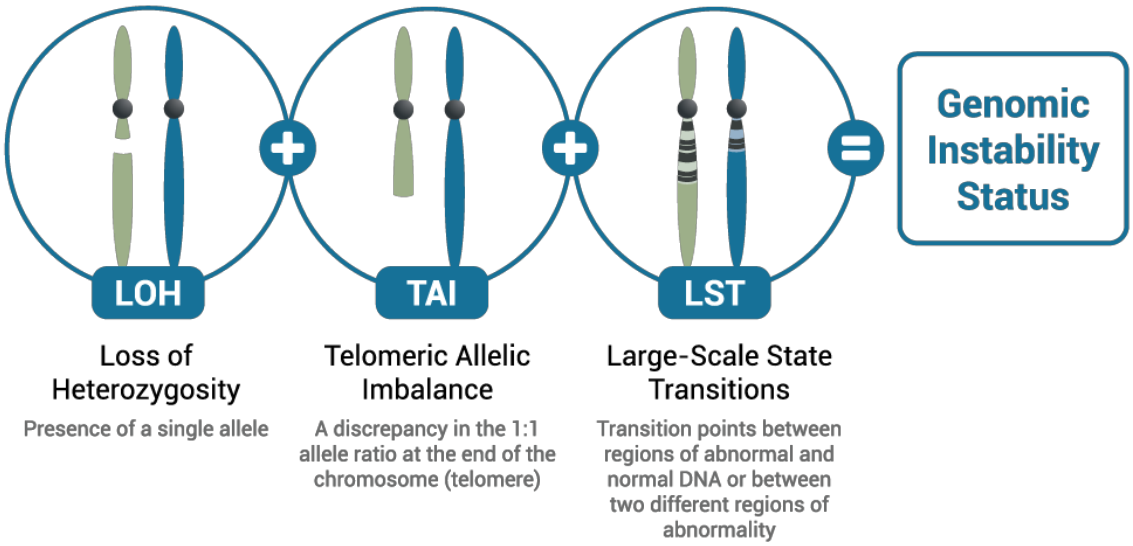

Figure 8: Loss of heterozygosity, Myriad Genetics BRCA mutation ("Loss of Heterozygosity Myriad Genetics BRCA Mutation BRCA1 BRCA2," n.d.)

By combining these and other parameters, HRD tests have been validated for clinical purposes in various settings looking at BRCA1/2 and HR-related genes. The FDA has approved two tests, the Myriad Genetics' myChoice CDx (*MyChoice® CDX FDA-Approved Targeted Therapies - Managed Care*, 2023), and the Foundation Medicine's FoundationOne CDx, which is a next generation sequencing based approach, identifying substitutions, copy number variations, insertions, and deletion alterations in over 324 genes. This test also detects microsatellite instability (MSI) ("FoundationOne CDX | Foundation Medicine,"n.d.).

Even though these models of testing for HRD have benefited patients in selecting the right treatments, it is still a long way until HRD can become an effective predictive biomarker. With the increasing number of genes related to the HR-network, many patients for potential treatment are still left out. This kind of genomic scar analysis misses significant factors for treatment options, like epigenetic changes, development of resistances, and restoration of the HR (De Lartigue PhD, 2020).

1.4.3.2. Other approaches: HR-signature by Peng et al. (2014)

An increasing number of genes are known to be involved in the HR pathway. Therefore, it is not easy to assess the status of HRD by looking at single genes. A study from the MDA cancer center (G. Peng et al., 2014) used a transcriptional profiling-based approach to identify molecular changes associated with HRD. By analyzing microarray data to search for genes differently expressed in control cells vs. HR-deficient cells, they could not only score the status of HRD but also predict specific sensitivity to PARPi in human cancer cells. A complex of 230 genes involved in DNA replication, DNA recombination and cell cycle regulation was selected to measure HRD-gene signature. The principle of this HRD signature suggests that the analysis of genetic alterations in individual genes involved in the HR pathway may not reflect the overall functional mechanism of the HR repair network (G. Peng et al., 2014). However, this method has not been implicated in clinical practice yet.

1.4.3.3. γH2AX and RAD51 foci formation as a functional readout for HRD

Since the analysis of the genomic scar alone will not provide a complete overview of the HRD status, a functional assay for assessing HR-proficiency can be applied. Using approaches to investigate the activity of DNA repair proteins or localization at damage sites will give a direct readout about the function of the HR repair mechanism. One such assay is the RAD51 foci formation assay. Forming RAD51 foci at the site of damage is one feature of a proficient HR repair. In an immune-fluorescent microscopic readout, RAD51 foci can be counted and analyzed (Ballabeni et al., 2013). As H2AX gets phosphorylated in the case of DSBs, it is used as an additional feature to screen DSB repair. It can be used as a biomarker for treatment, as it indicates DNA damage induced by genotoxic agents.

This approach can be used to assess HRD in cell culture, patient-derived xenograft (PDX) material, or direct formalin-fixed paraffin-embedded (FFPE) material from a cancer patient (Castroviejo-Bermejo et al., 2018)(see Figure 9).

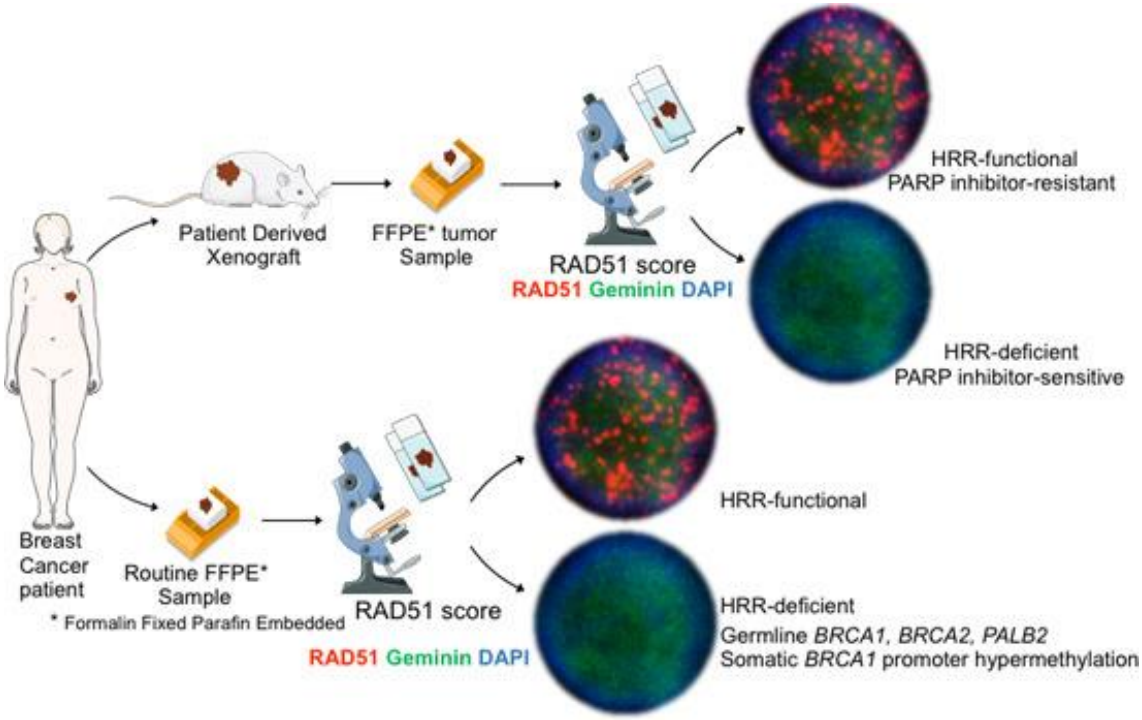

Figure 9: Method to validate HRD from patient material using RAD51 foci formation assay

The RAD51 score demonstrates a comprehensive ability to distinguish and effectively predict the response to PARPi in FFPE tumor samples. It is feasible to assess the RAD51 score in breast cancer samples even without previous exposure to DNA-damaging agents. Red dots indicate RAD51 foci, a functional HR, and following resistance to drugs like PARPi (figure from Castroviejo-Bermejo et al., 2018).

In a study by Cruz et al. (2018), they used RAD51 foci formation (immunofluorescence (IF) readout) and analysis of the genomic scar to determine the sensitivity to PARP inhibitors in PDX samples. In their hands, the RAD51 nuclear foci readout gave the most typical results in PDX and patient material (Cruz et al., 2018). To this date, no validated functional biomarkers for HRD have been implicated in clinical practice.

A summary of methods for HRD prediction can be found in Figure 10. Genetic and epigenetic alterations in specific genes have been identified as a key to HRD. Alterations can disrupt the HR repair (HRR) pathway, impairing DNA repair mechanisms. Consequences of HRD can be evaluated by investigating the genome for indications of genomic instability, such as chromosomal instability and other genomic signatures of functional assessment (Stewart et al., 2022).

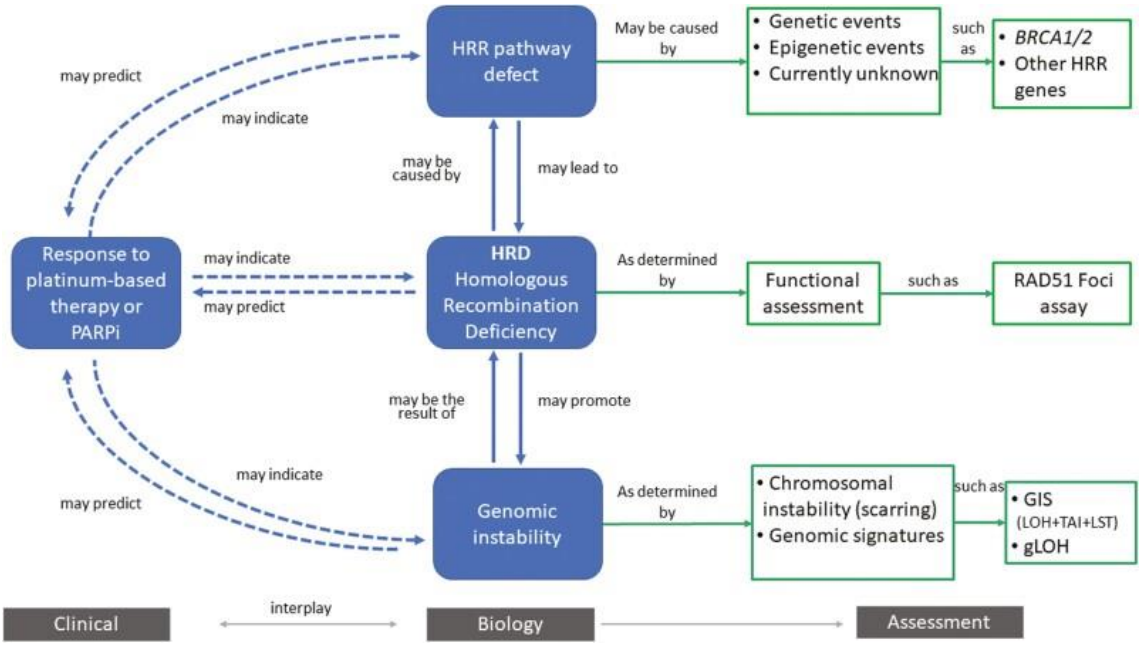

Figure 10: Homologous recombination deficiency: an overview

The biology of HRD interplays with the response to therapy (blue). Assessments that may cause HRD ((epi)genetic events) or help to determine HRD (functional assessment like RAD51 foci assay or analysis of genomic signature) are shown in green (figure from Stewart et al. 2022).

1.4.4. Downsides of PARPi

1.4.4.1. PARPi-resistance

Besides its downsides, targeted therapy via PARPi has shown clinical benefits. It has evolved as a potent target for an increasing list of cancer-types in single-agent therapy or combination with other treatments, including applications in the context outside of BRCA germline mutations (Esmo, 2023; H. S. Kim et al., 2020). Given the remarkable response observed in ovarian cancer patients, PARPi are undergoing evaluation in clinical trials involving individuals with endometrial and cervical cancer (Chelariu-Raicu et al., 2023; Kunos et al., 2015; Thaker et al., 2017). Furthermore, the phase III OReO/ENGOT Ov-38 trial revealed the advantages of PARP inhibitor rechallenge for patients experiencing platinum-sensitive relapsed ovarian cancer (Pujade-Lauraine et al., 2021). Niraparib demonstrated enhanced progression-free survival in patients when administered as maintenance therapy following first-line platinum-based chemotherapy in advanced stage (III to IV) high-grade ovarian cancer, as well as after platinum-based chemotherapy for recurrent disease (McLaren et al., 2021).

However, sustained antitumor responses were often hampered by the emergence of resistance. PARPi-resistance is widespread in clinical settings, with over 40 % of patients deficient in BRCA1/2 experiencing a lack of response to these inhibitors (H. Li et al., 2020). The broad inhibition of PARP activity may allow cancer cells to find alternative DNA repair mechanisms, rendering the inhibitors less effective over time (Dias et al., 2021).

Several mechanisms have been identified in preclinical models, including cellular extrusion of PARPi (Christie et al., 2019; Durmus et al., 2014), suppression of NHEJ (Choi et al., 2016), restoration of BRCA1/2 function (Lin et al., 2018; Pettitt et al., 2018), recovery of PARP activity via loss of poly (ADP-ribose) glycohydrolase (Gogola et al., 2018), PARP1 downregulation or deactivation (Murai et al., 2012; Pettitt et al., 2018), and restoration of replication fork stability (Murai et al., 2018; Rondinelli et al. 2017; Schlacher, 2017). These and many more factors limit PARPi-induced DNA damage and impair their efficacy. An overview of known mechanisms of PARPi-resistance was summarized by Franchet et al. (2021) (Figure 11).

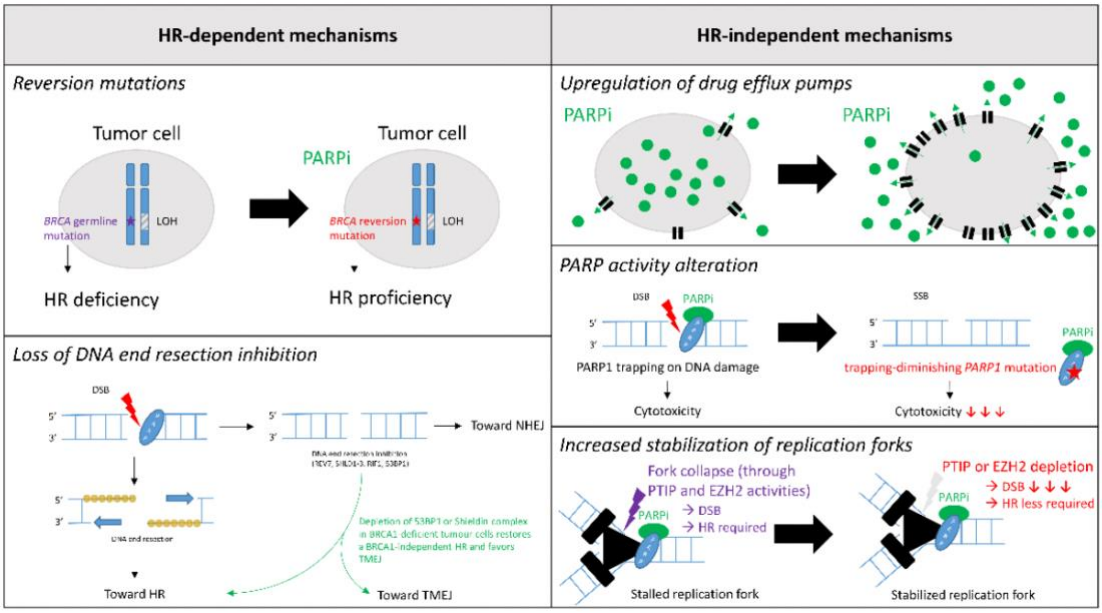

Figure 11: Possible mechanisms of PARPi-resistance
HR-dependent resistance mechanisms (left) include reversion mutations like BRCA1 or BRCA2 and loss of DNA end resection inhibition. HR-independent mechanisms (right) can occur through upregulated drug efflux pumps, PARP activity alteration, or increased stabilization of replication forks (figure from Franchet et al., 2021).

A recent study from Bhin et al. (2023) revealed the diverse non-reversion process of PARPi resistance in BRCA-deficient tumors. The study aimed to assess the influence of known non-reversion resistance mechanisms in the context of PARPi-resistant BRCA1-deficient vs. BRCA2-deficient mouse breast tumors. Integrating the assessment of homologous recombination (HR) status through the formation of RAD51 foci, along with a comprehensive multi-omics analysis of tumors exhibiting sensitivity or resistance to PARP inhibitors (PARPi), uncovered unique resistance profiles in tumors lacking BRCA1 or BRCA2 function. The investigation highlighted two predominant mechanisms of non-reversion resistance: HR reinstatement via 53BP1 loss in BRCA1-deficient tumors and the reinstatement of PARP signaling through PARG loss in BRCA2-deficient tumors. In BRCA1-deficient tumors, HRD and sensitivity to PARPi could be partially reversed by inactivating the 53BP1-RIF1-shieldin pathway. They suggest that inactivating the 53-BP1-RIF1shieldin pathway in BRCA1 KO tumors can rescue DNA end resection but will fail to restore HR repair. On the other hand, tumors lacking BRCA2 could not recover homologous recombination (HR) activity, underscoring the essential involvement of BRCA2 in the loading of RAD51 during the HR mechanism (Bhin et al., 2023).
In addition to resistance development, non-specific targeting of PARP enzymes (PARP4, PARP5) by PARPi can lead to undesirable toxicities (Goodman, 2022), affecting normal cellular functions and potentially causing adverse effects. Next to DDR, PARP1 is

involved in essential housekeeping functions within cells, including the maintenance of the regulation of gene expression (Ciccarone et al., 2017; Kraus & Lis, 2003; Marjanović et al., 2017). Disruption of these vital cellular processes by non-specific PARP inhibition can harm the overall cellular homeostasis.

Adverse effects of PARPi include a spectrum of hematologic toxicities. Also, gastrointestinal disorders, including vomiting, are associated with off-target kinase inhibition, a phenomenon commonly observed with kinase inhibitors (Tian et al., 2022). Additionally, cardiotoxicity events are evident, particularly with niraparib use, showcasing manifestations such as increased blood pressure, heart rate, and hypertension (Tian et al., 2022) . The NOVA trial results indicated that niraparib treatment resulted in Grade III-IV hypertension in 9% of patients, with a median duration of 15 days (del Campo et al., 2019; Tian et al., 2022).

While PARPi hold promise as therapeutic agents, the non-specificity of their action on PARP1 underscores the need for further research and development of more selective inhibitors to minimize off-target effects and maximize therapeutic benefits.

1.4.4.2. Overcoming PARPi-resistance and toxicity

Overcoming PARPi resistance and toxicity presents a critical challenge in cancer treatment. Two distinct pathways have been identified as potential contributors to this issue. Firstly, the trapping of PARP at DNA lesions may lead to unintended toxicity. Secondly, inhibiting essential housekeeping functions performed by PARP enzymes is another avenue through which toxicity may arise.

In the past few years, there has been a distinct focus on developing PARP1-specific inhibitors to minimize potential off-target effects targeting other PARP-family members (Goodman, 2022). On the other hand, researchers are actively investigating downstream targets of PARP1, aiming to create inhibitors that selectively modulate its DDR function while sparing its other essential roles. This approach holds promise in refining PARP1 inhibition strategies, providing potential solutions to overcome the challenges associated with its various functions, and paving the way for more targeted and effective therapies in cancer treatment. Among these is the emerging candidate ALC1, an ATP-dependent chromatin remodeler associated with DNA repair processes (Verma et al., 2021). Exploring the potential of ALC1 as a downstream target of PARP1 underscores the dynamic landscape of DNA repair strategies, offering prospects for enhancing the effectiveness of therapeutic interventions across a broader range of cancer types.

1.5. ALC1 (CHD1L)

1.5.1. Introducing ALC1

Amplified in Liver Cancer 1 (ALC1), alternatively known as Chromodomain-Helicase-DNA-Binding Protein 1-Like (CHD1L), is a poly (ADP-ribose)-regulated chromatin remodeling enzyme that has emerged as relevant in cancer, particularly in its response to PARP inhibitors (Hewitt et al., 2021; Verma et al., 2021). As a validated oncogene, ALC1 is amplified in BRCA1/2 deficient ovarian and breast cancer and potentiates cancer cell-killing properties of the PARPi olaparib (Juhász et al., 2020; Zimmermann et al., 2018).

ALC1 is an allosterically regulated remodeler that relaxes chromatin and plays a vital part in the DDR (Sellou et al., 2016).

The ALC1 enzyme features a two-lobed catalytic Snf2-like ATPase domain, sharing characteristics with ATP-dependent DExx-box helicases. This domain is linked to a C-terminal macrodomain, responsible for targeting chromatin in an activity-dependent manner influenced by PARP1 (Ahel et al., 2009; Gottschalk et al., 2009, 2012; Singh et al., 2017). The ALC1 ATPase and its macrodomain operate jointly, helping to regulate ALC1's activity through the activation of PARP1. When a small chain of at least three ADP-ribose units (called Tri-ADP-ribose) binds to ALC1's macrodomain, it initiates conformational alterations that interfere with self-inhibitory connections. This, in turn, enables DNA-dependent ATPase activity in vitro and chromatin remodeling in vivo (Dasovich et al., 2021; Singh et al., 2017).

This reciprocal interplay of the PAR-binding macrodomain and the catalytic ATPase component of ALC1 resembles the allostery found in DNA methyltransferases (Guo et al., 2014; Jeltsch & Jurkowska, 2016). The allosteric regulation of ALC1 is shown in Figure 12.

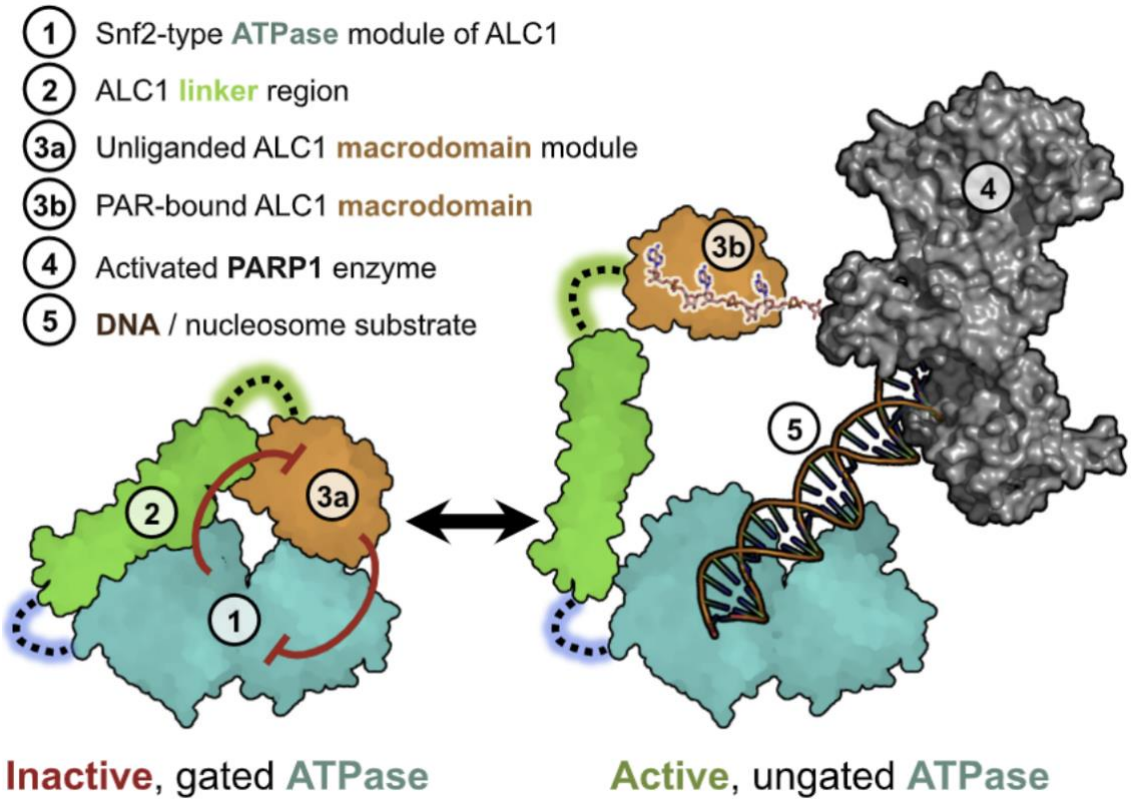

Figure 12: ALC1 is regulated by modular allostery
Autoinhibition is achieved through interactions of ALC1s ATPase (1) and macrodomain (3). As a product of PARP1 (4), PAR triggers ALC1-promoted chromatin relaxation as an allosteric activator in the event of DNA damage (figure from Singh et al., 2017).

ALC1 is crucial for chromatin dynamics. It uses ATP to slide nucleosomes, affecting how nucleosomes are arranged within the chromatin organization (Ahel et al., 2009; Gottschalk et al., 2009). Ahel et al. (2009) demonstrated that the wild-type ALC1 orchestrates ATP-dependent nucleosome sliding, whereas the ATPase-dead mutant K77R exhibited no such activity. The nucleosome repositioning function of ALC1 was dependent on the histone H4 tail, highlighting a specific molecular prerequisite for its activity. ALC1-mediated nucleosome movement exhibited a directional preference, tending to shift nucleosomes from central positions to regions proximal to the ends of DNA fragments. This directional propensity aligns ALC1's function with enhancing chromatin accessibility rather than conventional nucleosome reorganization or spacing (Ahel et al., 2009). ALC1 exhibits selectivity for oligo-ADP-ribose, and its ATPase activity prevents the macrodomain of ALC1 from binding to PARP1 under non-DNA damage conditions. This ensures that PARP1-dependent chromatin relaxation occurs exclusively when PARP1 is activated, such as during DNA damage (Singh et al., 2017).
In the study by Verma et al. (2021), ALC1 was identified as a critical factor influencing PARP inhibitor toxicity in HRD cells. Loss of ALC1 significantly decreased the viability of

BRCA-mutant cells and enhanced sensitivity to PARP inhibitors by approximately 250-fold. Chromatin accessibility was reduced with decreased association of repair factors leading to replication-associated DNA damage (Verma et al., 2021). Ding et al. (2022) showed that depletion of ALC1 can reverse acquired resistance to talazoparib.
All these findings suggest that substances promoting the stable inactive state of ALC1, diminishing its catalytic effectiveness, or interfering with its capacity to identify PAR may have the potential to inhibit the robust chromatin relaxation capabilities.

1.5.2. ALC1 impact on protein dynamics at DNA lesions

ALC1 is implicated in different repair pathways like BER, where ALC1-mediated nucleosome remodeling is essential in the sequence of events following base excision by DNA glycosylases but precedes the action of APEX1. The absence of ALC1 results in the generation of harmful BER intermediates, causing the formation of single-strand gaps and eventual collapse of replication forks (Hewitt et al., 2021; Ooka et al., 2018). Inhibiting this cellular process enhances sensitivity to PARPi, establishing a crucial reliance on HR (Hewitt et al., 2021).
Research conducted by Juhász et al. (2020) revealed that the chromatin remodeler ALC1 plays a significant role in facilitating the timely mobilization of PARP1 from DNA lesions. It was discovered that ALC1 can indirectly remove inactive PARP1 by associating with PARylated chromatin. As a result, ALC1 deficiency led to enhanced trapping of inhibited PARP1, which interfered with binding DNA repair factors involved in both NHEJ and HR repair to DNA lesions. Furthermore, they discovered that ALC1 overexpression, commonly observed in different tumor entities, decreases the sensitivity of BRCA-deficient cells to PARPi. These findings suggest that ALC1-dependent PARP1 mobilization is crucial in developing PARPi resistance. They propose a model where ALC1 impacts olaparib-mediated synthetic lethality through PARP trapping (Figure 13) (Juhász et al., 2020).

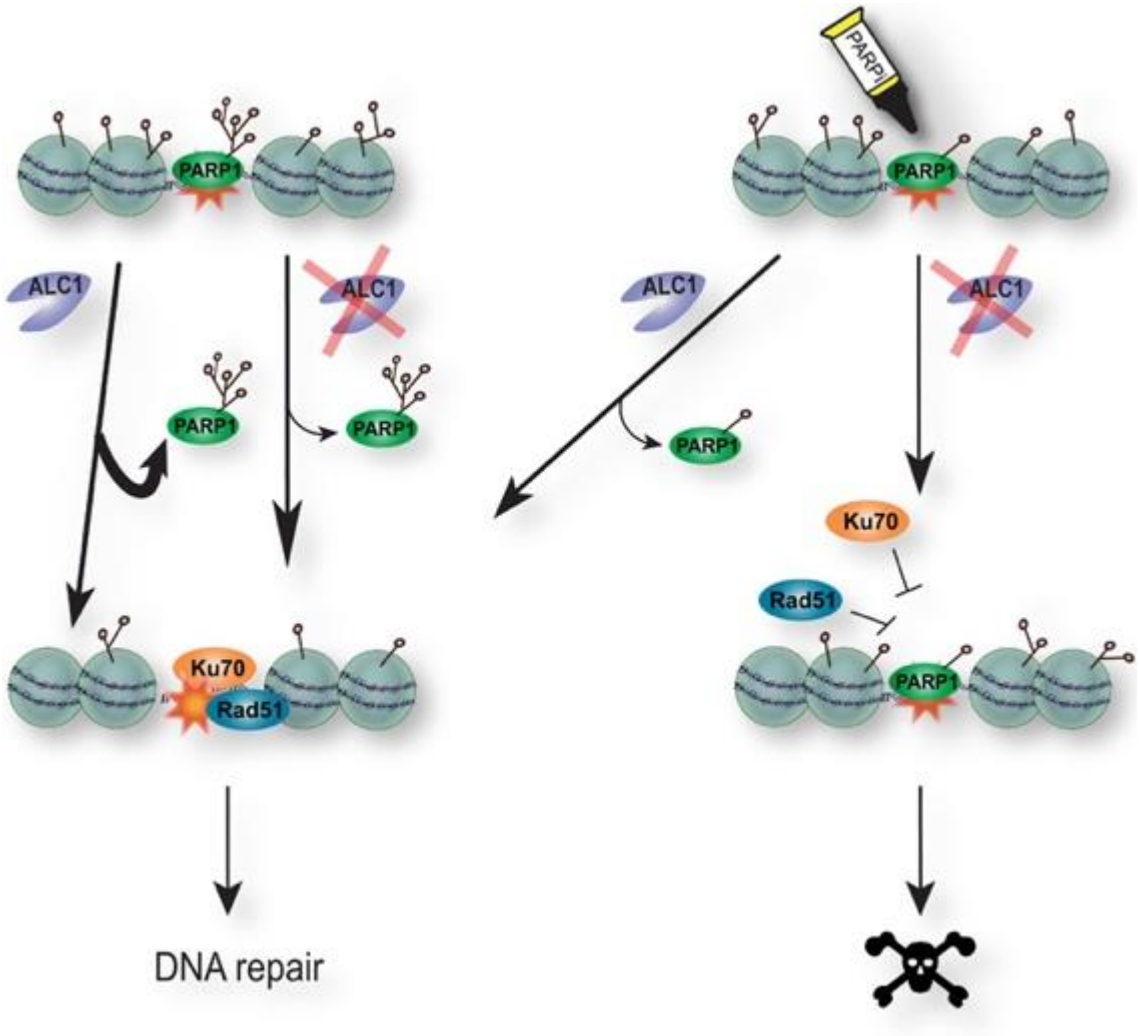

Figure 13: Olaparib-mediated synthetic lethality through ALC1
In case of DNA damage (red star), PARP1 recruits to the damaged area and PARylates proteins, including itself. The displacement of PARP1 from these locations encompasses a dual mechanism, combining auto-PARylation and ALC1-mediated mobilization. This process is essential for recruiting repair factors such as Ku70 or Rad51, leading to functional DNA repair (left path). Blocking auto-PARylation in ALC1-deficient cells, such as using PARP inhibitors (PARPi), impedes the disengagement of PARP1 from DNA lesions. This obstruction hampers the recruitment of subsequent repair factors, ultimately resulting in cell death (right path) (figure from Juhász et al., 2020).

When PARylation signaling is present, the absence of ALC1 affects the removal of PARP1 from DNA damage sites, but other processes like PARP1 auto PARylation can partially compensate, allowing DNA repair to proceed. When PARylation is impaired, ALC1 becomes crucial in mobilizing PARP1 from the damaged sites. Efficient removal of PARP1 by ALC1 is essential for the proper functioning of downstream DNA repair pathways. The study demonstrates that ALC1's ability to move along the chromatin fiber is responsible for displacing PARP1 from the damage sites (Juhász et al., 2020).

1.5.3. ALC1 inhibitors

Small molecule inhibitors targeting ALC1 offer a potential strategy to modulate the activity of this cancer-related poly (ADP-ribose)-regulated chromatin remodeler. By specifically targeting ALC1, researchers aim to overcome ALC1-related oncogenic effects and uncovering new opportunities for personalized and effective cancer treatments as an alternative to PARPi.

Since 2019, Eisbach Bio GmbH has worked on developing inhibitors targeting ALC1 (ALC1i). Eisbach Bio GmbH designed SMIs to target and inhibit the allosteric enzymatic activity of ALC1. In a high throughput screen (HTS), a FRET-based (fluorescence resonance energy transfer) biochemical assay was utilized, which enabled the evaluation of compound efficacy in inhibiting ALC1's nucleosome-sliding activity under allosteric activation. Promising hits from the initial screen were validated using compound titrations in the nucleosome-sliding assay and an ATPase-based readout, offering a comprehensive understanding of their inhibitory effects. This approach ensured the validation of hits across different functional aspects of ALC1's activity. The selected compounds' efficacy was also evaluated in cell-based assays, including survival-readouts and protein dynamics at DNA lesions under treatment conditions. A list of ALC1i used in this study can be found in Supplementary Table 1.

Inhibiting ALC1 using an allosteric inhibitor offers a targeted approach to modulating its activity. Unlike competitive inhibitors, which directly compete with the substrate at the enzyme's active site, allosteric inhibitors bind to specific allosteric sites on ALC1. This binding event triggers a carefully orchestrated conformational change in the enzyme's three-dimensional structure, leading to a controlled reduction in its catalytic activity. This allosteric modulation enables fine-tuning of ALC1's function, allowing for more precise and context-dependent regulation of cellular processes in response to specific signals or conditions.

Another attempt to create ALC1 inhibitors was started by Abbott et al. (2020). Their paper presents pioneering research on inhibitors targeting the oncogenic protein ALC1 in the background of colorectal cancer. The researchers unveiled a novel biological role for ALC1 as a DNA binding component of the TCF transcription complex, pivotal for fostering TCF-driven epithelial-mesenchymal transition (EMT) and other malignancy-associated traits. The findings presented in their study from 2018, and their follow-up study (Prigaro et al., 2022) establish a fundamental basis for the creation of more therapeutic approaches that target ALC1, offering a strategy to address colorectal cancer and other malignancies driven by ALC1 (Abbott et al., 2020).

1.6. Synergistic effects of ALC1i with approved and investigational drugs

1.6.1. Combining DDR-targeting drugs to enhance treatment outcome

Contemporary cancer therapy includes a wide range of approaches, from single treatment modalities to complex combinations. Although chemotherapy remains fundamental, its effectiveness is limited by side effects and drug resistance. Drug combinations have emerged as a strategy to overcome these challenges. Research has shown that combined therapies are more advantageous than monotherapy, emphasizing the need to achieve synergistic effects. These synergistic effects occur when the combined impact exceeds the sum of individual drug effects, allowing for dose reduction and reduced toxicity, ultimately improving treatment outcomes (Duarte & Vale, 2022; Foucquier & Guedj, 2015; J. Tang et al., 2015).

Examples of classical drug combinations include 5-fluorouracil with leucovorin for the treatment of colon cancer (Arkenau et al., 2003). Also, combination therapies pairing PARPi with agents that inhibit complementary DNA repair pathways or enhance immune responses, have demonstrated promising results (Bhamidipati et al., 2023). PARPis' ability to induce DNA damage in various cancer types has ignited interest in their potential as sensitizers to traditional chemotherapy or radiation therapy (Sim et al., 2021). In early-phase trials, the combination of olaparib with the pan-PI3K inhibitor buparlisib has shown promising preliminary efficacy, with an overall response rate of 30% observed in patients with breast and ovarian cancer (Matulonis et al., 2017).

Exploring synergistic effects between HRD-targeting drugs and FDA-approved drugs opens new avenues for enhancing cancer treatment efficacy and overcoming drug resistance. Combination therapies involving PARP inhibitors (PARPi), and other DNA damage response (DDR)-targeting drugs present a rational and promising strategy for further combination efforts. The DDR is crucial in coordinating cell cycle progression and DNA repair, providing essential time for damage repair (Clay & Fox, 2021).

Key DNA damage repair factors, including ATM and CHK2, regulate cell cycle checkpoints during the G1/S phase, allowing repair before replication initiation (Bertoli et al., 2013; O'Connor, 2015). S-phase checkpoint proteins, ATM, CHK1, and WEE1, are crucial in delaying replication to allow sufficient time for dealing with DNA damage (Barnum & O'Connell, 2014; O'Connor, 2015). These kinases respond to different types of DNA damage while regulating the cell cycle, making them potential targets for maximizing DNA damage at different cell cycle stages. Combining inhibitors targeting these enzymes with other HRD-synthetic lethal inhibitors presents a rational approach to cancer treatment.

A synergistic effect may be induced when ALC1i is combined with DNA-damaging agents, such as PARPi, topoisomerase inhibitors (TOP1i, TOP2i), or other agents targeting key components of the DDR. The inhibition of ALC1 may lead to inefficient DNA repair, rendering chromatin less accessible to DNA repair enzymes and accumulating DNA damage. By simultaneously exposing cells to further DNA-damaging agents, this synthetic lethal combination exploits the compromised DNA repair capacity caused by ALC1 inhibition, leading to selective cancer cell death. The synergy between ALC1i and DNA-damaging agents provides a hopeful approach to boost the effectiveness of cancer therapies and overcome resistance mechanisms, providing potential breakthroughs in personalized and effective cancer therapy.

The individual mechanism of action and the rationale for combining different DNA-damaging agents and FDA-approved or investigational drugs with an ALC1i are described in Table 1**.** The most common reference models for drug combinations were summarized by Duarte & Vale (2022) and are explained in the methods section of this thesis.

Table 1: Mechanism of action and rationale for drug combinations with ALC1i (for references, refer to Supplementary Table 2)

Drug	Target	Compounds	Effect on DDR	Impact on cell cycle	Additional information	Rationale for Synergy
PARPi	PARP enzymes	Talazoparib, Olaparib, Rucaparib, Niraparib, Veliparib, Pamiparib, AZD5305	Impaired SSB, BER, and partially DSB repair through lack of PAR and protein trapping	G2-M arrest	Direct activation of ALC1 upon PAR synthesis by PARPs; potentiation of PARPi sensitivity in ALC1 gene knockouts. ALC1 deficiency impacts PARP1 trapping, leading to impaired binding of NHEJ and HR proteins to DNA and suppressing these crucial DNA repair mechanisms.	ALC1i may enhance the trapping ability of PARPi by affecting the dynamics of PARP recruitment and release. Inhibition of ALC1 could potentially prolong the residence time of PARP enzymes on DNA lesions, increasing the likelihood of PARP trapping and consequently amplifying the therapeutic efficacy of PARPi
TOP1i	TOP1	Irinotecan (active metabolite SN-38), Topotecan	Interrupt DNA replication, induce DNA SSBs breaks via TOP1ccs; replication fork collapse	G2 arrest	PARP-trapping independent synergy between PARPi and TOP1i.	Combining ALC1i with TOP1i may promote replication fork disruption and contribute to additional accumulation of DNA damage, which cannot be effectively repaired due to changes in chromatin accessibility or reorganization. Co-administering ALC1i with TOP1i is expected to lead to a synergistic potentiation of cell-killing effects independent of the PARP-trapping ability.
TOP2i	TOP2	Teniposide	Increase levels of TOP2-DNA cleavage complex resulting in DSBs, DNA-protein crosslinks, and inhibition of DNA strand re-ligation	Late-S-G2 arrest	Lack of synergy between etoposide and PARPi, aligning with the minimal involvement of PARP in repairing etoposide-induced lesions.	TOP2i induces DSBs, activating DNA recombination and repair processes that involve ALC1. Additional ALC1i may lead to the accumulation of unrepaired DNA damage, enhancing cancer cell-killing when combined with TOP2i. Considering the close relation in the mechanism of action of PARPi and ALC1i, the effects of ALC1i combined with TOP2i are expected to be rather additive than synergistic
ATMi	ATM	AZ32, AZD-1056, AZD1390,	Phosphorylates CHK1 and CHK2 to inactivate CDK1 and induce G2-cell cycle arrest; initiates strand resection to generate tracts of ssDNA to form substrates for HR repair	G2/M checkpoint inhibition	ATMi with PARP1i initially triggers G2 delay, followed by checkpoint bypass, resulting in mitotic cell death. ATMi leads to suppression of HR repair and promotes the process of PARylation. PARPi with ATMi effectively counteract the PARylation induced by ATMi. A Combined treatment results in a significantly higher level of DNA damage. Synergy between ATMi and PARP1i is not reliant on PARP1 trapping.	Given the observed similarities between ALC1i and PARPi in inducing cell cycle arrest in the G2/M phase and potentially causing accumulation of DNA damage and PARP1 trapping, it can be hypothesized that ALC1i may also synergize with ATMi in promoting DNA damage accumulation and checkpoint activation.
ATRi	ATR	Ceralasertib, Elimusertib	ATR induces HR-dependent repair; responsible for signaling ssDNA, particularly in response to replication stress	G2/M checkpoint inhibition	ATR activation is triggered by extensive ssDNA structures. ALC1 inhibition leads to dysfunctional SSB-repair, necessitating the activation of the ATR pathway to initiate this DNA repair process.	Given the reliance on ATR activity in the context of ALC1i, it is reasonable to hypothesize that ATRi combined with ALC1i would demonstrate a synergistic antiproliferative effect. Combined with accumulating damage through ALC1i, cell cycle checkpoint inhibition may result in mitotic catastrophe, a state of cell death stemming from unresolved DNA damage during mitosis.

BRDi	BRD	BAY-299	BRDi disrupt interaction between the bromodomain and the acetyl group, resulting in the downregulation of specific genes	n.d.	Functional disruption of TAF1 bromodomain leads to impaired DNA end resection, reduced loading of RPA and Rad51, and compromised HR, ultimately resulting in genome instability and heightened sensitivity to DNA damage	It can be hypothesized that the deficiency in HR caused by the TAF1 inhibitor BAY-299 would synergize with the inhibition of other DNA repair pathways mediated by ALC1 inhibition.
Alkylating Agent	DNA-crosslinker	Mitomycin C	Crosslinking the complementary strands of DNA, mainly targeting the CpG sequence	Non-specific to cell cycle, but maximum effect during late G and early S-phases;	The diverse DNA damage caused by Mitomycin C leads to a significant impediment to cellular proliferation and extensive cell death. Treatment with Mitomycin C led to G2/M cell cycle arrest	The addition of ALC1i to Mitomycin C may further hinder the repair of this DNA damage, thereby enhancing the antiproliferative effect of Mitomycin C
Taxane	Microtubule	Paclitaxel	Inhibiting the process of mitosis; disrupting dynamics of microtubules, resulting in subsequent cell death; leading to increased generation of reactive oxygen species (ROS)	M-phase arrest	Paclitaxel enhances the activity of NADPH oxidase associated with plasma membranes, leading to increased generation of reactive oxygen species (ROS).	Paclitaxel exerts its effects by disrupting microtubule dynamics and causing cell cycle arrest, specifically in the mitotic phase. Conversely, ALC1i induce cell cycle arrest at the G2/M phase. Due to these distinct mechanisms of action, the likelihood of synergistic effects between ALC1i and paclitaxel is low. Instead, additive effects are more probable, given the diverse pathways targeted by each agent.
VEGFRi, FGFRi	VEGFR, FGFR	Lenvatinib	FGFRi have been shown to hinder DNA DSB repair	Induce G0/G1 cell cycle arrest	VEGFRi can induce a hypoxic and acidic tumor microenvironment, leading to DNA damage and sensitization of tumors to DNA repair pathway inhibitors. Previous studies have reported synergistic effects between VEGFR/FGFR inhibitors and PARPi.	As PARPi synergize with VEGFRi, a similar synergistic effect may be observed in combination with ALC1i.
Wee1i	Wee1	Adavosertib	Critical role in DNA damage recognition/repair; leads to apoptosis upon treatment with DNA-damaging agents	G2/M checkpoint inhibition	Cells lacking the G1 cell cycle checkpoint (like many p53-deficient cancer cells) rely on the G2 checkpoint in response to DNA damage. Inhibiting the G2 checkpoint can sensitize p53-deficient tumors to antineoplastic agents, enhancing their cytotoxic effects	The combination is expected to accumulate unrepaired DNA damage, as WEE1i prevents cell cycle arrest at the G2 checkpoint, pushing damaged cells into mitosis prematurely. This may trigger mitotic catastrophes, like combinations with ATMi or ATRi. The combination therapy may sensitize cancer cells that have developed resistance to single-agent treatments, potentially improving overall therapeutic efficacy.
Thymidylate Synthase Inhibitor	Thymidylate Synthase	5-Fluorouracil	Induces DNA damage, (DSBs and SSBs) by incorporating FdUTP into DNA during the S phase. Main repair mechanisms involve MMR and BER.	Activity during the S phase of the cell cycle and is inactive in G0 or G1 phases	DNA damage can occur in all cell cycle phases in proliferating cells, and the repair mechanisms involved vary depending on the specific phase	DNA damage, including SSBs and DSBs, arising from FdUTP incorporation during S-phase via 5-FU treatment in combination with DNA damage accumulating through ALC1i is expected to show at least additive effects.

1.6.2. Summary of DNA damage induction potential and cell cycle regulation of inhibitors used in this study

Combination therapies involving ALC1i exhibit significant synergistic potential in cancer treatment by leveraging their impact on cell cycle regulation and DNA repair. The summarized findings from the section above were used to create an overview of the mechanism of different inhibitors on DNA damage induction and cell cycle regulation to explain the rationale for potential synergistic effects in combination treatments with an ALC1i (Figure 14).

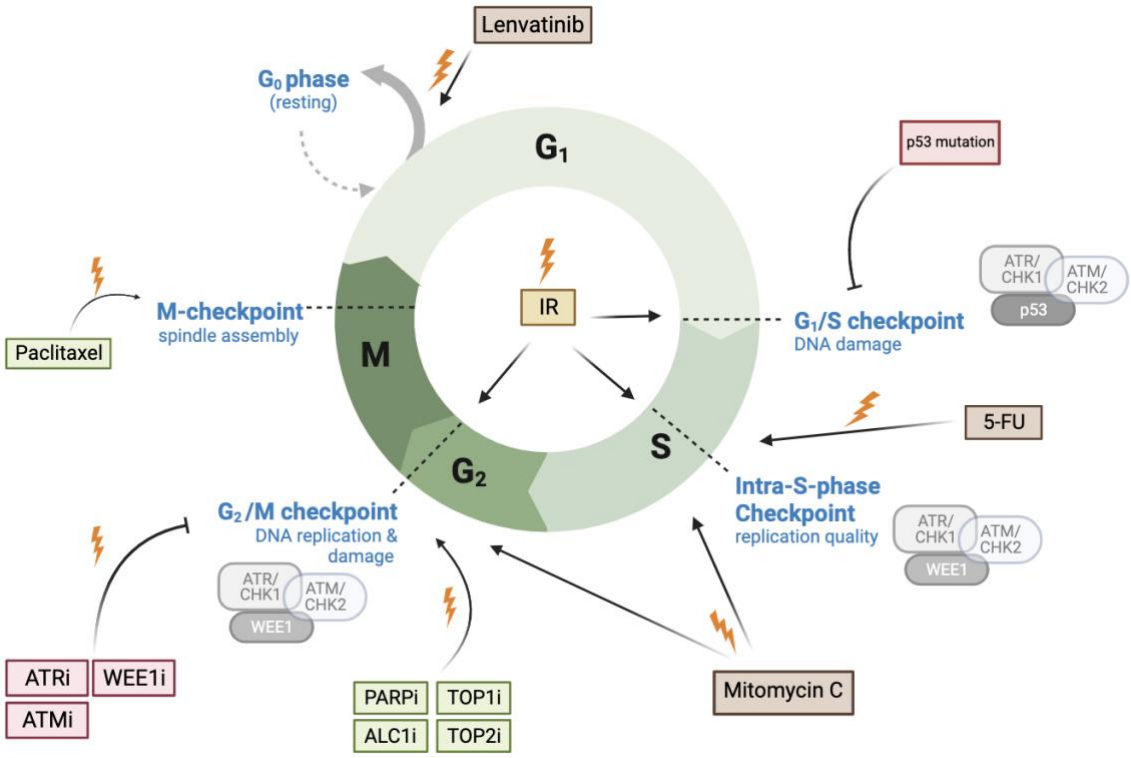

Figure 14: Effect of different inhibitors on DNA damage induction and the cell cycle
Cell cycle checkpoints are indicated in blue, and checkpoint regulators in grey (ATR, ATM, p53, WEE1). Inhibition of one of these enzymes (marked in red) leads to retraction of the checkpoint. Orange flashes indicate induced DNA damage. Inhibitors highlighted in green lead to cell cycle arrest at the G2/M phase (PARPi, TOP1i, TOP2i, ALC1i) or to arrest in the M-phase (Paclitaxel). Inhibitors shown in brown will lead to cell cycle arrest in S-phase (5-FU, Mitomycin C), G2-phase (Mitomycin C), or G1-phase (Lenvatinib). Ionizing radiation (IR) (yellow) induces DNA damage, leading to cell cycle arrest in the G1/S checkpoint, Intra-S-checkpoint, and G2/M-checkpoint (created with Scientific Image and Illustration Software | BioRender).

Dysfunctions in checkpoint regulators like p53 can result in the breakdown of checkpoint control, causing cells to become more dependent on alternative checkpoints. ATR, ATM, and WEE1 are vital in regulating the intra-S-phase and G2/M checkpoints. Inhibition of these enzymes (ATRi, ATMi, WEE1i) disturbs the checkpoints, causing cells to progress through the cell cycle, potentially leading to mitotic catastrophe. Most DDR-inhibitors that disrupt the cell cycle also induce DNA damage or lead to the accumulation of existing damage. Inhibitors that induce cell cycle arrest at the G2/M phase include PARPi, TOP1i, TOP2i, and ALC1i. Paclitaxel arrests the cells in the M-phase, while 5-FU leads to arrest in the S-phase. Mitomycin C shows the highest effect in G-and S-phases, whereas Lenvatinib affects the G1-phase. IR induces DNA damage, triggering cell cycle arrest at the G1/S, Intra-S, and G2/M checkpoints. Combining ALC1i with these inhibitors provides a multifaceted approach for testing combination therapies for a better clinical outcome (for references, see Supplementary Table 2).

2. Hypothesis and Objectives

2.1. Objective

PARP1 is a widely recognized and effective drug target in cancer therapy. However, ALC1, a downstream regulator, is emerging as a potentially superior target. Inhibiting ALC1 is expected to provide a higher level of specificity to DNA damage, avoiding the challenges linked to interfering with PARP1's essential roles in cellular maintenance. Inhibiting ALC1 may not only increase DNA damage but also interfere with HRD to effectively kill cancer cells with fewer side effects. Reducing ALC1 levels makes cells more sensitive to PARPi, potentially offering a way to overcome resistance to these drugs. Tackling PARPi resistance through ALC1 inhibition opens new treatment possibilities, especially in cancers with functional HR pathways. Combining ALC1 inhibition with FDA-approved drugs, similar to the effects seen with PARPi, could improve cancer treatment results.

2.2. Research Hypothesis

2.2.1. ALC1i is synthetic lethal with HRD and beyond

- PARPi-sensitive cells are also ALC1i-sensitive
- ALC1i kills cancer cells with HRD
- Mutations in BRCA1&BRCA2 can be used to predict ALC1i sensitivity
- Treatment with ALC1i leads to increased DNA damage accumulation
- Cells treated with ALC1i go into cell cycle arrest
- ALC1i changes protein dynamics at DNA lesions and leads to PARP trapping
- ALC1i monotherapy has tumor-suppressing activity in xenograft models
- ALC1i shows less toxicity and side effects than classical PARPi like olaparib or talazoparib

2.2.2. Combination of ALC1i with FDA-approved or investigational drugs will lead to synergistic cell-killing effects in cancer

- ALC1i is synergistic with PARPi and correlates with the trapping ability of PARPi
- ALC1i will synergize with different inhibitor classes that are involved in cell cycle inhibition and DDR

2.2.3. ALC1i treatment can overcome resistance to PARPi

- Long-time treatment of cancer cells with PARPi will lead to the development of drug resistance
- ALC1i can overcome PARPi resistance

3. Material and Methods

3.1. Cell line characterization and HR classification

3.1.1. Assay principle

Different methods were used to assess the HR repair capacity of cell lines. Methods include analysis of the mutational profile of cell lines, BRCA status, sensitivity to PARPi and functional readout by RAD51 foci formation assay.

3.1.2. BRCA status and PARPi sensitivity of a cell panel

BRCA status, HR-status, RAD51 foci formation, and PARPi sensitivity for the celllines were curated from publicly available databases. For each cell line, reported genetic alterations, functional DNA repair readouts, and pharmacological response data were collected. All sources used for the annotation of cell lines are listed in Supplementary Table 15. When discrepant results were reported across different references for the same parameter, these cases were flagged with **. Table 17 summarizes the results and compares the literature-derived annotations with in-house generated data.

3.1.3. Selection of previously reported HR-related genes

A compilation was made using public resources to generate a comprehensive list of genes involved in HR and its signature. The following studies were considered: K. B. Kim et al., 2021; Peng et al., 2014; Toh & Ngeow, 2021; Yamamoto & Hirasawa, 2021. A list of over 600 genes was curated. These genes were identified as directly or indirectly associated with HR and encompassed various aspects of the HR pathway. The list includes genes vital for DNA repair, replication, recombination, and genome stability. The list of genes can be found in Supplementary Table 3.

3.1.4. Mutational profiling of cell lines

Mutational profiles for HRD-related genes were retrieved from the DepMap project's public release 23Q2 (*DepMap: The Cancer Dependency Map Project at Broad Institute*, n.d.). The mutational information was extracted from the dataset associated with this release. The mutational profiles were derived from CRISPR knockout screens conducted in the project Achilles and genomic characterization data from the Cancer Cell Line Encyclopedia (CCLE) project, both integrated into the DepMap release. The mutational data were processed and reported according to the conventions outlined in the accompanying README.txt file. The mutational profiles for CHD1L are publicly available on figshare with the citation: DepMap, Broad (2023). The dataset can be accessed at https://doi.org/10.6084/m9.figshare.22765112.v2. Mutations were filtered for “deletions” and marked for mutations (Supplementary Table 4).

3.1.5. IR-induced γH2AX and RAD51 foci formation in cancer cell lines

The RAD51 foci formation capability of various cell lines was summarized using publicly available data. This information was obtained from previously published studies and databases, which provided insights into the response of different cell lines to DNA damage and their ability to form RAD51 foci in the context of HR. An in-house immunofluorescence assay was performed to validate RAD51 foci formation in selected cell lines.

Cancer cells were grown on glass coverslips overnight. The coverslips were placed in appropriate growth media culture dishes and incubated under standard cell culture conditions. The cells on the coverslips (at confluency >70 %) were subjected to irradiation to induce DNA damage. Two conditions were tested: 1 Gy and 0 Gy (control). Irradiation was performed at the specified dose rate. Following irradiation, the cells were allowed to recover for 2 h or 24 h. The recovery period allowed the cells to respond to DNA damage and initiate DNA repair processes. After the recovery period, the cells were fixed to preserve their morphology and retain RAD51 foci. Fixation was achieved by treating the cells with 4 % formaldehyde for 10 min. Iris Baur and Claudia Böhland from the Anna Friedl laboratory at the LMU, prepared immunofluorescence slides. The cells were subsequently treated as outlined in the methods section 3.8.

To better characterization the cell lines, spontaneous DNA damage before irradiation, and DNA repair function after 24 h (h), images were analyzed manually using contrast enhancement for the γH2AX-channel in Fiji (ImageJ). Foci were counted for each time point (2 h, 0 Gy, 2 h 1 Gy, 24 h 0 Gy, 24 h 1 Gy) (performed by Iris Baur and Claudia Böhland, Anna Friedl lab, LMU). The cells were categorized into the following groups: nuclei with no γH2AX foci, 1-10 γH2AX foci, 11-20 γH2AX foci and >20 γH2AX. A fraction diagram was created for the tested cell line using GraphPad Prism for Mac OS X (Version 9.4.1.).

3.2. Cell-culture maintenance

3.2.1. Cell-propagation of adherent cell lines

Cell lines were obtained from different vendors. The cell lines included in the cell-panel can be found in Supplementary Table 5.

Cells were maintained in the cell-culture media indicated in Table 2. All cell lines were routinely cultured in media containing antibiotics (100 U penicillin / 0.1 mg/mL streptomycin) if not stated otherwise, with a splitting-routine twice a week. Cells were grown in 5 % CO_2 and 95 % air at 37 °C.

3.2.2. Cell-freezing and thawing

Cells were trypsinized and collected in fresh medium containing 20 % FBS and 10 % DMSO. Mr. Frosty™ (Thermo Scientific) was used to freeze the cells down to -80 °C. The cells were transferred to a nitrogen tank and stored at <-160 °C. The cell amount frozen down was usually ½ T75 culture flask.

Cells were removed from the nitrogen storage tank for cell-thawing and slowly thawed to room temperature. The cells were added to 5 mL medium and spun down at 300 g for 5 minutes. The old medium was aspirated, and the cells were resuspended in fresh and pre-warmed cell culture medium and added to a T75 flask. Cells were incubated at 37 °C and 5 % CO2 until they reached 80 % confluency.

3.2.3. Material

Table 2: Material cell-culture maintenance

Consumable	Supplier	Catalog #	Storage, Aliquots
Pen Strep (Penicillin Streptomycin), 100 mL	Gibco	15140-122	-20 °C, 5 mL aliquots
FBS	Gibco	10270-106	-20 °C, 50 mL aliquots
FBS (Honduras origin)	Sigma	F7524 (443,00 €)	-20 °C, 50 mL aliquots
L-Glutamine, 100 mL	Gibco	25030-024	-20 °C, 5 mL aliquots
MEM NEAA, MEM Non-Essential Amino Acids	Gibco	11140-050	4 °C
Insulin, human	Sigma	I9278	4 °C
Hydrocortisone	Sigma	H4001	4 °C
HEPES, pH 7,5	Serva	25245	4 °C
Ham's F12	Sigma	N6658	4 °C
RPMI-1640	Gibco/Thermo Fisher Scientific	21875-034	4 °C
RPMI-1640 (w/o phenol red)	Gibco/Thermo Fisher Scientific	11835030	4 °C
DMEM-high glucose (+L-Glutamine)	Gibco	41965	4 °C
DMEM-high glucose	Sigma	D5671	4 °C
McCoy's 5A medium (+ L-Glutamine)	Gibco	16600-082	4 °C
MEM	Gibco	31095-029	4 °C
Mr. Frosty	Roth	AC96.1	
Trypsin-EDTA	Sigma	T3924	100 mL
1x PBS	Sigma	D8537	500 mL
Sterile tips Fisher brand SureOne	Thermo Fisher Scientific/Fisher scientific		
Serological pipettes	Greiner-Bio		5 mL, 10 mL and 25 mL
Cryovials	Thermo Fisher Scientific	377267	1.8 mL vials
Cell culture flasks T-75	TPP	90076, 90026	T-75, T-25

Consumable	Supplier	Catalog #	Storage, Aliquots
Glass tips	ROTH	4522	
Falcon tubes	Greiner-Bio	227 261, 188 271	15 mL and 50 mL falcons
Sterile DMSO	Sigma	34969	room temperature
Equipment	**Supplier**	**Catalog number**	**Comment**
Cell incubator	Heraeus	Hera Cell	
Laminar flow hood	Heraeus	Lamin Air HB2448	
Hemocytometer	NanoEn Tek (ordered by ROTH)	2N14712	Single-use, C-Chip
Inverted microscope	Zeiss	Axiovert 25	
Pipet boy	Thermo Scientific		
Vacuum pump	Vacuu-brand	BVC-21	
Water bath	P-D Industriegesellschaft GmbH	TYP WB 20	
Freedom Evo200	Tecan		With washer and Sunrise reader

3.3. SRB-cellular survival assay

3.3.1. Assay principle

The sulforhodamine B (SRB) assay is commonly employed to ascertain cell density and in vitro cytotoxicity screening, based on the measurement of cellular protein content. The assay depends on SRB's capacity to attach to the protein constituents of cells (under mild acidic conditions) that have been fixed to tissue-culture plates by tri-chlor-acetic acid (TCA). The dye dissociates under alkaline conditions. As the interaction between SRB and cellular components is stoichiometric, the quantity of dye extracted from stained cells correlates directly with the cell mass (Vichai & Kirtikara, 2006). The assay principle for the SRB survival readout modified by Eisbach Bio GmbH is shown in Figure 15.

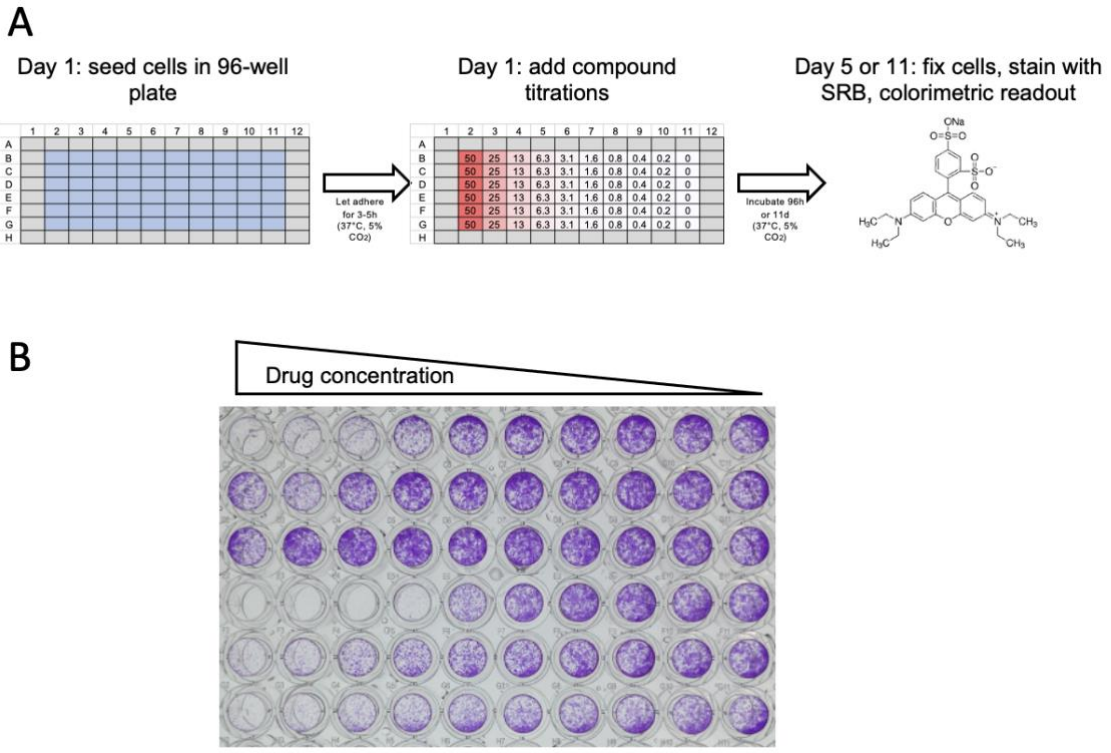

Figure 15: Assay principle of SRB-cellular survival assay

A) Cells were seeded in 96-well plates, let adhere for 3-5 h at 37 °C, 5 % CO2. cells were treated with compound titrations and incubated for 96h or 11 days. After fixation with 10 % ice-cold TCA, cells were stained with sulforhodamine-B sodium salt, washed with 1 % acetic acid, and dissolved using 10mM Tris pH10.5. B) picture of a typical SRB survival assay plate after SRB staining. Cells were treated with different inhibitors for 96h.

3.3.2. SRB-cellular survival assay

The assay was run based on the protocol modified from the patent (PCT/EP2021/084089, William Menzer et al., 2022). In short, cells were seeded in 96-well plates in 100 µL cell-culture medium. Cell count was adjusted to the doubling rate of each cell line. Results from the SRB-cellular survival assay exhibit-ed a linear range over densities from 100 – 10.000 cells per well, and the sensitivity was comparable to those of fluorometric methods.

A compound master-mix (11x) was prepared in cell-culture medium and added to the cells (10 µL). The dimethyl sulfoxide (DMSO) concentration in the master-mix was adjusted accordingly. The standard concentration range for cellular survival assay was 50- 0 µM in a 2x dilution. Vehicle (DMSO; final concentration on cells 0.5 %) was used as a control for 100 % survival rate. Empty wells filled with cell culture medium were used as a 0 % survival control. The outer wells of the 96-well plate were not used to avoid edge effects. Cells were cultured at 37 °C, CO2 5 % for 96 h or 11 days, and fixed with

100 µL ice-cold 10 %(w/v) TCA / well for 1h. After a 3x wash with 200 µL H_2O / well, Cells were stained with 0.057 % (w/v) sulforhodamine B (SRB) dissolved in 1 % (v/v) acetic acid. SRB was incubated for 30 minutes at room temperature (RT). After washing the cells 3x with 200 µL / well 1 $\%_{(v/v)}$ Acetic Acid, 100 µL / well 10 mM Tris (pH 10.5) solution was added to solubilize the stain. The 96-well plates were placed on a shaker at 800 rpm for 5 minutes, and absorbance was measured at 492 nm using the SUNRISE TECAN. The data was normalized to 100 % survival (=DMSO control) versus 0 % survival (empty wells) using the following formula: % survival= (ODsample – mean Odall-dead)/ (mean ODall-alive – mean Odall-dead) *100.
Each assay included 2 technical replicates. Inhibitor vs. response curves were fitted using GraphPad Prism for Mac OS X (Version 9.4.1.) non-linear regression, variable slope (four parameters). Half-maximal inhibitory concentration (IC50) values were determined by PRISM, half maximal effective concentration (EC50) values were estimated manually. For material, see Table 3.

3.3.3. Material

Table 3: Material SRB-cellular survival assay

Consumable	Vendor	Catalog #	Comment
96-well plates	Corning	3599, 3598, 3628	Flat-bottomed, clear, polystyrene, TC-treated
96-well plates	Greiner	655182, 65180	Flat-bottomed, clear, polystyrene, TC-treated
TCA	Sigma	T4885	Prepare fixation solution of 10 % TCA in MQ, store at 4 °C
Acetic acid	Sigma	33209	Prepare 1 % $_{(v/v)}$ acetic acid solution
Sulforhodamine B sodium salt	Sigma	S1402	make SRB solution: L , store at 4 °C
Sterile filter tips, Sapphire	Greiner-Bio	771261, 773261, 737265, 750261	10 µL, 20 µL, 200 µL, and 1250 µL
Serological pipettes	Greiner-Bio	606180, 607180, 760180	5 mL, 10 mL and 25 mL
Glass tips	ROTH	4522	
Falcon tubes	Greiner-Bio	227 261, 188 271	15 mL and 50 mL
Trypsin-EDTA	Sigma	T3924	100 mL
PBS	Sigma	D8537	500 mL
Integra sterile tips	Integra	4444, 4424, 4414	
Cell culture medium	see Table 2		
Equipment	**Supplier**	**Catalog Number**	**Comment**
Plate reader	Tecan	Sunrise	490-530nm
Cell incubator	Heraeus	HeraCell	
Laminar flow hood	Heraeus	LaminAir HB2448	

Hemocytometer	NanoEnTek (ordered by ROTH)	2N14712	Single-use, C-Chip
Inverted microscope	Zeiss	Axiovert 25	
Pipet boy	Thermo Scientific		
Vacuum pump	Vacuubrand	BVC-21	
Water bath	P-D Industriegesellschaft GmbH	TYP WB 20	
Freedom Evo200	Tecan		With washer and Sunrise reader

3.4. Synergy of ALC1i with approved and investigational drugs

3.4.1. Assay principle

The synergy assay is a technique used to evaluate the interaction between two or more drugs or treatments to determine whether their combined effect is greater than the sum of their individual effects. The principle of the synergy assay involves quantifying and comparing the effects of the individual treatments and their combination on a biological response, such as cell growth inhibition, apoptosis induction, or biomarker modulation. The summarized models for the analysis of drug combinations by Duarte & Vale (2022) are shown in Figure 16 and defined as follows:

The *Bliss Independence Model* assumes the independence of drug actions in combinations, with drugs acting on distinct sites and contributing to the observed effect, expressed as probabilities (Greco et al., 1995). Although its application depends on knowledge of mechanisms of action, it assumes exponential dose-response relationships and is limited to effects within a probability range (Foucquier & Guedj, 2015; Goldoni & Johansson, 2007; Mc, 1989).

The *Loewe* synergy model is a dose-effect-based approach for quantifying drug interactions. It defines an additive effect based on the isobole representation, assuming dose equivalence and sham combination principles. This model predicts drug interactions by comparing combined doses of two drugs to their individual doses. Isobologram analysis further visualizes these interactions graphically (Lederer et al., 2019; Sidorov et al., 2019). The model's applicability is limited to drugs following the Hill equation, with similar dose-response trends as well as equal peak effects (Sidorov et al., 2019).

The *Zero Interaction Potency (ZIP)* synergy model is a recent reference model designed to assess expected responses in drug combinations. It combines features from other models, including Bliss and Loewe. Unlike other models, ZIP evaluates how drugs interact by measuring variations in the potency of dose-response graphs for both single and combined treatments. This approach assumes that when drugs are combined, they

stay separate and do not influence each other, leading to only slight alterations in corresponding response patterns (Yadav et al., 2015). The effectiveness of this model relies on accurately modeling dose-response trends, particularly for determining factors like the relative half-maximal effect concentration (EC50), which becomes challenging if data quality is suboptimal (Vlot et al., 2019). In this thesis, the assessment of synergistic effects was conducted using the ZIP synergy model.

3.4.2. ZIP synergy score in 96h SRB survival assay

The synergy of ALC1i with other drugs was determined in the 96h survival assay in a 2-D titration format. The assay was run based on the protocol modified from Menzer, Sahiri, and Schomburg (2025).

In brief, different cancer cell lines from the cell-panel were tested using a combination of ALC1i and other drugs. Like in the SRB-cellular survival assay, cells were seeded into 96-well plates containing volume of 80 µL. Compounds were prepared as a master mix solution in single agent titrations in a separate 96-well plate as a 10x Stock. 10 µL of each compound concentration were added to the according wells of the plate containing the cancer cells. The final volume per well containing cells and both drugs was 100 µL total. Cells were incubated for 96 h and processed as described in 3.3.2 SRB-cellular survival assay. The ZIP synergy score was determined by adding the 96h-SRB readout of at least three technical replicates into an open-source program called “SynergyFinder”. As a stand-alone web application, the SynergyFinder (SynergyFinder - Documentation), by Aittokallio (2022); Ianevski et al. (2019), (2020) was used for an interactive analysis and visualization of drug combination screening data. Drug interaction patterns were determined by analyzing the variation in potency of the dose-dependent graphs between individual drugs and their combinations. Some frequently employed reference models in the SynergyFinder include the Highest Single Agent (HSA), Bliss, Loewe, and Zero Interaction Potency (ZIP) models. The ZIP model enables a comprehensive assessment of various types of drug interaction patterns that may arise in high-throughput drug combination screening and thus was used in this analysis (SynergyFinder - Documentation). As the default settings provide, the function of the cNMF algorithm was used to detect and replace outlier measurements, and the four-parameter logistic regression (LL4) was used for curve fitting (Ianevski et al., 2019). The SynergyFinder builds a dose-response matrix on the results of a two-drug combination and scores the synergy based on the chosen model (Figure 16).

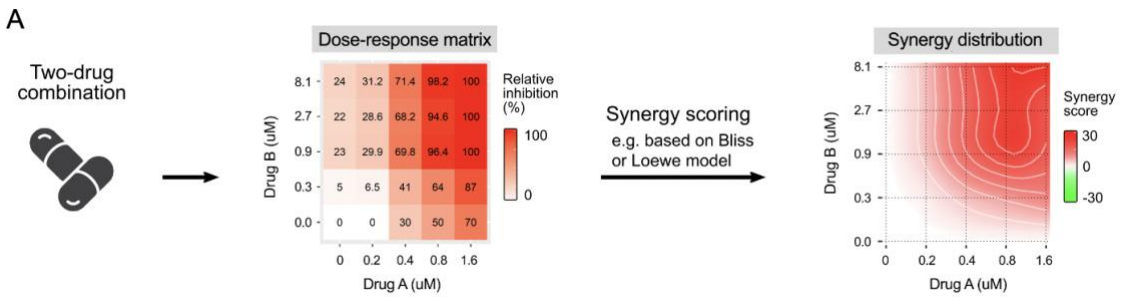

Figure 16: Visualization of synergy scoring by the SynergyFinder
Cell-viability results of a two-drug combination are used to build a dose-response matrix for each concentration used. The relative inhibition (%) is calculated and indicated in red. The synergy score is calculated based on the chosen model and shown in a 2-D synergy distribution diagram, where red color indicates higher synergy and green color indicates antagonistic effects (image from SynergyFinder - Documentation)

The data presented in this thesis was obtained using Version 2.0 and 3.0. The average summary synergy score is computed from all dose combinations in the 2-D titration matrix. The area with the highest level of synergy, referred to as the Most Synergistic Area (MSA), corresponds to the 3-by-3 dose-window with the greatest synergy in the dose-response matrix. For a comprehensive understanding of the synergy scores generated by this program, refer to Table 4.

Table 4: Synergy Score interpretation (SynergyFinder - Documentation)

Synergy score	Interpretation
Less than -10	interaction between two drugs is likely to be antagonistic
between -10 and 10	interaction between two drugs is likely to be additive
MSA higher than 10	interaction between two drugs is likely to be synergistic

3.4.3. Material

Refer to the material list in methods section 3.3.
All ALC1i used in this study are listed in Supplementary Table 1. All additional drugs used in this study are listed in Supplementary Table 6.

3.5. DNA damage detection in Comet assay

3.5.1. Assay principle

The comet assay, or single-cell gel electrophoresis, is a laboratory technique to evaluate DNA damage in individual cells. It involves subjecting cells to electrophoresis in an

agarose gel, allowing fragmented DNA to migrate toward the anode, producing a distinctive comet-like visual pattern that can be quantified to assess the extent of DNA damage (Olive & Banáth, 2006).

3.5.2. Comet assay

A modified version of the protocol from (Olive & Banáth, 2006) was used for the alkaline comet assay. In short, cells were plated in 6-well dishes and exposed to varying concentrations of EIS-1 (0.25 µM – 2.50 µM) or DMSO (0.00 µM) for 48 h. Dust-free frosted-end microscope slides were coated with 1 % agarose and dried overnight. Cells were trypsinized and collected in 0.4 mL cold cell-culture-medium. 1.2 mL 1 % low-gelling-temperature agarose (40 °C) was added to the cells, added onto the slides, and dried for 2 minutes. Alkaline lysis and electrophoresis were used to detect DNA breaks. The glass-slides were incubated in freshly prepared A1-lysis (1.2 M NaCl, 100 mM Na_2EDTA, 0.26 M NaOH (pH > 13)) solution at 4 °C for 3h in the dark following a 20-minute incubation in A2-rinse-solution (0.03 M NaOH, 2 mM Na_2EDTA (pH ~12.3)) at room temperature. Gel-electrophoresis of the glass-slides was conducted in A2 solution for 25 minutes at a voltage of 0.6 V/cm at a current of about 40mA. Glass slides were carefully washed with distilled water and stained with 2 µg/mL Hoechst in PBS for 20 minutes in the dark. Slides were imaged using a LEICA DMIL LED microscope with a LEICA DFC 3000 G camera system and a Cool LED pE-300 system for fluorescence imaging. The 20x/0.30 pH1 objective was used (Table 5). Individual comets were analyzed using the free software “OpenComet” (Version v1.3.1) (Gyori et al., 2014). In short, the Open-Comet plugin was run with default options (auto, background correction) for head finding. All images were reviewed and corrected manually by the following rules:

Color Threshold (IJ Iso Data, red) was used to visualize all cells. Comets were excluded if A) a comet included more than one cell, B) the surrounded cell did not reach the color threshold because it was out of focus (no red signal) or C) cells that were too small (artifact from agarose preparation) (Figure 17). After excluding all flagged cells, the raw data for the Tail Moments was plotted in GraphPad Prism for Mac OS X (Version 9.4.1.). The Tail Moment is calculated as the tail length times tail DNA % (Gyori et al., 2014). Contrast and brightness of images presented in this thesis were adjusted for better visualization purposes.

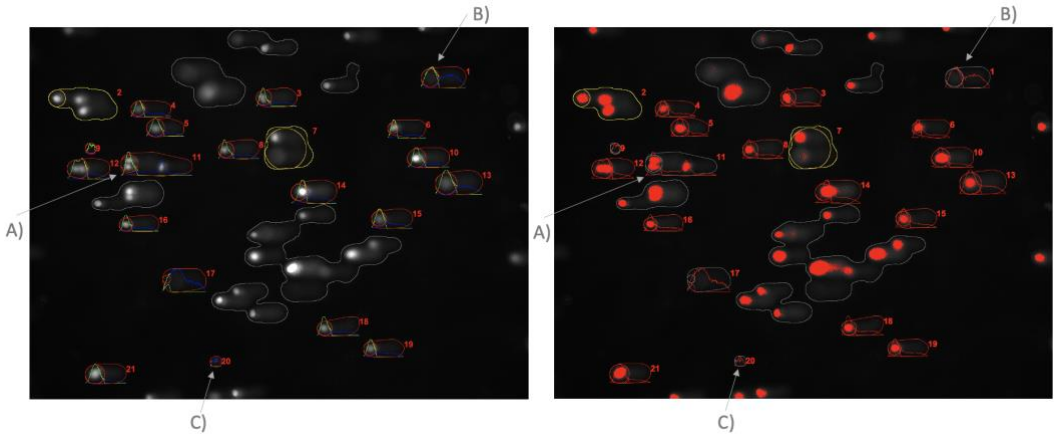

Figure 17: Adjustment to OpenComet Plugin for analysis of comets
Left image shows the output of the OpenComet macro, right image shows adjustment using the threshold method (red).

3.5.3. Material

Table 5: Material Comet assay

Consumable	Supplier	Catalog #	Comment
NaCl (g)	AQUA-Light GmbH		Lysis buffer
Na_2EDTA	Sigma	E5134	Lysis buffer/ Rinse solution
NaOH	ROTH	P031.5	Lysis buffer/ Rinse solution
1 % low melt agarose	Bio & Sell	BS.20.47.025	
Coverslips	VWR	ECN 631-1582	
Glasslides	Epredia	ISO 8037/1	
Trypsin	Sigma	T3924	
Cell medium	see Table 2		
Hoechst 33342	Fisher Scientific	H3570	
Equipment	**Supplier**	**Catalog #**	**Comment**
Cell incubator	Heraeus	HeraCell	
Laminar flow hood	Heraeus	LaminAir HB2448	
Hemocytometer	NanoEnTek (ROTH)	2N14712	Single-use, C-Chip
Inverted microscope	Zeiss	Axiovert 25	
Pipet boy	Thermo Scientific		
Vacuum pump	Vacuubrand	BVC-21	
Water bath	P-D Industriegesellschaft GmbH	TYP WB 20	
PowerPac™ Basic Power Supply	Bio-Rad	1645050	
fluorescence microscope	Leica		LEICA DMIL LED microscope (LEICA DFC 3000 G camera system & Cool LED pE-300 system)

3.6. γH2AX and cleaved PARPi protein levels in Western Blot

3.6.1. Assay principle

The assay principle for detecting γH2AX and cleaved PARP1 in a Western blot involves detecting and quantifying specific protein markers associated with DNA damage and apoptosis.

3.6.2. Western Blot

The assay was run based on the protocol modified from the patent Menzer, Sahiri, and Schomburg (2025).

Cancer cells were plated in 6-well plates and exposed to increasing concentrations of drugs or vehicle (DMSO) for different time points. Subsequently, the cells were collected and lysed using 1xSDS supplemented with benzonase (Millipore-E1014). The amount of 1xSDS was adjusted to the confluency in the 6-well; 100 µL 1xSDS was used for an 80 % confluent 6-well. Following denaturation for 10 minutes at 95 °C, lysates were spun down at 18.000 RCF for 10 minutes at room temperature, and the supernatant was transferred into fresh Eppendorf tubes. The lysate samples were loaded onto a gradient gel (Mini-PROTEAN TGX Stain-Free Precast Gels, 4-20 %, Bio-Rad 456-8095) for gel electrophoresis and run at 200 V, 400 mA for 25 minutes. The separated proteins were transferred onto a nitrocellulose membrane using the TransBlot turbo system (Bio-Rad) with the program pre-set “mixed molecular weight.” To prevent nonspecific binding, the membrane was incubated with intercept blocking buffer from LiCor for 1 h, following incubation with primary antibodies for 1h at room temperature and then secondary antibodies for another 1h at room temperature in the dark.

The following antibodies were used: Anti-ALC1, Anti- γH2AX, Anti- alpha-tubulin, 2 °AB (Licor): IRDye 800CW Goat anti-Rabbit, IRDye 680RD Donkey anti-Mouse (Supplementary Table 7). The membrane was imaged using the LiCor system. The protein quantity was assessed by analyzing the bands using FIJI (Image J), and the protein bands were normalized to the corresponding α-tubulin bands. For treatment analysis, the protein amounts in the different treatment groups were normalized to the DMSO control (Table 6).

3.6.3. Material

Table 6: Material Western Blot

Consumable	Supplier	Catalog #	Comment
Benzonase	Millipore	E1014	
Pierce BCA Protein Assay Kit	Thermo	23227	
4x SDS sample buffer	self-made	250 mM Tris HCl pH 6.5, 8 % SDS, 0,2 % Bromophenol-blue, 40 % Glycerol, 20 % Beta-mercaptoethanol	
Page Ruler Plus Pre-stained Protein Ladder	Thermo	26619	10-250 kDa
Mini-PROTEAN TGX Stain-Free Precast Gels,	Bio-Rad	456-8095	12 well or 15 well, 4-20%
TransBlot Turbo Midi-Size nitrocellulose	Bio-Rad	BR20200120	
TransBlot Turbo Midi-size Transfer Stacks	Bio-Rad	BR20201109	
Intercept Blocking buffer	Li-Cor	927-60001	
10x TBS	self-made	200 mM Tris, 1500 mM NaCl	
TBST	self-made	1x TBS + 0,1 % Tween	
Falcon tubes	Greiner Bio	227 261, 188 271	15 mL and 50 mL
Equipment	**Supplier**	**Catalog #**	**Comment**
Centrifuge	Eppendorf		Centrifuge 5427R
Thermoblock	Eppendorf		Thermomixer compact
Roller	CAT RM5		
PowerPac™ Basic Power Supply	Bio-Rad	1645050	
SDS-PAGE chamber	Bio-Rad	1658004EDU	Mini Protean Tetra System
Trans-Blot Turbo Transfer System	Bio-Rad	1704150	

3.7. γH2AX detection and Annexin V staining in FACS

3.7.1. Assay principle

The assay principle for detecting γH2AX using flow cytometry (FACS) is based on the principle of immunostaining. Cells are fixed to preserve their cellular structures and immobilize the proteins. The fixed cells are permeabilized using a suitable permeabilization agent to allow the antibodies to penetrate the cells and access their intracellular targets. The primary antibody is typically labeled with a fluorochrome, or a fluorophore-conjugated secondary antibody is used for detection. This antibody-antigen binding event enables the visualization and quantification of desired target proteins within the cells.

3.7.2. FACS analysis of γH2AX signal

MDA-MB-231 and SUM149PT cells were plated into 6-well plates and treated with EIS-1. SN-38 was used as a positive control for γH2AX signaling. The concentration of the vehicle (DMSO) was equal in all samples and the “no treatment” control. Cells were incubated at 37 °C and 5 % CO_2 for 120 h. FACS analysis was performed with the help of Dr. Markus Lechner (Eisbach Bio GmbH).

The cell supernatant was harvested, and the remaining adherent cells were trypsinized. All collected cells were combined in a centrifuge tube for further processing. The collected cells were washed once with 1xPBS to eliminate any residual media. Subsequently, the cells were stained with fixable live/dead far red dye at a dilution of 1:1000 in PBS, with a volume of 1 mL per sample. The staining was performed on ice for 15 minutes. Following staining, the cells were fixed by adding 3 times the volume of 4 % paraformaldehyde (PFA) and incubated for 15 minutes at room temperature. The fixed cells were centrifuged at 600g for 5 minutes, and the pellet was washed once with PBS.

The pellet was resuspended in 500 µL of ice-cold 100 % methanol to permeabilize the cells. After centrifugation at 600 g for 5 minutes, the permeabilized cells were washed once with PBS. Next, the cells were incubated with an anti- γH2AX antibody (Abcam, AB11174) at a dilution of 1:500 in FACS buffer (1 % BSA in PBS). A volume of 200 µL of the antibody solution was added per sample, and the cells were incubated for 40 min. at room temperature. Following the primary antibody incubation, the cells were washed once with PBS.

For secondary antibody staining, the cells were incubated with an anti-rabbit 488 antibody (Invitrogen, a11034) at a dilution of 1:3000 in FACS buffer for 40 minutes at room temperature (Supplementary Table 7). After the incubation, the cells were washed once with PBS. The stained cells were resuspended in FACS buffer and analyzed using a FACS Fortessa (BD Bioscience) flow cytometer. Gating was performed: Single-cell discrimination via SSC-A / SSC-H cutoff followed by dead cell discrimination via gating on APC-negative cells. Data analysis was performed using FlowJo 10.9.0 (Becton Dickinson & Company) (Material, Table 7).

For the apoptosis assay, MDA-MB-231 and SUM149PT cells were treated for only 48 h. Cell staining was performed using the protocol provided by the Annexin V-FITC/7-AAD Apoptosis Kit from Elabscience (E-CK-A212), and FACS analysis was performed with Dr. Markus Lechner (Eisbach Bio GmbH). In short, living cells were stained with Annexin V and counterstained with DAPI (for dead cells) right before FACS analysis.

3.7.3. Material

Table 7: Material FACS analysis of γH2AX signal

Consumable	Supplier	Catalog #	Comment
6-well plates	TPP	92006	
Trypsin-EDTA	Sigma	T3924	100 mL
1x PBS	Sigma	D8537	500 mL
fixable live/dead far red dye	Invitrogen	L34975	
Formaldehyde	Sigma-Aldrich	1.00496.0700	
Methanol	Roth	CP43.1	
FACS buffer	self-made		PBS + 1 % BSA
BSA	Sigma	A7030	
Annexin V-FITC/7-AAD Apoptosis Kit	Elabscience	E-CK-A212	
Equipment	**Supplier**	**Catalog #**	**Comment**
Cell incubator	Heraeus	HeraCell	
Laminar flow hood	Heraeus	LaminAir HB2448	
Hemocytometer	NanoEnTek (ordered by ROTH)	2N14712	Single-use, C-Chip
Inverted microscope	Zeiss	Axiovert 25	
Pipet boy	Thermo Scientific		
Vacuum pump	Vacuubrand	BVC-21	
FACS Fortessa flow cytometer	BD Bioscience		
FlowJo 10.9.0	Becton Dickinson & Company)		

3.8. γH2AX and RAD51 foci formation assay

3.8.1. Assay principle

The foci formation assay is used to assess DNA damage and DSBs within cells. This assay utilizes the phosphorylation of the histone variant H2AX at serine 139 (resulting in γH2AX formation) and the formation of RAD51 foci as a sensitive marker for DSBs. The principle of the foci formation assay involves the detection and quantification of these foci, which enables the assessment of DNA damage and repair kinetics within cells (Kuo & Yang, 2008).

3.8.2. Immunofluorescence for γH2AX and RAD51 foci detection

Cancer cells were plated on glass coverslips and treated with different concentrations of ALC1i or corresponding concentrations of DMSO for 24 h. After incubation, cells were washed 2x with PBS, fixed with 4 % Formaldehyde for 10 minutes, washed 2x with PBS, and permeabilized with 0.25 % Triton X-100 in PBS for 10 minutes. After blocking the cells with 3 % BSA in PBS for 1h, a primary antibody diluted in 3 %BSA/PBS was added

to the coverslips for 1h. Before adding the secondary antibody, cells were washed 3x with PBS. Alexa Fluor 488-con- jugated fluorescent secondary antibodies (Thermo Fisher) and Cy3 (Dianova) in 3 %BSA/PBS were added and incubated for 1h in the dark. All steps of slide preparation were performed at room temperature. After a last 3x PBS wash, coverslips were mounted in Fluoroshield (Sigma) containing DAPI and dried overnight at 4 °C in the dark. The following dilutions of antibodies were used: primary antibodies γH2AX (Novus, NB100-74435) 1:500 and RAD51 (Sigma, PC130) 1:200 and secondary antibodies Alexa Fluor 488 (Invitrogen, a11034) 1:1500 and Cy3 (Dianova, 515-165-062) 1:500 (Supplementary Table 7). Immunofluorescence slides were prepared with the help of Lucas Kalczynski.

Fluorescence imaging was performed on a Zeiss AxioObserver Z1 confocal spinning-disk microscope equipped with an sCMOS ORCA Flash 4.0 camera (Hamamatsu) using the C-Apo-63x water immersion objective lens. Images were taken as Z-Stacks with a range of 3.5 µM, 11 slices in 0.35 µM intervals with an optimum of 0.29 µM. The laser power of the DAPI and the AF488 channel was 10 %, and the laser power of the mCherry channel was set to 30.4 %.

For analysis of nuclear foci, czi. -images were processed with the following steps:

Using a self-written Fiji (ImageJ) Macro (“Image processing Z-project.ijm”), czi. - images were processed to a Z-Project with the projection of “Max Intensity”, channels were re-arranged in the order of red(γH2AX), green(RAD51), blue(DAPI) and saved as a “tiff”-file in a new folder. Next, images were normalized to 16-bit using a Python macro (”Z-project pixel norlaization.py”) that divided 32767 by each image array maximum. Contrast and brightness of images presented in this thesis were adjusted for better visualization purposes.

The BIC Macro-toolkit “FociCounter” for ImageJ from the University Konstanz (*FOCI Counter* | *BIC Macro Toolkit* | *Image Analysis* | *Service* | *Bioimaging Centre*, 2017) was used for foci analysis. The foci options are listed in section 7.3. Macros. The “Maxima Score “settings were adjusted accordingly to negative controls (cells with no treatment) and positive controls (cells with high dose DNA-damaging inducing agent like SN-38) in an HR-proficient, ALC1i-sensitive cell line (PSN-1). The program „Batch Co-localization Counter “was used to process all images (Material: Table 8).

The number of nuclei with <5 foci, ≥5 foci, and ≥15 foci for the γH2AX and RAD51 channels was determined and normalized to the total cell number per condition. The fraction of nuclear foci numbers was calculated. For statistical analysis, a two-way ANOVA test was used. The Macros used in this assay can be found in the supplement.

3.8.3. Material

Table 8: Material Foci assay

Consumable	Supplier	Catalog #	Comment
cell culture medium	see Table 2		
Coverslips	VWR	ECN 631-1582	
Glasslides	Epredia	ISO 8037/1	
6-well plates	TPP	92006	
10x PBS	Gibco (Thermo Fisher Scientific)	J62036.K2	
Formaldehyde	Sigma-Aldrich	1.00496.0700	
TritonX-100	Sigma	X100	
BSA	Sigma	A7030	
antibodies	Supplementary Table 7		
Fluoroshield	Sigma	F6057	
Nail-polish	Essence	Shine last & go!	
Equipment	**Supplier**	**Catalog #**	**Comment**
Confocal laser-scanning microscope	Zeiss	AxioObserver Z1	Capable of local photo-perturbation
Fiji software			OpenSource image processing program
Python software			
Cell incubator	Heraeus	HeraCell	
Hemocytometer	NanoEnTek (ordered by ROTH)	2N14712	Single-use, C-Chip
Inverted microscope	Zeiss	Axiovert 25	
Laminar flow hood	Heraeus	LaminAir HB2448	
Pipet boy	Thermo Scientific		
Vacuum pump	Vacuubrand	BVC-21	
Water bath	Lauda	E200	

3.9. Cell cycle analysis in FACS

3.9.1. Assay principle

Flow cytometry-based cell cycle analysis is a technique used to assess the distribution of cells within different phases of the cell cycle. This assay utilizes the ability of flow cytometry to measure the DNA content of individual cells, allowing the determination of cell cycle phases based on DNA content (Pozarowski & Darzynkiewicz, 2004). The principle of FACS (Fluorescence-Activated Cell Sorting) cell cycle analysis involves labeling cells with DNA-specific dyes, followed by their analysis using flow cytometry to quantify the DNA content and identify different cell cycle phases.

3.9.2. FACS analysis

The assay was run based on the protocol modified from the patent Menzer, Sahiri, and Schomburg (2025).

Cells were plated into 6-well plates and treated with EIS-1 or DMSO for 48 h. Further steps were performed with the help of Dr. Markus Lechner at Eisbach Bio GmbH.

Cells were trypsinized and washed in PBS before fixation/permeabilization via dropwise addition of ice-cold ethanol to a final concentration of 80 % ethanol while vortexing. Cells were centrifuged at 800 g for 10 minutes, ethanol was discarded, and the pellet was washed once with PBS. After another centrifugation step, cells were resuspended in 500 µL PBS and transferred into FACS tubes through a cell strainer. Cells were stained with 10 µg/mL DAPI (in PBS) for at least 10 minutes before analysis of cell cycle stages using a FACS Fortessa (BD Bioscience) flow cytometer. First, a forward scatter (FSC) versus side scatter (SSC) plot was used to identify the main population of intact cells. A gate was set to exclude debris and other small particles that may interfere with accurate cell cycle analysis. A gate was set to exclude doublets and aggregates to ensure the analysis of only single cells. This gate was based on DAPI signal height versus pulse width, where cells with similar DNA content but different pulse widths were considered single cells. After gating for single cells, the distribution in different cell cycle phases (G0/G1, S, and G2/M) was analyzed on a linear histogram for the DAPI signal using FlowJo 10.9.0 software. The determination of the proportion of cells in each phase was achieved by establishing gates or regions on the DNA content histogram to separate the distinct cell cycle phases into the G1 phase (2n DNA content), the intermitted S-phase followed by the G2/M phase peak (4n DNA content). (Material: Table 9)

3.9.3. Material

Table 9: Material cell cycle analysis FACS

Consumable	Supplier	Catalog #	Comment
6-well plates	TPP	92006	
Trypsin-EDTA	Sigma	T3924	100 mL
1x PBS	Sigma	D8537	500 mL
DAPI	Sigma	D9542	
Formaldehyde	Sigma-Aldrich	1.00496.0700	
Ethanol	Roth	P075.6	
FACS buffer	self-made		PBS + 1 % BSA
BSA	Sigma	A7030	
Equipment	**Supplier**	**Catalog #**	**Comment**
Cell incubator	Heraeus	HeraCell	
Laminar flow hood	Heraeus	LaminAir HB2448	

Hemocytometer	NanoEnTek (ordered by ROTH)	2N14712	Single-use, C-Chip
Inverted microscope	Zeiss	Axiovert 25	
Pipet boy	Thermo Scientific		
Vacuum pump	Vacuubrand	BVC-21	
Water bath	P-D Industriegesellschaft GmbH	TYP WB 20	
FACS Fortessa flow cytometer	BD Bioscience		
FlowJo 10.9.0	Becton Dickinson & Company)		

3.10. Live-cell recruitment assay

3.10.1.Assay principle

The Live Cell Recruitment assay (LCI) is used to study the dynamics of proteins in cells in real time. The assay uses time-lapse microscopy and involves monitoring protein dynamics in response to specific stimuli like micro-laser irradiation to induce DNA damage. The principle of the LCI assay applies the labeling of proteins and subsequent observation to assess recruitment and retention properties at the site of DNA lesions.
Using the 355 nm laser, a fast and local chromatin de-condensation is observed upon DNA damage. This decondensation is controlled by poly (ADP-ribosyl)-ation by PARP1. PARP1 modulates the chromatin structure by introducing the posttranslational modification poly-ADP-ribose, thereby recruiting different repair proteins. The chromatin remodeler ALC1 is such a protein that is recruited to these DNA damage sites through direct binding of PAR, and activated ALC1, in turn, relaxes the local chromatin structure. The assay principle is explained in Figure 18.

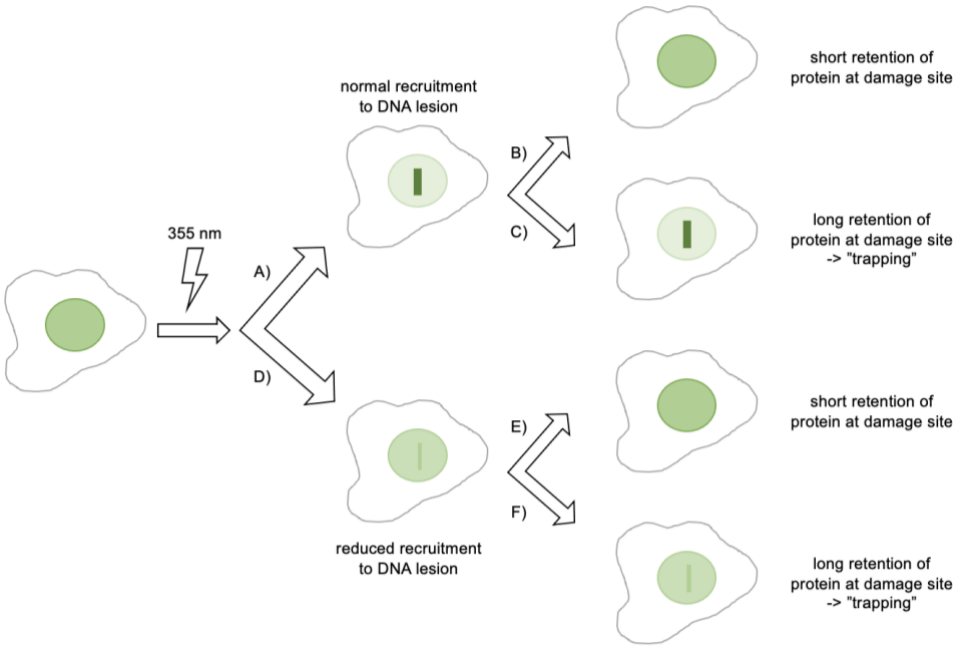

Figure 18: Principle of live-cell recruitment assay

U-2 OS cells are transiently transfected with a fluorophore-tagged nuclear protein (green). DNA damage is induced in the cell nucleus using a 355 nm laser. Dynamics of the protein at the damage site are indicated in a darker green color. Scenario A) shows regular recruitment of the protein to the DNA lesion. Under normal conditions, the protein has a short retention time at the damage site. It is released from the damage site (B). External factors, like treatment with a potent PARPi (e.g., talazoparib), can lead to longer protein retention at the damage site. The protein is “trapped” (C). Treatment of the cells with a specific inhibitor can change protein retention at damage site and alter the recruitment of the protein to the damage. D) shows reduced recruitment of the protein to the DNA lesion, with either a short retention time (E) or a prolonged retention time (F) (modified from (Sahiri et al., 2022) created using Microsoft PowerPoint).

3.10.2.Live-cell recruitment assay

The assay was run based on the protocol modified from Sahiri et al. (2022).

In brief, U-2 OS cells were seeded into 8-well Nunc Lab-Tek chambers in DMEM and cultured overnight at 37 °C, 5 % CO_2. Fluorophore-tagged plasmids with target inserts (Supplementary Table 8) were sequenced, and quality was checked using the IMPLEN Nanophotometer. The cells were transfected with the plasmids using XtremeGene HP DNA transfection reagent (Sigma) and incubated for 24 h at 37 °C, 5 % CO_2. 1 h before imaging, cells were treated with compounds (ALC1i or PARPi1) prepared in Leibovitz’s L-15 media containing 1 % PenStrep and 10 % FBS. DMSO (<1 %) was used as a vehicle control. Cells were imaged at 37 °C in the absence of CO_2 using a Zeiss AxioObserver Z1 confocal spinning-disk microscope with a sCMOS ORCA Flash 4.0

camera from Hamamatsu through a C-Apo 63× water immersion objective lens. Using the 355 nm laser operated through a single-point head (UGA-42 firefly, Rapp OptoElectronics), DNA damage was induced for 400 ms along a line of 74 pixels. The 355 nm laser power for the protein-trapping assay was set to 10 %. The 355 nm laser power in the protein-recruitment setup was adjusted to a lower laser power (2.5 %-5 %). Cells with a medium-low nuclear fluorophore intensity were imaged.
Imaging frames in seconds (s) for the protein-trapping and protein-recruitment assay are shown in Table 10. Contrast and brightness of images presented in this thesis were adjusted for better visualization purposes.

Table 10: Time-laps microscopy frames for recruitment and trapping LCI

recruitment

frame	1	laser damage	2	3	4	5	6	7	8	9	10	11	12	13	14	15	16	17	18	19	20	21	22	23
t [min]	0.00		0.08	0.17	0.25	0.33	0.42	0.50	0.58	0.67	0.75	0.83	0.92	1.00	1.08	1.17	1.25	2.25	3.25	4.25	5.25	6.25	7.25	8.25
t [s]	0.00		5.00	10.00	15.00	20.00	25.00	30.00	35.00	40.00	45.00	50.00	55.00	60.00	65.00	70.00	75.00	135.00	195.00	255.00	315.00	375.00	435.00	495.00

trapping

frame	1	laser damage	2	3	4	5	6	7	8	9	10
t [min]	0.00		0.25	0.50	5.33	10.33	15.33	20.33	25.33	30.33	35.33
t [s]	0.00		15.00	30.00	330.00	630.00	930.00	1230.00	1530.00	1830.00	2130.00

The signal intensity of fluorophore-tagged proteins at the site of DNA damage was analyzed as follows: A custom-made Fiji/ImageJ macro (Stackreg_extract single-nuclei.ijm) (modified from (Sahiri et al., 2022) was used to isolate single cells and fix their position using StackReg (Thevenaz et al., 1998). The single nuclei images were saved as a .tiff in a new folder. Another custom-made macro in Python was used for “Image Analysis for Peak Detection and Area Calculation “(written by Dr. Adrian Schomburg and William Menzer at Eisbach Bio GmbH). The macros can be found in the supplement.
The results were saved as CSV files. Cells that did not survive until the last imaging frame or created a hole in the damage site were flagged. All results per condition were compiled in a new Excel workbook as technical replicates. All flagged cells and cells with a signal intensity > 3.5 x10^6 were excluded from the analysis. Raw signal (as AUC) and values normalized to the maximum of all frames were plotted using GraphPad Prism for Mac OS X (Version 9.4.1.). Error bars indicate the SEM. All technical and biological replicates per condition were compiled into one graph. (Material: Table 11)

3.10.3.Material

Table 11: Material Live-cell recruitment assay

Consumable	Supplier	Catalog #	Comment
Lab-Tek II chambered	Thermo Scientific	155409	4- or 8-chambered
DMEM	Gibco/Thermo Fisher Scientific	31885-023	with 10% FBS, PS, FBS, L-glut
Leibovitz L-15 medium, Phenol red free	Gibco	21083-027	with 10% FBS, Pen/Strep

XtremeGene HP	Sigma	6366236001	Transfection reagent
XtremeGene HP	Sigma	6366546001	Transfection reagent
OPTI-MEM	Gibco	31985-062	100 mL
PBS	Sigma	D8537	500 mL
Trypsin-EDTA	Sigma	T3924	100 mL
Sterile tips Fisherbrand SureOne	Thermo Fisher Scientific		
Serological pipettes	Greiner-Bio		5 mL, 10 mL and 25 mL
Glass tips	ROTH	4522	
Falcon tubes	Greiner-Bio	227 261, 188 271	15 mL, 50 mL falcons
Equipment	**Supplier**	**Catalog #**	**Comment**
Nanophotometer	IMPLEN	N50	
Confocal laser-scanning microscope	Zeiss	AxioObserver Z1	Capable of local photoperturbation
Fiji software			OpenSource image processing program
Python software			
Cell incubator	Heraeus	HeraCell	
Hemocytometer	NanoEnTek (by ROTH)	2N14712	Single-use, C-Chip
Inverted microscope	Zeiss	Axiovert 25	
Laminar flow hood	Heraeus	LaminAir HB2448	
Pipet boy	Thermo Scientific		
Vacuum pump	Vacuubrand	BVC-21	

3.11. Resistant cell lines

3.11.1.Assay principle

Generating resistant cell lines is a valuable technique in biomedical research that allows scientists to study the mechanisms of drug resistance and develop more effective therapies. By exposing a cell line to a specific drug over time, the cells undergo genetic and phenotypic changes that enable them to survive and proliferate in the presence of the drug. These resistant cell lines provide a powerful tool to investigate the molecular pathways involved in drug resistance, identify novel targets for therapy, and test the efficacy of potential drug candidates. Furthermore, studying resistant cell lines can help researchers gain insights into the underlying mechanisms of disease progression and identify biomarkers that can support personalized medicine approaches. Overall, generating resistant cell lines contributes significantly to our understanding of drug resistance and facilitates the development of more targeted and efficient treatments for various diseases.

3.11.2.Generation of resistant cell lines

Resistant cell lines were obtained by culturing parental cancer cell lines with different mutational profiles in increasing concentrations of other drugs for over 4 months. In short, parental cell lines (DU-145, PSN-1, HCT 116) were seeded in culture dishes and treated with a low starting dose of the following compounds: talazoparib, olaparib. The medium was exchanged, and fresh compound was added every 2-4 days. As soon as cells reached 80% confluency, they were split into two new flasks. One flask was kept at the same concentration; the other was treated with an increased concentration of the same drug. The cell lines DU-145, 20 and DU-145, 23 were generated using different starting concentrations of talazoparib for acquiring drug resistance.

If the cells in the increased concentration survived, the lower-concentration cells were deleted. The procedure was repeated until high concentrations of the drugs were tolerated by the cells. Frozen stocks of the polyclonal cells were prepared, and colony-selection plates (dilution of cells over a plate for single-cell selection) were seeded in 96-well format. The cells were seeded in a drug-containing medium and incubated for >10 days at 37 °C and 5 % CO_2. Colonies were picked, expanded, and frozen stocks were prepared. Monoclonal cell lines were tested in the SRB-survival assay. Selected Clones were tested in an eight-week stability assay. Therefore, cells were maintained without the corresponding drug for over 8 weeks. Fold resistance was tested in the SRB assay.

3.11.3.Material

Refer to the material list in methods section 3.2. and 3.3.

3.12. In vivo studies

3.12.1.Assay principle

Mouse xenograft experiments involve transplanting human or non-murine animal tumor cells or tissues into immunodeficient mice to study tumor growth, metastasis, and the effects of various treatments. For better investigation of a drug effect in an organism, immunocompetent mice can be implanted with mouse-tumor cells. Here, the interplay of the drug with the immune system can be observed.

3.12.2.Mouse Xenograft

SUM149PT cells were cultured at 37 °C and 5 % CO_2. Before implantation, cells were trypsinized, checked for viability, and counted to the final working concentration of 6x10^6 cells/mouse in PBS 1to1 diluted with GelTrex (Gibco). Cells were implanted subcutaneously into the right flank of male NMRI nude mice, obtained from Charles River laboratories at 8-12 weeks. Tumor size was monitored 3 times a week using calipers

(length and width), and body weight was recorded. At the size of >250 mm^3, mice were randomized into groups of 8 and treated daily with different concentrations of EIS-1, formulated in SyrSpend or vehicle via oral gavage. A final necropsy was performed with mice bearing tumors >1500 mm^3 and >10mm width.

Tumor cells for the xenograft experiment were expanded and prepared following the cellular procedure protocol mentioned in Methods part 3.2. Xenograft experiments were run at the animal facility at the BMC by Dana Matzek, Dr. Adrian Schomburg, William Menzer, and Dr. Markus Lechner from Eisbach Bio GmbH. Tumor growth inhibition (TGI) was calculated using the following formula: %TGI= ((Vc1-Vt1)/(Vc1-Vt0))*100. The data was analyzed using GraphPad Prism (Version 9.4.1.).

3.12.3.Material

For cell line propagation and preparation, refer to the material list in Methods section 3.2.

Table 12: Material for cell line implantation

Consumable	Supplier	Catalog #	Comment
Gibco™ Geltrex™	Gibco	A1413302	LDEV-free, hESC-qualified basal-membrane-Matrix, reduced growth factors
PBS	Sigma	D8537	500 mL
Equipment	**Supplier**	**Catalog #**	**Comment**
Cell incubator	Heraeus	HeraCell	
Laminar flow hood	Heraeus	LaminAir HB2448	
Hemocytometer	NanoEnTek (by ROTH)	2N14712	Single-use, C-Chip
Inverted microscope	Zeiss	Axiovert 25	
Pipet boy	Thermo Scientific		
Vacuum pump	Vacuubrand	BVC-21	
Water bath	P-D Industriegesellschaft GmbH	TYP WB 20	

3.13. Statistical Analysis

For Data analysis, GraphPad Prism for Mac OS X (Version 9.4.1.) was used. All error bars indicate the Standard Error of Mean (SEM) of at least two replicates unless stated otherwise (Table 13).

Table 13: Statistical tests used

Assay	Figure	Statistical test	p-values
γH2AX and RAD51 foci formation	Figure 26, Figure 27, Figure 28	ordinary two-way ANOVA	GP: 0.1234 (ns), 0.0332 (*), 0.0021 (**), 0.0002 (***), <0.0001 (****)
Comet assay	Figure 30	ordinary one-way ANOVA	GP: 0.1234 (ns), 0.0332 (*), 0.0021 (**), 0.0002 (***), <0.0001 (****)

4. Results

4.1. Evaluation of ALC1i: Unveiling selectivity, toxicity, and correlation to PARPi sensitivity

4.1.1. Selectivity and cytotoxicity assessment of ALC1 inhibition in short term cellular survival assay

A wide range of Eisbach-ALC1i molecules from different chemical ALC1i-clusters (Supplementary Table 1) were tested for selectivity and cytotoxicity in the 96h SRB-cellular survival assay to evaluate the synthetic-lethal potential of ALC1i after biochemical validation (data not shown here). PARPi were used as a control for synthetic lethality with HRD. To further validate the hits, the 11-day assay format was used. The triple-negative breast cancer cell lines MDA-MB-231 and SUM149PT were used as a standard cell pair to evaluate compound selectivity as they showed different sensitivity in preliminary experiments. SUM149PT harbor a BRCA1 mutation leading to a short splice variant of the BRCA1-protein, which may be partially functional (Gu et al., 2016; Póti et al., 2018), while MDA-MB-231 are BRCA1 wild type (Drew et al., 2010) cells.

After extensive testing, the results highlighted the best-performing molecules that exhibited the most potent effects on cell survival. Results of the 96h cellular survival assay for the best ALC1i molecules are shown in Figure 19. The ALC1i differed in their chemical structure and were derived from compound clusters A (EIS-1, EIS-2, EIS-5), cluster C (EIS-4, EIS-6) and cluster B (EIS-3). Survival of the cells was normalized to vehicle control (DMSO), and inhibitor vs. response curves were fitted using GraphPad Prism. The values for all IC50, SEM, estimated EC50, and number of replicates are shown in Supplementary Table 9.

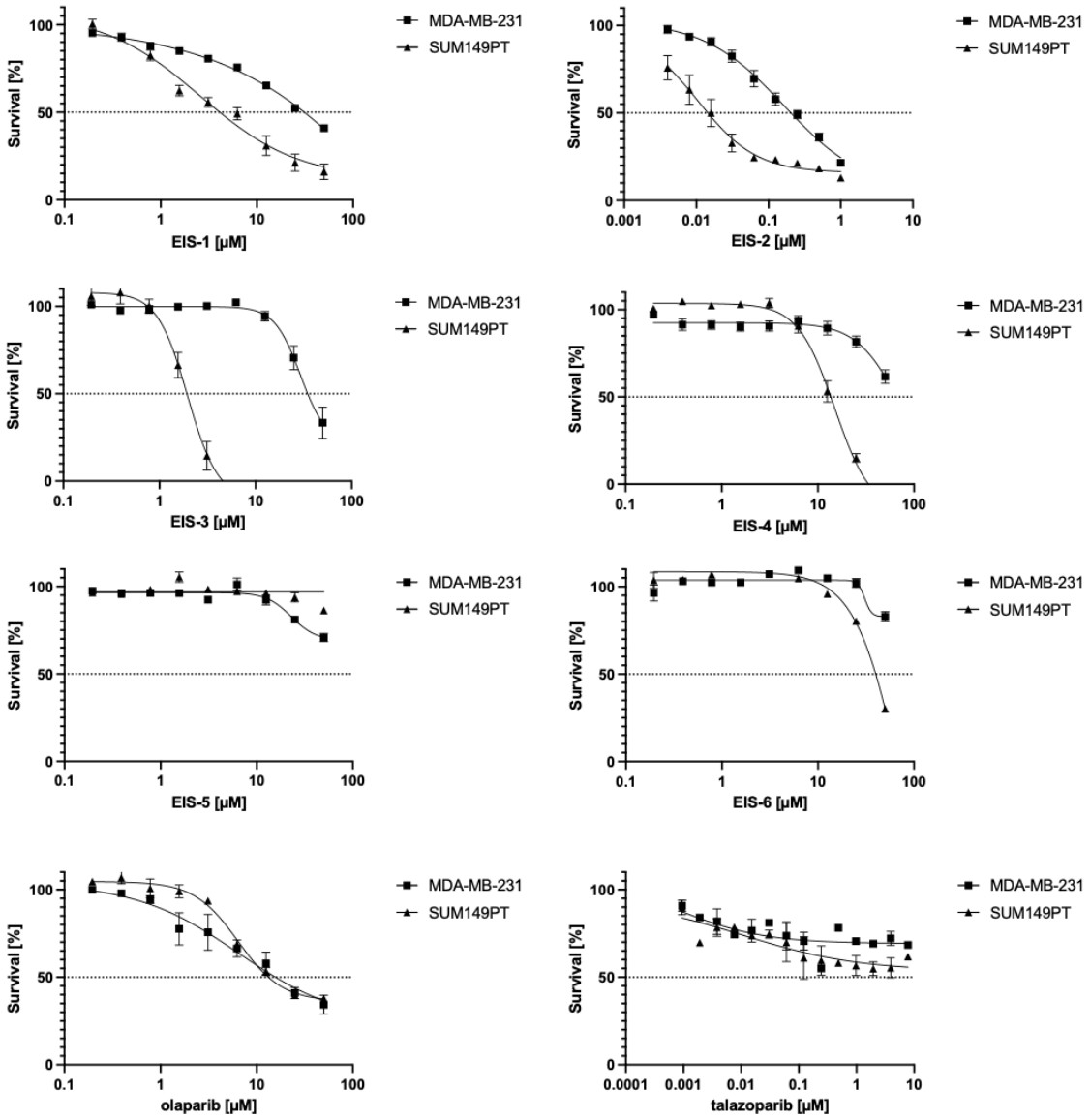

Figure 19: 96h cellular survival assay with HR-cell-pair

SUM149PT and MDA-MB-231 cells were treated with active ALC1i (EIS-1, EIS-2, EIS-3, EIS-4), inactive ALC1i (EIS-6, EIS-5) or PARPi (olaparib, talazoparib). Cells were cultured for 96h and stained with SRB to analyze cellular survival [%]. Survival was normalized to cells treated with vehicle (DMSO) and “all dead control”. Inhibitor vs. response curves were fitted using GraphPad Prism non-linear regression. Error bars indicate the SEM of all replicates (number of replicates are shown in Supplementary Table 9).

The 96h cellular survival assay results demonstrated distinct responses to ALC1 and PARP inhibition. Compared to MDA-MB-231 cells, SUM149PT cells displayed pronounced sensitivity to best-performing ALC1i (active ALC1i) while showing relatively low sensitivity to inactive ALC1i cluster members. EC50 values [µM] and the fold-selectivity between the two cell lines are shown in Table 14. Both cell lines exhibited comparable sensitivity to PARPi olaparib and talazoparib in the 96h format.

Table 14: EC50s and fold change selectivity of SUM149PT and MDA-MB-231 cells in 96h cellular survival assay

Chemical Cluster	EIS-Compound	EC50 SUM149PT [µM]	EC50 MDA-MB-231 [µM]	Fold Selectivity
A	EIS-1	4.000	33.000	8.250
A	EIS-2	0.014	0.200	14.286
A	EIS-5	>50.000	>50.000	1.000
B	EIS-3	2	38.000	19
C	EIS-4	13.5	>50.000	3.704
C	EIS-6	40.000	>50.000	1.250
PARPi	olaparib	14.000	16.000	1.143
PARPi	talazoparib	>10.000	>10.000	1.000

The effect of different ALC1i treatments was compared in other cell lines from the cell line panel to determine if there was a significant decrease in cell survival when a specific genetic alteration or deficiency was combined with the treatment. Bar graphs in Figure 20 represent the estimated EC50 values [µM] for all cell lines. Individual survival curves of all cell lines can be found in Supplementary Figure 4 - Supplementary Figure 10.

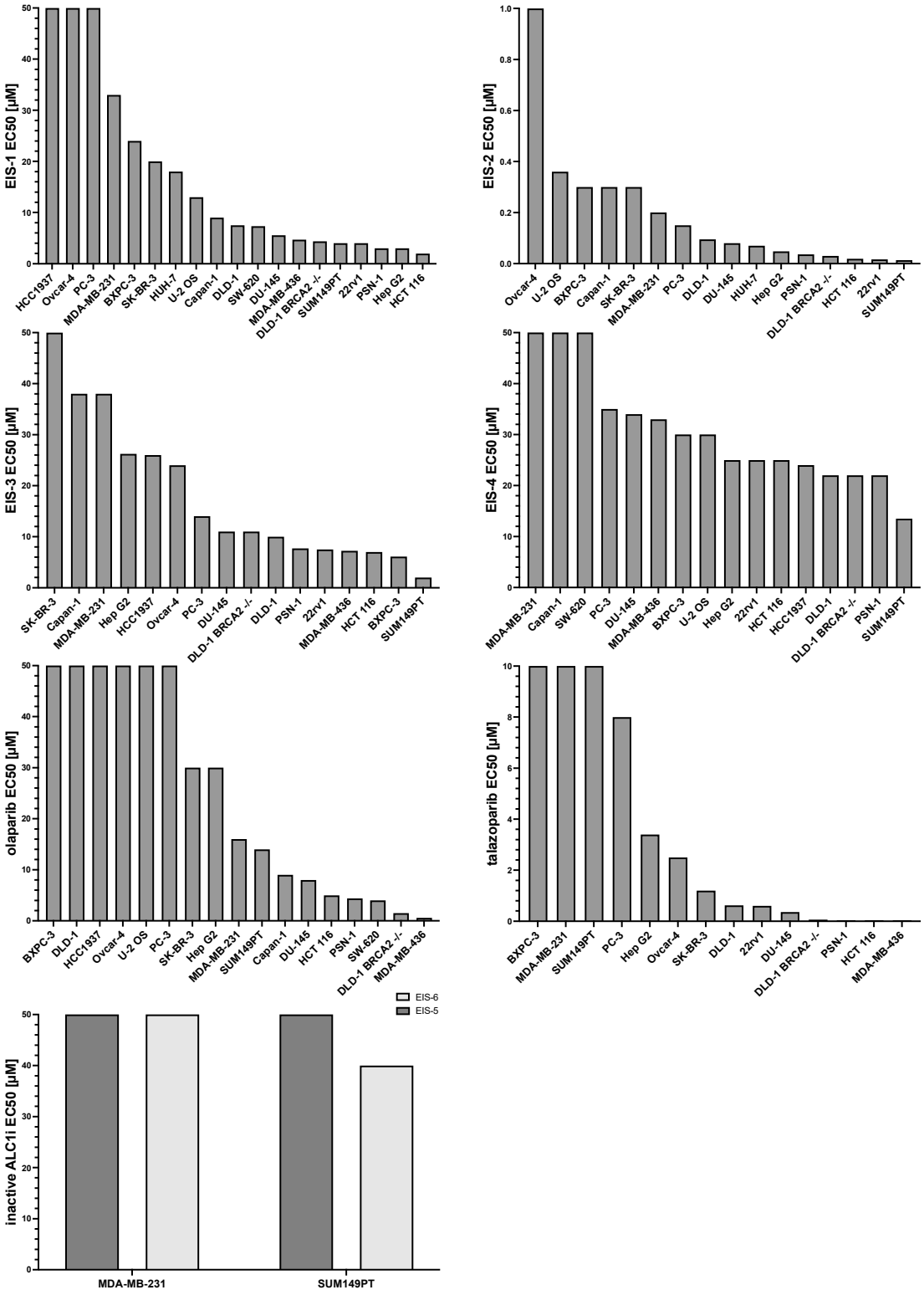

Figure 20: EC50 values of cell-panel in 96h survival assay

Different cancer cell lines were treated with titrations of active ALC1i (EIS-1, EIS-2, EIS-3, EIS-4), PARPi (olaparib, talazoparib) or inactive ALC1i (EIS-5, EIS-6). Cells were cultured for 96h and stained with SRB staining to analyze cell survival [%]. Inhibitor vs. response curves were fitted using GraphPad Prism non-linear regression. Bar graphs represent EC50 values of fitted survival curves. Due to the solubility limits of the

compounds, the highest assay concentration reached was 50 µM for ALC1i and olaparib and 10 µM for talazoparib. IC50 values, SEM, EC50, and number of replicates are indicated in Supplementary Table 9; full IC50 curves are shown in Supplementary Figure 4 - Supplementary Figure 10.

The 96h cellular survival assay demonstrated differential sensitivity among the cell lines, with some exhibiting high sensitivity and reduced survival rates. In contrast, others displayed resistance and higher cell survival, independent of their tumor origin.
Cell lines like HCT-116, PSN-1, SUM149PT, DLD-1, DLD-1 BRCA -/- and MDA-MB-436 showed high sensitivity to all active ALC1i, whereas cell lines like MDA-MB-231, Capan-1 or PC-3 exhibited low sensitivity. ALC1i EIS-4 was the least potent ALC1i tested, exhibiting minor variations in sensitivity between cell lines. While some cell lines showed simultaneous sensitivity to ALC1i and PARPi (e.g., HCT 116, PSN-1, DLD BRCA2-/-), others were less sensitive to PARPi despite pronounced ALC1i sensitivity (e.g., DLD-1, SUM149PT).

4.1.2. Correlation between PARPi and ALC1i sensitivity in various cell lines

As EIS-1 was the first compound from cluster A that showed a preferable selectivity between MDA-MB-231 and SUM149PT, its potency was compared to PARPi. Figure 21 compares sensitivity to olaparib with sensitivity to EIS-1. The 96h survival assay results revealed that many cell lines exhibited heightened sensitivity to ALC1i and PARPi.

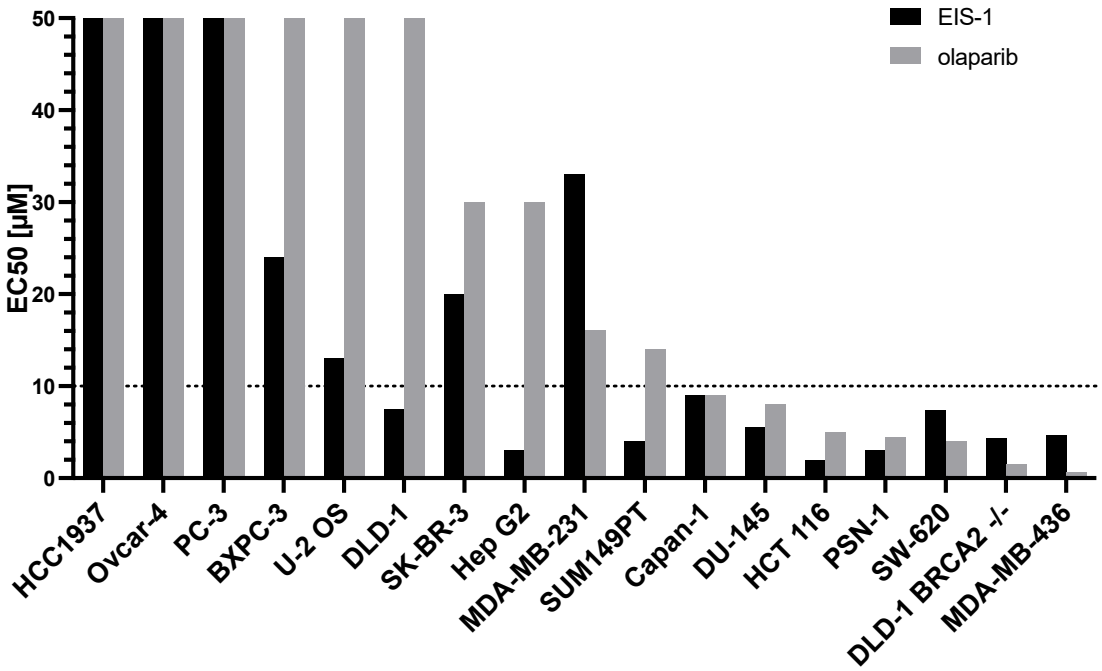

Figure 21: EC50 comparison of EIS-1 with olaparib in cellular survival
Different cancer cell lines were treated with EIS-1 or olaparib. Cells were cultured for 96h and stained with SRB to analyze cell survival [%]. Survival curves were normalized to 100% survival (DMSO control) and 0% survival (all cells dead). Inhibitor vs. response curves were fitted using GraphPad Prism non-linear regression. Bar graphs represent EC50 values of fitted survival curves. Due to the solubility limits of the compounds, the highest assay concentration reached for ALC1i and olaparib was 50 µM.

The experimental results demonstrate a correlation between sensitivity to olaparib and ALC1i, specifically ALC1i EIS-1, in various cell lines. Cell lines including MDA-MB-436, DLD-1 BRCA2 -/-, SW-620, PSN-1, and HCT116 exhibited a consistently high sensitivity to both olaparib and all active ALC1i tested. On the other hand, cell lines like MDA-MB-231, Capan-1, and PC-3 displayed lower sensitivity to both olaparib and ALC1i. However, certain cell lines, like DLD-1, HepG2, and SUM149PT, showed resistance to olaparib despite pronounced sensitivity to ALC1i. These highlight alternative vulnerabilities in these cells and emphasize the necessity of exploring multiple therapeutic targets.

4.1.3. Extended evaluation of ALC1 inhibition in long term cellular survival assay

The long-term impact of ALC1i on cell survival was tested utilizing the 11-day SRB cellular survival assay. Like the 96h assay format, cell lines were treated with ALC1i-titrations, and inhibitor vs. response curves were fitted for survival analysis. SUM149PT and MDA-MB-231 cells were used as the standard cell pair for general screening (see Figure 22). Raw values and number of replicates can be found in Supplementary Table 10.

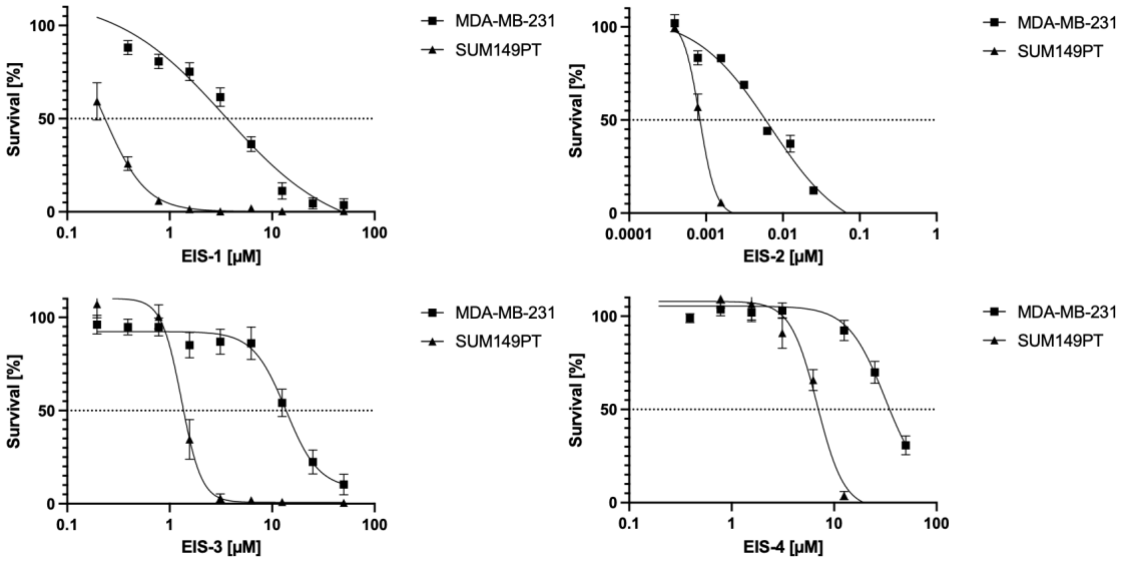

Figure 22: 11-day cellular survival assay of MDA-MB-231 and SUM149PT cells
SUM149PT and MDA-MB-231 cells were treated with titrations of ALC1i (EIS-1, EIS-2, EIS-3, EIS-4). Cells were cultured for 11 days and stained with SRB to analyze cell survival [%]. Survival was normalized to cells treated with vehicle (DMSO) and "all dead control". Inhibitor vs. response curves were fitted using GraphPad Prism non-linear regression. Error bars indicate the SEM of all replicates (the number of replicates is shown in Supplementary Table 10).

SUM149PT cells were susceptible to ALC1i EIS-1 and its cluster member EIS-2 with increased selectivity compared to MDA-MB-231 cells (see Table 15). Only EIS-1 from the A-cluster showed increased potency in the 11-day assay. The EC50 of EIS-2, EIS-3 and EIS-4 were similar or even lower to the 96-h survival assay.

Table 15: EC50 and selectivity of ALC1i in the 11-day survival assay

Chemical Cluster	EIS-Compound	EC50 SUM149PT [µM]	EC50 MDA-MB-231 [µM]	Fold Selectivity
A	EIS-1	0.1600	3.9000	24.3750
A	EIS-2	0.0009	0.0066	7.3333
B	EIS-3	1.4000	14.0000	10.0000
C	EIS-4	7.8000	36.0000	4.6154

Again, other cell lines were tested for sensitivity to ALC1i in the 11-day assay format. EC50 values are shown as bar graphs in Figure 23. Individual curves of cell lines are shown in Supplementary Figure 11- Supplementary Figure 14.

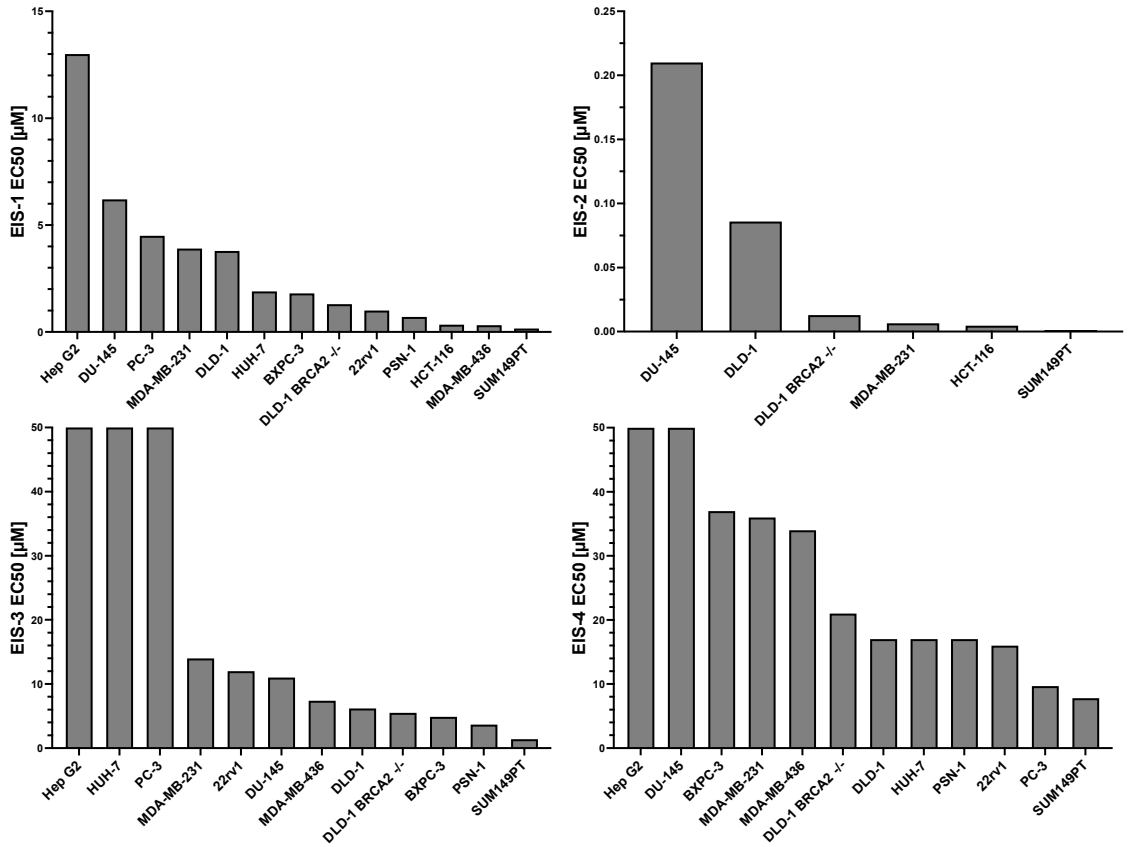

Figure 23: EC50 values of cell-panel in 11-day survival assay

Different cancer cell lines were treated with titrations of active ALC1i (EIS-1, EIS-4, EIS-3, EIS-2). Cells were cultured for 11 days and stained with SRB to analyze cell survival [%]. Inhibitor vs. response curves were fitted using GraphPad Prism non-linear regression. The Bar graphs represent the EC50 of fitted curves. Due to the solubility limits of the compounds, the highest assay concentration reached for ALC1i was 50 µM. IC50 values, SEM, EC50, and number of replicates are indicated in Supplementary Table 10.

MDA-MB-436 and 22Rv1 maintained high sensitivity to ALC1i, indicating sustained vulnerability in these cells, while MDA-MB-231 and PC-3 remained resistant to all ALC1i throughout the 11-day treatment period. DU-145 and Hep G2 cells, which initially displayed high sensitivity in the 96-h assay format, exhibited reduced sensitivity in the long-term treatment, suggesting potential adaptation or acquired resistance mechanisms like drug-transporter mutations. The fold-selectivity between the DLD-1 and DLD-1 BRCA2 -/- cell line increased, indicating a heightened sensitivity of the BRCA2 knockout cells to the tested drugs.

4.1.4. Summary of the results

In general, long-term treatment of cells with EIS-1 and EIS-2, which belong to the same cluster, led to drastically reduced EC50 values, while for EIS-3 and EIS-4, no systematic reduction was seen. The selectivity of EIS-1 increased from 8.250-fold in the 96h assay to 24.375-fold in the 11day assay. These results suggest that the underlying mechanism of ALC1 inhibition via ALC1i may vary between the different chemical clusters. The results emphasize the dynamic nature of cellular responses to different treatment durations and underscore the importance of varying assay setups in determining drug sensitivity. The effect of ALC1i on cancer cells suggests therapeutic opportunities for targeting ALC1 across different cancer subtypes. Thus, the observed differences in sensitivity among the cell lines highlight the need for further investigation into the underlying mechanisms driving these divergent responses to optimize treatment strategies for cancer subtypes and possible target mutations.

EIS-1 was chosen as the cluster representative due to its strong performance in initial biochemical and biophysical assays (data not shown here) and its notable selectivity between cell lines, particularly MDA-MB-231 and SUM149PT.

4.2. Potential ALC1i implications and HR-related insights through genomic profiling and functional readout

The partial correlation between ALC1i sensitivity and PARPi sensitivity in the cell line panel raises the question of whether HR deficiency influences sensitivity to ALC1i. The cell lines from this study were characterized by employing various genomic profiling techniques, such as protein expression, mutation analysis, HRD profiling from public data, and a functional assay.

4.2.1. ALC1 protein expression in different cell lines

To investigate the potential correlation between ALC1 protein expression and sensitivity to ALC1i, Western Blot analysis was employed to assess the ALC1 protein levels in the cell lines. Figure 24 shows a representative image of the Western Blot and the analysis of ALC1 levels normalized to α-tubulin. To test for a correlation of ALC1 expression and ALC1i sensitivity, cell lines that were sensitive to ALC1i in the 96h survival assay were highlighted in dark grey, cell lines that were less sensitive are shown in light grey.

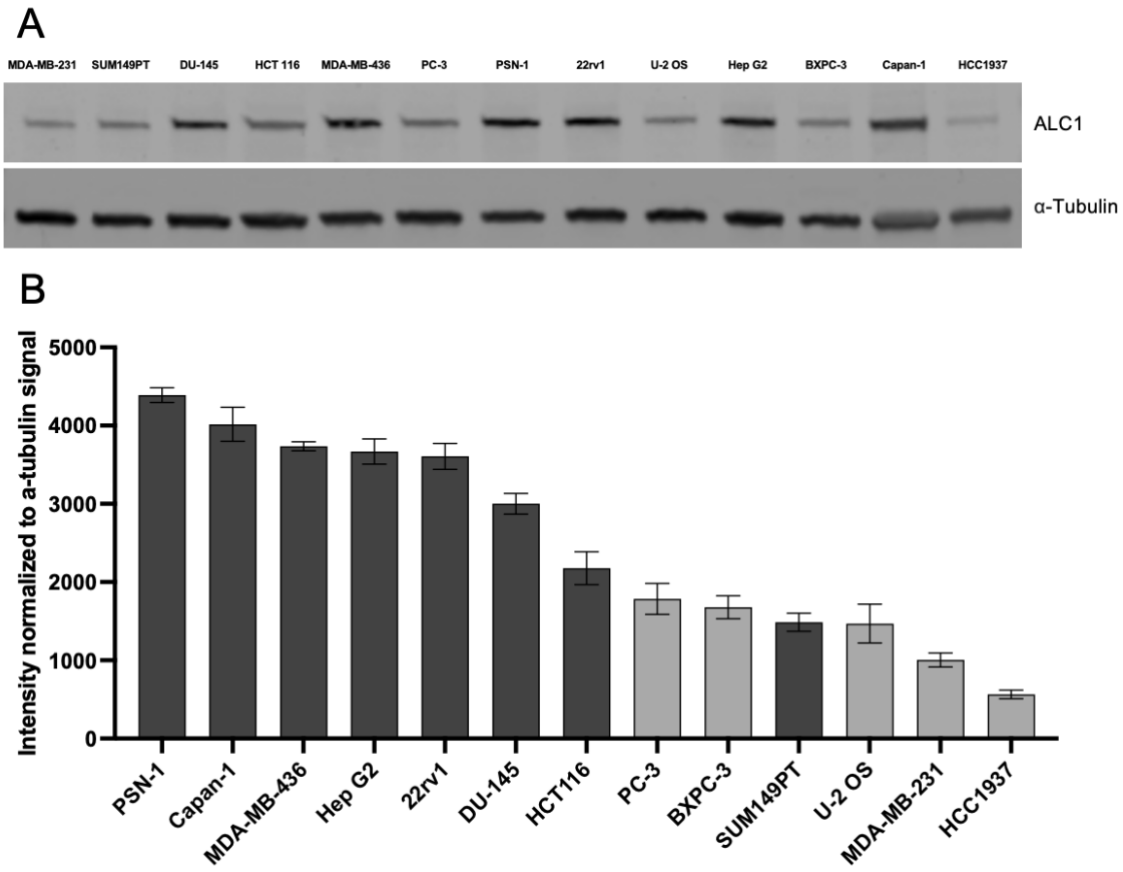

Figure 24: ALC1 expression in cell-panel

Western Blot analysis of cell lysates was performed using the indicated antibodies. A representative image is shown in A). Protein levels were quantified with FIJI (Image J) and plotted in GraphPad Prism (B). Bar graphs show ALC1 protein expression

normalized to α-tubulin, with error bars representing the SEM of two technical replicates. ALC1i-sensitive cell lines are marked in dark grey, and ALC1i-insensitive cell lines in light grey.

Out of the 13 cell lines tested, 8 were sensitive to ALC1 inhibition (ALC1i), while the remaining 5 were insensitive. Western Blot analysis revealed that among the ALC1i-sensitive cell lines, 6 exhibited high levels of ALC1 protein expression (PSN-1, Capan-1, MDA-MB-436, Hep G2, 22Rv1, DU-145), one showed a medium level (HCT116), and one cell line, specifically SUM149PT, demonstrated a lower level of ALC1 protein. In contrast, all 5 cell lines insensitive to ALC1i consistently displayed low expression levels of ALC1 protein (PC-3, BXPC-3, U-2 OS, MDA-MB-231, HCC1937). These findings suggest a strong correlation between high ALC1 protein expression and sensitivity to ALC1i. This relationship was mathematically confirmed via a Pearson correlation analysis between the quantified protein levels and $\log_{10}$-transformed EC_{50} values, which revealed a statistically significant inverse correlation ($r = -0.6721$, $P = 0.0119$; Supplementary Fig. 27). Approximately 45% of the variation in drug sensitivity could be attributed to ALC1 expression levels ($R^2 = 0.4518$).
These results indicate that cell lines with higher levels of ALC1 protein are more likely to be affected by ALC1 inhibition, while those with low ALC1 expression tend to be resistant. This relationship highlights the potential of ALC1 protein levels as a predictive biomarker for responsiveness to ALC1i treatment. However, based on the exceptional sensitivity of SUM149PT cells, ALC1 expression alone may not be the sole determinant for ALC1i sensitivity.

4.2.2. Complexities of BRCA mutations and their impact on PARPi sensitivity

While BRCA mutations are known indicators of impaired DNA repair pathways and increased susceptibility to PARPi, it is crucial to acknowledge the complexity of these interactions. Some cell lines with dysfunctional BRCA might display resistance to PARPi due to the presence of compensatory DNA repair mechanisms or other genetic alterations. Conversely, specific cell lines without BRCA mutations could exhibit sensitivity to PARPi due to defects in different DNA repair pathways or genetic contexts. Information about the BRCA status and PARPi-sensitivity of cell lines was compiled from public data and is summarized in Table 17. Cell lines with a known BRCA deficiency include DLD-1 BRCA2-/-, MDA-MB-436, 22Rv1, Capan-1, SK-BR-3, and HCC1937. SUM149PT expresses a truncated version of BRCA1 that may partially be functional (Gu et al., 2016). Cells with a high sensitivity to PARPi include HCT 116, PSN-1, DLD-1 BRCA2-/-, MDA-MB-436, and Capan-1. Only three of the cell lines sensitive to PARPi harbor a BRCA deficiency.

4.2.3. Exploring the HR-associated gene network within the cell-panel

Besides BRCA1 and BRCA2, many other factors contribute to HR proficiency. Therefore, a list of genes related to HR repair was compiled for this study, utilizing published resources as a reference. Multiple databases and scientific literature were combined to ensure the inclusion of well-established HR-associated genes. The compiled gene list encompassed key players involved in HR pathway regulation, including DNA repair genes, HR-specific genes, and genes involved in HR-related processes such as DNA strand exchange and Holliday junction resolution. This curated gene list can be found in Supplementary Table 3. The mutational profile of each cell line was downloaded from DepMap and screened to identify deletion mutations related to DNA repair. The number of deleterious mutations (hemizygous or homozygous) in HR-related genes can be found in Figure 25 A. In addition, the relationship between HR gene deletion burden and sensitivity to the ALC1 inhibitor EIS-1 was assessed by correlating deletion counts with log_{10}-transformed EC_{50} values after 96 h treatment, as shown in Figure 25B.

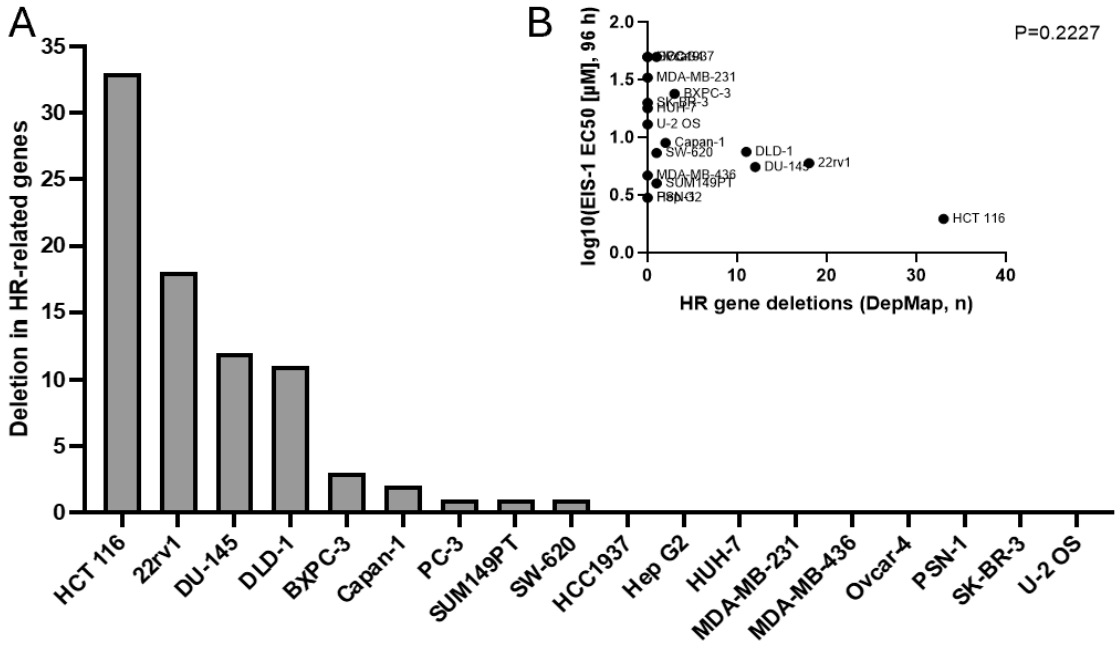

Figure 25: Deleterious mutations in HR-related genes in the cell-panel A) Mutational profiles of cell lines were obtained from DepMap (Corsello et al., 2019; DepMap). Variants were filtered for deletions in a predefined panel of HR-genes, shown as bar graphs. A detailed list of deleterious mutations is provided in Supplementary Table 4. B) Correlation analysis between HR gene deletion burden and sensitivity to EIS-1, assessed by log_{10}-transformed EC_{50} values after 96 h treatment. Each data point represents one cell line. Spearman correlation coefficients and two-tailed p values are shown.

The mutational analysis revealed a spectrum of deleterious mutations in HR-associated genes across the cell line panel. Cell lines with a high number of HR gene deletions included HCT 116, 22Rv1, DU-145, and DLD-1, whereas cell lines with few or no deletions included HepG2, MDA-MB-231, PSN-1, and others. However, HR gene deletion burden alone did not significantly correlate with sensitivity to the ALC1 inhibitor EIS-1, as assessed by $\log_{10}$-transformed EC_{50} values after 96 h treatment (Spearman $\rho = -0.30$, $p = 0.22$, $n = 18$).

4.2.4. Insights and discrepancies of RAD51 foci formation and HR repair capacity in cell panel

RAD51 foci formation analysis was performed in a subset of cell lines to verify literature-based data. The RAD51 protein is a key mediator of HR and forms nuclear foci at sites of DNA damage, indicating active HR repair. Cells were exposed to 1 Gy irradiation to induce DNA DSBs and subsequently immune-stained for nuclear γH2AX and RAD51 protein. Iris Baur and Claudia Böhland, Anna Friedl laboratory, LMU, performed the irradiation and staining of the cells. Confocal microscopy was used to visualize foci. The FociCounter plugin (*FOCI Counter* | *BIC Macro Toolkit* | *Image Analysis* | *Service* | *Bioimaging Centre*, 2017) in ImageJ was used to quantify fractions of cells with ≥5 γH2AX foci, as a sign of efficient DNA damage ınduction, and ≥5 RAD51 foci, as a sign of ability for active HR repair, in the nuclei of the cells. Representative images of all cell lines are shown in Figure 26 and Supplementary Figure 2. DNA damage was efficiently introduced by radiation, as shown in Figure 27 (γH2AX foci). RAD51 foci formation ratios are shown in Figure 28. The raw data for Foci formation can be found in Supplementary Table 11, Supplementary Table 12, Supplementary Table 13.

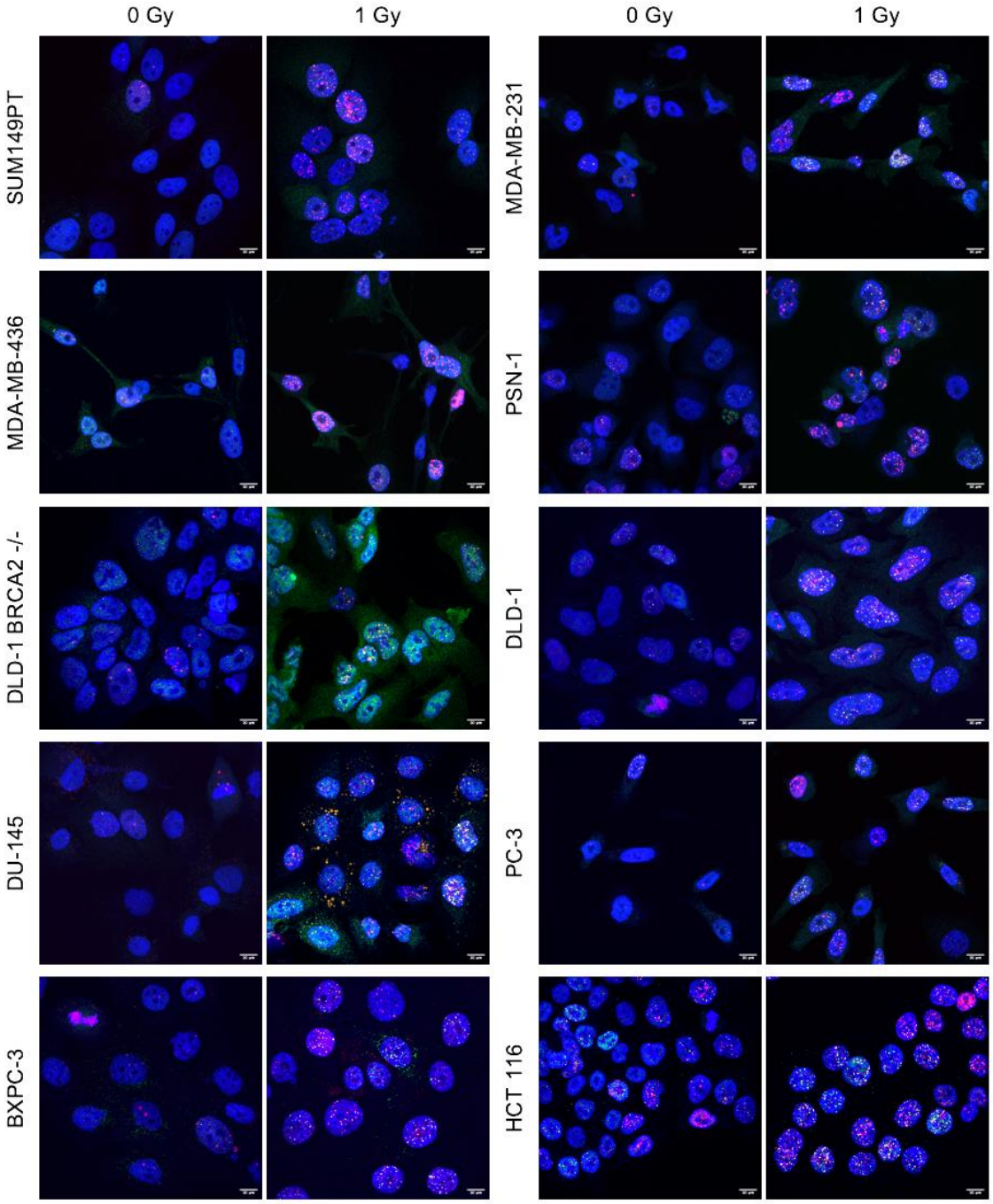

Figure 26: γH2AX and RAD51 foci formation capability of chosen cell lines

Nuclear foci formation was detected via IF in different cell lines. Cells were treated with 0/1 Gy for 2 h, fixed, stained for anti-γH2AX (red) and anti-RAD51 (green) foci, and counterstained with DAPI (blue). Z-stack images were taken using a spinning-disk-confocal microscope. Z-images were stacked using Fiji (ImageJ). Images represent merged channels of all three colors.

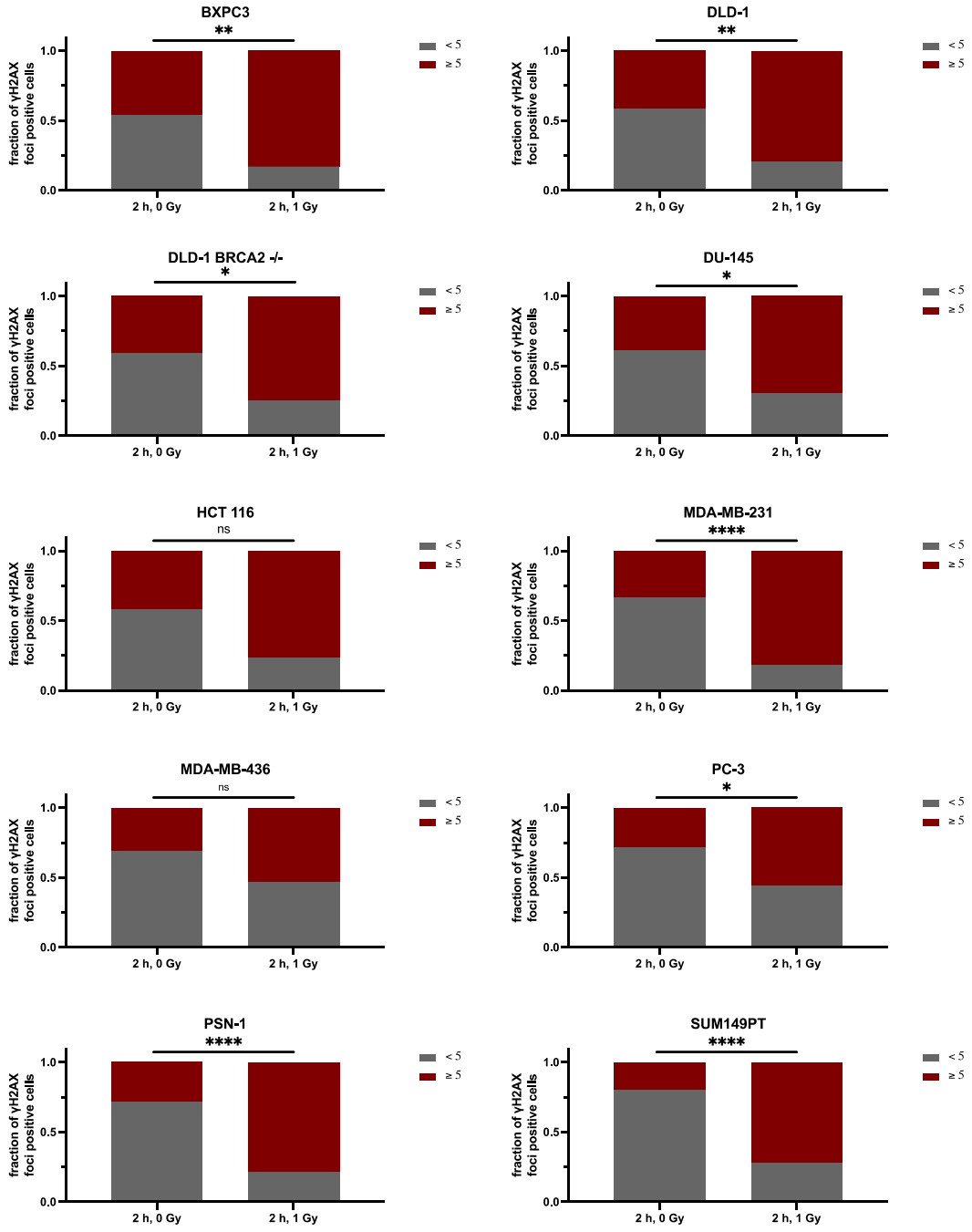

Figure 27: γH2AX foci formation capability of chosen cell lines

Nuclear foci formation was detected via IF in different cell lines. Cells were treated with 0 Gy or 1 Gy for 2 h, fixed, and stained for γH2AX. Data was analyzed using the Foci Counter Macro (ImageJ). Fractions of foci per nuclei were calculated. Bar graphs were fitted in GraphPad Prism for fractions of nuclei with <5 γH2AX foci (grey) and ≥ 5 γH2AX foci (red). Data represents the mean of 2-4 biological replicates. Statistical analysis includes a two-way ANOVA test. P-values and SD can be found in Supplementary Table 11, Supplementary Table 12.

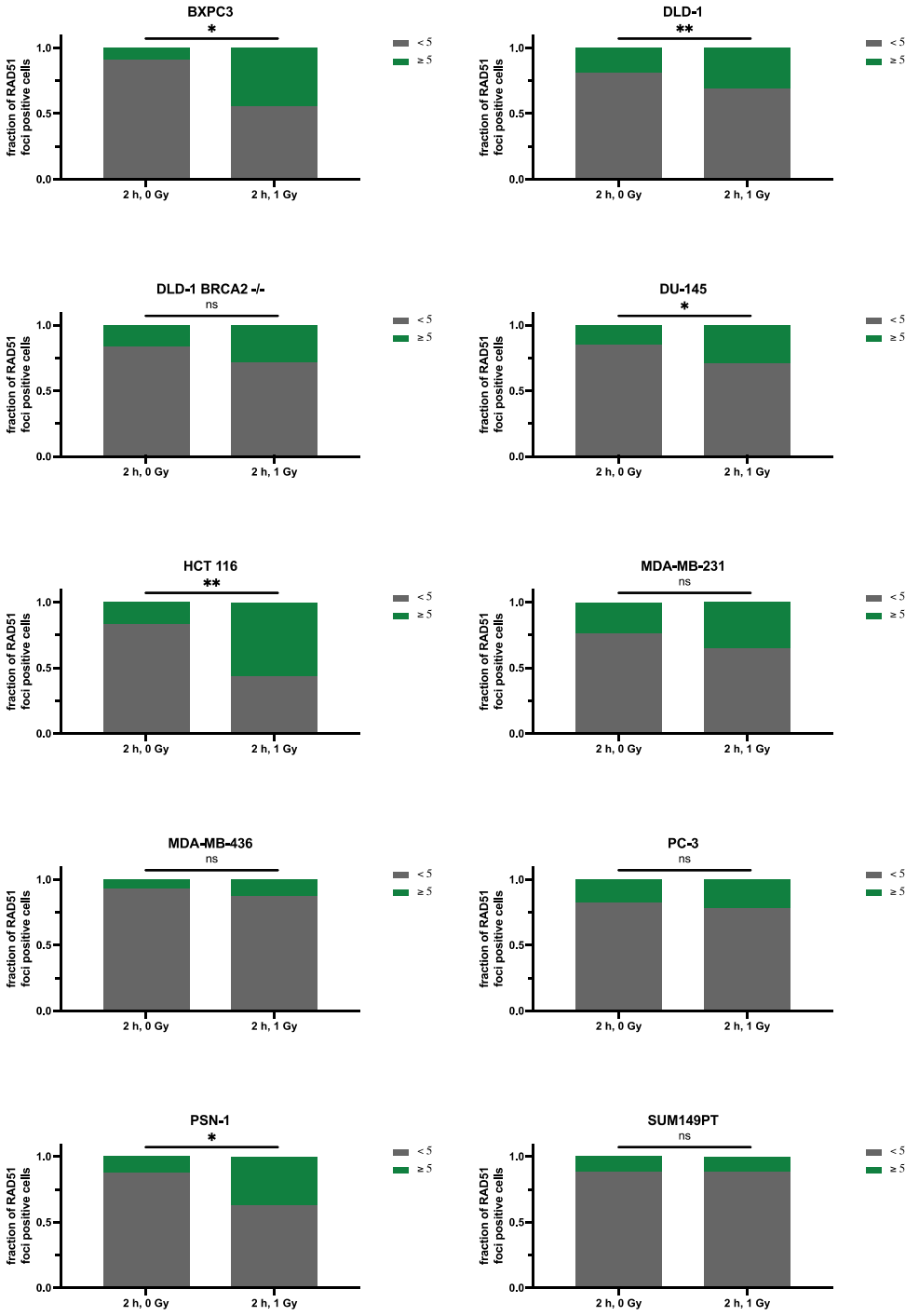

Figure 28: RAD51 foci formation capability of chosen cell lines

Nuclear foci formation was detected via IF in different cell lines. Cells were treated with 0 Gy or 1 Gy for 2 h, fixed, and stained for RAD51. Data was analyzed using the Foci Counter Macro (ImageJ). Fractions of foci per nuclei were calculated. Bar graphs were fitted in GraphPad Prism for fractions of nuclei with <5 RAD51 foci (grey) and ≥ 5 RAD51 foci (green). Data represents the mean of 2-4 biological replicates. Statistical analysis includes a two-way ANOVA test. P-values and SD can be found in Supplementary Table 11, Supplementary Table 13.

All cell lines at time point 2h showed a strong increase in fractions of γH2AX foci positive cells in at least 2 biological replicates after irradiation with 1Gy, except the MDA-MB-436 and HCT 116 cells, which revealed no significant result but showed the same trend as all other cell lines.

The results showed variation in RAD51 foci positive fractions across the cell lines, indicating differences in HR repair capacity.

The calculation indicates that the DLD1 BRCA2 -/- cells have increasing RAD51 foci counts, although no foci were detectable by eye (Supplementary Figure 1). This discrepancy was attributed to a high nuclear background intensity in the green channel, which led the ImageJ macro to count RAD51 foci erroneously. Thus, DLD-1 BRCA2 -/- cells were categorized as RAD51 foci negative. Also, the cell lines MDA-MB-436 and SUM149PT showed low or no fractions of RAD51 foci-positive cells after IR.

Although SUM149PT cells carry a BRCA1 mutation, it is noteworthy that they may still express a truncated version of BRCA1 (Gu et al., 2016). This truncated BRCA1 protein, while insufficient for efficient HR repair, may still participate in HR to some extent. The reliance on the truncated BRCA1 variant can result in incomplete HR, leading to the persistence of general DNA damage indicated by the low levels of IR-independent RAD51 foci fractions in those cells.

The cell lines BXPC3, DLD-1, DU-145, PSN-1, and HCT-116 significantly increased RAD51 foci formation after IR, indicating intact HR repair.

MDA-MB-231 cells showed no significant increase but shared the same trend as the other HR-proficient cell lines. They exhibit RAD51 foci positive fractions after IR, as shown in the images in Figure 26. Compared to other HR-proficient cell lines, PC-3 cells showed a mild but obvious increase in IR induced foci, which is why they were categorized as “medium” RAD51 foci proficient.

A summary of the results on the RAD51 foci formation capability of the Eisbach-cell panel compared to references is shown in Table 17.

For assessment of spontaneous DNA damage before and DNA damage repair capacity after irradiation, γH2AX foci were manually analyzed at the following time points: 0 Gy, 2 h; 0 Gy, 24 h; 1 Gy, 2 h; 1 Gy, 24 h (See Supplementary Figure 3,Supplementary Table 14). Despite notable standard deviations in the data, these results can shed light on the repair competence of the different cell lines.

Cells with a high level of DNA damage before irradiation, indicated by γH2AX foci positive fractions >25% (before IR), include DLD1 BRCA2 -/-, PC-3, BX-PC-3, MDA-MB-231, DU-145 and HCT 116.

Cell lines with high fractions (>25 %) of γH2AX negative nuclei 24 h after irradiation include HCT 116, SUM149PT, DU-145, DLD-1, and MDA-MB-436. >25 % γH2AX foci positive fractions at 24 h post-IR were detected in PSN-1 and DLD-1 BRCA2 -/- cells, but also in BX-PC-3, MDA-MB-231, and PC-3.

The results from the in-house foci formation assay are summarized in Table 16. Cells with a greater fraction of RAD51 positive cells at timepoint 1 Gy, 2 h were labeled as RAD51 foci formation “high”. Cells with γH2AX foci positive fractions >25% at timepoint 0 Gy, 2 h or 1 Gy, 24 h were labeled “high”.

Table 16: Results-summary of foci formation assay

Cell Line	EIS-1 EC50 [µM] 11-day	RAD51 Foci Formation	γH2AX Foci Level before IR	γH2AX Foci 24h after IR
SUM149PT	0.16	low	low	low
MDA-MB-436	0.32	low	low	low
HCT 116	0.34	high	high	low
PSN-1	0.71	high	low	high
DLD-1 BRCA2 -/-	1.30	low	high	high
BXPC-3	1.80	high	high	high
DLD-1	3.80	high	low	low
MDA-MB-231	3.90	high	high	high
PC-3	4.50	medium	high	high
DU-145	6.20	high	high	low

There is no overall correlation between the EC50 of EIS-1 in the 11-day survival assay with the capability to form RAD51 foci, the γH2AX level before IR, and the γH2AX level 24 h after IR. Cell lines with high γH2AX levels before irradiation include cells susceptible to ALC1i but also BXPC-3, MDA-MB-231, and PC-3, which low sensitivity to ALC1i. A similar correlation was found between the repair capacity of γH2AX foci 24 h after IR. HCT 116 cells that are highly sensitive to ALC1i have a low number of γH2AX foci 24 h

after IR, assuming a good DNA repair, compared to PSN-1 cells, which are also very sensitive to ALC1i but indicate a hampered repair at timepoint 24 h.

The results obtained from the in-house foci formation assay have been summarized in Table 17, elucidating the relationship between HR repair and ALC1i sensitivity. Notably, no consistent overall correlation exists between the EC50 of EIS-1 in the survival assay and the cells' capacity for RAD51 foci formation, as well as the levels of γH2AX before and 24 h after irradiation. However, a distinct pattern emerges from the data. The two cell lines that exhibited low or no IR-induced RAD51 foci were found to be sensitive to ALC1i treatment, suggesting an association between defective HR and heightened ALC1i sensitivity. Interestingly, this relationship presents distinctions in cases such as HCT 116 and PSN-1 cells. Despite their proficient formation of IR-induced RAD51 foci, their pronounced sensitivity to ALC1i suggests a more complex sensitivity mechanism that surpasses the scope of HR-related synthetic lethality.

4.2.5. Summary of the cell lines characterization

Cell lines within the Eisbach panel exhibited heterogeneous responses to ALC1 inhibition in both short- and long-term cellular survival assays. Sensitivity to ALC1 inhibitors partially overlapped with sensitivity to PARP inhibitors, while several cell lines displayed pronounced ALC1i sensitivity despite limited or absent PARPi responsiveness. Genomic profiling revealed a broad spectrum of deleterious mutations and deletions in HR-associated genes across the panel; HR gene deletion burden alone did not significantly correlate with ALC1 inhibitor sensitivity. While HR gene deletion burden alone was not predictive of ALC1i sensitivity, cell lines with a high number of deletions were frequently observed among the most sensitive models.

Functional analysis of homologous recombination capacity using RAD51 foci formation further differentiated cell line responses. Cell lines with impaired RAD51 foci formation were consistently sensitive to ALC1 inhibition, whereas several RAD51-proficient cell lines also exhibited sensitivity, indicating that functional HR deficiency alone does not fully explain ALC1i response patterns. Analysis of ALC1 protein expression showed that most ALC1i-sensitive cell lines expressed high levels of ALC1 protein, whereas ALC1i-insensitive cell lines consistently displayed low ALC1 expression, suggesting that target abundance contributes to ALC1 inhibitor sensitivity. A summary of the main results from the cell-line characterization can be found in Table 17.

Table 17: Cell line analysis (for references, see Supplementary Table 15)

Cell Line	EIS-1 EC50 [µM] 96h	EIS-1 EC50 [µM] 11d	BRCA-Deficient (*Partially functional allele, ** conflicting data)	HR-Gene Deletions (DepMap)	HR Status (functional test)	IR-induced RAD51 Foci (reference/in-house; ** conflicting data)	PARPi Sensitivity reference	Olaparib Sensitivity inhouse	Conclusion
HCT 116	1.97	0.34	-	33	HRP, MSI high	yes/yes	high	high	HRP, PARPi sensitive
Hep G2	3.00	13.00	-	0		yes/n.d.	high	medium	HRP, PARPi moderate
PSN-1	3.01	0.71	-	0		yes/yes	high	high	HRP, PARPi sensitive
SUM149PT	4.00	0.16	BRCA1*	1		no**/no	low	medium	HRD, PARPi moderate
DLD-1 BRCA2 -/-	4.36	1.30	BRCA2	n.d.		no/no	high	high	HRD, PARPi sensitive
MDA-MB-436	4.69	0.32	BRCA1	0		no/no	high	high	HRD, PARPi sensitive
DU-145	5.56	6.20	-	12	HRP	yes/yes	high	high	HRP, PARPi resistant
22rv1	6.00	1.00	BRCA1**	18		yes/n.d.	low	n.d.	HRP, PARPi resistant
SW-620	7.33	n.d.	-	1		n.d./n.d.	n.d.	high	n.d., PARPi sensitive
DLD-1	7.50	3.80	-	11		yes/yes	low	low	HRP, PARPi resistant
Capan-1	9.00	n.d.	BRCA2	2	HRD	no/n.d.	high	high	HRD, PARPi sensitive
U-2 OS	13.00	n.d.	-	0		yes/n.d.	medium	low	n.d., PARPi resistant
HUH-7	18.00	1.90	-	0		yes/n.d.	medium	n.d.	n.d.
SK-BR-3	20.00	n.d.	BRCA1**	0		yes/n.d.	medium	medium	n.d.
BXPC-3	24.00	1.80	-	3	HRP	yes/yes	low	low	HRP, PARPi resistant
MDA-MB-231	33.00	3.90	-	0		yes/yes	low	medium	HRP, PARPi moderate
PC-3	50.00	4.50	-	1		yes/yes	low-medium	low	HRP, PARPi resistant
HCC1937	>50	n.d.	BRCA1	0		yes/n.d.	high	low	n.d.
Ovcar-4	>50	n.d.	-	0		yes/n.d.	medium	low	n.d.

Within this broader panel-level characterization, the isogenic DLD-1 cell pair provides an illustrative example of the limitations of HRD-based stratification and the complexity of ALC1i sensitivity. Initially, these cells were used to predict HRD-selectivity, with DLD-1 cells being PARPi resistant and the BRCA2 knockout DLD-1 cell line displaying PARPi sensitivity and RAD51 foci deficiency. As ALC1 is closely associated with PARP proteins (Blessing et al., 2020; Juhász et al., 2020; Verma et al., 2021), a similar selectivity was expected for ALC1i. However, both DLD-1 cell lines were categorized as sensitive to ALC1i in the 96h cellular survival assays, contrary to the anticipated HRD-selective response. Notably, the DepMap analysis unveiled the presence of a BRCA2 deleterious mutation in the DLD-1 cells, suggesting a potential BRCAness phenotype even before complete BRCA2 knockout. This revelation indicates that the DLD-1 parental cell line was already partially deficient in BRCA2, which might have led to compensatory mechanisms. Consequently, knocking out BRCA2 might have disrupted these compensations completely.

These findings highlight the complexity of HRD-associated cellular responses and the need for a comprehensive understanding of underlying mechanisms in the context of targeted cancer therapies.

Cell lines with compromised HR function, demonstrated by low or no IR-induced RAD51 foci formation and mutations in BRCA1/2 (MDA-MB-436, SUM149PT, and DLD-1 BRCA2 -/-), were generally more sensitive to ALC1i, implying a potential synthetic lethal interaction with HR-deficiency. However, some cell lines that displayed proficient RAD51 foci formation also exhibited high ALC1i sensitivity (HCT 116, Hep G2, PSN-1, DU-145, and 22Rv1), indicating that HRD is not the sole determinant of ALC1i response.

The mutational analysis further emphasized the complexity of DNA repair capacity assessment. It revealed that relying solely on foci formation or the presence of BRCA mutations may not offer a complete picture. The interplay of various factors, including mutation type, genetic context, and repair pathway interactions, underscores the need for a holistic approach that combines genetic information and functional assays for a comprehensive assessment of DNA repair.

The observed complexity in ALC1i sensitivity is further underscored by the MSI-high status of HCT 116 cells. HCT 116 cells are known to be microsatellite instability-high (MSI-H), which means they have a higher frequency of mutations in microsatellite regions due to impaired DNA mismatch repair (MMR) mechanisms (Ellegren, 2004; Smeby et al., 2020). The MSI-H phenotype of HCT 116 can contribute to the high frequency of deletion mutations in HR-associated genes (Smeby et al., 2020). This additional layer of genetic alteration highlights that a multifaceted interplay of factors beyond HRD influences ALC1i sensitivity.

The compiled and summarized characterization data were employed to construct a comprehensive Venn diagram, providing an illustrative overview of the distinct cell lines' response to ALC1i. This visual representation concisely depicts the intersections and distinctions between the cell lines' BRCA status, PARPi sensitivity, DNA repair capacity via functional readout (RAD51 foci formation), and ALC1i sensitivity (see Figure 29).

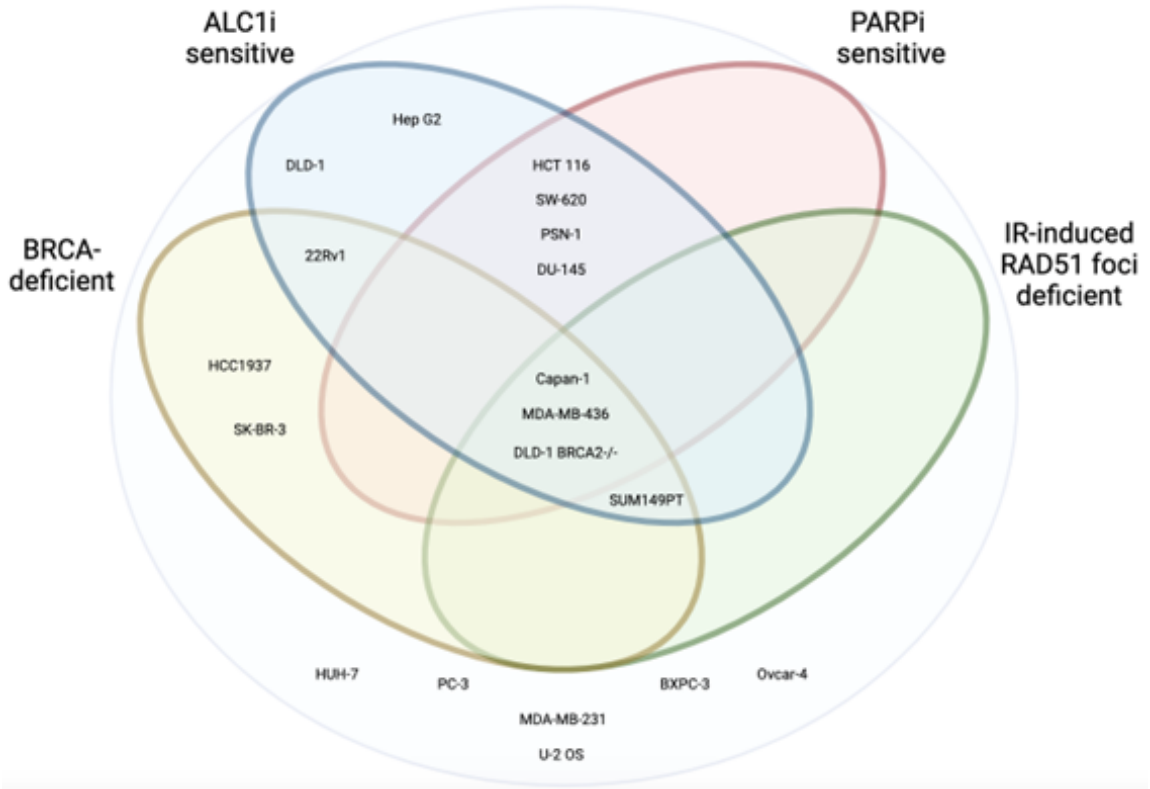

Figure 29: Venn diagram of cell line characterization for ALC1i sensitivity
Cell lines were categorized based on collected data. Categories include sensitivity to EIS-1 in 96-h survival assay (blue), sensitivity to PARPi (red), deficiency in IR-induced RAD51 foci formation (green), BRCA-deficiency (yellow), no category (grey) (created with Scientific Image and Illustration Software | BioRender).

This study highlights that while HR deficiency is a critical factor contributing to ALC1i sensitivity, it is not the sole determinant. All cell lines that exhibit sensitivity to PARPi consistently display sensitivity to ALC1i. This robust correlation between the responses to these two distinct classes of drugs suggests that the most reliable predictor for a cell line's sensitivity to ALC1i is its responsiveness to PARPi. Additional factors beyond HRD and PARPi sensitivity should be considered. Altogether, these findings hold significant promise for refining patient stratification and treatment selection, offering a practical and effective approach to optimizing therapeutic outcomes in cancer treatment.

4.3. Mechanisms of ALC1i: Assessing DNA damage levels and repair pathways

Their influence on DNA damage levels was investigated to understand the mode of action of ALC1i further. The comet assay assessed the induction of DNA strand breaks. In addition, DNA damage markers γH2AX and cleaved PARP1 were quantified to provide in-formation about the extent of DNA damage, activation of repair pathways, and potential cell fate decisions, such as repair or apoptosis. γH2AX is a marker for DSB, while cleaved PARP1 is an indicator of apoptotic cell death and is generated by caspase-mediated cleavage of PARP1 during DNA damage-induced cell death.

4.3.1. DNA damage detection under ALC1i treatment

The alkaline comet assay enables the visualization and quantification of DNA strand breaks (SSB and DSB), offering information about the genotoxic effects of different treatments or conditions. The higher the strand break level, the higher the fraction of nuclear DNA that leaves the nucleus, forming the tail of a comet-like structure upon applying an electric field.

SUM149PT cells were subjected to various concentrations of EIS-1 treatment for 48 h. The OpenComet software was utilized to assess comet formation and measure Tail Moments. Figure 30 displays images of the cells exhibiting comet formation, and the corresponding calculated Tail Moments of the comets are also presented.

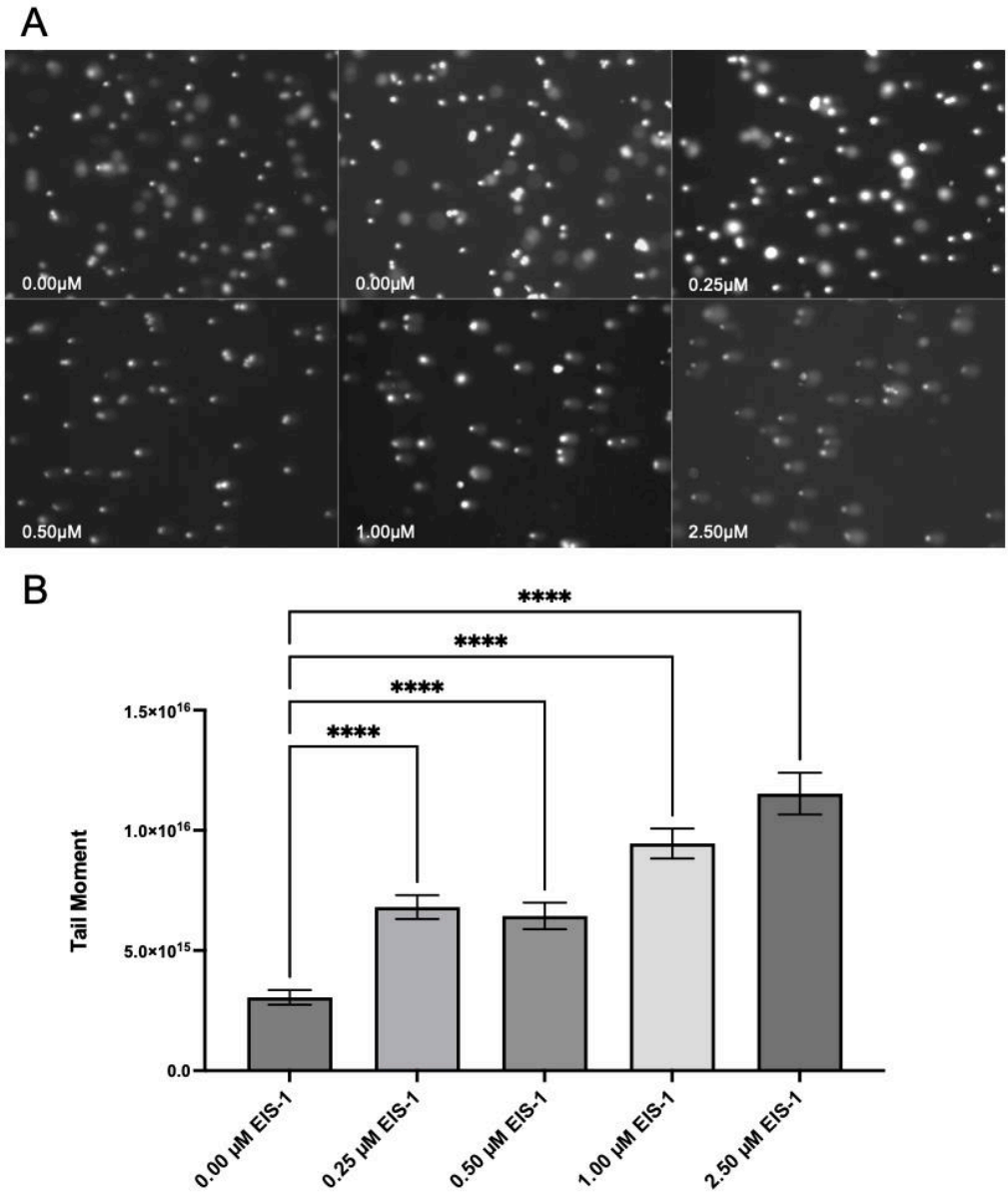

Figure 30: DNA damage detection using alkaline comet assay SUM149PT cells were treated for 48 h with EIS-1, and alkaline comet assay was run. Cells were stained with Hoechst and imaged using a fluorescence microscope. Comet images of SUM149PT cells are shown in A). Quantification of Comets is shown in B). Bar graphs represent the Tail Moment (TM). Differences in TM were tested by an ordinary one-way ANOVA test. Error bars indicate SEM of at two biological replicates (>190 cells per condition). Raw values of the TM values are shown in Supplementary Table 16. A positive control with talazoparib was run in a previous experiment. positive comet formation was detected under treatment with talazoparib as well as EIS-1 (data not shown).

Notably, comet formation was observed across all tested concentrations. Even at the lowest concentration of 250 nM, a significant increase in Tail Moments was observed, indicating the presence of DNA damage in response to EIS-1 treatment in ALC1i-sensitive cells.

4.3.2. Elevated levels of cleaved PARP1 and γH2AX as indicators of DNA damage in ALC1i response

Western blot analysis was employed to assess the impact of ALC1 inhibition on DNA damage and apoptosis. PSN-1 cells, selected as an ALC1i-sensitive and HR-proficient cell line, were subjected to EIS-1 treatment for 48 h. Protein levels of γH2AX and cleaved PARP1, an indicator of apoptosis, were analyzed (Figure 31). Analysis of biological replicates and a control with talazoparib can be found in Supplementary Figure 15. Treatment with EIS-1 resulted in a comparable increase in cleaved PARP1 levels.

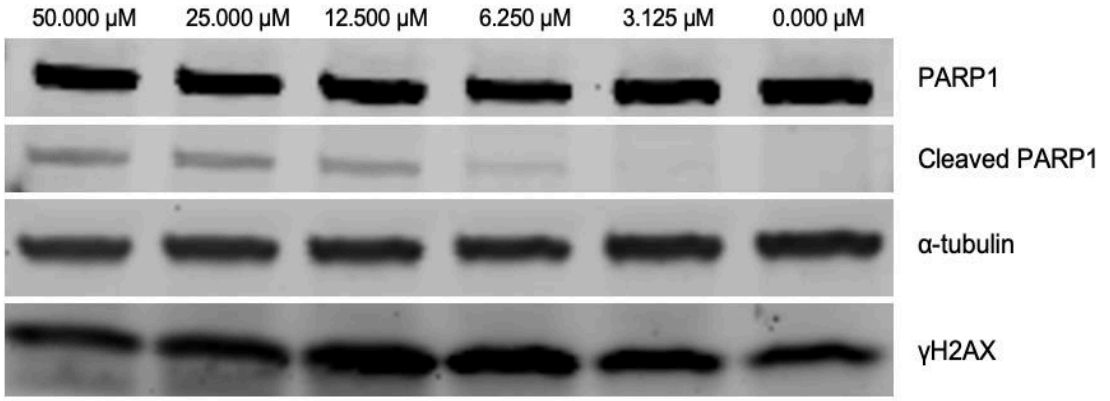

Figure 31: γH2AX and PARP1 protein expression in PSN-1 cells under EIS-1 treatment PSN-1 cells were treated with increasing concentrations of EIS-1 or DMSO for 48 h. For Immunodetection, the indicated antibodies were used. Image shows a representative Western Blot. For quantification of biological replicates and a control with talazoparib, see Supplementary Figure 15.

The results revealed a concentration-dependent increase in the DNA damage marker γH2AX, and the apoptosis marker cleaved PARP1 at concentrations exceeding 6.25 µM. These findings indicate that ALC1i treatment triggers DNA damage and apoptotic responses in PSN-1 cells, suggesting the involvement of ALC1 in maintaining genomic integrity and cell survival in HR-proficient ALC1i-sensitive cells.

To validate the γH2AX signal observed in the previous experiments, FACS analysis was performed on MDA-MB-231 and SUM149PT cells, treated with EIS-1 for 120h. Post-treatment, cells were fixed and permeabilized for antibody staining, including a live/dead stain and γH2AX-specific antibody. SN-38 served as the DNA damage-inducing control for γH2AX signal. Results for treatment with EIS-1 are shown in Figure 32.

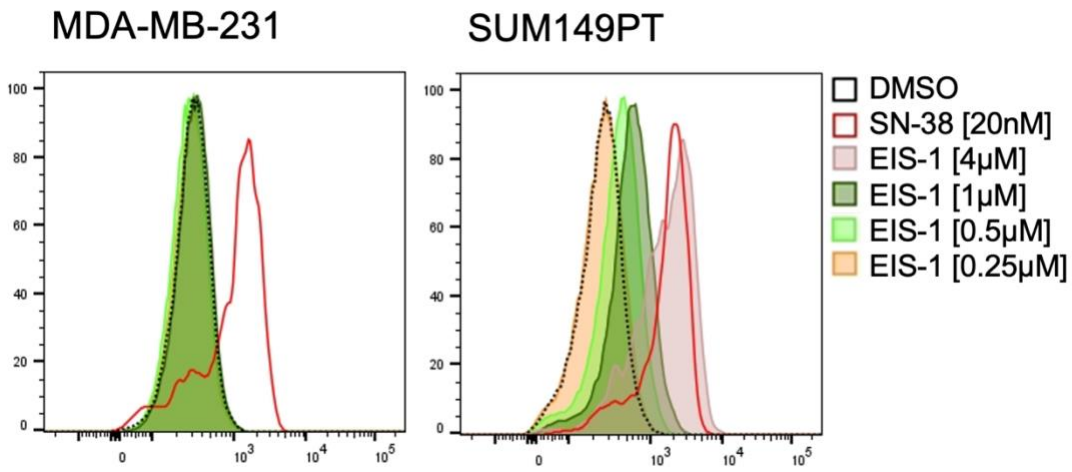

Figure 32: γH2AX levels under EIS-1 treatment

FACS analysis of SUM149PT and MDA-MB-231 cells treated with EIS-1 (orange, green, rose), SN-38 (red), or DMSO (black) for 120h. Cells were stained for γH2AX. One biological replicate is shown. The experiment was repeated once, showing similar results (see Supplementary Figure 16). FACS and graphical illustration were performed by Dr. Markus Lechner, Eisbach Bio GmbH.

FACS analysis of the γH2AX signal confirmed a concentration-dependent increase in ALC1i-sensitive SUM149PT cells. The lowest concentration of EIS-1 to elicit a noticeable rise in the γH2AX signal was 0.5 μM. This observation suggests that ALC1 inhibition led to DNA damage accumulation, as indicated by the increased γH2AX signal, specifically in the ALC1i-sensitive SUM149PT cells. In contrast, no significant change in the γH2AX signal was observed in ALC1i-resistant MDA-MB-231 cells following ALC1i treatment.
An Annexin V staining-based Fluorescence-Activated Cell Sorting (FACS) assay was employed for additional validation of apoptosis induction. In SUM149PT cells, a concentration-dependent elevation of Annexin V was observed upon treatment with EIS-1, indicative of apoptotic activity. However, this effect was not evident in MDA-MB-231 cells. Detailed data regarding these findings are shown in Supplementary Figure 17.
These results indicate a fundamentally differential response to ALC1 inhibition in ALC1i-sensitive vs. ALC1i-resistant cells.

4.3.3. ALC1 inhibition leads to formation of γH2AX and RAD51 foci

To further investigate the impact of ALC1i on the DNA damage response, a γH2AX and RAD51 foci formation assay was performed. HR-proficient, ALC1i-sensitive PSN-1 cells were selected for the dose-range finding experiment. A dose titration of EIS-1 was applied to the cells for 24 h. The cells were fixed and stained for γH2AX and RAD51. The number of foci per cell nucleus was quantified, and the fraction of cells exhibiting more than 15 foci for γH2AX and more than 5 foci for RAD51 was determined. These measurements allowed for assessing concentration-dependent changes in γH2AX and RAD51 foci formation, providing insights into the DNA damage and repair dynamics in response to ALC1i treatment. Merged images of the γH2AX channel (red), RAD51 channel (green), and DAPI channel (blue) are shown in Figure 33 A), and calculated fractions are shown in Figure 33 B, C). Single-channel images for all concentrations are shown in Supplementary Figure 18.

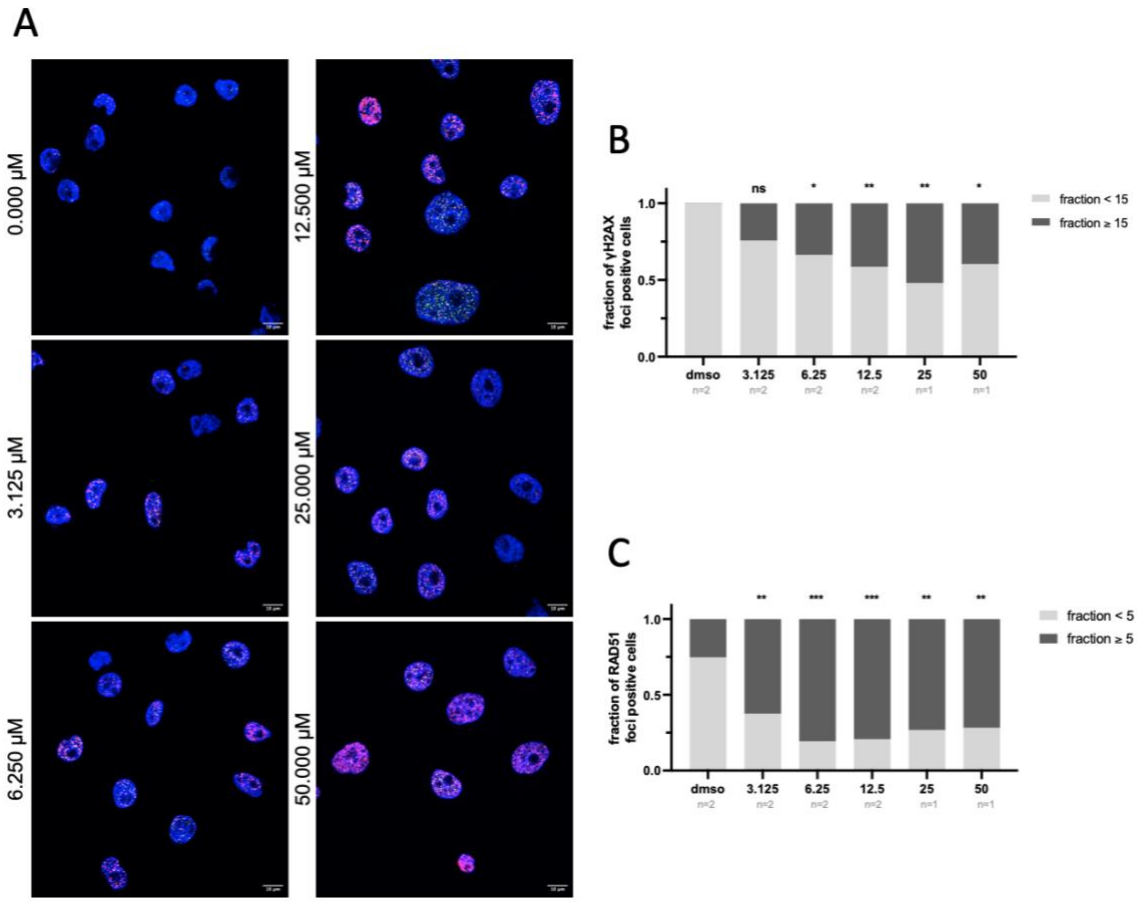

Figure 33: γH2AX and RAD51 foci formation under ALC1i treatment in PSN-1 cells

PSN-1 cells were treated with EIS-1 for 24 h, fixed and stained for γH2AX and RAD51, and counterstained with DAPI. Z-images were stacked using Fiji (ImageJ). Merged IF-images of nuclear foci formation DAPI (blue), RAD51 (green) and γH2AX (red) are shown in A). Quantification of (A) as fractions of cells with ≥15 or <15 γH2AX foci per nucleus

is shown in B) and quantification of A) in fractions of cells with ≥5 or <5 RAD51 foci per nucleus is shown in C). The mean of biological replicates (n) is indicated in grey. Each biological replicate included >30 cells. For statistical analysis, a two-way ANOVA test in GraphPad PRISM was used. P-values are indicated in Supplementary Table 17, Supplementary Table 18.

Treatment of PSN-1 cells with concentrations of EIS-1 exceeding 3.125 μM resulted in a notable and statistically significant increase in the fraction of cells exhibiting more than 15 γH2AX foci per nucleus. This observation suggests a concentration-dependent induction of DNA damage in response to ALC1 inhibition. Concurrently, there was also a corresponding increase in the fraction of cells displaying more than 5 RAD51 foci per nucleus, indicating an upregulation of HR-dependent repair processes. These findings suggest that ALC1 inhibition with EIS-1 triggers DNA damage and elicits a DNA repair response mediated by RAD51 in HR-proficient PSN-1 cells. The significant changes in the formation of γH2AX and RAD51 foci further support the notion that ALC1 is critical in the DNA damage response and repair pathways.

The cell pair MDA-MB-231 and SUM149PT was used to assess further differences in sensitivity to ALC1i in the foci formation assay. Both cell lines were subjected to a 24-h treatment with a titration of EIS-1, followed by the analysis of foci formation fractions as described in the assay above. Representative merged images (γH2AX (red), RAD51 (green), and DAPI (blue)) for chosen drug concentrations for both cell lines are shown in Figure 34; graphs represent the analysis of foci-positive cells for all concentrations used. Single-channel and merged images of the cell lines with the complete drug titration are shown in Supplementary Figure 19 and Supplementary Figure 20.

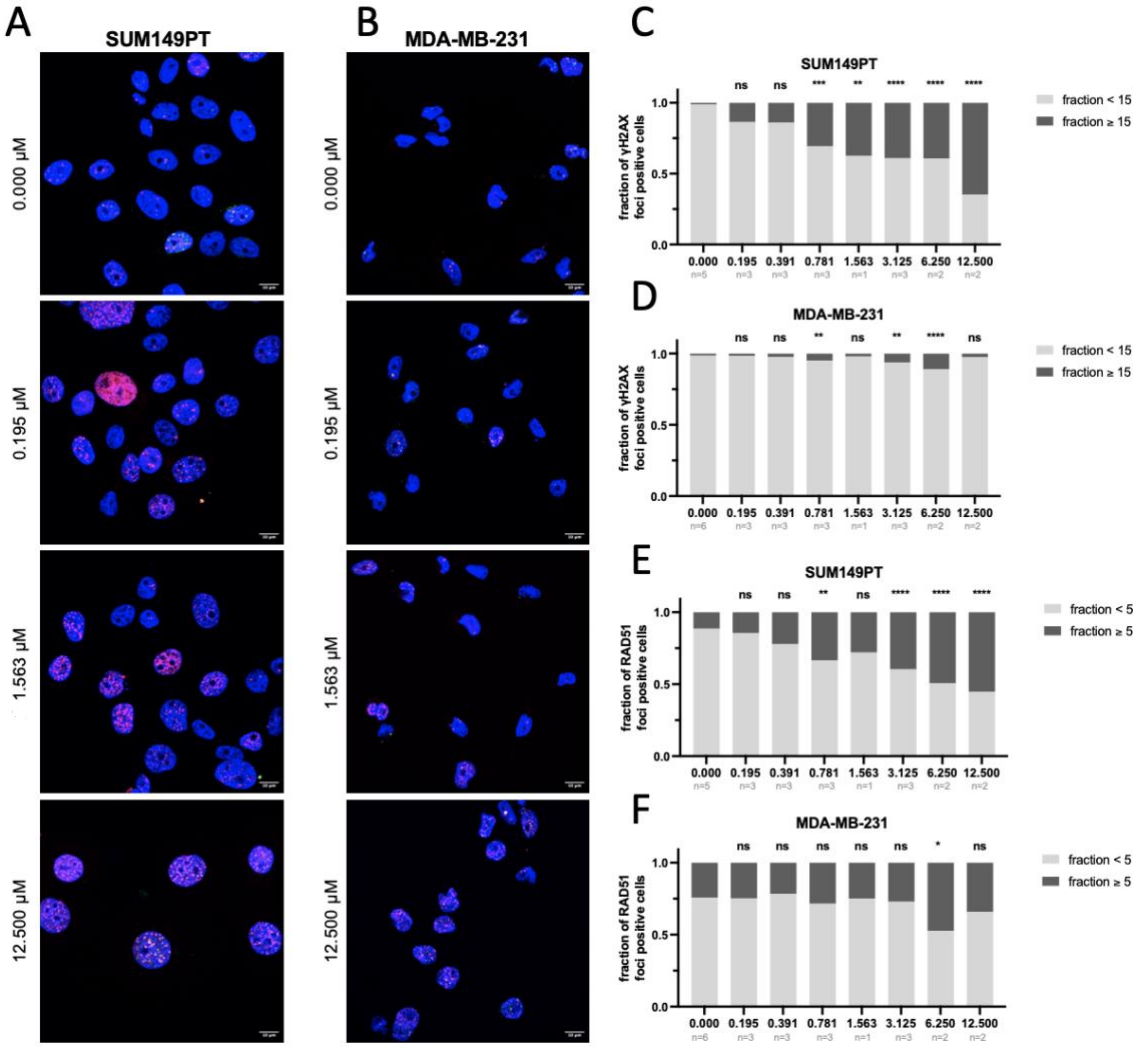

Figure 34: γH2AX and RAD51 foci formation under EIS-1 treatment in screening cell pair MDA-MB-231 and SUM149PT

Cells were treated with EIS-1 for 24 h, fixed and stained for γH2AX (red) and RAD51 (green), and counterstained with DAPI (blue). Z-images were stacked using Fiji (ImageJ). Representative IF-images of merged channels of A) SUM149PT and B) MDA-MB-231 cells are shown on the left. Quantification of γH2AX foci in fractions of cells with ≥15 or <15 foci per nucleus is shown in C) and D). Quantification of RAD51 foci in fractions of cells with ≥5 or <5 foci per nucleus is shown in E) and F). Data represent the mean of biological replicates (n) indicated in the graph. Each biological replicate included >30 cells. For statistical analysis, a two-way ANOVA test in GraphPad PRISM was used. P-values are indicated in Supplementary Table 17, Supplementary Table 18.

ALC1i-sensitive SUM149PT cells exhibited a significant concentration-dependent increase in both γH2AX and RAD51 positive fractions when treated with EIS-1 concentrations > 0.391 µM. This finding suggests that higher concentrations of EIS-1 induced DNA damage or lead to increased accumulation of DNA damage in SUM149PT

cells. As SUM149PT cells were deficient in IR-induced RAD51 foci formation, the RAD51 foci detected in SUM149PT cells indicate DNA damage beyond DSBs. In MDA-MB-231 cells, which are insensitive to ALC1i, no concentration-dependent increase in γH2AX or RAD51 positive fractions was observed. Only the highest concentrations (>6.25 µM) showed a mild increase in foci formation in the ALC1i insensitive cell line.

4.3.4. Selective G2/M arrest induced by EIS-1 in ALC1i sensitive cells

The impact of ALC1 inhibition on the cell cycle was investigated in MDA-MB-231 and SUM149PT cells. Both cell lines were treated with EIS-1 (10 µM to 250 nM) for 48 h, and DNA content was stained using DAPI. SN-38 was used as a positive control for cell cycle arrest. Cell cycle states were analyzed using FACS analysis. The results of the cell cycle analysis are presented in Figure 35.

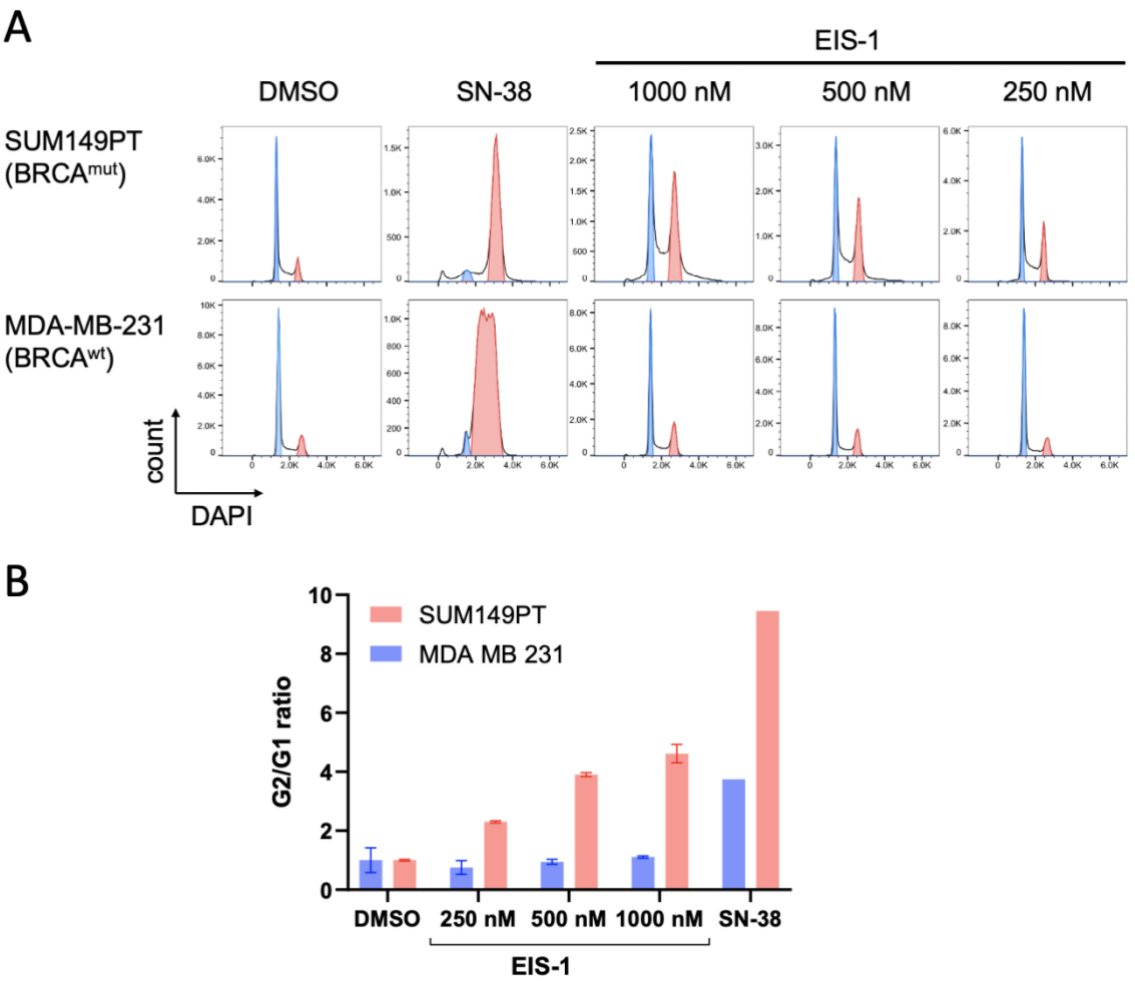

Figure 35: Cell cycle analysis of MDA-MB-231 & SUM149PT cells under EIS-1 treatment FACS analysis of SUM149PT and MDA-MB-231 cells treated with EIS-1 or SN-38 for 48h. G1 indicated in blue, G2/M indicated in red. B) normalized G2/G1 peak ratio to DMSO controls of either MDA-MB-231 (blue) or SUM149PT (red) cells. Error bars indicate SD of two biological replicates (SN-38 without error bars, no clear G1 phase visible for AUC fitting and

quantification). FACS and graphical illustration were performed by Dr. Markus Lechner, Eisbach Bio GmbH.

Treatment with EIS-1 in ALC1i-sensitive SUM149PT cells resulted in a concentration-dependent significant G2/M arrest even at very low concentrations, starting from 250 nM. In MDA-MB-231 cells, minimal effects on the cell cycle were observed. In contrast, both cell lines exhibited a substantial G2-phase arrest when treated with SN-38, the well-known cell cycle-arresting agent. These findings demonstrate the ability of EIS-1 to induce a concentration-dependent G2/M arrest selectively in ALC1i-sensitive cells, which correlates with the presence of DSB. An increase in Rad51 foci accumulation can thus, at least in part, be explained by a higher fraction of G2 phase cells.

4.3.5. Revealing changes in DNA repair protein dynamics at DNA lesions: Insights into ALC1i effects on protein recruitment and trapping

To understand the impact of ALC1 inhibition through small molecule inhibitors, different DDR proteins, like PARPs, ALC1, or XRCC1, were examined in their dynamics of recruiting to DNA lesions in live cell microscopy. U-2 OS cells were transiently transfected with fluorophore-tagged DNA repair proteins. DNA damage was introduced using a 355 nm laser, allowing the visualization of their localization at DNA damage sites in real time.

Protein retention was measured over 35 minutes. To induce a lot of DNA damage, the laser power was set to 10%. In this assay setup, strong protein trappers could be visualized. Protein trapping data was calculated as the area under the curve (AUC). This raw data was normalized to the maximum signal per nucleus to better visualize the trapping effect towards the end of the imaging time.

For a more specific analysis, protein behavior was analyzed using the 8-minute assay setup, where more imaging frames were added at the beginning of the assay. To also detect weak protein trappers and have the chance to analyze the protein recruitment to the damage site, less DNA damage was induced using reduced laser power. The raw data as AUC is shown to better visualize the protein recruitment.

4.3.5.1. Trapping of PARP enzymes through ALC1i

The first experiment aimed to replicate the known differences in PARP1 trapping ability exhibited by various PARPi using the here-developed assay conditions. U-2 OS cells were transiently transfected with PARP1-GFP and treated with ALC1i or different PARPi for 1 h before imaging. DNA damage was induced with 10% laser power, and images were captured over 35 minutes. The dynamics of PARP1-GFP retention at the damage site were analyzed and presented in Figure 36.

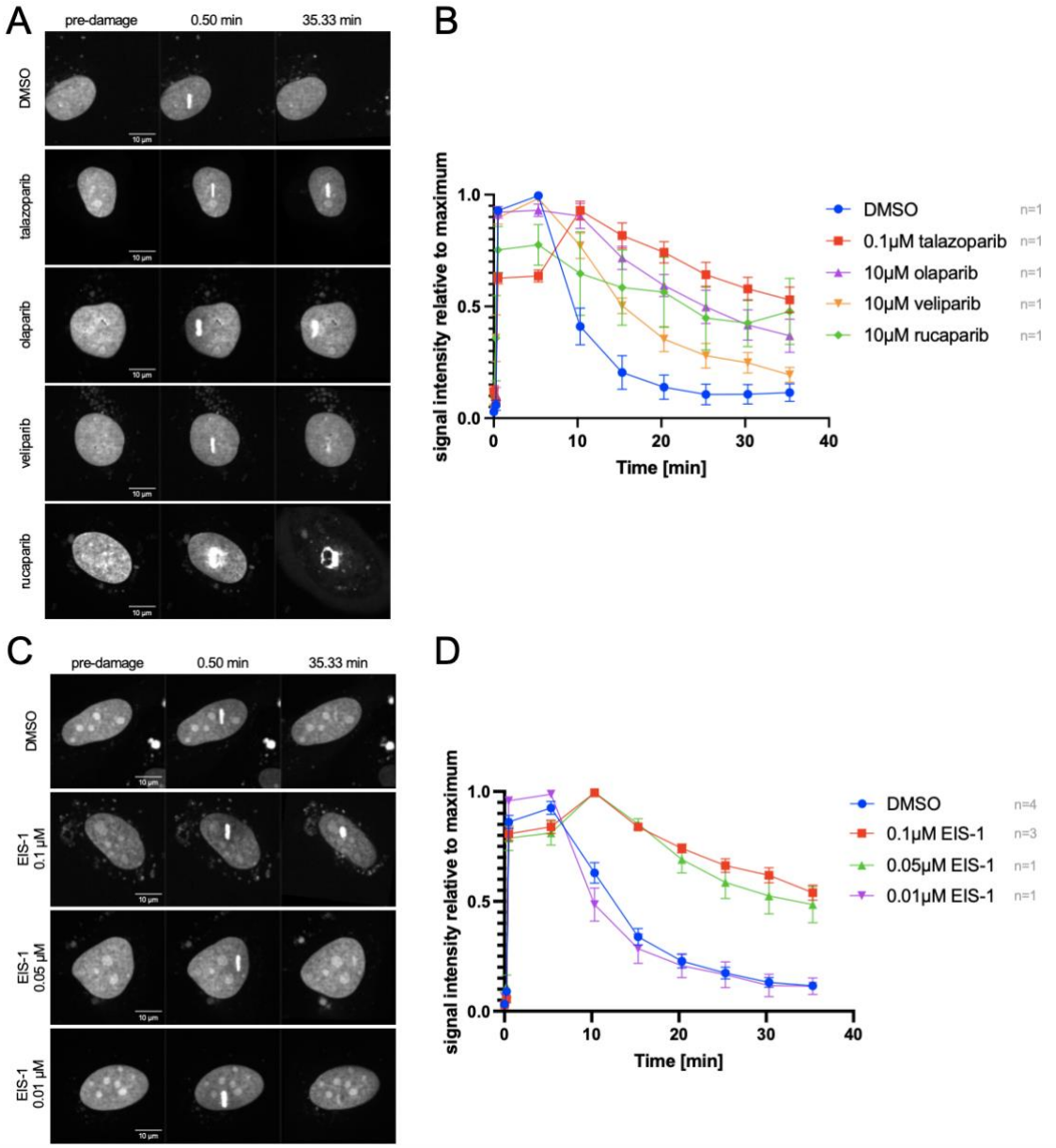

Figure 36: Effects of PARPi and ALC1i on retention dynamics of PARP1-GFP at DNA damage sites

U-2 OS cells were transiently transfected with PARP1-GFP. DNA damage was induced using a 355 nm laser with 10% laser power. Cells were treated with PARPi (A, B) or ALC1i (C, D) for 1h. PARP1-GFP retention at the DNA lesion was observed over time. Images of cells at t0 (before the damage; 0 min), t1 (right after damage induction; 0.5 min), and t2 (end of the assay; 35.33 min) are shown in A, C. Signal intensity relative to the maximum signal is shown in B, D. Curves were fitted using GraphPad Prism. The data includes 1-4 biological replicates. Error bars indicate the SEM of 6-39 nuclei per condition.

Representative images of the time points before the damage, 0.5 minutes after the damage, and at the end of the assay, 35.33 minutes after the damage, are shown in Figure 36, A, C). At 35.33 minutes, diverse effects of the PARPi on PARP1 retention at the lesion were observed. Under normal conditions, PARP1 rapidly recruited to the damage within milliseconds, and the signal dissipated entirely after 35 minutes. Treatment with talazoparib had the most significant impact on PARP1 retention, as the PARP1 signal persisted at the site of damage throughout the entire time course, a phenomenon referred to as protein trapping. Olaparib and rucaparib exhibited milder effects on PARP1 retention, while veliparib showed the weakest effect. These results reproduced the relative PARP1 trapping strengths reported in classical PARP trapping assays (Huan et al., 2020), thereby validating the live-cell imaging approach as a suitable method to assess and compare protein trapping dynamics at DNA damage sites. The impact of ALC1i on PARP1 retention dynamics is shown in C), D). EIS-1 exhibited the ability to trap PARP1 in a concentration dependent matter, as evidenced by increased retention dynamics. Concentrations as low as 0.05 µM lead to the trapping of PARP1.

Early recruitment dynamics of PARP1-GFP under PARPi and ALC1i treatment were analyzed in greater detail using the 8-minute imaging setup, where less DNA damage was induced. EIS-1, talazoparib, olaparib, and veliparib reduced the recruitment of PARP1-GFP, while rucaparib resulted in significantly increased recruitment. Supplementary Figure 21, A) displays representative images at various time points, including before the damage, 10 seconds after the damage, 30 seconds after the damage, and 495 seconds after the damage. The raw signal of the area under the curve highlights the differences in recruitment signals. Data normalized to the maximum reflects the effect on PARP1 trapping from the 35.33-minute assay. EIS-1, talazoparib and rucaparib trapped PARP1 the most, while olaparib and veliparib revealed milder effects.

The dose-dependent effect of EIS-1 on the retention of PARP2-GFP was also investigated; the results are presented in Supplementary Figure 22. In general, the recruitment of PARP2 to DNA lesions was weaker compared to PARP1 recruitment. Here, only at the highest concentration of EIS-1 (0.1 µM) had a noticeable trapping effect on PARP2. PARP-3-GFP dynamics at DNA lesions were also tested in the live cell imaging assay (see Supplementary Figure 23). Only a weak recruitment signal was observed after DNA damage induction with the 10% 355 nm laser in the control group. The effects were too weak to analyze compound effects in this assay setup. While this live-cell imaging assay allows sensitive detection of protein retention dynamics, classical PARP trapping assays based on protein extraction and washout conditions were not performed in this study.

4.3.5.2. Modulation of recruitment dynamics of other DNA repair proteins at DNA damages sites by ALC1i

Next, the dynamics of ALC1 at DNA lesions were examined by analyzing U-2 OS cells transiently transfected with EGFP-ALC1 and treated with different concentrations of EIS-1 for 1 h. ALC1 protein retention is illustrated in Supplementary Figure 24. In the 35-minute assay using 10% laser power, only the highest concentration of EIS-1 exhibited a modest effect on the protein trapping of ALC1.

A closer look at the protein dynamics using the 8-minute assay under less DNA damage (reduced laser power) revealed significant differences. When examining the raw signal represented by the AUC, a concentration-dependent effect on the recruitment of ALC1 in response to ALC1i treatment was evident (Figure 37).

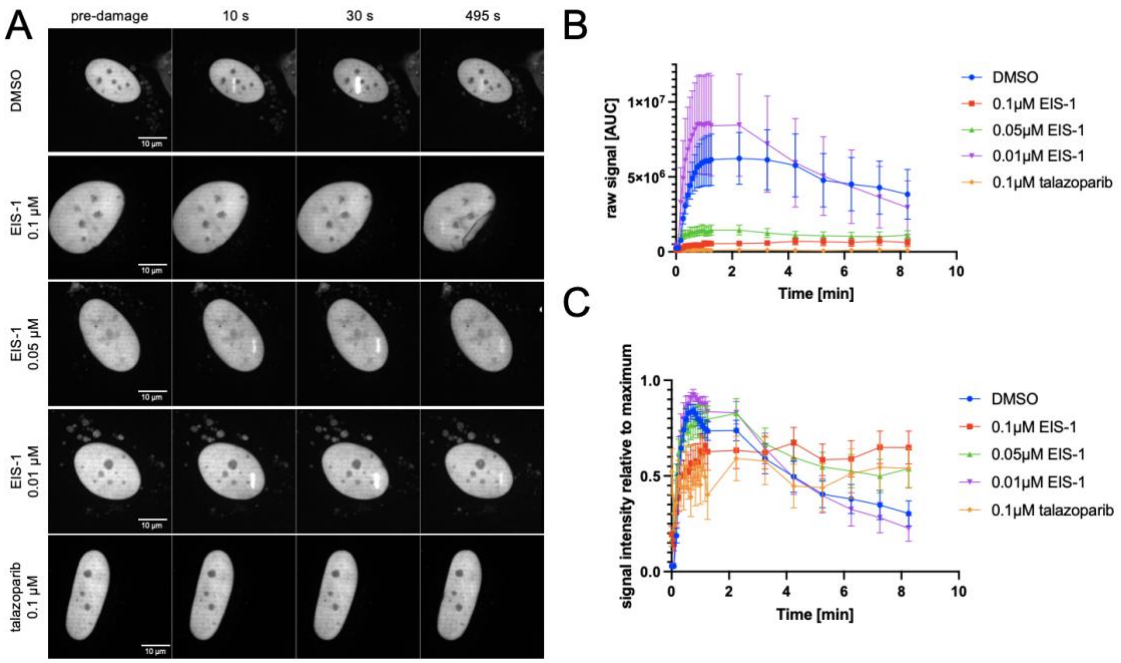

Figure 37: Effect of EIS-1 and PARPi on EGFP-ALC1 recruitment

U-2 OS cells were transfected with EGFP-ALC1 and subjected to DNA damage using a 355 nm laser with a laser power of 2.5%. Cells were treated with ALC1i or PARPi for 1h. Protein recruitment to the DNA lesion was observed over time. Images of cells at various timepoints are shown in A). The raw signal as the area under the curve (AUC) is shown in B) and signal intensity relative to the maximum signal is shown in C). The data includes 1 biological replicate. Error bars indicate the SEM of 7-16 nuclei per condition.

Concentrations of ALC1i >0.05 µM significantly decreased ALC1 recruitment. The signal intensity normalized to the maximum signal intensity also indicates a concentration-dependent ALC1-trapping effect that was not visible in the “high DNA damage” assay conditions from the long-term assay. As talazoparib is known to reduce PARylation,

which is necessary for ALC1 activation, it was used as a control for the reduction of ALC1 recruitment. Like EIS-1, talazoparib significantly decreased ALC1 recruitment and showed a trapping-like effect of ALC1. The signal intensity normalized to the maximum visualizes ALC1 trapping under EIS-1 and talazoparib treatment.

As another downstream effector of PARP1 PARylation at DNA damage sites, XRCC1 interacts with and recruits other repair proteins to damaged DNA sites, facilitating the repair process (Reber et al., 2022). The effect of ALC1i and PARPi on XRCC1 protein dynamics at DNA lesions was tested and is shown in Supplementary Figure 25 and Figure 38. U-2 OS cells were transiently transfected with XRCC1-YFP and treated with talazoparib or EIS-1 for 1 h before imaging. The retention of XRCC1 was monitored for 35.33 minutes (Supplementary Figure 25). Under vehicle treatment, a substantial amount of XRCC1 was recruited to the DNA damage, resulting in a strong signal that exceeded the imaging time limit of the assay. No protein trapping in the “high DNA damage” long-term assay was observed under the treatment with EIS-1 or talazoparib, as the signal of XRCC1 was still present at the end of the assay under control conditions. The raw signal (AUC) analysis indicated a concentration-dependent effect of EIS-1 and talazoparib on XRCC1 recruitment.

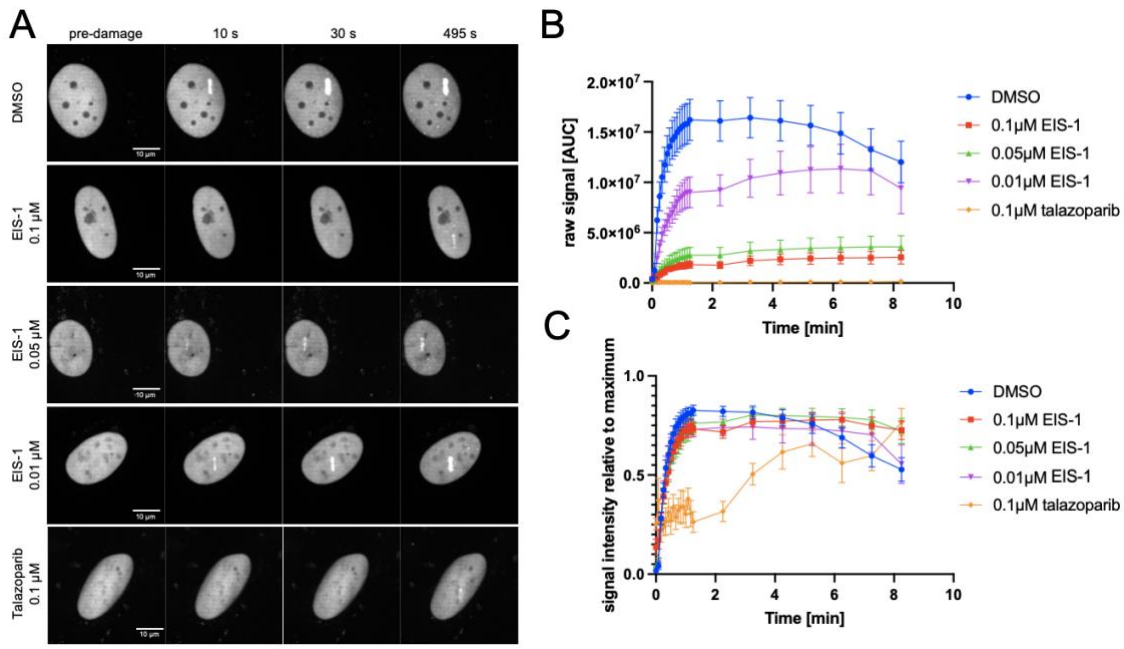

Figure 38: Effect of ALC1i and PARPi treatment on XRCC1-YFP recruitment

U-2 OS cells were transiently transfected with XRCC1-YFP. DNA damage was induced in the nucleus using a 355 nm laser with a laser power of 2.5 %. Cells were treated with different concentrations of EIS-1 or PARPi for 1h. Protein recruitment to the DNA lesion was observed over time. Images of cells at t0 (before the damage; 0 s), t1 (right after the damage; 10 s), t2 (30 s) and t3 (end of the assay; 495 s) are shown in A. For visualization

of diverse signal intensities, raw signal as area under the curve (AUC) is shown in B. Signal intensity relative to the maximum signal is shown in C. Curves were fitted using GraphPad Prism. The data includes 1-3 biological replicate. Error bars indicate the SEM of 7-34 nuclei per condition.

The raw signal (AUC) in panel B shows that talazoparib and EIS-1 significantly reduced XRCC1 recruitment in a concentration dependent manner.

4.3.6. Summary of the results

ALC1 inhibition triggered DNA damage and apoptotic responses in ALC1i-sensitive cells. Concentration-dependent increases in the DNA damage marker γH2AX and the apoptosis marker cleaved PARP1 were observed, indicating the involvement of ALC1 in maintaining genomic integrity and cell survival in ALC1i-sensitive cells. FACS analysis confirmed the selective increase in DNA damage in ALC1i-sensitive cells. Treatment with ALC1i increased the fraction of cells displaying DNA damage foci (γH2AX) and RAD51 foci independent of the HR-status of the ALC1i-sensitve cell lines, PSN-1 (HRP) and SUM149PT (HRD). Only a mild increase in foci positive fractions was observed in ALC1i-insensitvie MDA-MB-231 cells. This underscores the notion that the sensitivity to ALC1i is not exclusively reliant on the HR-status.

ALC1i-sensitive cells treated with EIS-1 showed a concentration-dependent increase in apoptotic cells and a cell cycle arrest in the G2/M phase.

EIS-1 exhibited significantly impacts on protein dynamics at DNA damage sites, similar to talazoparib. Concentrations as low as 50 nM reduced recruitment of essential damage repair proteins such as PARP1, PARP2, ALC1, and XRCC1. Notably, EIS-1 demonstrated trapping effects on PARP1 and PARP2 and reduced the recruitment of ALC1 and XRCC1 to DNA lesions.

While these effects were assessed using live-cell imaging, additional biochemical trapping assays employing permeabilized cells could further refine the mechanistic understanding of ALC1 inhibitor–mediated trapping.

4.4. Evaluation of the tumor suppressing potential of ALC1i monotherapy in xenograft models

The monotherapy potential of ALC1 inhibition was tested in xenograft experiments. ALC1i-sensitive SUM149PT cells were implanted subcutaneously in immunosuppressed NMRI nude mice. EIS-1 was administered daily as oral gavage, with concentrations ranging from 3.91 mg/ko to 125mg/kg, formulated in SyrSpend. Tumor volume was measured 3 times a week. Tumor cells for the xenograft experiment were expanded and prepared following the cellular procedure protocol mentioned in the methods section.

Further steps of the xenograft experiments were run at the animal facility at the BMC by Dana Matzek, William Menzer, Dr. Adrian Schomburg and Dr. Markus Lechner at Eisbach Bio GmbH. The average tumor volume per group is shown in Figure 39, A). Growth curves of individual animals are shown in Figure 39, B).

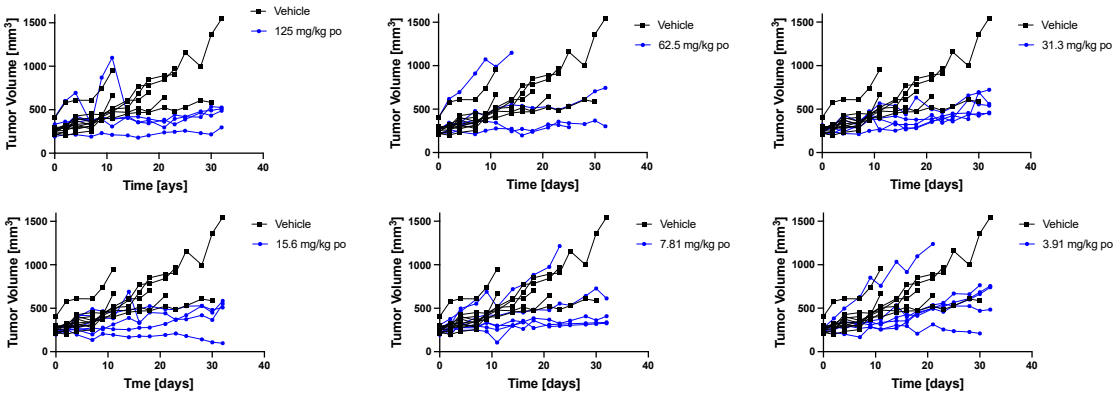

Figure 39: In vivo efficacy of EIS-1 SUM149PT xenograft

The efficacy of EIS-1 was tested in a SUM149PT breast cancer xenograft model in NMRI nude mice. EIS-1 was given daily via oral gavage at doses from 3.91 mg/kg to 125 mg/kg in SyrSpend. Tumor growth curves for individual mice (6-11 per group) are shown, with the vehicle group in black and treated groups in blue.

Treatment with EIS-1 demonstrated consistent TGI effects between 50% and 87% across all tested concentrations. There was no pronounced observed concentration-dependent effect on tumor growth inhibition. The individual growth curves showed significant tumor regression in all concentration groups, with few escapers and no resistance observed. This indicates that EIS-1 exhibits potent anti-tumor activity at concentrations as low as 3.91mg/kg in the background of BRCA1 mutant, HR-deficient tumor cells. Raw data of the xenograft is shown in Supplementary Table 19.

4.4.1. Summary of the results

The study evaluated the monotherapy potential of ALC1 inhibition using the ALC1 inhibitor EIS-1 in xenograft experiments. The individual growth curves of the tumors exhibited significant tumor growth inhibition in all concentration groups, indicating potent anti-tumor activity of EIS-1, even at low concentrations, in the context of BRCA1 mutations. Any mice removed from the xenograft experiment were withdrawn due to tumor volume exceeding limits or the development of tumor ulcerations.

An external toxicology profile assessment was conducted for EIS-1 (data not shown here). Despite ALC1i's ability to trap PARP, the study subjects exhibited no signs of toxicity, even at the highest tested dose of 1000 mg/kg, as indicated by stable weight and other markers.

4.5. The synergistic potential of ALC1i with PARPi and other drugs

This section explores the synergistic effects observed when ALC1i is combined with other therapeutic agents, shedding light on the potential for enhanced treatment outcomes through combination therapy. By elucidating the potential synergistic cell-killing capabilities of ALC1i in combination with existing or emerging drugs, this study provides insights into developing more effective treatment strategies in oncology. For information about the drug mechanism and rationale for combination with ALC1i, see Table 1.

4.5.1. Correlation of PARPi's trapping ability with synergistic action of ALC1i

Demonstrating the synergy of ALC1 inhibition with PARP inhibitors is crucial as it holds the potential to effectively overcome PARP inhibitor resistance, thereby enhancing the therapeutic efficacy and addressing a critical challenge in cancer treatment.

The synergistic effects of ALC1i in combination with PARPi were investigated in cell lines with different genetic backgrounds and tumor origins. 2-D titrations of the compounds were administered to the cells in the 96-h cellular survival assay format. Following the SRB readout, the survival data was analyzed using the SynergyFinder platform, which utilized the ZIP model for synergy detection. To explain the synergy model used in this thesis, refer to the methods section.

Figure 40 displays the most synergistic area scores and synergy maps obtained from the analysis. ZIP-synergy scores, SEM, MSA scores, and curve fitting for all cell lines are shown in Supplementary Table 20. More data can be found in patent Menzer, Sahiri, and Schomburg (2025).

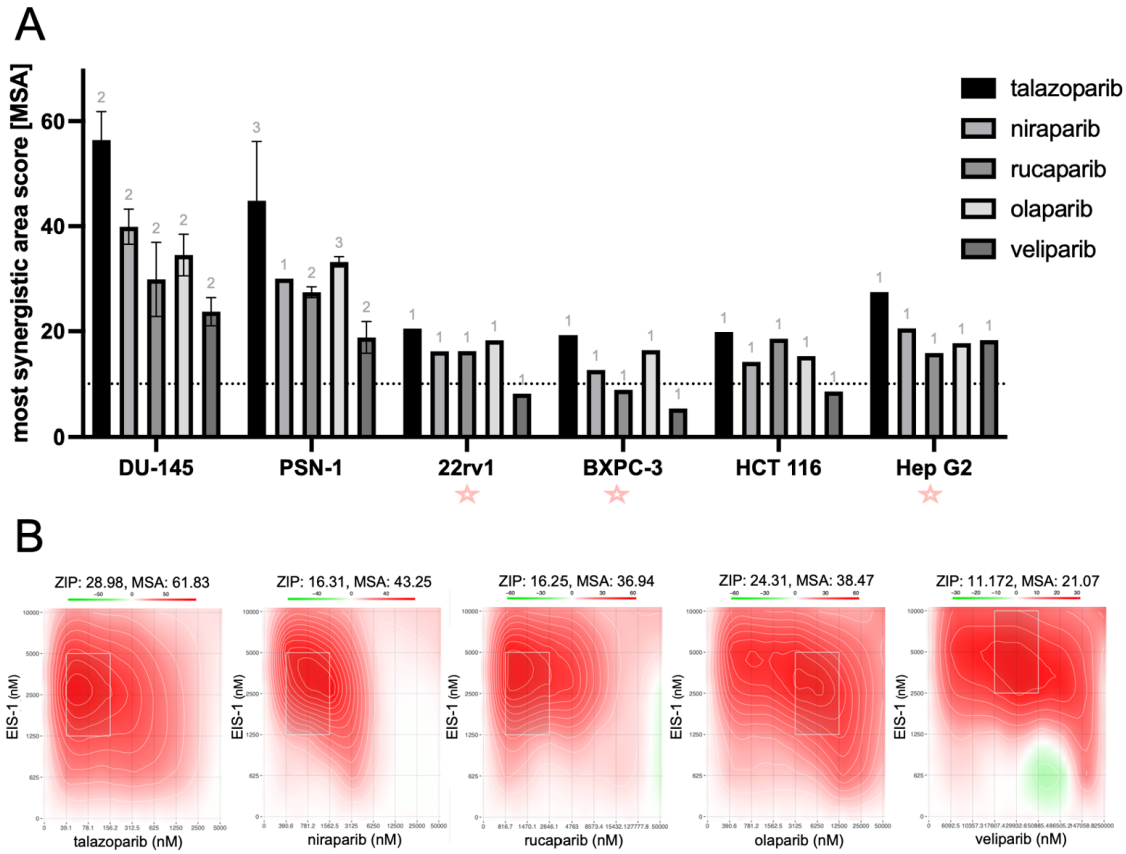

Figure 40: Synergy of ALC1i with PARPi

EIS-1 was tested in combination with various PARP inhibitors (talazoparib, olaparib, rucaparib, niraparib, veliparib) across different cell lines using a 96-h survival assay with a 2-D titration of ALC1i vs. PARPi. ZIP Synergy scores and MSA scores were determined using SynergyFinder. Bar graphs of MSA scores in multiple cell lines are presented in (A), with error bars indicating SEM and grey numbers indicating the number of biological replicates. Each biological replicate included three technical replicates. Red stars mark the cell lines that did not show a good curve fit for at least one of the agents dosed. Synergy Maps (B) were created to visualize the synergy of EIS-1 with different PARPi in DU-145 cells, showing the synergy distribution diagram based on cell growth inhibition. Red indicates higher synergy (>0), while green indicates antagonistic effects (<0).

As mentioned in the methods section, precise curve fitting is critical for the ZIP-synergy model. The concentration of each compound was adjusted to create a total cell growth inhibition curve in the individual cell lines. The cell lines BXPC3, 22Rv1, and Hep G2 were categorized as "less sensitive to PARPi" in the cell line categorization; thus, a good curve fit for single-agent PARPi could not be achieved for all the cell lines. The cell lines with an incomplete curve fit in the single-agent titration were marked with a red star (see Figure 40, A).

Despite the incomplete curve fitting, the results of the different cell lines show the same trend. The data demonstrated reproducibility, as indicated by the error bars in the DU-145 and PSN-1 cell lines. The highest synergy scores were observed in DU-145 cells and PSN-1 cells.

The synergy of PARPi with ALC1i could be achieved in cell lines independent of their tumor origin, mutational profile, or drug sensitivity towards ALC1i and PARP1i:

HepG2 (ALC1i-sensitive, PARPi-insensitive), DU-145, PSN-1 and HCT 116 (PARPi-sensitive, ALC1i-sensitive), 22Rv1 (ALC1i-sensitive, BRCA-deficient, PARPi-insensitive) and BXPC-3 (ALC1i-insensitive, PARPi-insensitive).

Specifically, the combination treatment of EIS-1 with talazoparib exhibited high synergy scores in all cell lines tested. The degree of synergy was found to correlate with the trapping ability of the PARPi, as previously established in the study.

4.5.2. Enhanced efficacy through combination of ALC1i with other FDA-approved or investigational drugs

The synergistic effects of ALC1i with various other FDA-approved and investigational drugs were explored using the 96-h cellular survival assay and analyzed through the SynergyFinder platform. The mechanism of action and rationales for combination with ALC1i are shown in Table 1. The results, depicted in Figure 41, include the most synergistic area scores and synergy maps obtained from treating the PARPi-sensitive and ALC1i-sensitive PSN-1 cell line with EIS-1 combined with different drugs. Overall ZIP synergy scores, SEM, and most synergistic area (MSA) for all drug combinations are shown inSupplementary Table 21.

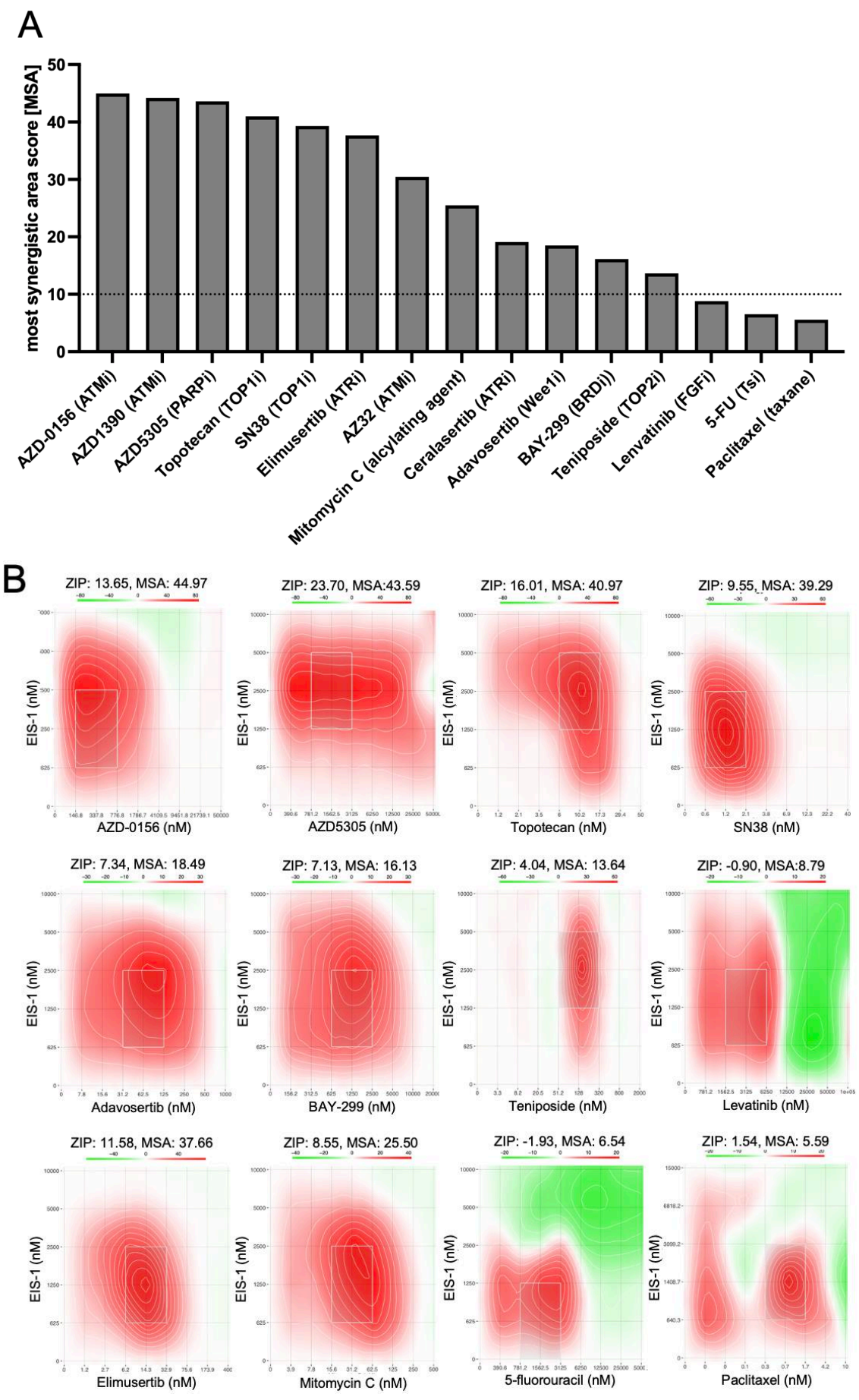
A
most synergistic area score [MSA]
0
10
20
30
40
50
AZD-0156 (ATMi)
AZD1390 (ATMi)
AZD5305 (PARPi)
Topotecan (TOP1i)
SN38 (TOP1i)
Elimusertib (ATRi)
AZ32 (ATMi)
Mitomycin C (alcylating agent)
Ceralasertib (ATRi)
Adavosertib (Wee1i)
BAY-299 (BRDi)
Teniposide (TOP2i)
Lenvatinib (FGFi)
5-FU (Tsi)
Paclitaxel (taxane)
B
ZIP: 13.65, MSA: 44.97
ZIP: 23.70, MSA:43.59
ZIP: 16.01, MSA: 40.97
ZIP: 9.55, MSA: 39.29
ZIP: 7.34, MSA: 18.49
ZIP: 7.13, MSA: 16.13
ZIP: 4.04, MSA: 13.64
ZIP: -0.90, MSA:8.79
ZIP: 11.58, MSA: 37.66
ZIP: 8.55, MSA: 25.50
ZIP: -1.93, MSA: 6.54
ZIP: 1.54, MSA: 5.59
EIS-1 (nM)
AZD-0156 (nM)
AZD5305 (nM)
Topotecan (nM)
SN38 (nM)
Adavosertib (nM)
BAY-299 (nM)
Teniposide (nM)
Levatinib (nM)
Elimusertib (nM)
Mitomycin C (nM)
5-fluorouracil (nM)
Paclitaxel (nM)

Figure 41: Synergy of EIS-1 with other cancer therapeutics in PSN-1 cells
The synergy of EIS-1 with different cancer therapeutics was tested in PSN-1 cells in the 96h SRB survival assay with a 2-D titration of ALC1i vs. different drugs. ZIP synergy score and MSA score were determined using the SynergyFinder. The MSA scores are shown as bar graphs in A). Synergy Maps (B) were created for EIS-1 in combination with different cancer therapeutics, showing the synergy distribution diagram based on cell growth inhibition. Red indicates higher synergy (>0), while green indicates antagonistic effects (<0). Results include one biological replicate and three technical replicates.

Significant synergy was observed in combinations of EIS-1 with TOP1i and other PARPi. These combinations exhibited high synergy scores, indicating an enhanced cell-killing effect when the drugs were used together. Combination with TOP2i and BRDi revealed lower overall ZIP scores but also reached an MSA score >10.
Cell cycle checkpoint inhibitors (CCCi) (ATMi, ATRi, and WEE1i) also revealed high MSA scores in combination with EIS-1, with WEE1i being the weakest synergizing agent.
In contrast, FGFRi, 5-FU, and Paclitaxel did not demonstrate significant synergistic effects. The MSA scores for these combinations remained below 10, indicating limited or no synergy.
While in vitro experiments, such as those involving monolayer cell cultures, provided insights into potential treatments like ALC1i, it is essential to acknowledge their limitations in predicting in vivo outcomes accurately.
Building upon the promising in vitro results, the in vivo efficacy of the combination treatment of EIS-1 and irinotecan (active metabolite for cellular testing: SN-38) was tested by Xin Zhang (Eisbach Bio GmbH) in a PSN-1 xenograft model (data not presented). When administered as a single agent, EIS-1 displayed mild effectiveness in promoting tumor regression. Similarly, irinotecan demonstrated a moderate impact on tumor regression when administered alone. When combined, EIS-1 with irinotecan exhibited a remarkable synergistic effect, substantially reducing tumor size. The observed tumor growth inhibition (TGI) exceeded 100%, indicating that the combination therapy yielded more significant effects than either agent alone. These findings underline the potential of EIS-1 and irinotecan as a synergistic treatment strategy for enhancing tumor regression in PSN-1 xenograft models.
The reasons behind the sensitivity of PSN-1 in vitro remain unclear and warrant further investigation. The results obtained in cell-based studies may not always perfectly reflect the responses observed in living organisms. The in vivo context introduces additional complexities and factors that can influence the effectiveness of therapeutic interventions and highlights the necessity of in vivo testing in addition to cellular assays.

4.5.3. Summary of the results

The combination treatment of EIS-1 with talazoparib showed high synergy scores, which correlated with the trapping ability of PARPi. Significant synergy was observed in combinations of EIS-1 with ATMi, ATRi, TOP1i, and other PARPi. Wee1 inhibitors, BRD inhibitors, and TOP2i showed milder synergistic effects, whereas drugs like FGFRi, 5-FU, and Paclitaxel did not demonstrate significant synergy. High synergistic effects of ALC1i were observed when combined with talazoparib and TOP1i.

4.6. Overcoming PARPi resistance in cancer cell lines

Exploring PARPi resistance as a potential biomarker for ALC1i-sensitivity is an essential endeavor in the context of cancer treatment. Overcoming resistance to PARP inhibitors is a critical challenge in cancer therapy. Results from the cellular survival assay and cell line characterization showed ALC1i-sensitivity in cells that exhibited low or no sensitivity to PARPi. Generating resistant cell lines aimed to facilitate the development of more efficacious treatment strategies, investigate the potential of ALC1i in PARPi resistance, and study the cross-resistance of the different ALC1 inhibitor classes.

4.6.1. Unlocking the potential of ALC1 inhibition to overcome PARPi resistance

To investigate the development of drug resistance to PARPi, three cell lines were subjected to increasing concentrations of different PARPi over four months. Clones were selected from these treated cells, and monoclonal cell lines were established. The chosen clones were then assessed for their resistance level to PARPi and their sensitivity to ALC1i using the 96-h SRB-cellular survival assay. To evaluate the stability of the drug resistance, the cell lines were maintained without treatment for eight weeks, and their survival was monitored for several weeks. The EC50 values obtained from the stability assay are presented in Figure 42.

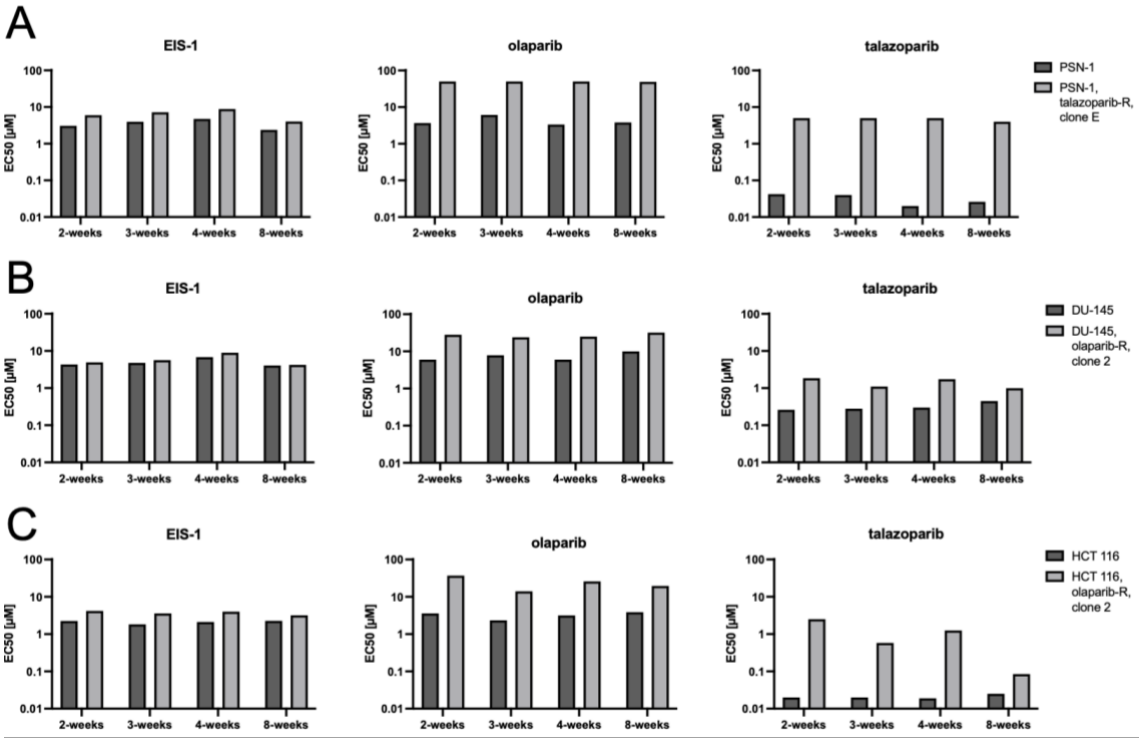

Figure 42: Stable sensitivity to EIS-1 in PARPi resistant cell lines Talazoparib-resistant PSN-1 clone E (A), Olaparib resistant DU-145 clone 2 (B), and Olaparib resistant HCT 116 clone 2 (C) were maintained without PARPi for over 8 weeks. Resistance against EIS-1 and PARPi was tested in the 96h SRB-survival readout. Data represents a mean of two technical replicates per assay. Resistant cells were tested against their parental cell lines. Inhibitor vs. response curves were fitted using GraphPad Prism. Bar graphs represent EC50 values of fitted survival curves over 8 weeks. Due to solubility limits of the compounds, the highest assay concentration was 50 µM for ALC1i and Olaparib, and 5 µM for talazoparib. Raw values of the fold resistance (EC50) to parental cell line are indicated in Supplementary Table 22.

The talazoparib-resistant PSN-1 cell line (Clone E) (A), olaparib-resistant DU-145 cell line (Clone 2) (B), and olaparib-resistant HCT 116 cell line (Clone 2) (C) were compared to their respective parental cell lines. The resistance to PARPi remained stable over the eight weeks, even in the absence of PARPi, as indicated by the increased EC50 values observed in the resistant cell lines. Overall, the PARPi-sensitive cell lines PSN-1 and HCT 116 developed higher fold resistance to PARPi than DU-145 cells. Resistance to one PARPi always leads to resistance to the other PARPi.

As demonstrated by the stability assay, the EC50 values for all the tested drugs remained stable over the eight-week period. Despite their resistance to PARPi, all three PARPi-resistant cell lines retained their sensitivity to ALC1i. The development of resistance to talazoparib corresponded to resistance against olaparib and vice versa. For a detailed

compilation of the EC50 values, please refer to Supplementary Table 22. The findings emphasize the potential of ALC1i in overcoming PARPi resistance and underscore the interplay between different PARPi molecules in the context of drug resistance.

P-glycoprotein (P-gp) contributes to drug resistance in cancer through inherent or acquired overexpression. It hinders the accumulation of anticancer drugs within cells, preventing their cytotoxic effects. P-gp achieves this by using ATP to actively transport drugs across the plasma membrane against concentration gradients. As a member of the eukaryotic ATP binding cassette (ABC) superfamily, P-gp's role in drug efflux is a significant factor in cancer resistance (Steinbach & Legrand, 2007) .

To further assess the sensitivity of talazoparib-resistant cell lines to ALC1i, a whole set of resistant clones was investigated in the 96h cellular survival assay. SN-38, a substrate of p-glycoprotein, was used as a control for potential mutations related to drug transporter efflux pumps.

Talazoparib-resistant monoclonal cell lines derived from two different parental DU-145 cell lines (20 and 23; resistance acquired through different starting concentrations of talazoparib) and one parental PSN-1 cell line (resistance acquired through same starting concentration of talazoparib) were tested against ALC1i, PARPi, and SN-38. Figure 43 presents the fold-change in EC50 of different resistant clones compared to the parental cell line. EC50 values and fold-resistance are shown in Supplementary Table 23, Supplementary Table 24. Survival curves are shown in Supplementary Figure 26.

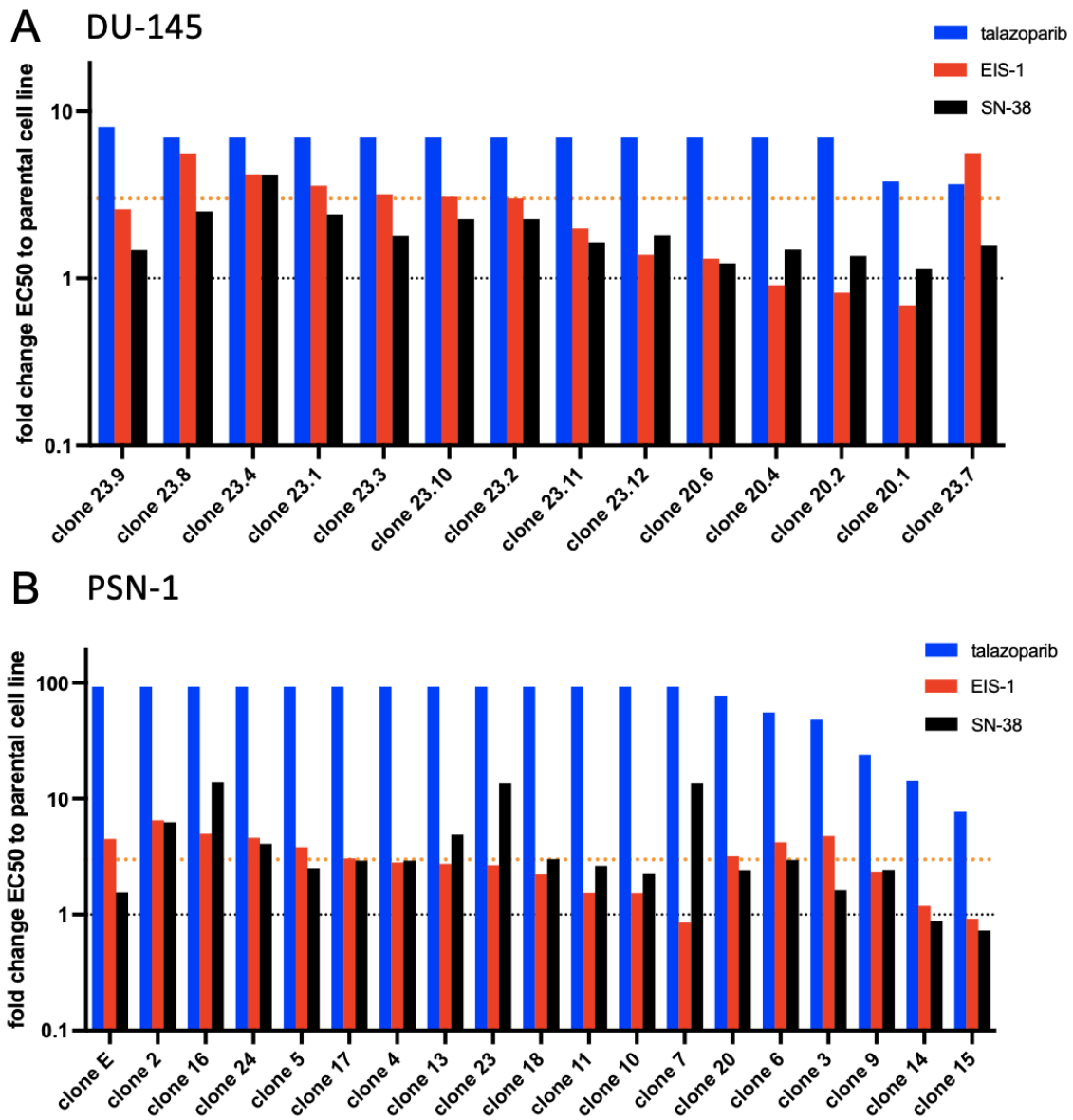

Figure 43: Diversity of talazoparib-resistant monoclonal cell lines Talazoparib-resistant DU-145 (A) and PSN-1 (B) monoclonal cell lines were tested against their parental cell line in the 96h SRB-survival readout. Cells were treated with talazoparib, EIS-1, or SN-38. Inhibitor vs. response curves were fitted using GraphPad Prism non-linear regression. Bar graphs represent the fold change in EC50 values compared to the parental cell line based on two technical replicates. Dashed lines at 1 represents no change in EC50, orange dashed line at 3 indicates a 3-fold-resistance. Due to the solubility limits of the compounds, the highest assay concentration reached for EIS-1 was 50 µM, and for talazoparib, 5 µM. EC50 values above the solubility limit were marked with the value of the highest dose possible. Raw values of the fold resistance (EC50) to parental cell line are indicated in Supplementary Table 23, Supplementary Table 24. Corresponding survival curves are shown in Supplementary Figure 26.

Figure 43 displays the EC50 values of the parental cell lines compared to the monoclonal cell lines resistant to PARPi. A table containing the fold change EC50 values can be found in Supplementary Table 25.

All the clones exhibited >3-fold resistance to talazoparib. All DU-145 clones derived from cell line 20 and the clones 23.9, 23.11 and 23.12 showed <3-fold resistance to ALC1i or SN-38, suggesting that ALC1i treatment might overcome PARPi resistance in these cell lines. 6/14 DU-145 clones exhibited >3-fold resistance to EIS-1, with one cell line showing increased resistance to SN-38.

Since PSN-1 cells are more sensitive to PARPi, the resistance to talazoparib was even more pronounced than the DU-145 cells. Most of the clones displayed >10-fold increase in resistance to PARPi. Only 9/19 PSN-clones showed a >3-fold increase in resistance to ALC1i. 3/9 of those clones also showed increased resistance to SN-38. These findings indicate a potential alteration in the drug efflux transporter rather than a resistance to ALC1i. 4/10 clones that showed elevated resistance to SN-38 were still sensitive to ALC1i.

4.6.2. Summary of the results

The study's results demonstrate the development and stability of drug resistance to PARPi in different cell lines. The resistant cell lines exhibited increased resistance to the PARPi talazoparib and olaparib. Despite their resistance to PARPi, some resistant cell lines remained sensitive to ALC1i, highlighting the potential of ALC1i to overcome PARPi resistance in selected patient cohorts. The study also revealed the interplay between different PARPi molecules, with the development of resistance to one PARPi corresponding to resistance against other PARPi.

5. Discussion and Conclusion

5.1. Discussion

5.1.1. ALC1 is synthetic lethal with HRD and beyond

The exploration of ALC1 as a downstream target of PARP1 has shown encouraging results, revealing ALC1 inhibition as a promising strategy to overcome resistance and reduce the toxicity linked to PARP inhibitors. By specifically focusing on ALC1, an ATP-dependent chromatin remodeler linked to DNA repair processes by sliding nucleosomes, the research has unveiled a targeted strategy to modulate PARP-dependent DDR function. This approach addresses the persistent challenge of PARP1's involvement in essential housekeeping functions and offers a potential solution to PARPi resistance. Using an HTS approach, Eisbach Bio GmbH discovered a set of allosteric-regulated ALC1i with the potential to inhibit the nucleosome-sliding activity of ALC1. This study highlights the potential of ALC1 inhibition as a viable alternative to PARPi.

5.1.1.1. Cell line characterization for ALC1i-sensitivity assessment

The findings from the cell line study provide insights into potential biomarkers for patient cohort selection of ALC1 inhibition. In the short-term cellular survival assay, all active ALC1i compounds, regardless of their chemical cluster, demonstrated an effect by selectively targeting ALC1i-sensitive cells (SUM149PT) over ALC1i-insensitive cells (MDA-MB-231). However, the outcomes of long-term cell treatment with ALC1i compounds revealed variations between the chemical clusters. Specifically, EIS-1 and EIS-2, which share the same chemical cluster (A), demonstrated a substantially increased sensitivity to ALC1i over time. In contrast, EIS-3 (B cluster) and EIS-4 (C cluster) displayed no systematic reduction in EC50 values over time, indicating a potential divergence in the mechanisms underlying ALC1 inhibition among different chemical clusters. These findings underscore the complexity of ALC1i responses and hint at the possibility of varying underlying mechanisms across distinct chemical groups. The conventional approach to selecting patient cohorts for PARPi treatment focused primarily on identifying HRD, with a significant focus on BRCA deficiency as a defining criterion. However, the findings presented in this study challenge this theory. The observation that only 3 out of 7 cell lines with BRCA deficiency exhibited sensitivity to PARPi underscores this subgroup's complexity of treatment response. Cells lacking any obvious HRD markers, such as BRCA mutations or RAD51 foci, still exhibited sensitivity to PARPi, suggesting that the potential for treating patients extends beyond HRD. Notably, the results from this thesis results indicate that this may also apply to ALC1i.

Consistent with the principle of synthetic lethality, the outcomes of the cellular survival assay established a pronounced sensitivity to ALC1i among cell lines harboring HR deficiencies characterized by the RAD51 foci formation capacity. All cell lines marked as HRD (low or no IR-induced RAD51 foci after irradiation) were sensitive to ALC1i (MDA-MB-436, SUM149PT, DLD-1 BRCA2 -/-, Capan-1). All cell lines sensitive to olaparib also displayed sensitivity to EIS-1. These cell lines include HCT 116, SW-620, PSN-1, DU-145 (RAD51 foci positive) and Capan-1, MDA-MB-436 and DLD-1 BRCA -/- (RAD51 foci deficient). The strong correlation of PARPi sensitivity with ALC1i sensitivity was the most predictive biomarker in the cell lines tested. Cell lines with low sensitivity to Olaparib that demonstrated potential sensitivity to ALC1i include DLD-1 and Hep G2 cells. Those cell lines were not categorized as BRCA deficient nor HRD (indicated by RAD51 foci), suggesting alternative vulnerabilities in these cells. Among the cell lines studied, those categorized as BRCA-deficient also exhibited varying responses. 5/7 BRCA-deficient cell lines were sensitive to ALC1i, and 3/7 were sensitive to PARPi. This observation further underscores the complexity of cell line characterization and the need for more refined biomarkers beyond BRCA mutations. In summary, 9/11 ALC1i-sensitive cell lines were categorized as exhibiting at least one of the following biomarkers: BRCA-deficient, PARPi-sensitive, or RAD51 foci deficient. All cell lines insensitive to ALC1i were characterized as RAD51 foci proficient, had no known BRCA mutation, and were insensitive to PARPi.

ALC1i sensitivity was also explored by analyzing ALC1 protein expression. Among the cell lines categorized as ALC1i-sensitive, all except the SUM149PT cells exhibited high levels of ALC1 expression compared to ALC1i-insensitive cells. The cell lines Hep G2 and PSN-1 demonstrated the highest ALC1 expressions within the cell panel. Given that ALC1 overexpression is a common feature in many tumors, the observed correlation between ALC1i sensitivity and elevated ALC1 expression suggests that ALC1 expression could serve as a predictive biomarker for ALC1i sensitivity. This overexpression may indicate a dependency of these cells on ALC1-related pathways, highlighting their potential vulnerability to ALC1 inhibition. To validate this hypothesis, future investigations may involve testing an expanded cell line panel or including patient material.

The study suggests that patient cohorts for ALC1i treatment may initially be selected based on HRD, given the strong correlation between HRD and ALC1i sensitivity in the cell lines tested. This approach mirrors the patient cohort selection strategy for PARPi and is already established in the clinic. However, the sensitivity to ALC1i is not limited to HRD. Additional biomarkers like ALC1 protein level or MSI, demonstrated by the highly

sensitive HCT116 cells, can refine patient selection and accommodate individuals who may benefit from ALC1i treatment despite not fitting the conventional HRD criteria.

5.1.1.2. ALC1 inhibition leads to DNA damage accumulation and apoptosis

This study's combination of multiple assays furnished substantial evidence that ALC1 inhibition selectively leads to accumulation of DNA damage and induces apoptotic responses in ALC1i-sensitive cells. The comet assay revealed clear signs of accumulated DNA damage, as demonstrated by the increased presence of comet-like tails indicative of DNA fragmentation. Western blot analysis further supported these findings in ALC1i-sensitive cells, showing elevated levels of the apoptosis marker cleaved PARP1 and γH2AX, a well-established marker of DNA damage. Flow cytometry-based analysis confirmed the accumulation of DNA damage with high γH2AX positive cells and apoptotic cells, further validating the presence of DNA damage. Concentrations <1 µM led to increased γH2AX levels in HR-deficient, ALC1i sensitive SUM149PT cells, while no signs of DNA damage were observed in HR-proficient, ALCi insensitive MDA-MB-231 cells at concentrations as high as 4 µM. ALC1i demonstrated concentration-dependent effects on the accumulation of DNA damage.

Similarly, accumulation of γH2AX and RAD51 foci indicates the activation of DDR pathways. At EIS-1 concentrations as low as 200 nM, foci formation was visible in ALC1i-sensitive SUM149PT cells, while at concentrations >12.5 µM, ALC1i insensitive MDA-MB-231 cells did not show a significant increase of foci-positive fractions, highlighting the strong selectivity of ALC1i. As SUM149PT cells were categorized as deficient in forming IR-induced RAD51 foci, RAD51 foci induced via ALC1i treatment indicate DNA damage beyond double-ended DSBs. RAD51 foci have been noted in cells during the mitotic S-phase, and they are hypothesized to mark the locations where repair processes occur for stalled or damaged replication forks (Tarsounas et al., 2003; Tashiro et al., 1996).

Recent evidence suggests that RAD51, in addition to its known role following replication fork collapse, also has a role besides fork breakage (Wassing & Esashi, 2021). It promotes the process of replication fork reversal, where stalled replication forks are reversed. Fork reversal is independent of the strand exchange function of RAD51 that is essential in HR (Mason et al., 2019). RAD51 is attracted to stalled replication forks without the involvement of BRCA2 even in the absence of an extended RAD51 nucleoprotein structure (Chaudhuri et al., 2016; Schlacher et al., 2011; Tarsounas et al., 2003; Wassing & Esashi, 2021; Zadorozhny et al., 2017).

Fork reversal, mediated by RAD51, helps protect stalled replication forks, but without BRCA1 or BRCA2 stabilizing RAD51, it can lead to fork degradation and genome instability (Lemaçon et al., 2017).
This suggests that RAD51-mediated fork reversal, instead of protecting against genomic instability, can trigger mutagenic replication in BRCA-deficient cancer cells (Lemaçon et al., 2017), which may lead to high sensitivity to inhibitors interfering with DNA repair in cell lines like SUM149PT.

5.1.1.3. ALC1 inhibition leads to cell cycle arrest

The results from this study demonstrate that cells treated with ALC1i undergo G2 phase cell cycle arrest, highlighting ALC1 inhibition's significant role in regulating cell cycle dynamics. ALC1 inhibition induced a concentration-dependent G2-phase arrest in ALC1i-sensitive SUM149PT cells, starting from as low as 100 nM of EIS-1, indicating the potency of this compound. In contrast, minimal effects on the cell cycle were observed in MDA-MB-231 cells treated with EIS-1, suggesting that ALC1 inhibition has minimal impact on cell cycle modulation in HR-proficient cells. The concentration-dependent increase in RAD51 foci-positive cells in combination with the G2 arrest suggests a link between ALC1 inhibition, DNA damage accumulation, and cell cycle arrest. Cells treated with ALC1i experience G2 phase cell cycle arrest as a consequence of accumulating DNA damage that cannot be effectively repaired. This leads to accumulating unrepaired DNA lesions, ultimately triggering cell death pathways and providing a therapeutic advantage in cells with defects in DNA repair.
The G2-phase arrest observed in ALC1i-sensitive SUM149PT cells, even at low concentrations of EIS-1, mirrors the response seen in cells treated with DNA damage-inducing agents like PARP inhibitors (Jelinic & Levine, 2014; Kruglov et al., 2020). This is particularly notable in HR-deficient cells, where the inability to repair DNA damage efficiently leads to sustained G2 arrest. These studies suggest that ALC1 inhibition might exploit similar vulnerabilities, causing a failure to repair DNA damage effectively, which could trigger cell death pathways.
ALC1's known interactions with key cell cycle regulators, such as cyclin-dependent kinases (CDKs) and their activation by proteins like TCTP (Cheng et al., 2013; Xiong et al., 2021), further support the mechanism behind the G2 arrest observed in this study. The disruption of ALC1 function may interfere with the proper activation of CDKs, crucial for G2/M transition, as also noted by Cheng et al. (2013). This could explain the G2/M

arrest observed in ALC1i-sensitive cells, further validating the idea that ALC1 plays an essential role in regulating cell cycle progression and maintaining DNA repair capacity.

5.1.1.4. ALC1 inhibition changes protein dynamics at DNA damage sites

PARPi have shown efficacy in cancer therapy by trapping PARP enzymes to hinder DNA repair. Murai et al. (2014) suggest that the importance of PARP trapping in cytotoxicity is context-dependent. While trapping PARPs at DNA lesions is considered crucial for inhibition, it is essential for this action to be specific to the context of DNA damage, avoiding indiscriminate targeting of other cellular processes, such as transcription factors. A potential strategy to achieve this specificity involves targeting ALC1, an enzyme activated in response to DNA damage through PARP1-mediated poly-ADP-ribosylation (PARylation). Notably, Juhász et al. (2020) demonstrated that an ALC1 knockout resulted in PARP trapping. Focusing on ALC1 as a target allows for the introduction of PARP trapping only in the presence of DNA damage, thereby sparing other non-damaging cellular contexts.

Protein kinetics at DNA lesions were assessed using the live-cell recruitment assay. The findings of this study highlight distinct effects of various PARPi and ALC1i on the retention and recruitment of essential proteins involved in DNA repair processes. Previously reported variations in PARP-trapping abilities among different PARPi were confirmed in this study. While talazoparib exhibited the most substantial effect on PARP1 trapping, veliparib showed the weakest effect, highlighting the importance of understanding the specific characteristics of each inhibitor. Treatment with the ALC1 inhibitor EIS-1 also induced PARP1 trapping. With concentrations as low as 0.05 µM, EIS-1 was even more potent than talazoparib in trapping PARP1.

The study also shed light on the dynamics of other DDR-associated proteins at DNA lesions. While EIS-1 modestly increased ALC1 protein trapping at higher concentrations, it significantly decreased ALC1 recruitment at concentrations > 0.05 µM. As expected, talazoparib decreased ALC1 recruitment and displayed trapping-like effects. Since PARPi are specifically developed to compete with NAD+ for binding to the catalytic cages of PARP enzymes, they disrupt PARylation-dependent biological processes (Murai et al., 2012; Rouleau et al., 2010), necessary for ALC1 activation and recruitment. The investigation of XRCC1 protein dynamics revealed concentration-dependent effects of talazoparib and EIS-1 on XRCC1 recruitment. Both PARPi and ALC1i reduced XRCC1 recruitment, indicating their impact on the downstream repair processes mediated by XRCC1. These findings contribute to understanding the complex interactions between PARPi, ALC1i, and other DNA repair proteins at the site of DNA damage. Further

research is warranted to elucidate the underlying mechanisms driving these observed effects and to explore the clinical implications of these findings.

5.1.1.5. ALC1i shows promising in vivo efficacy as monotherapy

Building upon the promising results observed in the in-vitro studies, the effect of ALC1 inhibition was tested in vivo. The results obtained from the xenograft experiments highlight the potential of ALC1 inhibition as a monotherapy for cancer treatment. In the xenograft model using HR-deficient SUM149PT cells, treatment with the ALC1i EIS-1 resulted in consistent tumor growth inhibition across various concentrations. Notably, even the lowest tested concentration of 3.91mg/kg demonstrated potent anti-tumor activity. These findings support that ALC1 inhibition holds promise as an effective monotherapy for various cancer treatments even at low concentrations.

These results provide a strong rationale for further exploring the therapeutic potential of ALC1i in preclinical and clinical settings. Safety pharmacology studies conducted following GLP guidelines have indicated that EIS-1 has no impact on the central nervous or cardiovascular and respiratory systems (Eisbach Bio GmbH data not shown here).

The results presented allow crucial insights into the potential toxicity mechanisms associated with PARPi. In spite of the demonstrated efficiency of the ALC1i EIS-1 in trapping PARP1 at DNA lesions, EIS-1 exhibits a very favorable toxicity profile. This observation implies that the adverse effects commonly associated with PARPi may be linked more closely to their impact on essential cellular functions rather than the intended PARP trapping mechanism. The safe tox profile of ALC1i, particularly in comparison to traditional PARPi, suggests the potential for a more targeted and selective approach in cancer therapy.

5.1.2. Combination of ALC1i with FDA-approved and investigational drugs leads to synergistic cancer cell-killing

Combination therapies have succeeded in oncology, particularly when established cancer drugs are combined. Achieving synergistic effects with two different medications in treating proliferative diseases remains the exception rather than the norm. There is a pressing medical need to develop novel combination therapies that combine chemotherapeutic agents with established effectiveness in cancer treatment with novel anticancer drugs that enhance the effects of established treatment regimens.

5.1.2.1. ALC1i is synergistic with PARPi

Based on the hypothesis in the introduction, combinatorial effects of ALC1i using small molecules from different chemical clusters were tested in combinations with PARPi and other FDA-approved or investigational drugs in different genetic backgrounds.

The results of this study support the hypothesis that ALC1 is closely associated with PARP proteins, based on several lines of evidence from previous studies (Blessing et al., 2020; Juhász et al., 2020; Verma et al., 2021). ALC1's ability to be directly activated upon poly-(ADP-ribose) synthesis by PARP1 and other PARP family members, its influence on the recruitment and release of PARP family members to damaged chromatin, and the potentiation of PARPi function upon genetic interference with the ALC1 gene all suggest a strong connection between ALC1 and PARPs.

The combinatorial effect of ALC1i with different PARPi was tested in various cell lines with diverse genetic backgrounds. The results revealed high synergy scores between EIS-1 and PARPi, including talazoparib, olaparib, rucaparib, niraparib, and veliparib. Additionally, the synergy scores correlated with the trapping ability of these PARPi. The results imply that the combination therapy involving ALC1 inhibition can potentially enhance the effectiveness of PARP inhibition in various cancer types, irrespective of their tumor origin. By utilizing specific ALC1 inhibitors like EIS-1, the trapping ability of PARPi can further be potentiated, enhancing the efficacy of DNA repair inhibition in cancer treatment. The synergy observed in this study underscores the importance of targeting ALC1 alongside PARP inhibition for improved therapeutic outcomes. The results also underline the potential of combinations in treatment resistant cells. Tumor cell killing could be achieved in ALC1i insensitive, as well as PARPi insensitive cells in combination treatments.

5.1.2.2. ALC1i synergizes with TOPi

Following previous results of Murai et al. (2014) that showed synergy of PARPi with TOP1i independent of PARP-trapping, we hypothesized that the inhibition of ALC1, in conjunction with TOP1 inhibition, could potentiate the inhibition of cancer cell proliferation through additive or synergistic effects. Findings from the present study demonstrate that inhibiting ALC1 synergistically impacts the cellular response to DNA damage induced by TOP1i. A synergistic enhancement of the effects of both inhibitors was observed through the combination of TOP1i and ALC1i. Notably, irinotecan and topotecan exhibited high synergy scores in combination with ALC1i, indicating the potential for synergistic interactions with other TOP1i. In vivo, the efficacy of the combination treatment of Irinotecan with EIS-1 was tested in a xenograft mouse model using PSN-1 cells (data not shown here). This combination exhibited a significant synergistic effect, resulting in a substantial reduction in tumor size. These findings provide compelling evidence for the potential clinical relevance of combining ALC1 inhibition with TOP1 inhibition in cancer treatment. The synergistic interaction allows for achieving therapeutic efficacy with lower doses of irinotecan, which may help reduce the

incidence and severity of side effects associated with the drug. This can lead to improved patient tolerance and adherence to treatment. The results of ALC1i in combination with TOP1i hold exceptional interest, as Irinotecan shares the same mechanism of action as the payload of promising novel antibody-drug conjugates such as Enhertu (Nami et al., 2018). Combination treatment with Enhertu also revealed high synergy with EIS-1 in the HER2-positive cell line SK-BR-3 (Eisbach data not shown).

After exploring the synergistic potential of a TOP1 inhibitor with ALC1i, the combination of TOP2i with ALC1i was investigated for synergistic effects. The results align with the hypothesis that combining ALC1 inhibition with TOP2 inhibitors, such as teniposide, may lead to increased cancer cell-killing but yield milder synergy than the combination with TOP1i. The data supports the idea that DSBs through TOP2 poisons in combination with additionally inhibited ALC1i results in the accumulation of DNA damage, that cannot effectively be repaired. The observed mild but noticeable synergistic effects when combining the specific EIS-1 with teniposide further validate this hypothesis. The heightened synergistic effects observed between ALC1i and TOP1i, in contrast to TOP2i, can be explained by the distinct nature of DNA damage induced by these inhibitors and the specific repair mechanisms engaged by the cell. TOP1i triggers the formation of DNA SSBs through the creation of TOP1ccs (see Table 1), necessitating efficient repair mechanisms. In this context, the cell heavily relies on ALC1 to repair SSBs. The close functional relationship between ALC1 and TOP1, coupled with their collaborative involvement in particular DNA repair pathways, likely contributes to the observed synergy. On the other hand, TOP2i induces DSBs, repairable through HR or NHEJ, pathways that are not as intricately tied to ALC1. The specificity of ALC1's involvement in the repair of TOP1i-induced SSBs may explain the higher synergy observed with TOP1i compared to the repair processes associated with TOP2i-induced DSBs.

5.1.2.3. ALC1i synergizes with cell cycle checkpoint inhibitors

Combining cell cycle checkpoint inhibitors (CCCi), such as ATM, ATR, or WEE1 inhibitors (ATRi, ATMi, and WEE1i) with ALC1i has demonstrated a striking synergistic effect in cancer cell-killing. This synergy arises from their complementary mechanisms of action in the cell cycle context, culminating in enhanced therapeutic outcomes. Based on findings from combination treatments with PARPi and CCCi, the synergy can be explained as follows: ALC1i leads to DNA damage accumulation, which activates the ATR Pathway (Barnieh et al., 2021) to initiate DDR mechanism and cell cycle arrest. This leads to cell cycle delay, preventing cells from progressing into the sensitive phases like mitotic phase or S-phase. When combined with CCCi, such as ATRi, ATMi, or WEE1i, the cell cycle checkpoints are compromised. The cell cycle can progress even

with a lot of DNA damage present. The cells eventually enter S-phase or mitosis, but in an uncontrolled and aberrant manner. The accumulation of DNA damage becomes cytotoxic, leading to a potentiated cellular response and, ultimately, cancer cell death.
This versatility allows for tailored treatment strategies based on the specific characteristics of the cancer type and patient, enhancing the clinical relevance of this approach. In conclusion, combining CCCi with ALC1 inhibition represents a promising avenue in cancer therapy.

5.1.2.4. Synergistic effects of ALC1i with other therapeutic agents

Mitomycin C generates oxygen radicals, leading to alkylating DNA and interstrand crosslinks (Tomasz & Palom, 1997). These effects inhibit DNA synthesis and can induce various types of DNA damage including NER or HR (Lee et al., 2005; Palom et al., 2002). It was hypothesized that the inhibition of ALC1 would impair the repair of mitomycin C-induced DNA damage, thereby potentiating the anti-proliferative effect of mitomycin C. The results of the co-dosing experiments with an ALC1i and mitomycin C revealed a high degree of synergy. The synergy observed suggests that when ALC1 is inhibited, it may interfere with the repair of DNA damage caused by mitomycin C, leading to stronger anti-cancer effects. These findings emphasize the potential benefit of combining ALC1 inhibitors with mitomycin C in clinical treatment strategies.
Inhibitors that target bromodomains disrupt the interaction between bromodomains and acetyl groups, resulting in the downregulation of specific genes like MYC (Pérez-Salvia & Esteller, 2016). Bromodomain inhibitor BAY-299, targeting TAF1 (Thesgc.Org/Chemical-Probes, 2022), plays a crucial role in inhibiting HR, highlighting its potential as a therapeutic agent in disrupting DNA repair mechanisms (H. Peng et al., 2021). Based on these findings, it was hypothesized that the inhibition of TAF1 bromodomain function by BAY-299 would lead to insufficient HR repair, which, when combined with inhibiting other DNA repair pathways through ALC1 inhibition (ALC1i), would result in synergistic effects. A synergy-survival assay was performed using EIS-1 in combination with BAY-299 to test this hypothesis. ALC1 and TAF1 bromodomain inhibition demonstrated synergistic effects with MSA scores >10. This suggests that the inhibition of ALC1, in conjunction with the impaired HR repair caused by TAF1 bromodomain inhibition, enhances the disruption of DNA repair mechanisms and impairs genome instability. The synergistic effects observed suggest that targeting multiple DNA repair pathways can increase genomic instability while enhancing sensitivity to DNA damage.
Although 5-FU can induce DNA damage mainly repaired by MMR and BER (Wyatt & Wilson, 2008) and affects the cell cycle, combining it with ALC1 inhibition did not show

any synergistic effect. MSA scores lower than ten were observed in the combinatorial treatment of EIS-1 with 5-FU, tested in PSN-1 cells. The lack of synergy between these treatments could be attributed to several factors, including potential variations in the effects of 5-FU on the cell cycle across different cell lines. Although 5-FU is known to cause DNA damage and disrupt DNA replication, its precise impact on the cell cycle can differ depending on the specific cellular context (Yoshikawa et al., 2001). The diverse responses of different cell lines to 5-FU treatment may explain why there is no synergy observed when combined with ALC1 inhibition. Another reason might be that 5-FU primarily exerts its effects during the S-phase of the cell cycle, where it interferes with DNA synthesis and replication (Shah & Schwartz, 2001). Treatment of cells with EIS-1 led to G2/M cell cycle arrest. The differences in how 5-FU and ALC1 inhibition affect the cell cycle might potentially limit 5-FU's ability to function as intended when ALC1 inhibitors are present. The lack of synergy in this combination highlights the complex interactions between different therapeutic agents and the diverse responses of cancer cells to treatment. Thus, higher synergy scores could be observed in different cellular contexts.

The study conducted by Lai et al. (2020) demonstrated the synergistic effects of combining a PARPi with an FGFR inhibitor. Their findings revealed that single-agent treatment with olaparib or PD173074 (FGFRi) had limited efficacy in PANC-1 and SUIT-2 cells. When these agents were combined at low doses, a significant and dose-dependent reduction in cell viability was observed. Given the connection between PARP1 activity and ALC1-mediated DDR, it was expected that ALC1 inhibition would also exhibit synergistic effects with FGFRi. In this study, where Levatinib was combined with the EIS-1 in PSN-1 cells, results revealed an MSA score of 8.79, indicating an additive effect with a mild tendency towards synergy. The observed effect was less pronounced than expected. Further investigations are needed to explore the underlying mechanisms and optimize the combination approach for enhanced therapeutic efficacy.

The hypothesis regarding the combinatorial treatment of taxanes with ALC1i suggested no expected synergy. This hypothesis was based on the understanding that taxanes, such as paclitaxel, disrupt microtubule dynamics and induce cell cycle arrest, specifically in the mitotic phase, while ALC1 inhibitors lead to G2/M-phase arrest. The results from this study showed no indication of synergy between the specific ALC1i, EIS-1, and paclitaxel. A rather additive effect was observed. Additional DNA damage might be required to induce synergistic effects of taxanes with ALC1i.

A key advantage of combining ALC1i with targeted therapies like PARPi or TOPi is their ability to not only prevent resistance development but also achieve high tumor specificity. This specificity arises from genetic defects in tumor cells, such as mentioned impaired DNA repair mechanisms, which make them particularly susceptible to these combinations. By targeting these vulnerabilities, ALC1i enhances the efficacy of these therapies while sparing normal cells, which have intact DNA repair pathways.

In contrast, non-targeted chemotherapeutics like mitomycin C, which traditionally exert cytotoxic effects on both tumor and normal cells, can also benefit significantly from combination with ALC1i. By inhibiting ALC1, the ability of tumor cells to repair or tolerate the DNA damage induced by these agents is substantially compromised. Meanwhile, normal cells, with their more robust repair systems, experience less disruption. This selective impairment amplifies the cytotoxic effects in tumor cells, effectively increasing the therapeutic window. Consequently, the combination of ALC1i with these non-selective agents improves their specificity and efficacy, offering a refined approach to cancer treatment that leverages tumor-specific vulnerabilities.

5.1.2.5. The potential of ALC1i in combination with ionizing radiation as a new treatment cohort

The investigation also explored the synergistic potential of combining ionizing radiation (IR) with ALC1 inhibition (data not presented here). Radiation therapy provides significant advantages in treating solid tumors due to its ability to precisely target the tumor while minimizing damage to surrounding healthy tissues. It induces DNA damage in cancer cells, leading to cell death or impaired division. Combining radiation with ALC1i enhances this effect, as ALC1i inhibits the cancer cells' ability to repair radiation-induced DNA damage, making them more vulnerable. This dual approach prevents repair mechanisms, improving tumor control and potentially increasing the chances of tumor cell killing.

Preliminary tests conducted on the PSN-1 cell line yielded promising outcomes. This combination approach warrants further investigation due to its potential to leverage the DNA-damaging effects of ionizing radiation in conjunction with ALC1i, possibly leading to enhanced therapeutic effects. In addition to cellular tests, future plans include conducting in vivo experiments combining IR and EIS-1. These experiments will utilize a subcutaneous mouse xenograft model to further assess potential synergistic effects, where EIS-1 will be orally administered to the mice alongside localized irradiation at the tumor site. This comprehensive in vivo approach aims to provide insights into the combination's effectiveness in a more complex physiological context, potentially opening avenues for its clinical use. The prospect of synergizing IR with ALC1i holds promise for enhancing patient outcomes in cancer therapy. Optimizing treatment regimens and

dosages to minimize potential toxicities while maximizing therapeutic benefits is crucial for realizing the full potential of this combined approach, ultimately leading to improved patient outcomes in cancer management. Combining ALC1i with IR provides the advantage of localized treatment, allowing focused intervention at the tumor site. This approach minimizes the potential for systemic interactions and synergistic effects in other regions of the body.

5.1.3. Overcoming resistance to PARPi and ALC1i: A path towards personalized cancer treatments

PARPi have succeeded in treating cancers with HR deficiencies, such as those with BRCA1/2 mutations, leading to their approval for various cancer types. However, the emergence of resistance often hampers sustained antitumor responses. Preclinical models have identified multiple mechanisms of resistance, including restoration of HR (Tan et al., 2021), cellular extrusion of PARPi (Rottenberg et al., 2007) or inhibition or downregulation of PARP1 (Murai et al., 2012; Pettitt et al., 2013, 2018). These factors limit PARP inhibitor-induced DNA damage, impairing their overall efficacy. As suggested by (Juhász et al., 2020), ALC1-dependent PARP1 mobilization could be vital in overcoming PARPi resistance. Altering the activity levels of ALC1 via small molecule inhibitors could overcome PARPi resistance.

5.1.3.1. ALC1i can overcome PARPi resistance

PARPi-resistant cell lines were generated and tested for the sensitivity of PARPi and ALC1i. This resistance remained stable over eight weeks, indicating that once developed, it can persist even without treatment. These findings highlight the need for alternative treatment strategies to overcome PARPi resistance.

An interplay between different PARPi molecules was observed, where resistance developed through talazoparib led to cross-resistance to olaparib, suggesting common underlying mechanisms in resistance to various PARPi. Understanding these mechanisms can aid in developing targeted therapies and combination approaches to combat PARPi resistance.

Over 30 clones were derived from two distinct cell lines treated with PARPi for over 4 months, and potential mutations in drug transporters were evaluated using SN-38, a substrate of P-glycoprotein. All clones developed a resistance to talazoparib, along with a resistance to olaparib. In addition, the clones exhibited diverse changes in sensitivity to SN-38 and ALC1i, suggesting that the clones developed independent resistance mechanisms. Despite their resistance to PARPi, most cell lines remained sensitive to ALC1i. This highlights ALC1i as a potential treatment option for patients who have developed resistance to PARPi during their treatment.

If resistance to ALCi was seen, in most cases it correlated with a resistance to SN-38. This suggests a mutation in the drug efflux pump, leading broad resistance to multiple drugs due to the pump's active removal of compounds from the cell. A subset of clones displaying resistance to ALC1i, despite lacking resistance to SN-38, suggests the presence of a distinct mechanism specific to ALC1i. These observations underscore the need for further analysis of these clones to unravel the specific factors associated with ALC1i resistance. Investigating these mechanisms could provide valuable insights into the target engagement and downstream factors of ALC1i, potentially overcoming resistance in cancer treatment. The ability of ALC1i to overcome PARPi resistance provides new possibilities for therapeutic intervention and offers hope for patients who have exhausted PARPi options.

5.1.3.2. Characterization of Resistance

The study provides insights into the development and stability of resistance to PARPi, paving the way for personalized treatment strategies based on the specific mechanisms of resistance encountered in individual patients. These findings have significant implications for improving therapeutic outcomes.

Future research can build upon these findings to optimize combination therapies and develop novel treatment approaches for patients with PARPi resistance. The following steps include the identification of patient biomarkers for the treatment of individuals with developed PARPi resistance by further profiling the PARPi-resistant cell lines. Comparing multi-omics profiles of clones that exhibit no significant decrease in sensitivity to EIS-1 with clones that display decreased sensitivity to EIS-1 will help identify genetic alterations or protein changes associated with resistance to EIS-1. To validate the identified biomarkers, further studies will involve functional assays to determine the consequences of the genetic or protein alterations in vivo. EIS-1 sensitivity will be tested in CDX models derived from PARPi-resistant patients.

5.2. Conclusion and Outlook

This study highlights the potential of ALC1 inhibition as a novel therapeutic strategy in cancer treatment. By modulating DNA damage response mechanisms, ALC1i provide a new alternative to traditional PARPi. Despite its ability to trap PARP1 at DNA lesions, ALC1i exhibited a low toxicity profile, suggesting a more targeted approach to cancer therapy while minimizing risks to essential cellular functions. This favorable tolerability is supported by in vivo xenograft experiments, in which daily oral administration of the ALC1 inhibitor EIS-1 resulted in robust tumor growth inhibition without overt signs of intolerability, as well as by GLP-compliant safety pharmacology studies indicating no adverse effects on the central nervous, cardiovascular, or respiratory systems.

The results highlight ALC1i as a potential solution for overcoming resistance to PARPi. This finding provides an alternative for patients who have developed resistance to conventional therapies and lack further treatment options.

An important distinguishing feature of ALC1 inhibition is its favorable toxicity profile. While PARP inhibitors are clinically effective, their use is frequently limited by hematological toxicities, which are thought to arise from interference with essential PARP-dependent housekeeping functions in normal cells. In contrast, ALC1 is recruited to chromatin predominantly in response to PARP-dependent DNA damage signaling, suggesting that its inhibition may preferentially affect damage-associated repair processes rather than basal cellular homeostasis. Consistent with this concept, ALC1i achieved robust antitumor activity in vivo without signs of intolerability, and GLP-compliant safety pharmacology studies revealed no adverse effects on central nervous, cardiovascular, or respiratory systems. Although comprehensive repeat-dose and tissue-specific toxicology studies will be required to fully define the clinical safety profile, these findings support the notion that ALC1i may offer a wider therapeutic window than conventional PARP inhibitors.

The synergistic effects of ALC1i in combination with approved chemotherapeutics offer an opportunity to improve treatment efficacy. ALC1i can synergize with various agents, such as PARPi, ATRi, and TOPi. This approach can maximize the effectiveness of chemotherapy by targeting critical pathways in cancer cells. Importantly, these combinations may allow dose reductions of established agents, potentially mitigating treatment-associated toxicities while maintaining or enhancing antitumor efficacy.

While HRD is an important biomarker for predicting sensitivity to ALC1i, functional drug testing in cell lines shows that mutational profiles alone are insufficient for predicting drug response. ALC1 protein expression and factors like MSI are also crucial for understanding therapeutic outcomes. These observations emphasize that ALC1i sensitivity arises from a multifactorial interplay of genetic, functional, and protein-level determinants rather than from a single genomic alteration.

The potential of ALC1i highlights the need for improved patient selection and tumor characterization. Traditional biomarkers like HRD may not predict drug sensitivity across all tumors, so functional drug testing on patient-derived cells offers a more reliable approach. New strategies are needed for functional testing that align with clinical practice, addressing challenges such as clinician preferences and compatibility with other tests. Developing clinically feasible functional assays will be critical for translating the therapeutic promise of ALC1 inhibition into routine patient care.

Incorporating personalized treatment strategies, combining functional assays with mutational profiling, can optimize therapy and help overcome resistance to existing treatments. Refining tumor characterization and functional testing methods will be essential for integrating ALC1i into routine cancer care and improving patient outcomes.

6. References

Abbott, J. M., Zhou, Q., Esquer, H., Pike, L. A., Broneske, T. P., Rinaldetti, S., Abraham, A. D., Ramirez, D., Lunghofer, P. J., Pitts, T. M., Regan, D., Tan, A. C., Gustafson, D. L., Messersmith, W. A., & LaBarbera, D. V. (2020). First-in-Class Inhibitors of Oncogenic CHD1L with Preclinical Activity against Colorectal Cancer. *Molecular Cancer Therapeutics*, *19*(8), 1598–1612. https://doi.org/10.1158/1535-7163.mct-20-0106

Abkevich, V., Timms, K., Hennessy, B. T., Potter, J. S., Carey, M. S., Meyer, L. A., Smith-McCune, K., Broaddus, R., Lu, K. H., Chen, J., Tran, T., Williams, D. P., Iliev, D., Jammulapati, S., Fitzgerald, L., Krivak, T. C., DeLoia, J. A., Gutin, A., Mills, G. B., & Lanchbury, J. S. (2012). Patterns of genomic loss of heterozygosity predict homologous recombination repair defects in epithelial ovarian cancer. *British Journal of Cancer*, *107*(10), 1776–1782. https://doi.org/10.1038/bjc.2012.451

Aguilar-Quesada, R., Muñoz-Gámez, J. A., Martín-Oliva, D., Peralta, A., Valenzuela, M. T., Matínez-Romero, R., Quiles-Pérez, R., Murcia, J. M., De Murcia, G., De Almodóvar, M. R., & Oliver, F. J. (2007). Interaction between ATM and PARP-1 in response to DNA damage and sensitization of ATM deficient cells through PARP inhibition. *BMC Molecular Biology*, *8*(1). https://doi.org/10.1186/1471-2199-8-29

Ahel, D., Hořejší, Z., Wiechens, N., Polo, S. E., Garcia-Wilson, E., Ahel, I., Flynn, H. R., Skehel, J. M., West, S. C., Jackson, S. P., Owen-Hughes, T., & Boulton, S. J. (2009). Poly(ADP-ribose)–Dependent regulation of DNA repair by the chromatin remodeling enzyme ALC1. *Science*, *325*(5945), 1240–1243. https://doi.org/10.1126/science.1177321

Aittokallio, T. (2022). SynergyFinder 3.0: an interactive analysis and consensus interpretation of multi-drug synergies across multiple samples. *Nucleic Acids Research*, *50*(W1), W739–W743. https://doi.org/10.1093/nar/gkac382

Akimov, Y., & Aittokallio, T. (2021). Re-defining synthetic lethality by phenotypic profiling for precision oncology. *Cell Chemical Biology*, *28*(3), 246–256. https://doi.org/10.1016/j.chembiol.2021.01.026

Alexandre, J., Hu, Y., Lu, W., Pelicano, H., & Huang, P. (2007). Novel Action of Paclitaxel against Cancer Cells: Bystander Effect Mediated by Reactive Oxygen Species. *Cancer Research*, *67*(8), 3512–3517. https://doi.org/10.1158/0008-5472.can-06-3914

Arkenau, H. T., Bermann, A., Rettig, K., Strohmeyer, G., & Porschen, R. (2003). 5-Fluorouracil plus leucovorin is an effective adjuvant chemotherapy in curatively resected stage III colon cancer:long-term follow-up results of the adjCCA-01 trial. *Annals of Oncology*, *14*(3), 395–399. https://doi.org/10.1093/annonc/mdg100

Arun, B. K., Akar, U., Gutierrez-Barrera, A. M., Hortobagyi, G. N., & Ozpolat, B. (2015). The PARP inhibitor AZD2281 (Olaparib) induces autophagy/mitophagy in BRCA1 and BRCA2 mutant breast cancer cells. *International Journal of Oncology*, *47*(1), 262–268. https://doi.org/10.3892/ijo.2015.3003

Bakr, A., Hey, J., Sigismondo, G., Liu, C., Sadik, A., Goyal, A., Cross, A.-I., Iyer, R. L., Müller, P., Trauernicht, M., Breuer, K., Lutsik, P., Opitz, C. A., Krijgsveld, J., Weichenhan, D., Plass, C., Popanda, O., & Schmezer, P. (2021). ID3 promotes homologous recombination via non-transcriptional and transcriptional mechanisms and its loss confers sensitivity to PARP inhibition. *Nucleic Acids Research*, *49*(20), 11666–11689. https://doi.org/10.1093/nar/gkab964

Ballabeni, A., Zamponi, R., Moore, J. K., Helin, K., & Kirschner, M. W. (2013). Geminin deploys multiple mechanisms to regulate Cdt1 before cell division thus ensuring the proper execution of DNA replication. *Proceedings of the National Academy of Sciences of the United States of America*, *110*(30). https://doi.org/10.1073/pnas.1310677110

Barnieh, F. M., Loadman, P. M., & Falconer, R. J. (2021). Progress towards a clinically-successful ATR inhibitor for cancer therapy. *Current Research in Pharmacology and Drug Discovery*, *2*, 100017. https://doi.org/10.1016/j.crphar.2021.100017

Barnum, K. J., & O'Connell, M. J. (2014). *Cell Cycle Regulation by Checkpoints* (pp. 29–40). https://doi.org/10.1007/978-1-4939-0888-2_2

Baudino, T. A. (2015). Targeted Cancer therapy: the next generation of cancer treatment. *Current Drug Discovery Technologies*, *12*(1), 3–20. https://doi.org/10.2174/1570163812666150602144310

Bian, L., Meng, Y., Zhang, M., & Li, D. (2019). MRE11-RAD50-NBS1 complex alterations and DNA damage response: implications for cancer treatment. Molecular Cancer, 18(1). https://doi.org/10.1186/s12943-019-1100-5

Beard, W. A., Horton, J. K., Prasad, R., & Wilson, S. H. (2019). Eukaryotic base excision repair: New approaches shine light on mechanism. *Annual Review of Biochemistry*, *88*(1), 137–162. https://doi.org/10.1146/annurev-biochem-013118-111315

Bertoli, C., Skotheim, J. M., & De Bruin, R. A. M. (2013). Control of cell cycle transcription during G1 and S phases. *Nature Reviews Molecular Cell Biology*, *14*(8), 518–528. https://doi.org/10.1038/nrm3629

Bhamidipati, D., Haro-Silerio, J. I., Yap, T. A., & Ngoi, N. Y. L. (2023). PARP inhibitors: enhancing efficacy through rational combinations. *British Journal of Cancer*. https://doi.org/10.1038/s41416-023-02326-7

Bhin, J., Dias, M. P., Gogola, E., Rolfs, F., Piersma, S. R., De Bruijn, R., De Ruiter, J. R., Van Den Broek, B., Duarte, A. A., Sol, W., Van Der Heijden, I., Andronikou, C., Kaiponen, T. S., Bakker, L., Lieftink, C., Morris, B., Beijersbergen, R. L., Van De Ven, M., Jimenez, C. R., … Jonkers, J. (2023). Multi-omics analysis reveals distinct non-reversion mechanisms of PARPi resistance in BRCA1- versus BRCA2-deficient mammary tumors. *Cell Reports*, *42*(5), 112538. https://doi.org/10.1016/j.celrep.2023.112538

Birkbak, N. J., Wang, Z., Kim, J.-E., Eklund, A. C., Li, Q., Tian, R., Bowman-Colin, C., Li, Y., Greene-Colozzi, A., Iglehart, J. D., Tung, N., Ryan, P. D., Garber, J., Silver, D., Szallasi, Z., & Richardson, A. L. (2012). Telomeric allelic imbalance indicates defective DNA repair and sensitivity to DNA-Damaging agents. *Cancer Discovery*, *2*(4), 366–375. https://doi.org/10.1158/2159-8290.cd-11-0206

Blessing, C., Mandemaker, I. K., Gonzalez-Leal, C., Preisser, J., Schomburg, A., & Ladurner, A. G. (2020). The Oncogenic Helicase ALC1 Regulates PARP Inhibitor Potency by Trapping PARP2 at DNA Breaks. *Molecular Cell*, *80*(5), 862–875.e6. https://doi.org/10.1016/j.molcel.2020.10.009

Bonnet, E., Haddad, V., Quesada, S., Baffert, K.-A., Lardy-Cléaud, A., Treilleux, I., Pissaloux, D., Attignon, V., Wang, Q., Buisson, A., Heudel, P.-E., Bachelot, T., Dufresne, A., Eberst, L., Toussaint, P., Bonadona, V., Lasset, C., Viari, A., Sohier, E., … Trédan, O. (2022). Alterations in homologous Recombination-Related genes and distinct platinum response in metastatic Triple-Negative breast cancers: a subgroup analysis of the ProfiLER-01 trial. *Journal of Personalized Medicine*, *12*(10), 1595. https://doi.org/10.3390/jpm12101595

Boone, C., Bussey, H., & Andrews, B. (2007). Exploring genetic interactions and networks with yeast. *Nature Reviews Genetics*, *8*(6), 437–449. https://doi.org/10.1038/nrg2085

Bowman, K. F., Newell, D. R., Calvert, A. H., & Curtin, N. J. (2001). Differential effects of the poly (ADP-ribose) polymerase (PARP) inhibitor NU1025 on topoisomerase I and II inhibitor cytotoxicity in L1210 cells in vitro. *British Journal of Cancer*, *84*(1), 106–112. https://doi.org/10.1054/bjoc.2000.1555

Bradbury, A., Zenke, F., Curtin, N. J., & Drew, Y. (2022). The role of ATR inhibitors in ovarian Cancer: Investigating Predictive biomarkers of response. *Cells*, *11*(15), 2361. https://doi.org/10.3390/cells11152361

Brough, R., Frankum, J., Costa-Cabral, S., Lord, C. J., & Ashworth, A. (2011). Searching for synthetic lethality in cancer. *Current Opinion in Genetics & Development*, *21*(1), 34–41. https://doi.org/10.1016/j.gde.2010.10.009

Brown, J. A., O'Carrigan, B., Jackson, S. P., & Yap, T. A. (2017). Targeting DNA repair in cancer: Beyond PARP inhibitors. *Cancer Discovery*, *7*(1), 20–37. https://doi.org/10.1158/2159-8290.cd-16-0860

Bryant, H. E., Schultz, N., Thomas, H. D., Parker, K. M., Flower, D., López, E., Kyle, S., Meuth, M., Curtin, N. J., & Helleday, T. (2005). Specific killing of BRCA2-deficient tumours with inhibitors of poly(ADP-ribose) polymerase. *Nature*, *434*(7035), 913–917. https://doi.org/10.1038/nature03443

Cahuzac, M., Péant, B., Mes-Masson, A.-M., & Saad, F. (2022). Development of Olaparib-Resistance Prostate Cancer Cell Lines to Identify Mechanisms Associated with Acquired Resistance. *Cancers*, *14*(16), 3877. https://doi.org/10.3390/cancers14163877

Caldecott, K. W. (2019). XRCC1 protein; Form and function. *DNA Repair*, *81*, 102664. https://doi.org/10.1016/j.dnarep.2019.102664

Caldecott, K. W. (2022). DNA single-strand break repair and human genetic disease. *Trends in Cell Biology*, *32*(9), 733–745. https://doi.org/10.1016/j.tcb.2022.04.010

Cannan, W. J., & Pederson, D. S. (2015). Mechanisms and Consequences of Double-Strand DNA break formation in Chromatin. *Journal of Cellular Physiology*, *231*(1), 3–14. https://doi.org/10.1002/jcp.25048

Cantor, S. B., & Calvo, J. A. (2017). Fork protection and therapy resistance in hereditary breast cancer. *Cold Spring Harbor Symposia on Quantitative Biology*, *82*, 339–348. https://doi.org/10.1101/sqb.2017.82.034413

Caracciolo, D., Montesano, M., Tagliaferri, P., & Tassone, P. (2019). Alternative non-homologous end joining repair: a master regulator of genomic instability in cancer. *Precision Cancer Medicine*, *2*, 8–8. https://doi.org/10.21037/pcm.2019.02.05

Castroviejo-Bermejo, M., Cruz, C., Llop-Guevara, A., Gutiérrez-Enríquez, S., Ducy, M., Ibrahim, Y. H., Gris-Oliver, A., Pellegrino, B., Bruna, A., Guzman, M., Rodríguez, O., Grueso, J., Bonache, S., Moles-Fernández, A., Villacampa, G., Viaplana, C., Gómez, P. C., Vidal, M., Peg, V., … Serra, V. (2018). A <scp>RAD</scp> 51 assay feasible in routine tumor samples calls <scp>PARP</scp> inhibitor response beyond <scp>BRCA</scp> mutation. *Embo Molecular Medicine*, *10*(12). https://doi.org/10.15252/emmm.201809172

Ceccaldi, R., Liu, J. C., Amunugama, R., Hajdu, I., Primack, B., Petalcorin, M. I. R., O'Connor, K. W., Konstantinopoulos, P. A., Elledge, S. J., Boulton, S. J., Yusufzai, T., & D'Andrea, A. D. (2015). Homologous-recombination-deficient tumours are dependent on Polθ-mediated repair. *Nature*, *518*(7538), 258–262. https://doi.org/10.1038/nature14184

Ceccaldi, R., Liu, J. C., Amunugama, R., Hajdú, I., Primack, B., Petalcorin, M. I. R., O'Connor, K. W., Konstantinopoulos, P. A., Elledge, S. J., Boulton, S. J., Yusufzai, T., & D'Andrea, A. D. (2015). Homologous-recombination-deficient tumours are dependent on Polθ-mediated repair. *Nature*, *518*(7538), 258–262. https://doi.org/10.1038/nature14184

Cejka, P., & Symington, L. S. (2021). DNA end resection: mechanism and control. Annual Review of Genetics, 55(1), 285–307. https://doi.org/10.1146/annurev-genet-071719-020312

Chaudhuri, A. R., Callen, E., Ding, X., Gogola, E., Duarte, A. A., Lee, J., Wong, N., Lafarga, V., Calvo, J. A., Panzarino, N. J., John, S., Day, A., Crespo, A. V., Shen, B., Starnes, L. M., De Ruiter, J. R., Daniel, J., Konstantinopoulos, P. A., Chen, D., … Nussenzweig, A. (2016). Replication fork stability confers chemoresistance in BRCA-deficient cells. *Nature*, *535*(7612), 382–387. https://doi.org/10.1038/nature18325

Chaudhuri, A. R., & Nussenzweig, A. (2017). The multifaceted roles of PARP1 in DNA repair and chromatin remodelling. *Nature Reviews Molecular Cell Biology*, *18*(10), 610–621. https://doi.org/10.1038/nrm.2017.53

Chelariu-Raicu, A., Trillsch, F., Burges, A., Czogalla, B., Hester, A., Wuerstlein, R., Harbeck, N., & Mahner, S. (2023). PARP inhibitors: risk factors for toxicity and matching patients to the proper poly (ADP-ribose) polymerase inhibitor (PARPi) therapy. *International Journal of Gynecologic Cancer*, *33*(5), 812–822. https://doi.org/10.1136/ijgc-2022-003990

Chen, C.-Y., Chen, C.-Y., Cheng, S.-F., Shieh, T.-M., Leu, Y.-L., Chuang, W.-Y., Liu, K.-T., Ueng, S.-H., Shih, Y.-H., Chou, L. F., & Wang, T.-H. (2021). Hydroxygenkwanin Increases the Sensitivity of Liver Cancer Cells to Chemotherapy by Inhibiting DNA Damage Response in Mouse Xenograft Models. *International Journal of Molecular Sciences*, *22*(18), 9766. https://doi.org/10.3390/ijms22189766

Cheng, W., Su, Y., & Xu, F. (2013). CHD1L: a novel oncogene. *Molecular Cancer*, *12*(1), 170. https://doi.org/10.1186/1476-4598-12-170

Choi, Y. E., Meghani, K., Brault, M., Leclerc, L., He, Y. J., Day, T. A., Elias, K. M., Drapkin, R., Weinstock, D. M., Dao, F., Shih, K. K., Matulonis, U., Levine, D. A., Konstantinopoulos, P. A., & Chowdhury, D. (2016). Platinum and PARP inhibitor resistance due to overexpression of MicroRNA-622 in BRCA1-Mutant ovarian cancer. Cell Reports, 14(3), 429–439. https://doi.org/10.1016/j.celrep.2015.12.046

Christie, E. L., Pattnaik, S., Beach, J., Copeland, A., Rashoo, N., Fereday, S., Hendley, J., Alsop, K., Brady, S. L., Lamb, G., Pandey, A., deFazio, A., Thorne, H., Bild, A., & Bowtell, D. D. L. (2019). Multiple ABCB1 transcriptional fusions in drug resistant high-grade serous ovarian and breast cancer. Nature Communications, 10(1). https://doi.org/10.1038/s41467-019-09312-9

Ciccarone, F., Zampieri, M., & Caiafa, P. (2017). PARP1 orchestrates epigenetic events setting up chromatin domains. *Seminars in Cell & Developmental Biology*, *63*, 123–134. https://doi.org/10.1016/j.semcdb.2016.11.010

Clay, D. E., & Fox, D. A. (2021). DNA Damage Responses during the Cell Cycle: Insights from Model Organisms and Beyond. *Genes*, *12*(12), 1882. https://doi.org/10.3390/genes12121882

Corsello, S. M., Nagari, R. T., Spangler, R. D., Rossen, J. W. A., Kocak, M., Bryan, J. G., Humeidi, R., Peck, D. J., Wu, X., Tang, A., Wang, V. Y., Bender, S., Lemire, E. G., Narayan, R., Montgomery, P., Ben-David, U., Chen, Y., Rees, S. E., Lyons, N. J., … Golub, T. R. (2019). Non-oncology drugs are a source of previously unappreciated anti-cancer activity. *BioRxiv (Cold Spring Harbor Laboratory)*. https://doi.org/10.1101/730119

Cruz, C. D., Castroviejo-Bermejo, M., Gutiérrez-Enríquez, S., Llop-Guevara, A., Ibrahim, Y. H., Gris-Oliver, A., Bonache, S., Morancho, B., Bruna, A., Rueda, O. M., Lai, Z., Polanska, U. M., Jones, G. T., Kristel, P., De Bustos, L., Guzmán, M. G., Rodríguez, O. P., Grueso, J., Montalban, G., … Serra, V. (2018). RAD51 foci as a functional biomarker of homologous recombination repair and PARP inhibitor resistance in germline BRCA-mutated breast cancer. *Annals of Oncology*, *29*(5), 1203–1210. https://doi.org/10.1093/annonc/mdy099

Curtin, N. J. (2012). DNA repair dysregulation from cancer driver to therapeutic target. *Nature Reviews Cancer*, *12*(12), 801–817. https://doi.org/10.1038/nrc3399

Curtin, N. J., Harris, A. L., & Aherne, G. W. (1991). Mechanism of cell death following thymidylate synthase inhibition: 2'-deoxyuridine-5'-triphosphate accumulation, DNA damage, and growth inhibition following exposure to CB3717 and dipyridamole. *PubMed*, *51*(9), 2346–2352. https://pubmed.ncbi.nlm.nih.gov/2015598

Das, B. B., Huang, S.-Y. N., Murai, J., Rehman, I., Amé, J., Sengupta, S., Das, S., Majumdar, P., Zhang, H., Biard, D., Majumder, H. K., Schreiber, V., & Pommier, Y. (2014). PARP1–TDP1 coupling for the repair of topoisomerase I–induced DNA damage. *Nucleic Acids Research*, *42*(7), 4435–4449. https://doi.org/10.1093/nar/gku088

Dasovich, M., Beckett, M. Q., Bailey, S., Ong, S., Greenberg, M. M., & Leung, A. K. L. (2021). Identifying Poly(ADP-ribose)-Binding Proteins with Photoaffinity-Based

Proteomics. Journal of the American Chemical Society, 143(8), 3037–3042. https://doi.org/10.1021/jacs.0c12246

De Bernardi, M. A., Gobelli, D., Serna, J., Nawrocka, P. M., March-Rosselló, G. A., Orduña, A., Kozlowski, P., Simarro, M., & De La Fuente, M. A. (2021). Novel fluorescent-based reporter cell line engineered for monitoring homologous recombination events. *PLOS ONE*, *16*(4), e0237413. https://doi.org/10.1371/journal.pone.0237413

De Lartigue PhD, J. (2020). *HRD testing heralds a new biomarker, but questions linger*. https://www.onclive.com/view/hrd-testing-heralds-a-new-biomarker-but-questions-linger

Debela, D. T., Muzazu, S. G., Heraro, K. D., Ndalama, M. T., Mesele, B. W., Haile, D. C., Kitui, S. K., & Manyazewal, T. (2021). New approaches and procedures for cancer treatment: Current perspectives. *Sage Open Medicine*, *9*, 205031212110343. https://doi.org/10.1177/20503121211034366

del Campo, J. M., Matulonis, U. A., Malander, S., Provencher, D., Mahner, S., Follana, P., Waters, J., Berek, J. S., Woie, K., Oza, A. M., Canzler, U., Gil-Martin, M., Lesoin, A., Monk, B. J., Lund, B., Gilbert, L., Wenham, R. M., Benigno, B., Arora, S., … Mirza, M. R. (2019). Niraparib Maintenance Therapy in Patients With Recurrent Ovarian Cancer After a Partial Response to the Last Platinum-Based Chemotherapy in the ENGOT-OV16/NOVA Trial. *Journal of Clinical Oncology*, *37*(32), 2968–2973. https://doi.org/10.1200/JCO.18.02238

Demény, M. Á., & Virág, L. (2021). The PARP Enzyme Family and the Hallmarks of Cancer Part 1. Cell Intrinsic hallmarks. *Cancers*, *13*(9), 2042. https://doi.org/10.3390/cancers13092042

DepMap: The Cancer Dependency Map Project at Broad Institute. (n.d.). https://depmap.org/portal/

Di Rorà, A. G. L., Cerchione, C., Martinelli, G., & Lanza, F. (2020). A WEE1 family business: regulation of mitosis, cancer progression, and therapeutic target. *Journal of Hematology & Oncology*, *13*(1). https://doi.org/10.1186/s13045-020-00959-2

Dias, M. P., Moser, S., Ganesan, S., & Jonkers, J. (2021). Understanding and overcoming resistance to PARP inhibitors in cancer therapy. *Nature Reviews Clinical Oncology*, *18*(12), 773–791. https://doi.org/10.1038/s41571-021-00532-x

Dillon, K. M., Bekele, R., Sztupinszki, Z., Hanlon, T., Rafiei, S., Szallasi, Z., Choudhury, A. D., & Mouw, K. W. (2022). PALB2 or BARD1 loss confers homologous recombination deficiency and PARP inhibitor sensitivity in prostate cancer. *Npj Precision Oncology*, *6*(1). https://doi.org/10.1038/s41698-022-00291-7

Ding, X., Zhu, Z., Lapek, J. D., McMillan, E. A., Zhang, A., Chung, C., Dubbury, S., Lapira, J., Firdaus, S. J., Kang, X., Gao, J., Oyer, J. A., Chionis, J., Rollins, R. A., Li, L., Niessen, S., Bagrodia, S., Zhang, L., & VanArsdale, T. (2022). PARP1-SNAI2 transcription axis drives resistance to PARP inhibitor, Talazoparib. *Scientific Reports*, *12*(1). https://doi.org/10.1038/s41598-022-16623-3

Dobzhansky, Th. (1946). GENETICS OF NATURAL POPULATIONS. XIII. RECOMBINATION AND VARIABILITY IN POPULATIONS OF DROSOPHILA PSEUDOOBSCURA. *Genetics*, *31*(3), 269–290. https://doi.org/10.1093/genetics/31.3.269

Drew, Y., Mulligan, E. A., Vong, W., Thomas, H. D., Kahn, S., Kyle, S., Mukhopadhyay, A., Los, G., Hostomsky, Z., Plummer, E. R., Edmondson, R. J., & Curtin, N. J. (2010). Therapeutic potential of Poly(ADP-ribose) polymerase inhibitor AG014699 in human cancers with mutated or methylated BRCA1 or BRCA2. *Journal of the National Cancer Institute*, *103*(4), 334–346. https://doi.org/10.1093/jnci/djq509

Duarte, D., & Vale, N. (2022). Evaluation of synergism in drug combinations and reference models for future orientations in oncology. *Current Research in Pharmacology and Drug Discovery*, *3*, 100110. https://doi.org/10.1016/j.crphar.2022.100110

Durmus, S., Sparidans, R. W., Van Esch, A., Wagenaar, E., Beijnen, J. H., & Schinkel, A. H. (2014). Breast cancer resistance protein (BCRP/ABCG2) and P-glycoprotein (P-GP/ABCB1) restrict oral availability and brain accumulation of the PARP inhibitor Rucaparib (AG-014699). Pharmaceutical Research, 32(1), 37–46. https://doi.org/10.1007/s11095-014-1442-z

Ellegren, H. (2004). Microsatellites: simple sequences with complex evolution. *Nature Reviews Genetics*, *5*(6), 435–445. https://doi.org/10.1038/nrg1348

Engelke, C. G., Parsels, L. A., Qian, Y., Zhang, Q., Karnak, D., Robertson, J. R., Tanska, D. M., Wei, D., Davis, M. A., Parsels, J. D., Zhao, L., Greenson, J. K., Lawrence, T. S., Maybaum, J., & Morgan, M. A. (2013). Sensitization of pancreatic cancer to chemoradiation by the CHK1 inhibitor MK8776. *Clinical Cancer Research*, *19*(16), 4412–4421. https://doi.org/10.1158/1078-0432.ccr-12-3748

Esmo. (2023). *Talazoparib beyond BRCA prospective study identifies the sensitivity of GPALB2-Associated breast cancers to PARP inhibition*. https://www.esmo.org/oncology-news/talazoparib-beyond-brca-prospective-study-identifies-the-sensitivity-of-gpalb2-associated-breast-cancers-to-parp-inhibition

Eustermann, S., Wu, W., Langelier, M.-F., Yang, J., Easton, L. E., Riccio, A. A., Pascal, J. M., & Neuhaus, D. (2015). Structural Basis of detection and Signaling of DNA Single-Strand Breaks by human PARP-1. *Molecular Cell*, *60*(5), 742–754. https://doi.org/10.1016/j.molcel.2015.10.032

Falchi, F., Giacomini, E., Masini, T., Boutard, N., Di Ianni, L., Manerba, M., Farabegoli, F., Rossini, L., Robertson, J., Minucci, S., Pallavicini, I., Di Stefano, G., Roberti, M., Pellicciari, R., & Cavalli, A. (2017). Synthetic Lethality Triggered by Combining Olaparib with BRCA2–Rad51 Disruptors. *ACS Chemical Biology*, *12*(10), 2491–2497. https://doi.org/10.1021/acschembio.7b00707

Fan, Z., Zhang, Y., Chen, S., Weng, X., Rao, Y., & Hongmei, F. (2020). Mechanism and current progress of Poly ADP-ribose polymerase (PARP) inhibitors in the treatment of ovarian cancer. *Biomedicine & Pharmacotherapy*, *123*, 109661. https://doi.org/10.1016/j.biopha.2019.109661

Farmer, H., McCabe, N., Lord, C. J., Tutt, A., Johnson, D. A., Richardson, T. B., Santarosa, M., Dillon, K. J., Hickson, I., Knights, C., Martin, N. M. B., Jackson, S., Smith, G. C. M., & Ashworth, A. (2005). Targeting the DNA repair defect in BRCA mutant cells as a therapeutic strategy. *Nature*, *434*(7035), 917–921. https://doi.org/10.1038/nature03445

Faulhaber, E.-M., Jost, T., Symank, J., Scheper, J., Bürkel, F., Fietkau, R., Hecht, M., & Distel, L. (2021). Kinase Inhibitors of DNA-PK, ATM and ATR in Combination with Ionizing Radiation Can Increase Tumor Cell Death in HNSCC Cells While Sparing Normal Tissue Cells. *Genes*, *12*(6), 925. https://doi.org/10.3390/genes12060925

Feiersinger, G. E., Trattnig, K., Leitner, P., Guggenberger, F., Oberhuber, A., Peer, S., Hermann, M., Skvortsova, I., Vrbkova, J., Bouchal, J., Culig, Z., & Santer, F. R. (2018). Olaparib is effective in combination with, and as maintenance therapy after, first-line endocrine therapy in prostate cancer cells. *Molecular Oncology*, *12*(4), 561–576. https://doi.org/10.1002/1878-0261.12185

Ferrarelli, L. K. (2019). FGFR inhibitors get to nuclear PTEN. *Science Signaling*, *12*(577), eaax6492. https://doi.org/10.1126/scisignal.aax6492

FOCI Counter | BIC Macro Toolkit | Image Analysis | Service | Bioimaging Centre. (2017). https://www.biologie.uni-konstanz.de/bioimaging-centre/service/image-analysis/bic-macro-toolkit/foci-counter/

Fokas, E., Prevo, R., Pollard, J., Reaper, P. M., Charlton, P., Cornelissen, B., Vallis, K. A., Hammond, E., Olcina, M. M., McKenna, W., Muschel, R. J., & Brunner, T. (2012). Targeting ATR in vivo using the novel inhibitor VE-822 results in selective sensitization of pancreatic tumors to radiation. *Cell Death and Disease*, *3*(12), e441. https://doi.org/10.1038/cddis.2012.181

for Biotechnology Information, N. C. (2023a). *Compound Summary for CID 452548, Teniposide*. https://pubchem.ncbi.nlm.nih.gov/compound/Teniposide.

for Biotechnology Information, N. C. (2023b). *Compound Summary for CID 24856436, Adavosertib*. https://pubchem.ncbi.nlm.nih.gov/compound/Adavosertib.

Foucquier, J., & Guedj, M. (2015). Analysis of drug combinations: current methodological landscape. *Pharmacology Research & Perspectives*, *3*(3), e00149. https://doi.org/10.1002/prp2.149

FoundationOne CDX | Foundation Medicine. (n.d.). https://www.foundationmedicine.com/test/foundationone-cdx

Franchet, C., Hoffmann, J.-S., & Dalenc, F. (2021). Recent advances in enhancing the therapeutic index of PARP inhibitors in breast cancer. *Cancers*, *13*(16), 4132. https://doi.org/10.3390/cancers13164132

Franzese, E., Centonze, S., Diana, A., Carlino, F., Guerrera, L. P., Di Napoli, M., De Vita, F., Pignata, S., Ciardiello, F., & Orditura, M. (2019). PARP inhibitors in ovarian cancer. *Cancer Treatment Reviews*, *73*, 1–9. https://doi.org/10.1016/j.ctrv.2018.12.002

Friedberg, E. C., Walker, G. C., & Siede, W. (2006). *DNA repair and mutagenesis*. http://ci.nii.ac.jp/ncid/BA74872267

Garai, Á., Zeke, A., Gógl, G., Töro, I., Fördos, F., Blankenburg, H., Bárkai, T., Varga, J., Alexa, A., Emig, D., Albrecht, M., & Reményi, A. (2012). Specificity of Linear Motifs That Bind to a Common Mitogen-Activated Protein Kinase Docking Groove. *Science Signaling*, *5*(245). https://doi.org/10.1126/scisignal.2003004

Giglia-Mari, G., Zotter, A., & Vermeulen, W. (2010). DNA damage response. *Cold Spring Harbor Perspectives in Biology*, *3*(1), a000745. https://doi.org/10.1101/cshperspect.a000745

Gogola, E., Duarte, A., De Ruiter, J. R., Wiegant, W. W., Schmid, J., De Bruijn, R., James, D. I., Llobet, S. G., Vis, D. J., Annunziato, S., Van Den Broek, B., Barazas, M., Kersbergen, A., Van De Ven, M., Tarsounas, M., Ogilvie, D. J., Van Vugt, M. A. T. M., Wessels, L. F. A., Bartkova, J., … Rottenberg, S. (2018). Selective loss of PARG restores parylation and counteracts PARP inhibitor-mediated synthetic lethality. *Cancer Cell*, *33*(6), 1078–1093.e12. https://doi.org/10.1016/j.ccell.2018.05.008

Gol, T. M., Rodemann, H. P., & Dittmann, K. (2019). Depletion of Akt1 and Akt2 Impairs the Repair of Radiation-Induced DNA Double Strand Breaks via Homologous Recombination. *International Journal of Molecular Sciences*, *20*(24), 6316. https://doi.org/10.3390/ijms20246316

Goldoni, M., & Johansson, C. (2007). A mathematical approach to study combined effects of toxicants in vitro: Evaluation of the Bliss independence criterion and the Loewe additivity model. *Toxicology in Vitro*, *21*(5), 759–769. https://doi.org/10.1016/j.tiv.2007.03.003

Goodman, A. (2022). *PARP1-Selective Inhibitor Offers Significant Benefits Over Older Predecessors in Treatment of Solid Tumors - The ASCO Post*. https://ascopost.com/issues/may-25-2022/parp1-selective-inhibitor-offers-significant-benefits-over-older-predecessors-in-treatment-of-solid-tumors/

Gottifredi, V., & Prives, C. (2005). The S phase checkpoint: When the crowd meets at the fork. *Seminars in Cell & Developmental Biology*, *16*(3), 355–368. https://doi.org/10.1016/j.semcdb.2005.02.011

Gottschalk, A. J., Timinszky, G., Kong, S. E., Jin, J., Cai, Y., Swanson, S. K., Washburn, M. P., Florens, L., Ladurner, A. G., Conaway, J. W., & Conaway, R. C. (2009). Poly(ADP-ribosyl)ation directs recruitment and activation of an ATP-dependent chromatin remodeler. *Proceedings of the National Academy of Sciences*, *106*(33), 13770–13774. https://doi.org/10.1073/pnas.0906920106

Gottschalk, A. J., Trivedi, R., Conaway, J. W., & Conaway, R. C. (2012). Activation of the SNF2 family ATPAse ALC1 by Poly(ADP-ribose) in a stable ALC1·PARP1·Nucleosome intermediate. *Journal of Biological Chemistry*, *287*(52), 43527–43532. https://doi.org/10.1074/jbc.m112.401141

Greco, W. R., Bravo, G., & Parsons, J. (1995). The search for synergy: a critical review from a response surface perspective. *PubMed*, *47*(2), 331–385. https://pubmed.ncbi.nlm.nih.gov/7568331

Gu, Y., Helenius, M., Väänänen, K., Bulanova, D., Saarela, J., Sokolenko, A. P., Martens, J. W. M., Imyanitov, E. N., & Kuznetsov, S. G. (2016). BRCA1-deficient breast cancer cell lines are resistant to MEK inhibitors and show distinct sensitivities to 6-thioguanine. *Scientific Reports*, *6*(1). https://doi.org/10.1038/srep28217

Guillot, C., Favaudon, V., Herceg, Z., Sagne, C., Sauvaigo, S., Merle, P., Hall, J., & Chemin, I. (2014). PARP inhibition and the radiosensitizing effects of the PARP inhibitor ABT-888 in in vitrohepatocellular carcinoma models. *BMC Cancer*, *14*(1). https://doi.org/10.1186/1471-2407-14-603

Guo, X., Wang, L., Li, J., Ding, Z., Xiao, J., Yin, X., He, S., Shi, P., Dong, L., Li, G., Tian, C., Wang, J., Cong, Y., & Xu, Y. (2014). Structural insight into autoinhibition and histone H3-induced activation of DNMT3A. *Nature*, *517*(7536), 640–644. https://doi.org/10.1038/nature13899

Gyori, B. M., Venkatachalam, G., Thiagarajan, P. S., Hsu, D., & Clement, M.-V. (2014). OpenComet: An automated tool for comet assay image analysis. *Redox Biology*, *2*, 457–465. https://doi.org/10.1016/j.redox.2013.12.020

Haince, J. F., Kozlov, S., Dawson, V. L., Dawson, T. M., Hendzel, M. J., Lavin, M. F., & Poirier, G. G. (2007). Ataxia telangiectasia mutated (ATM) signaling network is modulated by a novel Poly(ADP-ribose)-dependent pathway in the early response to DNA-damaging agents. *Journal of Biological Chemistry*, *282*(22), 16441–16453. https://doi.org/10.1074/jbc.m608406200

Haince, J.-F., McDonald, D., Rodrigue, A., Déry, U., Masson, J., Hendzel, M. J., & Poirier, G. G. (2008). PARP1-dependent Kinetics of Recruitment of MRE11 and NBS1 Proteins to Multiple DNA Damage Sites. *Journal of Biological Chemistry*, *283*(2), 1197–1208. https://doi.org/10.1074/jbc.m706734200

Hanahan, D., & Weinberg, R. A. (2011). Hallmarks of Cancer: The next generation. *Cell*, *144*(5), 646–674. https://doi.org/10.1016/j.cell.2011.02.013

Hanzlikova, H., Kalasova, I., Demin, A. A., Pennicott, L. E., Cihlarova, Z., & Caldecott, K. W. (2018). The Importance of Poly(ADP-Ribose) Polymerase as a Sensor of Unligated Okazaki Fragments during DNA Replication. *Molecular Cell*, *71*(2), 319-331.e3. https://doi.org/10.1016/j.molcel.2018.06.004

Hassler, M., & Ladurner, A. G. (2012). Towards a structural understanding of PARP1 activation and related signalling ADP-ribosyl-transferases. *Current Opinion in Structural Biology*, *22*(6), 721–729. https://doi.org/10.1016/j.sbi.2012.08.005

Helleday, T. (2011). The underlying mechanism for the PARP and BRCA synthetic lethality: Clearing up the misunderstandings. *Molecular Oncology*, *5*(4), 387–393. https://doi.org/10.1016/j.molonc.2011.07.001

Hewitt, G., Borel, V., Segura-Bayona, S., Takaki, T., Ruis, P., Bellelli, R., Lehmann, L. C., Sommerová, L., Vančevska, A., Tomás-Loba, A., Zhu, K., Cooper, C. D. O., Fugger, K., Patel, H., Goldstone, R., Schneider-Luftman, D., Herbert, E., Stamp, G. W., Brough, R., … Boulton, S. J. (2021). Defective ALC1 nucleosome remodeling confers PARPi sensitization and synthetic lethality with HRD. *Molecular Cell*, *81*(4), 767–783.e11. https://doi.org/10.1016/j.molcel.2020.12.006

Hill, S. J., Clark, A., Silver, D. P., & Livingston, D. M. (2014). BRCA1 pathway function in Basal-Like breast cancer cells. *Molecular and Cellular Biology*, *34*(20), 3828–3842. https://doi.org/10.1128/mcb.01646-13

Hopkins, T. A., Ainsworth, W., Ellis, P. D., Donawho, C. K., Digiammarino, E. L., Panchal, S. C., Abraham, V. C., Algire, M. A., Shi, Y., Olson, A., Johnson, E., Wilsbacher, J. L., & Maag, D. (2019). PARP1 trapping by PARP inhibitors drives cytotoxicity in both cancer cells and healthy bone marrow. *Molecular Cancer Research*, *17*(2), 409–419. https://doi.org/10.1158/1541-7786.mcr-18-0138

Hu, Y., Petit, S. J., Ficarro, S. B., Toomire, K. J., Xie, A., Lim, E., Cao, S., Park, E. Y., Eck, M. J., Scully, R., Brown, M., Marto, J. A., & Livingston, D. M. (2014). PARP1-

Driven Poly-ADP-Ribosylation regulates BRCA1 function in homologous Recombination–Mediated DNA Repair. *Cancer Discovery*, *4*(12), 1430–1447. https://doi.org/10.1158/2159-8290.cd-13-0891

Huan, T. D., Wang, X., & Yu, Y. (2020). PARP1 inhibitors trigger innate immunity via PARP1 trapping-induced DNA damage response. *ELife*, *9*. https://doi.org/10.7554/elife.60637

Huang, D., & Kraus, W. L. (2022). The expanding universe of PARP1-mediated molecular and therapeutic mechanisms. *Molecular Cell*, *82*(12), 2315–2334. https://doi.org/10.1016/j.molcel.2022.02.021

Huang, J., Luo, H., Pan, H., Qiu, C., Hao, T., & Zhu, Z. (2018). Interaction between RAD51 and MCM complex is essential for RAD51 foci forming in colon cancer HCT116 cells. *Biokhimiya*, *83*(1), 69–75. https://doi.org/10.1134/s0006297918010091

Hucl, T., Rago, C., Gallmeier, E., Brody, J. R., Gorospe, M., & Kern, S. E. (2008). A Syngeneic Variance Library for Functional Annotation of Human Variation: Application to *BRCA2*. *Cancer Research*, *68*(13), 5023–5030. https://doi.org/10.1158/0008-5472.can-07-6189

Ianevski, A., Giri, A. K., & Aittokallio, T. (2020). SynergyFinder 2.0: visual analytics of multi-drug combination synergies. *Nucleic Acids Research*, *48*(W1), W488–W493. https://doi.org/10.1093/nar/gkaa216

Ianevski, A., Giri, A. K., Gautam, P., Kononov, A. V, Potdar, S., Saarela, J., Wennerberg, K., & Aittokallio, T. (2019). Prediction of drug combination effects with a minimal set of experiments. *Nature Machine Intelligence*, *1*(12), 568–577. https://doi.org/10.1038/s42256-019-0122-4

Ikegami, M., Kohsaka, S., Ueno, T., Momozawa, Y., Inoue, S., Tamura, K., Shimomura, A., Hosoya, N., Kobayashi, H., Tanaka, S., & Mano, H. (2020). High-throughput functional evaluation of BRCA2 variants of unknown significance. *Nature Communications*, *11*(1). https://doi.org/10.1038/s41467-020-16141-8

Iliakis, G., Murmann, T., & Soni, A. (2015). Alternative end-joining repair pathways are the ultimate backup for abrogated classical non-homologous end-joining and homologous recombination repair: Implications for the formation of chromosome translocations. *Mutation Research/Genetic Toxicology and Environmental Mutagenesis*, *793*, 166–175. https://doi.org/10.1016/j.mrgentox.2015.07.001

Ivy, S. P., Liu, J. F., Lee, J. P., Matulonis, U. A., & Kohn, E. C. (2016). Cediranib, a pan-VEGFR inhibitor, and olaparib, a PARP inhibitor, in combination therapy for high grade serous ovarian cancer. *Expert Opinion on Investigational Drugs*, *25*(5), 597–611. https://doi.org/10.1517/13543784.2016.1156857

Jackson, L. M., & Moldovan, G.-L. (2022). Mechanisms of PARP1 inhibitor resistance and their implications for cancer treatment. *NAR Cancer*, *4*(4). https://doi.org/10.1093/narcan/zcac042

Jelinic, P., & Levine, D. A. (2014). New Insights into PARP Inhibitors' Effect on Cell Cycle and Homology-Directed DNA Damage Repair. *Molecular Cancer Therapeutics*, *13*(6), 1645–1654. https://doi.org/10.1158/1535-7163.mct-13-0906-t

Jeltsch, A., & Jurkowska, R. Z. (2016). Allosteric control of mammalian DNA methyltransferases – a new regulatory paradigm. *Nucleic Acids Research*, *44*(18), 8556–8575. https://doi.org/10.1093/nar/gkw723

Jimenez-Sainz, J., Mathew, J. I., Moore, G., Lahiri, S., Garbarino, J., Eder, J. P., Rothenberg, E., & Jensen, R. R. (2022). BRCA2 BRC missense variants disrupt RAD51-dependent DNA repair. *ELife*, *11*. https://doi.org/10.7554/elife.79183

Johnson, N. F., Johnson, S. P., Yao, W., Li, Y., Choi, Y. D., Bernhardy, A. J., Wang, Y., Capelletti, M., Sarosiek, K. A., Moreau, L. A., Chowdhury, D., Wickramanayake, A., Harrell, M. I., Liu, J. F., D'Andrea, A. D., Miron, A., Swisher, E. M., & Shapiro, G. I. (2013). Stabilization of mutant BRCA1 protein confers PARP inhibitor and platinum resistance. *Proceedings of the National Academy of Sciences*, *110*(42), 17041–17046. https://doi.org/10.1073/pnas.1305170110

Jordan, M. A., Toso, R. J., Thrower, D., & Wilson, L. (1993). Mechanism of mitotic block and inhibition of cell proliferation by taxol at low concentrations. *Proceedings of the National Academy of Sciences of the United States of America*, *90*(20), 9552–9556. https://doi.org/10.1073/pnas.90.20.9552

Jordan, M. A., & Wilson, L. (1998). Microtubules and actin filaments: dynamic targets for cancer chemotherapy. *Current Opinion in Cell Biology*, *10*(1), 123–130. https://doi.org/10.1016/s0955-0674(98)80095-1

Juhász, S., Smith, R. K., Schauer, T., Spekhardt, D., Mamar, H., Zentout, S., Chapuis, C., Huet, S., & Timinszky, G. (2020). The chromatin remodeler ALC1 underlies resistance to PARP inhibitor treatment. *Science Advances*, *6*(51). https://doi.org/10.1126/sciadv.abb8626

Kanev, P.-B., Atemin, A., Stoynov, S., & Aleksandrov, R. (2023). PARP1 roles in DNA repair and DNA replication: The basi(c)s of PARP inhibitor efficacy and resistance. *Seminars in Oncology*. https://doi.org/10.1053/j.seminoncol.2023.08.001

Kastan, M. B., & Bartek, J. (2004). Cell-cycle checkpoints and cancer. *Nature*, *432*(7015), 316–323. https://doi.org/10.1038/nature03097

Keung, M. Y., Wu, Y., Badar, F., & Vadgama, J. V. (2020). Response of breast cancer cells to PARP inhibitors is independent of BRCA status. *Journal of Clinical Medicine*, *9*(4), 940. https://doi.org/10.3390/jcm9040940

Khodyreva, S. N., & Lavrik, O. I. (2016). Poly(ADP-Ribose) polymerase 1 as a key regulator of DNA repair. *Molecular Biology*, *50*(4), 580–595. https://doi.org/10.1134/s0026893316040038

Kim, D.-H., & Nam, H. Y. (2022). PARP inhibitors: clinical limitations and recent attempts to overcome them. *International Journal of Molecular Sciences*, *23*(15), 8412. https://doi.org/10.3390/ijms23158412

Kim, H. S., Xu, H., George, E., Hallberg, D., Kumar, S., Jagannathan, V., Medvedev, S. P., Kinose, Y., Devins, K., Verma, P., Ly, K., Wang, Y., Greenberg, R. A., Schwartz, L. E., Johnson, N. F., Scharpf, R. B., Mills, G. B., Zhang, L., Velculescu, V. E., … Simpkins, F. (2020). Combining PARP with ATR inhibition overcomes PARP inhibitor and platinum resistance in ovarian cancer models. *Nature Communications*, *11*(1). https://doi.org/10.1038/s41467-020-17127-2

Kim, H.-J., Min, A., Im, S.-A., Jang, H., Lee, K.-H., Lau, A. P. T., Lee, M. H., Kim, S., Yang, Y., Kim, J., Kim, T. Y., Oh, D. Y., Brown, J. R., O'Connor, M. J., & Bang, Y.-J. (2016). Anti-tumor activity of the ATR inhibitor AZD6738 in HER2 positive breast cancer cells. *International Journal of Cancer*, *140*(1), 109–119. https://doi.org/10.1002/ijc.30373

Kim, K. B., Soroceanu, L., De Semir, D., Millis, S. Z., Ross, J. S., Vosoughi, E., Dar, A. A., Nosrati, M., Campisi, J., Ice, R. J., Chen, M. M., Chetal, K., Bhattacharjee, A., Moretto, J., Leong, S. P. L., Singer, M. I., Parrett, B. M., Minor, D. R., McAllister, S. D., … Kashani-Sabet, M. (2021). Prevalence of homologous recombination pathway gene mutations in melanoma: Rationale for a new targeted therapeutic approach. *Journal of Investigative Dermatology*, *141*(8), 2028–2036.e2. https://doi.org/10.1016/j.jid.2021.01.024

Kim, M.-N., Zhang, T., & Kraus, W. L. (2005). Poly(ADP-ribosyl)ation by PARP-1: `PAR-laying' NAD^+ into a nuclear signal. *Genes & Development*, *19*(17), 1951–1967. https://doi.org/10.1101/gad.1331805

Konecny, G. E., & Kristeleit, R. (2016). PARP inhibitors for BRCA1/2-mutated and sporadic ovarian cancer: current practice and future directions. *British Journal of Cancer*, *115*(10), 1157–1173. https://doi.org/10.1038/bjc.2016.311

Kraus, W. L., & Lis, J. T. (2003). PARP goes transcription. *Cell*, *113*(6), 677–683. https://doi.org/10.1016/s0092-8674(03)00433-1

Krishnakumar, R., & Kraus, W. L. (2010). The PARP side of the nucleus: molecular actions, physiological outcomes, and clinical targets. *Molecular Cell*, *39*(1), 8–24. https://doi.org/10.1016/j.molcel.2010.06.017

Kruglov, O., Wu, X., Hwang, S. T., & Akilov, O. E. (2020). The synergistic proapoptotic effect of PARP-1 and HDAC inhibition in cutaneous T-cell lymphoma is mediated

via Blimp-1. *Blood Advances*, *4*(19), 4788–4797. https://doi.org/10.1182/bloodadvances.2020002049

Kunos, C., Deng, W., Dawson, D., Lea, J. S., Zanotti, K. M., Gray, H. J., Bender, D. P., Guaglianone, P. P., Carter, J. S., & Moore, K. N. (2015). A Phase I-II Evaluation of Veliparib (NSC #737664), Topotecan, and Filgrastim or Pegfilgrastim in the Treatment of Persistent or Recurrent Carcinoma of the Uterine Cervix. *International Journal of Gynecological Cancer*, *25*(3), 484–492. https://doi.org/10.1097/IGC.0000000000000380

Kuo, L., & Yang, L.-X. (2008). Gamma-H2AX - a novel biomarker for DNA double-strand breaks. *PubMed*, *22*(3), 305–309. https://pubmed.ncbi.nlm.nih.gov/18610740

Lee, Y., Park, S., Ciccone, S. L. M., Kim, C., & Lee, S. (2005). An in vivo analysis of MMC-induced DNA damage and its repair. Carcinogenesis, 27(3), 446–453. doi.org/10.1093/carcin/bgi254

Lai, S.-W., Bamodu, O. A., Chen, J., Wu, A. T. H., Lee, W., Chao, T. Y., & Yeh, C. T. (2020). Targeted PARP Inhibition Combined with FGFR1 Blockade is Synthetically Lethal to Malignant Cells in Patients with Pancreatic Cancer. *Cells*, *9*(4), 911. https://doi.org/10.3390/cells9040911

Langelier, M.-F., & Pascal, J. M. (2013). PARP-1 mechanism for coupling DNA damage detection to poly(ADP-ribose) synthesis. *Current Opinion in Structural Biology*, *23*(1), 134–143. https://doi.org/10.1016/j.sbi.2013.01.003

Lederer, S., Dijkstra, T. M. H., & Heskes, T. (2019). Additive dose response models: defining synergy. *Frontiers in Pharmacology*, *10*. https://doi.org/10.3389/fphar.2019.01384

Leidecker, O., Bonfiglio, J. J., Colby, T., Zhang, Q., Atanassov, I., Žaja, R., Palazzo, L., Stockum, A., Ahel, I., & Matić, I. (2016). Serine is a new target residue for endogenous ADP-ribosylation on histones. *Nature Chemical Biology*, *12*(12), 998–1000. https://doi.org/10.1038/nchembio.2180

Lemaçon, D., Jackson, J., Quinet, A., Brickner, J. R., Li, S., Yazinski, S. A., You, Z., Ira, G., Zou, L., Mosammaparast, N., & Vindigni, A. (2017). MRE11 and EXO1 nucleases degrade reversed forks and elicit MUS81-dependent fork rescue in BRCA2-deficient cells. *Nature Communications*, *8*(1). https://doi.org/10.1038/s41467-017-01180-5

Leung, A. K. L. (2020). Poly(ADP-ribose): A Dynamic Trigger for Biomolecular Condensate Formation. *Trends in Cell Biology*, *30*(5), 370–383. https://doi.org/10.1016/j.tcb.2020.02.002

Li, H., Liu, Z., Wu, N., Chen, Y., Cheng, Q., & Wang, J. (2020). PARP inhibitor resistance: the underlying mechanisms and clinical implications. *Molecular Cancer*, *19*(1). https://doi.org/10.1186/s12943-020-01227-0

Li, J., Wang, R., Kong, Y., Broman, M. M., Carlock, C., Chen, L., Li, Z., Farah, E., Ratliff, T. L., & Liu, X. (2017). Targeting PLK1 to enhance efficacy of Olaparib in Castration-Resistant prostate Cancer. *Molecular Cancer Therapeutics*, *16*(3), 469–479. https://doi.org/10.1158/1535-7163.mct-16-0361

Li, M., & Yu, X. (2013). Function of BRCA1 in the DNA damage response is mediated by ADP-Ribosylation. *Cancer Cell*, *23*(5), 693–704. https://doi.org/10.1016/j.ccr.2013.03.025

Li, X., & Heyer, W. D. (2008). Homologous recombination in DNA repair and DNA damage tolerance. *Cell Research*, *18*(1), 99–113. https://doi.org/10.1038/cr.2008.1

Lin, K. K., Harrell, M. I., Oza, A. M., Oaknin, A., Ray-Coquard, I., Tinker, A. V., Helman, E., Radke, M. R., Say, C., Vo, L., Mann, E., Isaacson, J. D., Maloney, L., O'Malley, D. M., Chambers, S. K., Kaufmann, S. H., Scott, C. L., Konecny, G. E., Coleman, R. L., . . . Swisher, E. M. (2018). BRCA reversion mutations in circulating tumor DNA predict primary and acquired resistance to the PARP inhibitor Rucaparib in High-Grade ovarian carcinoma. Cancer Discovery, 9(2), 210–219. https://doi.org/10.1158/2159-8290.cd-18-0715

Liu, J., Qu, L., Meng, L., & Shou, C. (2019). Topoisomerase inhibitors promote cancer cell motility via ROS-mediated activation of JAK2-STAT1-CXCL1 pathway. *Journal of Experimental & Clinical Cancer Research*, *38*(1). https://doi.org/10.1186/s13046-019-1353-2

Liu, X., Shi, Y., Maag, D., Palma, J. P., Patterson, M. J., Ellis, P., Surber, B. W., Ready, D., Soni, N. B., Ladror, U. S., Xu, A. J., Iyer, R. R., Harlan, J. E., Solomon, L. R., Donawho, C. K., Penning, T. D., Johnson, E. F., & Shoemaker, A. R. (2012). Iniparib Nonselectively Modifies Cysteine-Containing Proteins in Tumor Cells and Is Not a *Bona Fide* PARP Inhibitor. *Clinical Cancer Research*, *18*(2), 510–523. https://doi.org/10.1158/1078-0432.ccr-11-1973

Lord, C. J., & Ashworth, A. (2017). PARP inhibitors: Synthetic lethality in the clinic. *Science*, *355*(6330), 1152–1158. https://doi.org/10.1126/science.aam7344

Lord, C. J., McDonald, S. D., Swift, S., Turner, N. J., & Ashworth, A. (2008). A high-throughput RNA interference screen for DNA repair determinants of PARP inhibitor sensitivity. *DNA Repair*, *7*(12), 2010–2019. https://doi.org/10.1016/j.dnarep.2008.08.014

Löser, D. A., Shibata, A., Shibata, A., Woodbine, L., Jeggo, P. A., & Chalmers, A. J. (2010). Sensitization to radiation and alkylating agents by inhibitors of Poly(ADP-ribose) polymerase is enhanced in cells deficient in DNA Double-Strand break repair. *Molecular Cancer Therapeutics*, *9*(6), 1775–1787. https://doi.org/10.1158/1535-7163.mct-09-1027

Loss of heterozygosity Myriad Genetics BRCA mutation BRCA1 BRCA2. (n.d.). https://www.pngwing.com/en/free-png-ytvbc

Lu, X., He, Y., Johnston, R. L., Nanayakarra, D., Sankarasubramanian, S., Lopez, J. A., Friedlander, M., Kalimutho, M., Hooper, J. N. A., Raninga, P. V, & Khanna, K. K. (2022). CBL0137 impairs homologous recombination repair and sensitizes high-grade serous ovarian carcinoma to PARP inhibitors. *Journal of Experimental & Clinical Cancer Research*, *41*(1). https://doi.org/10.1186/s13046-022-02570-4

Luijsterburg, M. S., De Krijger, I., Wiegant, W. W., Shah, R. G., Smeenk, G., De Groot, A. J. L., Pines, A., Vertegaal, A. C. O., Jacobs, J. J. L., Shah, G. M., & Van Attikum, H. (2016). PARP1 links CHD2-Mediated chromatin expansion and H3.3 deposition to DNA repair by non-homologous End-Joining. *Molecular Cell*, *61*(4), 547–562. https://doi.org/10.1016/j.molcel.2016.01.019

Mak, J. P. Y., Tang, H., & Poon, R. Y. C. (2020). Synergism between ATM and PARP1 Inhibition Involves DNA Damage and Abrogating the G2 DNA Damage Checkpoint. *Molecular Cancer Therapeutics*, *19*(1), 123–134. https://doi.org/10.1158/1535-7163.mct-19-0474

Mansour, W. Y., Tennstedt, P., Volquardsen, J., Oing, C., Kluth, M., Hube-Magg, C., Borgmann, K., Simon, R., Petersen, C., Dikomey, E., & Rothkamm, K. (2018). Loss of PTEN-assisted G2/M checkpoint impedes homologous recombination repair and enhances radio-curability and PARP inhibitor treatment response in prostate cancer. *Scientific Reports*, *8*(1). https://doi.org/10.1038/s41598-018-22289-7

Marjanović, M., Crawford, K., & Ahel, I. (2017). PARP, transcription and chromatin modeling. *Seminars in Cell & Developmental Biology*, *63*, 102–113. https://doi.org/10.1016/j.semcdb.2016.09.014

Marquard, A. M., Eklund, A. C., Joshi, T., Krzystanek, M., Favero, F., Wang, Z., Richardson, A. L., Silver, D., Szallasi, Z., & Birkbak, N. J. (2015). Pan-cancer analysis of genomic scar signatures associated with homologous recombination deficiency suggests novel indications for existing cancer drugs. *Biomarker Research*, *3*(1). https://doi.org/10.1186/s40364-015-0033-4

Martello, R., Leutert, M., Jungmichel, S., Bilan, V., Buch-Larsen, S. C., Young, C., Hottiger, M. O., & Nielsen, M. L. (2016). Proteome-wide identification of the endogenous ADP-ribosylome of mammalian cells and tissue. *Nature Communications*, *7*(1). https://doi.org/10.1038/ncomms12917

Masani, S., Han, L., Meek, K., & Yu, K. (2016). Redundant function of DNA ligase 1 and 3 in alternative end-joining during immunoglobulin class switch recombination. *Proceedings of the National Academy of Sciences of the United States of America*, *113*(5), 1261–1266. https://doi.org/10.1073/pnas.1521630113

Mason, J., Chan, Y.-L., Weichselbaum, R. R., & Bishop, D. K. (2019). Non-enzymatic roles of human RAD51 at stalled replication forks. *Nature Communications*, *10*(1). https://doi.org/10.1038/s41467-019-12297-0

Mateos-Gómez, P. A., Gong, F., Nair, N., Miller, K. M., Denchi, E. L., & Sfeir, A. (2015). Mammalian polymerase θ promotes alternative NHEJ and suppresses recombination. *Nature*, *518*(7538), 254–257. https://doi.org/10.1038/nature14157

Mateos-Gomez, P. A., Kent, T., Deng, S. K., McDevitt, S., Kashkina, E., Hoang, T. M., Pomerantz, R. T., & Sfeir, A. (2017). The helicase domain of Polθ counteracts RPA to promote alt-NHEJ. *Nature Structural & Molecular Biology*, *24*(12), 1116–1123. https://doi.org/10.1038/nsmb.3494

Matulonis, U. A., Wulf, G. M., Barry, W. T., Birrer, M., Westin, S. N., Farooq, S., Bell-McGuinn, K. M., Obermayer, E., Whalen, C., Spagnoletti, T., Luo, W., Liu, H., Hok, R. C., Aghajanian, C., Solit, D. B., Mills, G. B., Taylor, B. S., Won, H., Berger, M. F., … Winer, E. (2017). Phase I dose escalation study of the PI3kinase pathway inhibitor BKM120 and the oral poly (ADP ribose) polymerase (PARP) inhibitor olaparib for the treatment of high-grade serous ovarian and breast cancer. *Annals of Oncology*, *28*(3), 512–518. https://doi.org/10.1093/annonc/mdw672

Maurya, D. K., Ayuzawa, R., Doi, C., Troyer, D. L., & Tamura, M. (2011). Topoisomerase I inhibitor SN-38 effectively attenuates growth of human non-small cell lung cancer cell lines in vitro and in vivo. *Journal of Environmental Pathology Toxicology and Oncology*, *30*(1), 1–10. https://doi.org/10.1615/jenvironpatholtoxicoloncol.v30.i1.10

Mc, B. (1989). What is synergy? *PubMed*, *41*(2), 93–141. https://pubmed.ncbi.nlm.nih.gov/2692037

McLaren, A., Cartwright, D., Ross, E., & Roxburgh, P. (2021). First-Line PARP Inhibitors—Emerging Side Effects Require Caution: A Case of PARPi-Induced Pneumonitis. *Journal of Immunotherapy and Precision Oncology*, *4*(3), 171–174. https://doi.org/10.36401/JIPO-20-33

Menzer, W. M., Sahiri, K., Schomburg, A., Ladurner, A., & Sennhenn, P. (2022). Use of ALC1 inhibitors and synergy with PARPI (Patent No. WO/2023/213833). Zwicker Schnappauf & Partner Patentanwälte PartG mbB. https://patentscope.wipo.int/search/en/detail.jsf?docId=WO2023213833&_cid=P12-M2SZCT-38262-1

Menzer, W. M., Sahiri, K., & Schomburg, A. (2025). Inhibitors for use in treating cancer by potentiating the effects of FDA approved cancer drugs (Patent No. EP23205931.1, EP23207212.4 & EP 24185254.0). Zwicker Schnappauf & Partner Patentanwälte PartG mbB.

Menzer, W. M., Sahiri, K., Zhang, X., Schomburg, A., Ladurner, A., & Sieveke, J. (2025). ALC1 inhibitors ALC1i-1 and ALC1i-2 for use in treating pancreatic cancer by potentiating the effect of irinotecan (Patent No. EP23207219.9). Zwicker Schnappauf & Partner Patentanwälte PartG mbB.

Miao, C., Tsujino, T., Takai, T., Gui, F., Tsutsumi, T., Sztupinszki, Z., Wang, Z., Azuma, H., Szallasi, Z., Mouw, K. W., Zou, L., Kibel, A. S., & Jia, L. (2022). *RB1* loss overrides PARP inhibitor sensitivity driven by *RNASEH2B* loss in prostate cancer. *Science Advances*, *8*(7). https://doi.org/10.1126/sciadv.abl9794

Middleton, M. R., Dean, E., Evans, T. M., Shapiro, G. I., Pollard, J. D., Hendriks, B. S., Falk, M., Diaz-Padilla, I., & Plummer, R. (2021). Phase 1 study of the ATR inhibitor berzosertib (formerly M6620, VX-970) combined with gemcitabine ± cisplatin in patients with advanced solid tumours. *British Journal of Cancer*, *125*(4), 510–519. https://doi.org/10.1038/s41416-021-01405-x

Mimitou, E. P., & Symington, L. S. (2009). DNA end resection: Many nucleases make light work. *DNA Repair*, *8*(9), 983–995. https://doi.org/10.1016/j.dnarep.2009.04.017

Murai, J., Huang, S.-Y. N., Das, B. B., Renaud, A., Zhang, Y., Doroshow, J. H., Ji, J., Takeda, S., & Pommier, Y. (2012). Trapping of PARP1 and PARP2 by Clinical PARP Inhibitors. *Cancer Research*, *72*(21), 5588–5599. https://doi.org/10.1158/0008-5472.can-12-2753

Murai, J., Huang, S.-Y. N., Renaud, A., Zhang, Y., Ji, J., Takeda, S., Morris, J., Teicher, B. A., Doroshow, J. H., & Pommier, Y. (2014). Stereospecific PARP Trapping by BMN 673 and Comparison with Olaparib and Rucaparib. *Molecular Cancer Therapeutics*, *13*(2), 433–443. https://doi.org/10.1158/1535-7163.mct-13-0803

Murai, J., Tang, S.-W., Leo, E., Baechler, S., Redon, C. E., Zhang, H. Y., Abo, M. Al, Rajapakse, V. N., Nakamura, E., Jenkins, L. M. M., Aladjem, M. I., & Pommier, Y. (2018). SLFN11 blocks stressed replication forks independently of ATR. *Molecular Cell*, *69*(3), 371–384.e6. https://doi.org/10.1016/j.molcel.2018.01.012

Murai, J., Zhang, Y., Morris, J., Ji, J., Takeda, S., Doroshow, J. H., & Pommier, Y. (2014). Rationale for Poly(ADP-ribose) Polymerase (PARP) Inhibitors in Combination Therapy with Camptothecins or Temozolomide Based on PARP Trapping versus Catalytic Inhibition. *Journal of Pharmacology and Experimental Therapeutics*, *349*(3), 408–416. https://doi.org/10.1124/jpet.113.210146

MyChoice® CDX FDA-Approved Targeted Therapies - Managed Care. (2023). https://myriad.com/managed-care/products/mychoice-cdx/

Nagaraju, G., Odate, S., Xie, A., & Scully, R. (2006). Differential Regulation of Short- and Long-Tract Gene Conversion between Sister Chromatids by Rad51C. *Molecular and Cellular Biology*, *26*(21), 8075–8086. https://doi.org/10.1128/mcb.01235-06

Nakahara, M., Fujihara, S., Iwama, H., Takuma, K., Oura, K., Tadokoro, T., Fujita, K., Tani, J., Morishita, A., Kobara, H., Himoto, T., & Masaki, T. (2022). Effect of Lenvatinib treatment on the cell cycle and microRNA profile in hepatocellular carcinoma cells. *Biomedical Reports*, *17*(4). https://doi.org/10.3892/br.2022.1561

Nakayama, T., Nozawa, N., Kawada, C., Yamamoto, S., Ishii, T., Ishizuka, M., Namikawa, T., Ogura, S., Hanazaki, K., Inoue, K., & Karashima, T. (2020). Mitomycin C-induced cell cycle arrest enhances 5-aminolevulinic acid-based photodynamic therapy for bladder cancer. *Photodiagnosis and Photodynamic Therapy*, *31*, 101893. https://doi.org/10.1016/j.pdpdt.2020.101893

Nami, B., Maadi, H., & Wang, Z. (2018). Mechanisms Underlying the Action and Synergism of Trastuzumab and Pertuzumab in Targeting HER2-Positive Breast Cancer. *Cancers*, *10*(10), 342. https://doi.org/10.3390/cancers10100342

Nitiss, J. L. (2009). Targeting DNA topoisomerase II in cancer chemotherapy. *Nature Reviews Cancer*, *9*(5), 338–350. https://doi.org/10.1038/nrc2607

Nurgali, K., Jagoe, R. T., & Abalo, R. (2018). Editorial: Adverse Effects of Cancer Chemotherapy: Anything new to improve tolerance and reduce sequelae? *Frontiers in Pharmacology*, *9*. https://doi.org/10.3389/fphar.2018.00245

O'Cearbhaill, R. E. (2018). Using PARP inhibitors in advanced ovarian cancer. *PubMed*, *32*(7), 339–343. https://pubmed.ncbi.nlm.nih.gov/30080919

O'Connor, M. K. (2015). Targeting the DNA damage response in cancer. *Molecular Cell*, *60*(4), 547–560. https://doi.org/10.1016/j.molcel.2015.10.040

Olive, P. L., & Banáth, J. P. (2006). The comet assay: a method to measure DNA damage in individual cells. *Nature Protocols*, *1*(1), 23–29. https://doi.org/10.1038/nprot.2006.5

O'Neil, N. J., Bailey, M. L., & Hieter, P. (2017). Synthetic lethality and cancer. *Nature Reviews Genetics*, *18*(10), 613–623. https://doi.org/10.1038/nrg.2017.47

Ooka, M., Abe, T., Cho, K., Koike, K., Takeda, S., & Hirota, K. (2018). Chromatin remodeler ALC1 prevents replication-fork collapse by slowing fork progression. *PLOS ONE*, *13*(2), e0192421. https://doi.org/10.1371/journal.pone.0192421

Palagyi, A., Neveling, K., Plinninger, U., Ziesch, A., Targosz, B. S., Denk, G., Ochs, S., Rizzani, A., Meier, D. T., Thasler, W. E., Hanenberg, H., De Toni, E. N., Bassermann, F., Schäfer, C., Göke, B., Schindler, D., & Gallmeier, E. (2010). Genetic inactivation of the Fanconi anemia gene FANCC identified in the hepatocellular carcinoma cell line HuH-7 confers sensitivity towards DNA-interstrand crosslinking agents. *Molecular Cancer*, *9*(1). https://doi.org/10.1186/1476-4598-9-127

Palom, Y., Kumar, G. S., Tang, L.-Q., Paz, M. M., Musser, S. M., Rockwell, S., & Tomasz, M. (2002). Relative Toxicities of DNA Cross-Links and Monoadducts: New Insights from Studies of Decarbamoyl Mitomycin C and Mitomycin C. *Chemical Research in Toxicology*, *15*(11), 1398–1406. https://doi.org/10.1021/tx020044g

Papież, M., & Krzyściak, W. (2021). Biological Therapies in the Treatment of Cancer—Update and new directions. *International Journal of Molecular Sciences*, *22*(21), 11694. https://doi.org/10.3390/ijms222111694

Paviolo, N. S., De La Vega, M. B., Pansa, M. F., García, I. A., Calzetta, N. L., Soria, G., & Gottifredi, V. (2020). Persistent double strand break accumulation does not precede cell death in an Olaparib-sensitive BRCA-deficient colorectal cancer cell model. *Genetics and Molecular Biology*, *43*(1 suppl 1). https://doi.org/10.1590/1678-4685-gmb-2019-0070

Pedrioli, D. M. L., Leutert, M., Bilan, V., Nowak, K., Gunasekera, K., Ferrari, E., Imhof, R., Malmström, L., & Hottiger, M. O. (2018). Comprehensive ADP-ribosylome analysis identifies tyrosine as an ADP-ribose acceptor site. *EMBO Reports*, *19*(8). https://doi.org/10.15252/embr.201745310

Peng, G., Lin, C. C. J., Mo, W., Dai, H., Park, Y.-Y., Kim, S., Peng, Y., Mo, Q., Siwko, S., Hu, R., Lee, J., Hennessy, B. T., Hanash, S. M., Mills, G. B., & Lin, S. Y. (2014). Genome-wide transcriptome profiling of homologous recombination DNA repair. *Nature Communications*, *5*(1). https://doi.org/10.1038/ncomms4361

Peng, H., Zhang, S., Peng, Y., Zhu, S., Zhao, X., Zhao, X., Yang, S., Liu, G., Dong, Y., Gan, X., Li, Q., Zhang, X., Pei, H., & Chen, X. (2021). Yeast Bromodomain Factor 1 and Its Human Homolog TAF1 Play Conserved Roles in Promoting Homologous Recombination. *Advanced Science*, *8*(15). https://doi.org/10.1002/advs.202100753

Peng, H.-Y., Zhang, S., Peng, Y.-H., Zhu, S., Zhao, X., Zhao, X.-C., Yang, S., Liu, G.-X., Dong, Y., Gan, X., Li, Q. X., Zhang, X., Pei, H., & Chen, X. (2021). Yeast Bromodomain Factor 1 and its human homolog TAF1 play conserved roles in promoting homologous recombination. *Advanced Science*, *8*(15), 2100753. https://doi.org/10.1002/advs.202100753

Pérez-Salvia, M., & Esteller, M. (2016). Bromodomain inhibitors and cancer therapy: From structures to applications. *Epigenetics*, *12*(5), 323–339. https://doi.org/10.1080/15592294.2016.1265710

Peters, G. J., Van Triest, B., Backus, H. H. J., Kuiper, C. M., Van Der Wilt, C. L., & Pinedo, H. M. (2000). Molecular downstream events and induction of thymidylate synthase in mutant and wild-type p53 colon cancer cell lines after treatment with 5-fluorouracil and the thymidylate synthase inhibitor raltitrexed. *European Journal of Cancer*, *36*(7), 916–924. https://doi.org/10.1016/s0959-8049(00)00026-5

Pettitt, S. J., Krastev, D. B., Brandsma, I., Dréan, A., Song, F., Aleksandrov, R., Harrell, M. I., Menon, M., Brough, R., Campbell, J., Frankum, J., Ranes, M., Pemberton, H., Rafiq, R., Fenwick, K., Swain, A., Guettler, S., Lee, J. P., Swisher, E. M., … Lord, C. J. (2018). Genome-wide and high-density CRISPR-Cas9 screens identify point mutations in PARP1 causing PARP inhibitor resistance. *Nature Communications*, *9*(1). https://doi.org/10.1038/s41467-018-03917-2

Pettitt, S. J., Rehman, F. L., Bajrami, I., Brough, R., Wallberg, F., Kozarewa, I., Fenwick, K., Assiotis, I., Chen, L., Campbell, J., Lord, C. J., & Ashworth, A. (2013). A genetic screen using the Piggybac transposon in haploid cells identifies

PARP1 as a mediator of olaparib toxicity. *PLOS ONE*, *8*(4), e61520. https://doi.org/10.1371/journal.pone.0061520

Pilié, P. G., Tang, C., Mills, G. B., & Yap, T. A. (2018). State-of-the-art strategies for targeting the DNA damage response in cancer. *Nature Reviews Clinical Oncology*, *16*(2), 81–104. https://doi.org/10.1038/s41571-018-0114-z

Pommier, Y., Huang, S.-Y. N., Gao, R., Das, B. B., Murai, J., & Marchand, C. (2014). Tyrosyl-DNA-phosphodiesterases (TDP1 and TDP2). *DNA Repair*, *19*, 114–129. https://doi.org/10.1016/j.dnarep.2014.03.020

Pommier, Y., O'Connor, M. J., & De Bono, J. S. (2016). Laying a trap to kill cancer cells: PARP inhibitors and their mechanisms of action. *Science Translational Medicine*, *8*(362). https://doi.org/10.1126/scitranslmed.aaf9246

Popova, T., Manié, E., Rieunier, G., Caux-Moncoutier, V., Tirapo, C., Dubois, T., Delattre, O., Sigal-Zafrani, B., Bollet, M. A., Longy, M., Houdayer, C., Sastre-Garau, X., Vincent-Salomon, A., Stoppa-Lyonnet, D., & Stern, M.-H. (2012). Ploidy and Large-Scale Genomic Instability Consistently Identify Basal-like Breast Carcinomas with *BRCA1/2* Inactivation. *Cancer Research*, *72*(21), 5454–5462. https://doi.org/10.1158/0008-5472.can-12-1470

Porcelli, L., Quatrale, A. E., Mantuano, P., Leo, M. G., Silvestris, N., Rolland, J.-F., Carioggia, E., Lioce, M., Paradiso, A., & Azzariti, A. (2012). Optimize radiochemotherapy in pancreatic cancer: PARP inhibitors a new therapeutic opportunity. *Molecular Oncology*, *7*(3), 308–322. https://doi.org/10.1016/j.molonc.2012.10.002

Póti, Á., Berta, K., Xiao, Y., Pipek, O., Klus, G. T., Ried, T., Csabai, I., Wilcoxen, K., Mikule, K., Szallasi, Z., & Szüts, D. (2018). Long-term treatment with the PARP inhibitor niraparib does not increase the mutation load in cell line models and tumour xenografts. *British Journal of Cancer*, *119*(11), 1392–1400. https://doi.org/10.1038/s41416-018-0312-6

Pozarowski, P., & Darzynkiewicz, Z. (2004). Analysis of cell cycle by flow cytometry. In *Humana Press eBooks*. https://doi.org/10.1385/1-59259-811-0:301

Prigaro, B. J., Esquer, H., Zhou, Q., Pike, L. A., Awolade, P., Lai, X.-H., Abraham, A. D., Abbott, J. M., Matter, B., Kompella, U. B., Messersmith, W. A., Gustafson, D. L., & LaBarbera, D. V. (2022). Design, synthesis, and biological evaluation of the first inhibitors of oncogenic CHD1L. *Journal of Medicinal Chemistry*, *65*(5), 3943–3961. https://doi.org/10.1021/acs.jmedchem.1c01778

Priya, B., Ravi, S., & Kirubakaran, S. (2023). Targeting ATM and ATR for cancer therapeutics: inhibitors in clinic. *Drug Discovery Today*, *28*(8), 103662. https://doi.org/10.1016/j.drudis.2023.103662

Pujade-Lauraine, E., Selle, F., Scambia, G., Asselain, B., Marmé, F., Lindemann, K., Colombo, N., Madry, R., Glasspool, R. M., Dubot, C., Oaknin, A., Zamagni, C., Heitz, F., Gladieff, L., Rubio-Pérez, M. J., Scollo, P., Blakeley, C., Shaw, B., Ray-Coquard, I. L., & Redondo, A. (2021). LBA33 Maintenance olaparib rechallenge in patients (pts) with ovarian carcinoma (OC) previously treated with a PARP inhibitor (PARPi): Phase IIIb OReO/ENGOT Ov-38 trial. *Annals of Oncology*, *32*, S1308–S1309. https://doi.org/10.1016/j.annonc.2021.08.2110

Rack, J. G. M., Palazzo, L., & Ahel, I. (2020). (ADP-ribosyl)hydrolases: structure, function, and biology. *Genes & Development*, *34*(5–6), 263–284. https://doi.org/10.1101/gad.334631.119

Re, G., & Af, D. (1993). Paclitaxel: A New Antineoplastic Agent for Refractory Ovarian Cancer. *American Journal of Health-System Pharmacy*. https://doi.org/10.1093/ajhp/50.7.1491

Reber, J. M., Božić-Petković, J., Lippmann, M., Mazzardo, M., Dilger, A., Warmers, R., Bürkle, A., & Mangerich, A. (2022). PARP1 and XRCC1 exhibit a reciprocal relationship in genotoxic stress response. *Cell Biology and Toxicology*, *39*(1), 345–364. https://doi.org/10.1007/s10565-022-09739-9

Robert, I., Dantzer, F., & Reina-San-Martin, B. (2009). Parp1 facilitates alternative NHEJ, whereas Parp2 suppresses IgH/c-myc translocations during

immunoglobulin class switch recombination. *Journal of Experimental Medicine*, *206*(5), 1047–1056. https://doi.org/10.1084/jem.20082468

Rondinelli, B., Gogola, E., Yücel, H., Duarte, A. A., Van De Ven, M., Van Der Sluijs, R., Konstantinopoulos, P. A., Jonkers, J., Ceccaldi, R., Rottenberg, S., & D'Andrea, A. D. (2017). EZH2 promotes degradation of stalled replication forks by recruiting MUS81 through histone H3 trimethylation. Nature Cell Biology, 19(11), 1371–1378. https://doi.org/10.1038/ncb3626

Rottenberg, S., Nygren, A., Timpson, P., Van Leeuwen, F. W. B., Van Der Heijden, I., Van De Wetering, K., Liu, X., De Visser, K. E., Gilhuijs, K. G. A., Van Tellingen, O., Schouten, J. S. A. G., Jonkers, J., & Borst, P. (2007). Selective induction of chemotherapy resistance of mammary tumors in a conditional mouse model for hereditary breast cancer. *Proceedings of the National Academy of Sciences of the United States of America*, *104*(29), 12117–12122. https://doi.org/10.1073/pnas.0702955104

Rouleau, M., Patel, A. G., Hendzel, M. J., Kaufmann, S. H., & Poirier, G. G. (2010). PARP inhibition: PARP1 and beyond. *Nature Reviews Cancer*, *10*(4), 293–301. https://doi.org/10.1038/nrc2812

Ruscetti, T., Lehnert, B. E., Halbrook, J., Trong, H. Le, Hoekstra, M. F., Chen, D. J., & Peterson, S. (1998). Stimulation of the DNA-dependent protein kinase by Poly(ADP-Ribose) polymerase. *Journal of Biological Chemistry*, *273*(23), 14461–14467. https://doi.org/10.1074/jbc.273.23.14461

Sahiri, K., Blessing, C., Schomburg, A., & Ladurner, A. (2022). *Method to evaluate the capability of compounds on the trapping of proteins* (Issue PCT/EP2021/084088). https://patentscope.wipo.int/search/de/detail.jsf?docId=WO2022117781&_cid=P11-LM977Z-71903-1

Saxena, S., & Zou, L. (2022). Hallmarks of DNA replication stress. Molecular Cell, 82(12), 2298–2314. https://doi.org/10.1016/j.molcel.2022.05.004

Schiewer, M. J., & Knudsen, K. E. (2014). Transcriptional roles of PARP1 in cancer. *Molecular Cancer Research*, *12*(8), 1069–1080. https://doi.org/10.1158/1541-7786.mcr-13-0672

Schiff, P. B., & Horwitz, S. B. (1980). Taxol stabilizes microtubules in mouse fibroblast cells. *Proceedings of the National Academy of Sciences of the United States of America*, *77*(3), 1561–1565. https://doi.org/10.1073/pnas.77.3.1561

Schlacher, K. (2017). PARPi focus the spotlight on replication fork protection in cancer. Nature Cell Biology, 19(11), 1309–1310. https://doi.org/10.1038/ncb3638

Schlacher, K., Christ, N., Siaud, N., Egashira, A., Wu, H. G., & Jasin, M. (2011). Double-Strand Break Repair-Independent role for BRCA2 in blocking stalled replication fork degradation by MRE11. *Cell*, *145*(4), 529–542. https://doi.org/10.1016/j.cell.2011.03.041

Schultz, N., López, E., Saleh-Gohari, N., & Helleday, T. (2003). Poly(ADP-ribose) polymerase (PARP-1) has a controlling role in homologous recombination. *Nucleic Acids Research*, *31*(17), 4959–4964. https://doi.org/10.1093/nar/gkg703

Scientific image and illustration software | BioRender. (n.d.). https://www.biorender.com/

Scully, R., Panday, A., Elango, R., & Willis, N. A. (2019). DNA double-strand break repair-pathway choice in somatic mammalian cells. *Nature Reviews Molecular Cell Biology*, *20*(11), 698–714. https://doi.org/10.1038/s41580-019-0152-0

Scully, R., & Xie, A. (2013). Double strand break repair functions of histone H2AX. *Mutation Research: Fundamental And Molecular Mechanisms Of Mutagenesis*, *750*(1–2), 5–14. https://doi.org/10.1016/j.mrfmmm.2013.07.007

Sefer, A., Kallis, E., Eilert, T., Röcker, C., Kolesnikova, O., Neuhaus, D., Eustermann, S., & Michaelis, J. (2022). Structural dynamics of DNA strand break sensing by PARP-1 at a single-molecule level. Nature Communications, 13(1). https://doi.org/10.1038/s41467-022-34148-1

Sellou, H., Lebeaupin, T., Chapuis, C., Smith, R. K., Hegele, A., Singh, H., Kozlowski, M., Bultmann, S., Ladurner, A. G., Timinszky, G., & Huet, S. (2016). The

poly(ADP-ribose)-dependent chromatin remodeler Alc1 induces local chromatin relaxation upon DNA damage. *Molecular Biology of the Cell*, *27*(24), 3791–3799. https://doi.org/10.1091/mbc.e16-05-0269

Thesgc.Org/Chemical-Probes. (2022). BAY-299. *Https://Www.Thesgc.Org/Chemical-Probes/BAY-299*.

Shah, M. A., & Schwartz, G. E. (2001). Cell cycle-mediated drug resistance: an emerging concept in cancer therapy. *PubMed*, *7*(8), 2168–2181. https://pubmed.ncbi.nlm.nih.gov/11489790

Shen, Y., Aoyagi-Scharber, M., & Gao, B. (2015). Trapping Poly(ADP-Ribose) polymerase. *Journal of Pharmacology and Experimental Therapeutics*, *353*(3), 446–457. https://doi.org/10.1124/jpet.114.222448

Shenoy, T., Boysen, G., Wang, M. Y., Xu, Q., Guo, W., Koh, F. M., Wang, C., Zhang, L. Z., Wang, Y., Gil, V., Aziz, S., Christova, R., Rodrigues, D. N., Crespo, M., Rescigno, P., Tunariu, N., Riisnaes, R., Zafeiriou, Z., Flohr, P., … Wu, H. (2017). CHD1 loss sensitizes prostate cancer to DNA damaging therapy by promoting error-prone double-strand break repair. *Annals of Oncology*, *28*(7), 1495–1507. https://doi.org/10.1093/annonc/mdx165

Sidorov, P., Naulaerts, S., Ariey-Bonnet, J., Pasquier, E., & Ballester, P. J. (2019). Predicting synergism of cancer drug combinations using NCI-ALMANAC data. *Frontiers in Chemistry*, *7*. https://doi.org/10.3389/fchem.2019.00509

Sim, H.-W., McDonald, K. L., Lwin, Z., Barnes, E. H., Rosenthal, M., Foote, M., Koh, E.-S., Back, M., Wheeler, H., Sulman, E. P., Buckland, M. E., Fisher, L., Leonard, R., Hall, M., Ashley, D. M., Yip, S., Simes, J., & Khasraw, M. (2021). A randomized phase II trial of veliparib, radiotherapy, and temozolomide in patients with unmethylated*MGMT*glioblastoma: the VERTU study. *Neuro-Oncology*, *23*(10), 1736–1749. https://doi.org/10.1093/neuonc/noab111

Singh, H., Nardozza, A. P., Möller, I. R., Knobloch, G., Kistemaker, H. A. V, Hassler, M., Harrer, N., Blessing, C., Eustermann, S., Kotthoff, C., Huet, S., Mueller-Planitz, F., Filippov, D. V, Timinszky, G., Rand, K. D., & Ladurner, A. G. (2017). A Poly-ADP-Ribose trigger releases the Auto-Inhibition of a chromatin remodeling oncogene. *Molecular Cell*, *68*(5), 860–871.e7. https://doi.org/10.1016/j.molcel.2017.11.019

Smeby, J., Kryeziu, K., Berg, K. C. G., Eilertsen, I. A., Eide, P. A. W., Johannessen, B., Guren, M. G., Nesbakken, A., Bruun, J., Lothe, R., & Sveen, A. (2020). Molecular correlates of sensitivity to PARP inhibition beyond homologous recombination deficiency in pre-clinical models of colorectal cancer point to wild-type TP53 activity. *EBioMedicine*, *59*, 102923. https://doi.org/10.1016/j.ebiom.2020.102923

Spagnolo, L., Barbeau, J., Curtin, N. J., Morris, E. P., & Pearl, L. H. (2012). Visualization of a DNA-PK/PARP1 complex. *Nucleic Acids Research*, *40*(9), 4168–4177. https://doi.org/10.1093/nar/gkr1231

Spies, J., Polasek-Sedlackova, H., Lukas, J., & Somyajit, K. (2021). Homologous Recombination as a Fundamental Genome Surveillance Mechanism during DNA Replication. *Genes*, *12*(12), 1960. https://doi.org/10.3390/genes12121960

Steinbach, D., & Legrand, O. (2007). ABC transporters and drug resistance in leukemia: was P-gp nothing but the first head of the Hydra? *Leukemia*, *21*(6), 1172–1176. https://doi.org/10.1038/sj.leu.2404692

Stewart, M. G., Vega, D. E., Arend, R. C., Baden, J. F., Barbash, O., Beaubier, N., Collins, G., French, T., Ghahramani, N., Hinson, P., Jelinic, P., Marton, M. J., McGregor, K., Parsons, J., Ramamurthy, L., Sausen, M., Sokol, E., Stenzinger, A., Stires, H., … Allen, J. (2022). Homologous Recombination Deficiency: Concepts, Definitions, and Assays. *The Oncologist*, *27*(3), 167–174. https://doi.org/10.1093/oncolo/oyab053

Sung, P., & Klein, H. L. (2006). Mechanism of homologous recombination: mediators and helicases take on regulatory functions. *Nature Reviews Molecular Cell Biology*, *7*(10), 739–750. https://doi.org/10.1038/nrm2008

SynergyFinder - documentation. (n.d.). https://synergyfinder.fimm.fi/synergy/synfin_docs/

Taglialatela, A., Alvarez, S., Leuzzi, G., Sannino, V., Ranjha, L., Huang, J.-W., Madubata, C. J., Anand, R., Levy, B., Rabadan, R., Cejka, P., Costanzo, V., & Ciccia, A. (2017). Restoration of Replication Fork Stability in BRCA1- and BRCA2-Deficient Cells by Inactivation of SNF2-Family Fork Remodelers. *Molecular Cell*, *68*(2), 414–430.e8. https://doi.org/10.1016/j.molcel.2017.09.036

Tan, J., Zheng, X., Li, M., Ye, F., Song, C., Xu, C., Zhang, X., Li, W., Wang, Y., Zeng, S., Li, H., Chen, G., Huang, X., Ma, D., Liu, D., & Gao, Q. (2021). C/EBPβ promotes poly(ADP-ribose) polymerase inhibitor resistance by enhancing homologous recombination repair in high-grade serous ovarian cancer. Oncogene, 40(22), 3845–3858. https://doi.org/10.1038/s41388-021-01788-4

Tang, H., & Poon, R. Y. C. (2011). How protein kinases co-ordinate mitosis in animal cells. *Biochemical Journal*, *435*(1), 17–31. https://doi.org/10.1042/bj20100284

Tang, J., Wennerberg, K., & Aittokallio, T. (2015). What is synergy? The Saariselkä agreement revisited. *Frontiers in Pharmacology*, *6*. https://doi.org/10.3389/fphar.2015.00181

Tarsounas, M., Davies, D., & West, S. C. (2003). BRCA2-dependent and independent formation of RAD51 nuclear foci. *Oncogene*, *22*(8), 1115–1123. https://doi.org/10.1038/sj.onc.1206263

Tashiro, S., Kotomura, N., Shinohara, A., Tanaka, K., Ueda, K., & Kamada, N. (1996). S phase specific formation of the human Rad51 protein nuclear foci in lymphocytes. *PubMed*, *12*(10), 2165–2170. https://pubmed.ncbi.nlm.nih.gov/8668342

Teloni, F., & Altmeyer, M. (2016). Readers of poly(ADP-ribose): designed to be fit for purpose. *Nucleic Acids Research*, *44*(3), 993–1006. https://doi.org/10.1093/nar/gkv1383

Teus, M. A., De Benito-Llopis, L., & Alió, J. L. (2009). Mitomycin C in corneal refractive surgery. *Survey of Ophthalmology*, *54*(4), 487–502. https://doi.org/10.1016/j.survophthal.2009.04.002

Thaker, P. H., Salani, R., Brady, W. E., Lankes, H. A., Cohn, D. E., Mutch, D. G., Mannel, R. S., Bell-McGuinn, K. M., Di Silvestro, P. A., Jelovac, D., Carter, J. S., Duan, W., Resnick, K. E., Dizon, D. S., Aghajanian, C., & Fracasso, P. M. (2017). A phase I trial of paclitaxel, cisplatin, and veliparib in the treatment of persistent or recurrent carcinoma of the cervix: an NRG Oncology Study (NCT#01281852). *Annals of Oncology*, *28*(3), 505–511. https://doi.org/10.1093/annonc/mdw635

Thevenaz, P., Ruttimann, U. E., & Unser, M. (1998). A pyramid approach to subpixel registration based on intensity. *IEEE Transactions on Image Processing*, *7*(1), 27–41. https://doi.org/10.1109/83.650848

Tian, X., Chen, L., Gai, D., He, S., Jiang, X., & Zhang, N. (2022). Adverse Event Profiles of PARP Inhibitors: Analysis of Spontaneous Reports Submitted to FAERS. *Frontiers in Pharmacology*, *13*. https://doi.org/10.3389/fphar.2022.851246

Timinszky, G., Till, S., Hassa, P. O., Hothorn, L. A., Kustatscher, G., Nijmeijer, B., Colombelli, J., Altmeyer, M., Stelzer, E. H. K., Scheffzek, K., Hottiger, M. O., & Ladurner, A. G. (2009). A macrodomain-containing histone rearranges chromatin upon sensing PARP1 activation. *Nature Structural & Molecular Biology*, *16*(9), 923–929. https://doi.org/10.1038/nsmb.1664

Toh, M.-R., & Ngeow, J. (2021). Homologous Recombination deficiency: cancer predispositions and treatment implications. *Oncologist*, *26*(9), e1526–e1537. https://doi.org/10.1002/onco.13829

Tomasz, M. (1995). Mitomycin C: small, fast and deadly (but very selective). *Chemistry & Biology*, *2*(9), 575–579. https://doi.org/10.1016/1074-5521(95)90120-5

Tomasz, M., & Palom, Y. (1997). The mitomycin bioreductive antitumor agents: Cross-linking and alkylation of DNA as the molecular basis of their activity. *Pharmacology & Therapeutics*, *76*(1–3), 73–87. https://doi.org/10.1016/s0163-7258(97)00088-0

Topatana, W., Juengpanich, S., Li, S., Cao, J., Hu, J., Lee, J.-Y., Suliyanto, K., Ma, D., Zhang, B., Chen, M., & Cai, X. (2020). Advances in synthetic lethality for cancer therapy: cellular mechanism and clinical translation. *Journal of Hematology & Oncology*, *13*(1). https://doi.org/10.1186/s13045-020-00956-5

Tsuda, M., Cho, K., Ooka, M., Shimizu, N., Watanabe, R., Yasui, A., Nakazawa, Y., Ogi, T., Harada, H., Agama, K., Nakamura, J., Asada, R., Fujiike, H., Sakuma, T., Yamamoto, T., Murai, J., Hiraoka, M., Koike, K., Pommier, Y., … Hirota, K. (2017). ALC1/CHD1L, a chromatin-remodeling enzyme, is required for efficient base excision repair. *PLOS ONE*, *12*(11), e0188320. https://doi.org/10.1371/journal.pone.0188320

Tubbs, A., & Nussenzweig, A. (2017). Endogenous DNA damage as a source of genomic instability in cancer. *Cell*, *168*(4), 644–656. https://doi.org/10.1016/j.cell.2017.01.002

Verma, P., Zhou, Y., Cao, Z.-D., Deraska, P., Deb, M., Arai, E., Li, W., Shao, Y., Puentes, L. N., Li, Y., Patankar, S., Mach, R. H., Faryabi, R. B., Shi, J., & Greenberg, R. A. (2021). ALC1 links chromatin accessibility to PARP inhibitor response in homologous recombination-deficient cells. *Nature Cell Biology*, *23*(2), 160–171. https://doi.org/10.1038/s41556-020-00624-3

Vichai, V., & Kirtikara, K. (2006). Sulforhodamine B colorimetric assay for cytotoxicity screening. *Nature Protocols*, *1*(3), 1112–1116. https://doi.org/10.1038/nprot.2006.179

Vlot, A. H. C., Aniceto, N., Menden, M. P., Ulrich-Merzenich, G., & Bender, A. (2019). Applying synergy metrics to combination screening data: agreements, disagreements and pitfalls. *Drug Discovery Today*, *24*(12), 2286–2298. https://doi.org/10.1016/j.drudis.2019.09.002

Wang, M., Wu, W.-Z., Wu, W., Rosidi, B., Zhang, L., Wang, H., & Iliakis, G. (2006). PARP-1 and Ku compete for repair of DNA double strand breaks by distinct NHEJ pathways. *Nucleic Acids Research*, *34*(21), 6170–6182. https://doi.org/10.1093/nar/gkl840

Wang, Y., Sun, C., Mao, A., Zhang, X., Zhou, X., Wang, Z., & Zhang, H. (2015). Radiosensitization to X-ray radiation by telomerase inhibitor MST-312 in human hepatoma HepG2 cells. *Life Sciences*, *123*, 43–50. https://doi.org/10.1016/j.lfs.2014.12.027

Wassing, I. E., & Esashi, F. (2021). RAD51: Beyond the break. *Seminars in Cell & Developmental Biology*, *113*, 38–46. https://doi.org/10.1016/j.semcdb.2020.08.010

Wesierska-Gadek, J., & Heinzl, S. (2014). Interactions between ataxia telangiectasia mutated kinase inhibition, Poly(ADP-ribose) polymerase-1 inhibition and BRCA1 status in breast cancer cells. *Journal of Cancer Prevention*, *19*(2), 125–136. https://doi.org/10.15430/jcp.2014.19.2.125

Wilkerson, P. M., Dedes, K. J., Samartzis, E. P., Dedes, I., Lambros, M. B. K., Natrajan, R., Gauthier, A., Piscuoglio, S., Töpfer, C., Vukovic, Daley, F., Weigelt, B., & Reis-Filho, J. S. (2016). Preclinical evaluation of the PARP inhibitor BMN-673 for the treatment of ovarian clear cell cancer. *Oncotarget*, *8*(4), 6057–6066. https://doi.org/10.18632/oncotarget.14011

William Menzer, Gunnar Knobloch, Corinna Lieleg, Adrian Schomburg, Andreas Ladurner, & Peter Sennhenn. (2022). ALC1 inhibitors and synergy with PARPi. *Https://Patentscope.Wipo.Int/Search/de/Detail.Jsf?DocId=WO2022117782&_cid=P11-LP5JJO-42042-1*, *PCT/EP2021/084089*.

Williamson, C. T., Muzik, H., Turhan, A. G., Zamò, A., O'Connor, M. J., Bebb, D. G., & Lees-Miller, S. P. (2010). ATM deficiency sensitizes mantle cell lymphoma cells to Poly(ADP-Ribose) polymerase-1 inhibitors. *Molecular Cancer Therapeutics*, *9*(2), 347–357. https://doi.org/10.1158/1535-7163.mct-09-0872

Wyatt, D. W., Feng, W., Conlin, M. P., Yousefzadeh, M. J., Roberts, S. A., Mieczkowski, P. A., Wood, R. D., Gupta, G. P., & Ramsden, D. A. (2016). Essential roles for Polymerase Θ-Mediated end joining in the repair of

chromosome breaks. *Molecular Cell*, *63*(4), 662–673. https://doi.org/10.1016/j.molcel.2016.06.020

Wyatt, M. D., & Wilson, D. M. (2008). Participation of DNA repair in the response to 5-fluorouracil. Cellular and Molecular Life Sciences, 66(5), 788–799. https://doi.org/10.1007/s00018-008-8557-5

Xiao, W., Graham, P., Hao, J., Chang, L., Ni, J., Power, C., Dong, Q., Kearsley, J. H., & Li, Y. (2013). Combination Therapy with the Histone Deacetylase Inhibitor LBH589 and Radiation Is an Effective Regimen for Prostate Cancer Cells. *PLOS ONE*, *8*(8), e74253. https://doi.org/10.1371/journal.pone.0074253

Xiong, X., Lai, X., Li, A., Liu, Z., & Ma, N.-F. (2021). Diversity roles of CHD1L in normal cell function and tumorigenesis. *Biomarker Research*, *9*(1). https://doi.org/10.1186/s40364-021-00269-w

Yadav, B., Wennerberg, K., Aittokallio, T., & Tang, J. (2015). Searching for Drug Synergy in Complex Dose–Response Landscapes Using an Interaction Potency Model. *Elsevir*, *13*, 504–513. https://doi.org/10.1016/j.csbj.2015.09.001

Yamamoto, H., & Hirasawa, A. (2021). Homologous recombination deficiencies and hereditary tumors. *International Journal of Molecular Sciences*, *23*(1), 348. https://doi.org/10.3390/ijms23010348

Yang, G., Liu, C., Chen, S.-H., Kassab, M. A., Hoff, J. D., Walter, N. G., & Yu, X. (2018). Super-resolution imaging identifies PARP1 and the Ku complex acting as DNA double-strand break sensors. *Nucleic Acids Research*, *46*(7), 3446–3457. https://doi.org/10.1093/nar/gky088

Yoshikawa, R., Kusunoki, M., Yanagi, H., Noda, M., Furuyama, J.-I., Yamamura, T., & Hashimoto-Tamaoki, T. (2001). Dual antitumor effects of 5-fluorouracil on the cell cycle in colorectal carcinoma cells: a novel target mechanism concept for pharmacokinetic modulating chemotherapy. *PubMed*, *61*(3), 1029–1037. https://pubmed.ncbi.nlm.nih.gov/11221829

You, Z., Shi, L. Z., Zhu, Q., Wu, P., Zhang, Y., Basilio, A. C., Tonnu, N., Verma, I. M., Berns, M. W., & Hunter, T. (2009). CTIP links DNA Double-Strand Break sensing to resection. *Molecular Cell*, *36*(6), 954–969. https://doi.org/10.1016/j.molcel.2009.12.002

Yuan, S.-S. F., Lee, S. C., Chen, G., Song, M., Tomlinson, G. E., & Lee, E. K. (1999). BRCA2 is required for ionizing radiation-induced assembly of Rad51 complex in vivo. *PubMed*, *59*(15), 3547–3551. https://pubmed.ncbi.nlm.nih.gov/10446958

Yum, S., Li, M., & Chen, Z. J. (2020). Old dogs, new trick: classic cancer therapies activate cGAS. *Cell Research*, *30*(8), 639–648. https://doi.org/10.1038/s41422-020-0346-1

Zadorozhny, K., Sannino, V., Beláň, O., Mlčoušková, J., Špírek, M., Costanzo, V., & Krejci, L. (2017). Fanconi-Anemia-Associated Mutations Destabilize RAD51 Filaments and Impair Replication Fork Protection. *Cell Reports*, *21*(2), 333–340. https://doi.org/10.1016/j.celrep.2017.09.062

Zatreanu, D., Robinson, H. M. R., Alkhatib, O., Boursier, M., Finch, H., Geo, L., Grande, D., Grinkevich, V., Heald, R. A., Langdon, S., Majithiya, J. B., McWhirter, C., Martin, N. M. B., Moore, S., Neves, J., Rajendra, E., Ranzani, M., Schaedler, T., Stockley, M. L., … Lord, C. J. (2021). Polθ inhibitors elicit BRCA-gene synthetic lethality and target PARP inhibitor resistance. *Nature Communications*, *12*(1). https://doi.org/10.1038/s41467-021-23463-8

Zhang, H., Gao, H., Gu, Y., John, A., Wei, L., Huang, M., Yu, J., Adeosun, A. A., Weinshilboum, R. M., & Wang, L. (2022). 3D CRISPR screen in prostate cancer cells reveals PARP inhibitor sensitization through TBL1XR1-SMC3 interaction. *Frontiers in Oncology*, *12*. https://doi.org/10.3389/fonc.2022.999302

Zhang, J., Sun, J., Chen, J., Yao, L., Ouyang, T., Li, J., Wang, T., Fan, Z., Fan, T., Lin, B., & Xie, Y. (2016). Comprehensive analysis of BRCA1 and BRCA2 germline mutations in a large cohort of 5931 Chinese women with breast cancer. *Breast Cancer Research and Treatment*, *158*(3), 455–462. https://doi.org/10.1007/s10549-016-3902-0

Zhao, X., Wei, C., Li, J., Xing, P., Li, J., Zheng, S.-J., & Chen, X. (2017). Cell cycle-dependent control of homologous recombination. *Acta Biochimica et Biophysica Sinica*, *49*(8), 655–668. https://doi.org/10.1093/abbs/gmx055

Zhao, Y., Zhou, K., Xia, X., Guo, Y., & Li, T. (2022). Chk1 inhibition-induced BRCAness synergizes with olaparib in p53-deficient cancer cells. *Cell Cycle*, *22*(2), 200–212. https://doi.org/10.1080/15384101.2022.2111769

Zhou, S., Dai, Z., Wang, L., Gao, X., Yang, L., Wang, Z., Wang, Q., & Liu, Z. (2021). MET inhibition enhances PARP inhibitor efficacy in castration-resistant prostate cancer by suppressing the ATM/ATR and PI3K/AKT pathways. *Journal of Cellular and Molecular Medicine*, *25*(24), 11157–11169. https://doi.org/10.1111/jcmm.17037

Zhu, X. L., Chen, L., Huang, B., Li, X., Liu, Y., Hu, X., Jiang, Y.-Z., Shao, Z., & Wang, Z. (2021). Efficacy and mechanism of the combination of PARP and CDK4/6 inhibitors in the treatment of triple-negative breast cancer. *Journal of Experimental & Clinical Cancer Research*, *40*(1). https://doi.org/10.1186/s13046-021-01930-w

Zimmermann, M., Murina, O., Reijns, M. A. M., Agathanggelou, A., Challis, R., Tarnauskaitė, Ž., Muir, M., Fluteau, A., Aregger, M., McEwan, A., Yuan, W., Clarke, M., Lambros, M. B., Paneesha, S., Moss, P., Chandrashekhar, M., Angers, S., Moffat, J., Brunton, V. G., … Durocher, D. (2018). CRISPR screens identify genomic ribonucleotides as a source of PARP-trapping lesions. *Nature*, *559*(7713), 285–289. https://doi.org/10.1038/s41586-018-0291-z

7. Appendix A:

7.1. Supplementary figures

7.1.1. Nuclear Foci formation after irradiation with 1gy

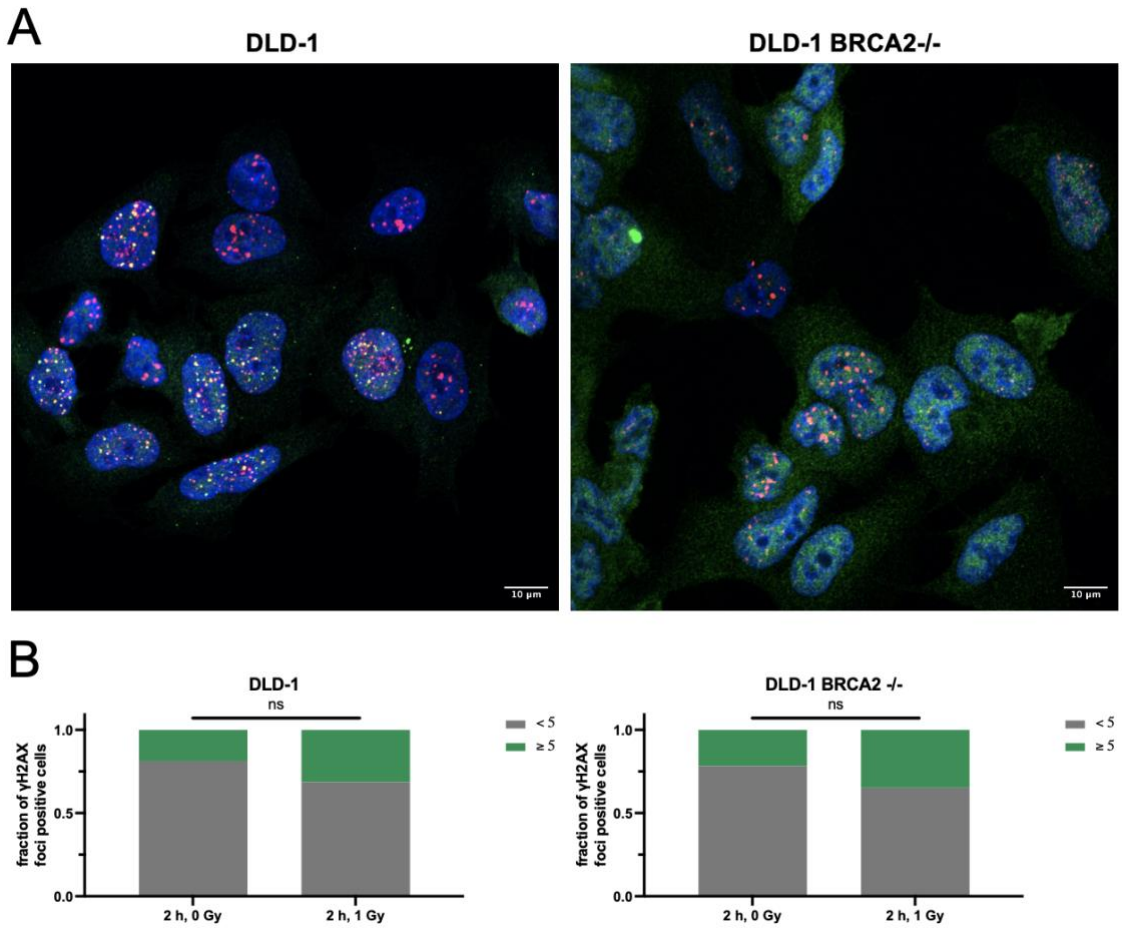

Supplementary Figure 1: Foci formation in DLD-1 and DLD-1 BRCA2-/-

Cells were treated with 1 Gy for 2 h, fixed and stained with primary antibodies anti-γH2AX (Novus) (red), anti-RAD51 (Sigma) (green), secondary antibodies Goat anti-Rabbit IgG Alexa Fluor™ 488 (Invitrogen) and sheep IgG anti-mouse IgG-Cy3 (Dianova), and counterstained with DAPI (blue). A) IF-images represent merged channels of all three colors. High background signal for RAD51 channel in DLD-1 BRCA2-/- is shown in the right image. Fractions of cells with RAD51 foci were calculated using Fiji (ImageJ) and are shown in B).

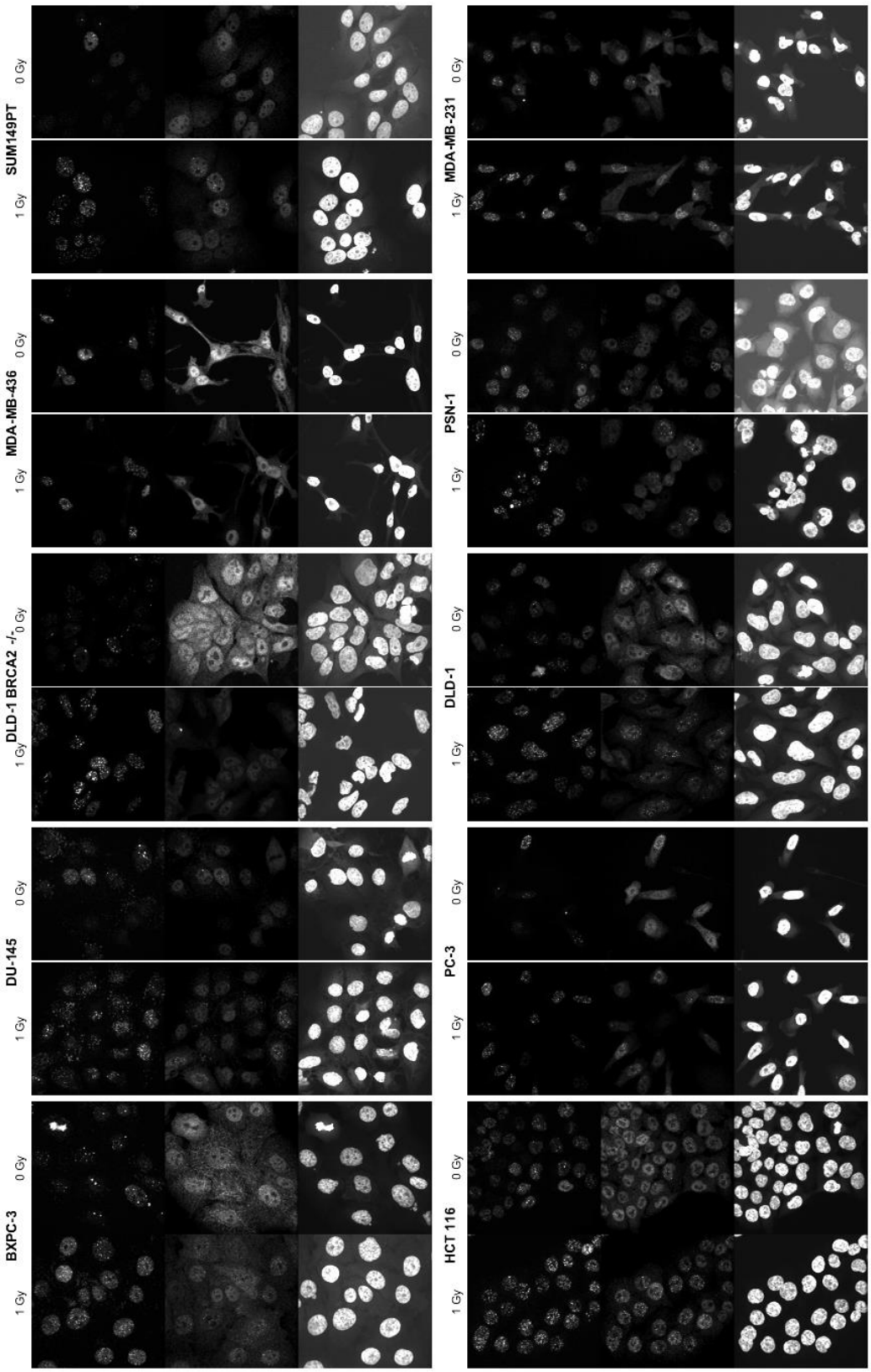

Supplementary Figure 2: Single channel images of foci formation after irradiation
Cells were treated with 1 Gy for 2 h, fixed and stained with anti-γH2AX (left), anti-RAD51 (middle), and counterstained with DAPI (right). Single channel images are shown in greyscale.

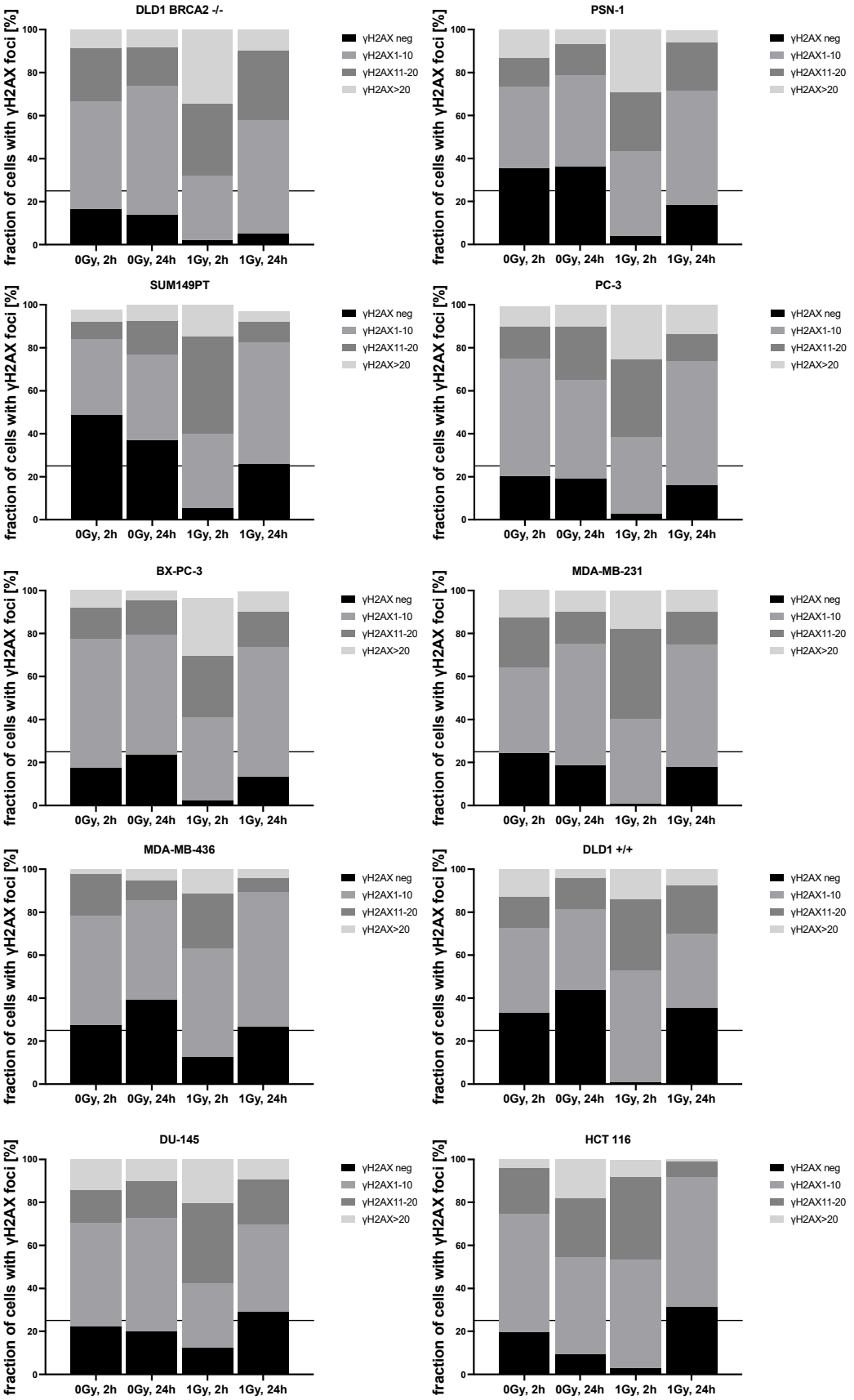
DLD1 BRCA2 -/-
PSN-1
SUM149PT
PC-3
BX-PC-3
MDA-MB-231
MDA-MB-436
DLD1 +/+
DU-145
HCT 116
fraction of cells with γH2AX foci [%]
0
20
40
60
80
100
0Gy, 2h
0Gy, 24h
1Gy, 2h
1Gy, 24h
γH2AX neg
γH2AX1-10
γH2AX11-20
γH2AX>20

Supplementary Figure 3: Spontaneous DNA damage before irradiation and DNA damage 24 h after irradiation.

Cells were treated with 0 Gy or 1 Gy for 2 h and 24 h, fixed and stained with anti-γH2AX (Novus) and sheep IgG anti-mouse IgG-Cy3 (Dianova). Stacked IF-images were analyzed for fractions of γH2AX foci per nuclei. Bar graphs were fitted in GraphPad PRISM for foci-fractions of nuclei with no γH2AX foci (black), 1-10 γH2AX foci (medium grey), 11-20 γH2AX foci (dark grey) and >20 γH2AX foci (light grey). Each Bar represents a timepoint and radiation (0 Gy, 2 h 0 Gy, 24 h; 1 Gy, 2 h; 1 Gy, 24 h). The line at 25 % was set as a limit for the categorization of yH2AX negative cells indicating a low level of DNA damage.

7.1.2. 96h cell survival assay

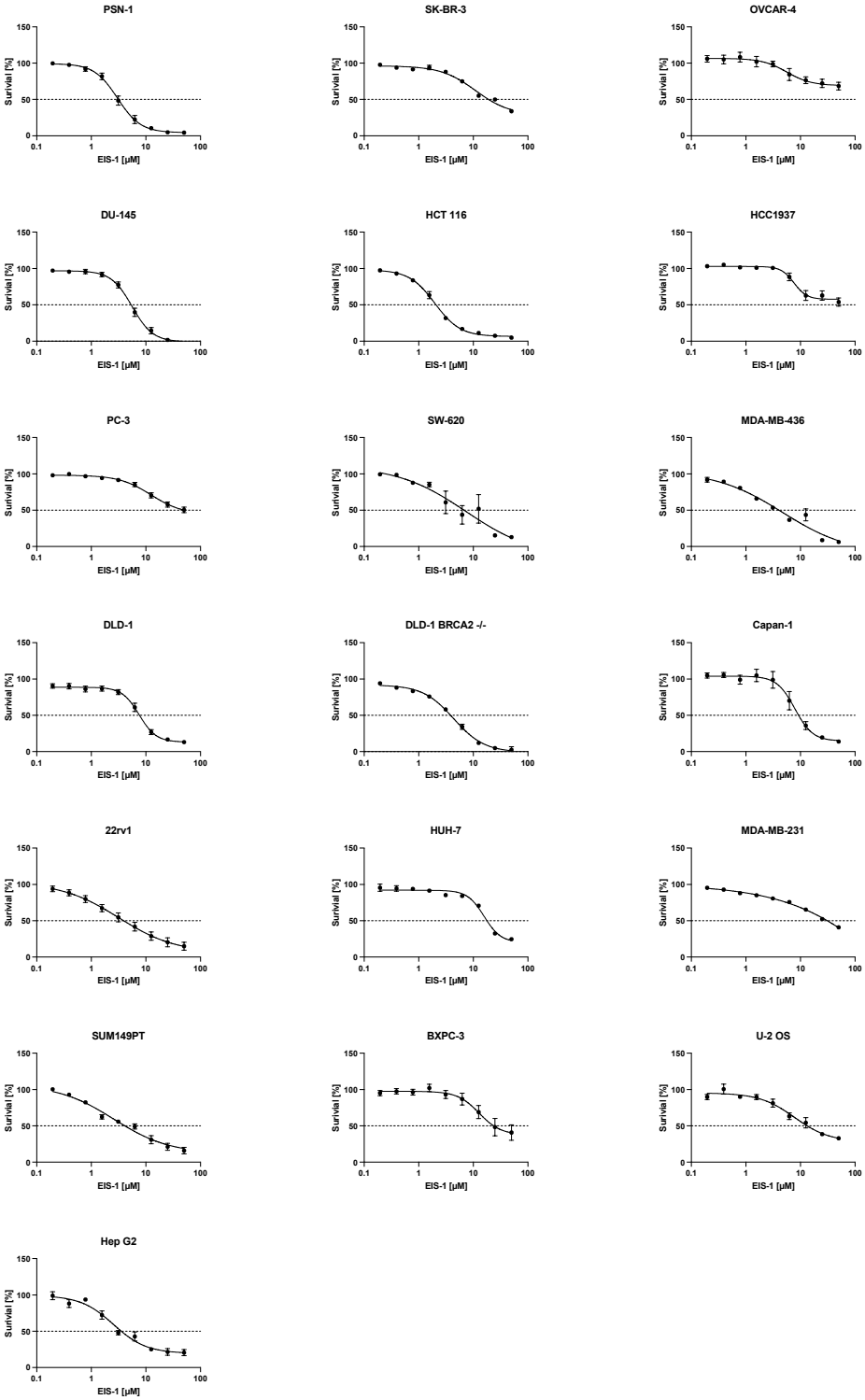

Supplementary Figure 4: 96h cellular survival assay of EIS-1 in the cell-panel
Different cancer cell lines were treated with EIS-1. Cells were cultured for 96h and stained with SRB to analyze cell survival [%]. Survival was normalized to cells treated with vehicle (DMSO) and an “all dead control”. Inhibitor vs. response curves were fitted using GraphPad Prism non-linear regression. Error bars indicate SEM of all replicates. Number of replicates is indicated in Supplementary Table 9.

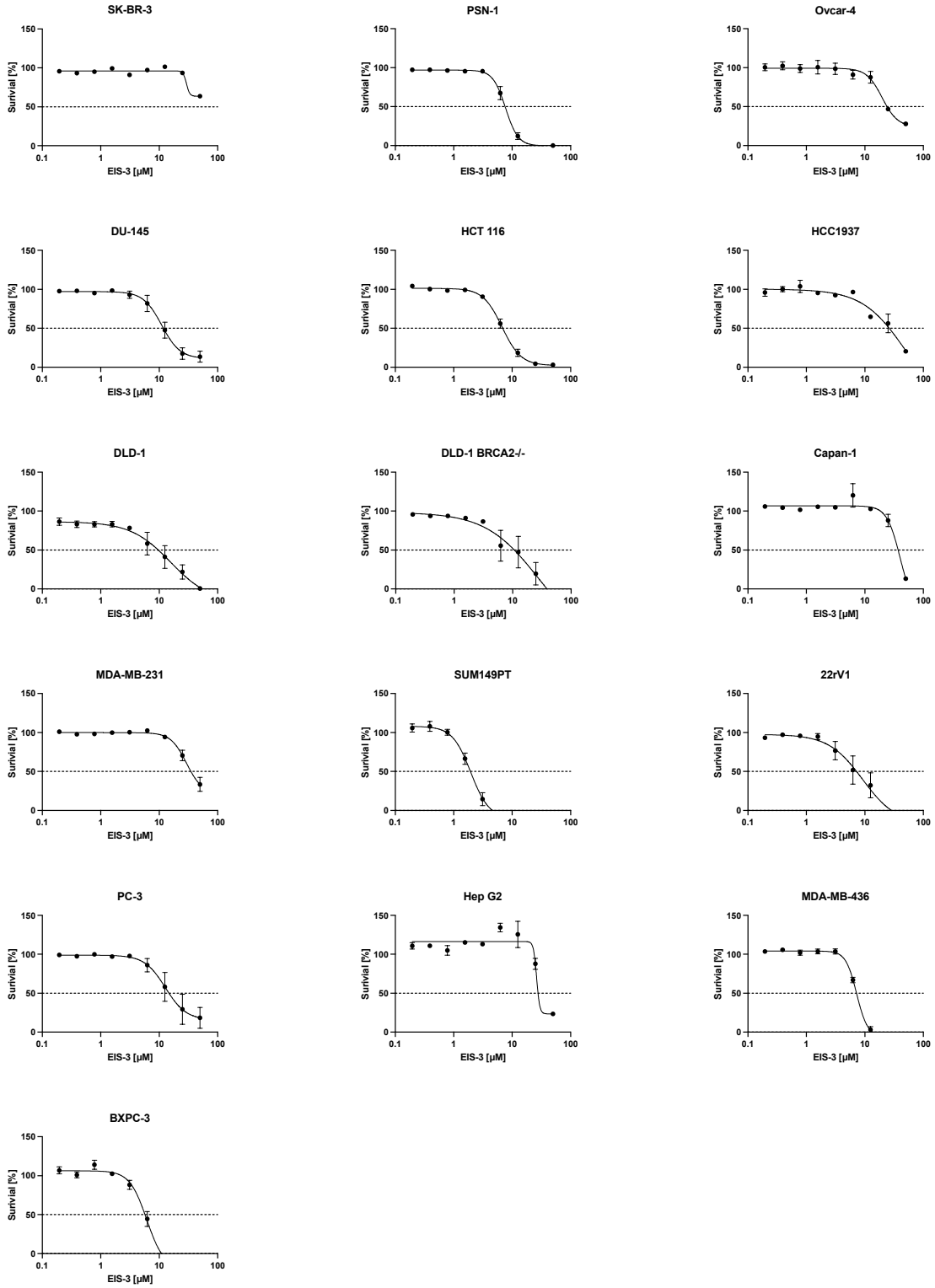

Supplementary Figure 5: 96h cellular survival assay of EIS-3 in the cell-panel

Different cancer cell lines were treated with EIS-3. Cells were cultured for 96h and stained with SRB to analyze cell survival [%]. Survival was normalized to cells treated with vehicle (DMSO) and an “all dead control”. Inhibitor vs. response curves were fitted using GraphPad Prism non-linear regression. Error bars indicate SEM of all replicates. Number of replicates is indicated in Supplementary Table 9.

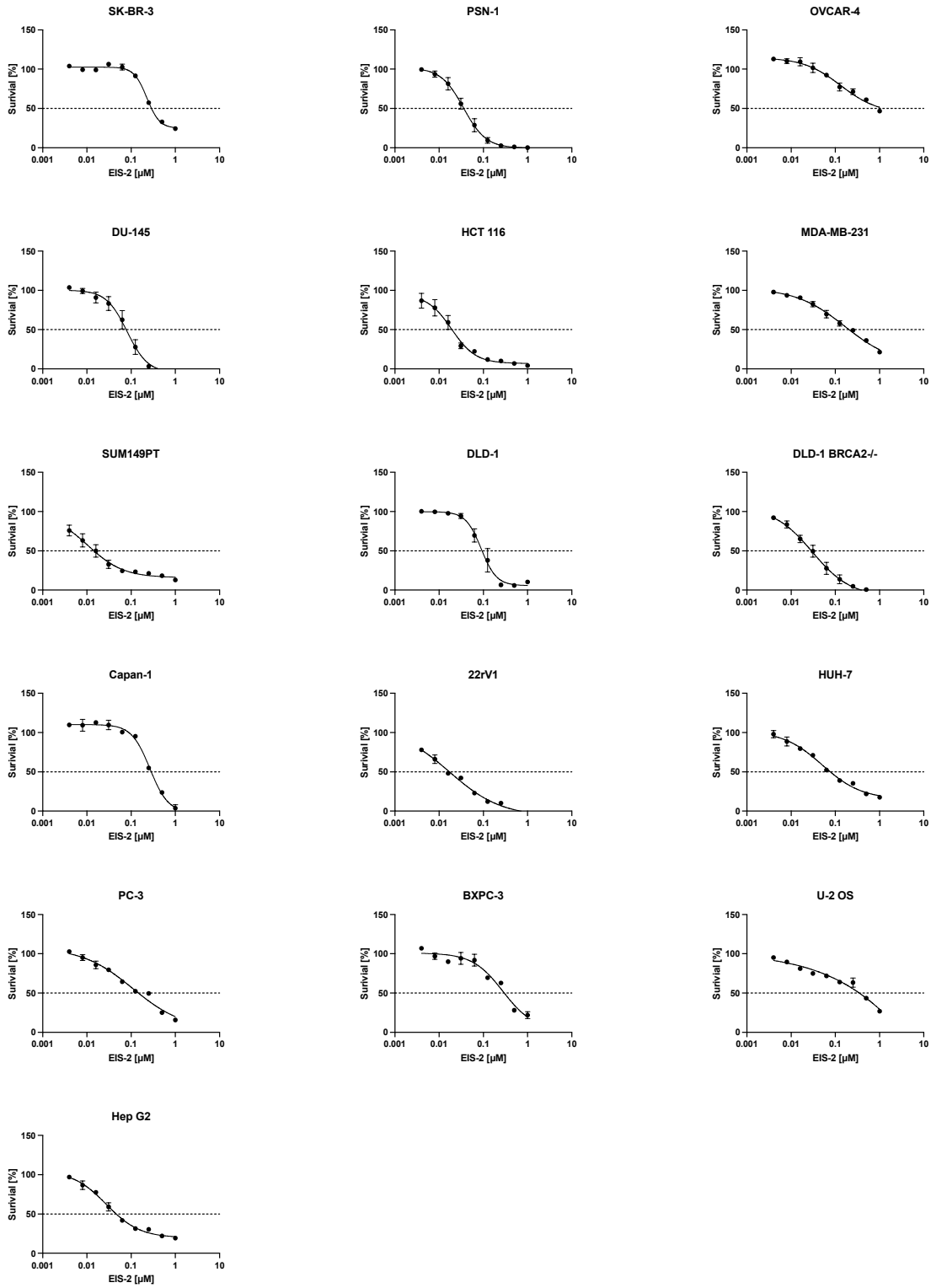

Supplementary Figure 6: 96h cellular survival assay of EIS-2 in the cell-panel

Different cancer cell lines were treated with EIS-2. Cells were cultured for 96h and stained with SRB to analyze cell survival [%]. Survival was normalized to cells treated with vehicle (DMSO) and an “all dead control”. Inhibitor vs. response curves were fitted using GraphPad Prism non-linear regression. Error bars indicate SEM of all replicates. Number of replicates is indicated in Supplementary Table 9.

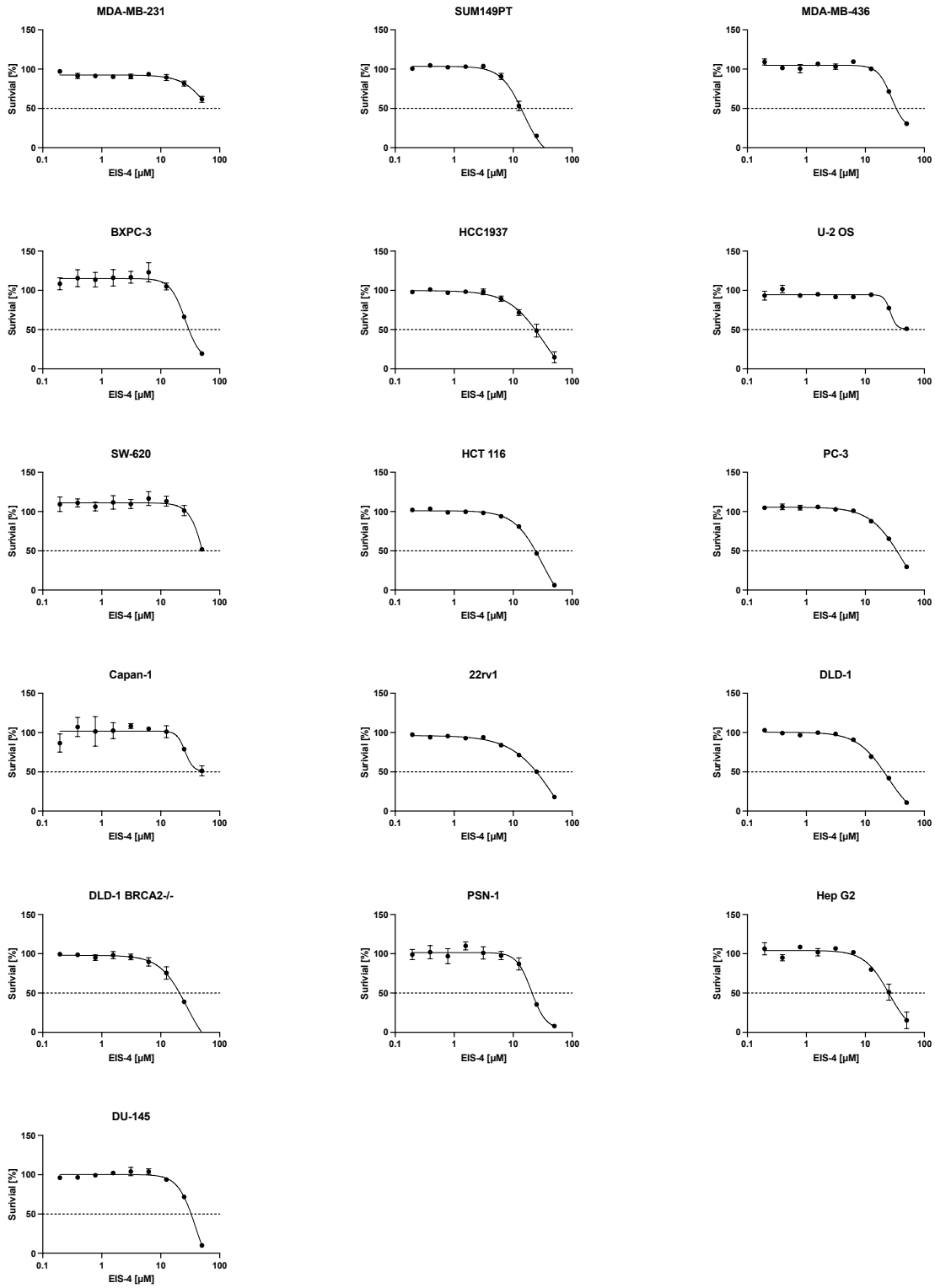

Supplementary Figure 7: 96h cellular survival assay of EIS-4 in the cell-panel

Different cancer cell lines were treated with EIS-4. Cells were cultured for 96h and stained with SRB to analyze cell survival [%]. Survival was normalized to cells treated with vehicle (DMSO) and an “all dead control”. Inhibitor vs. response curves were fitted using GraphPad Prism non-linear regression. Error bars indicate SEM of all replicates. Number of replicates is indicated in Supplementary Table 9.

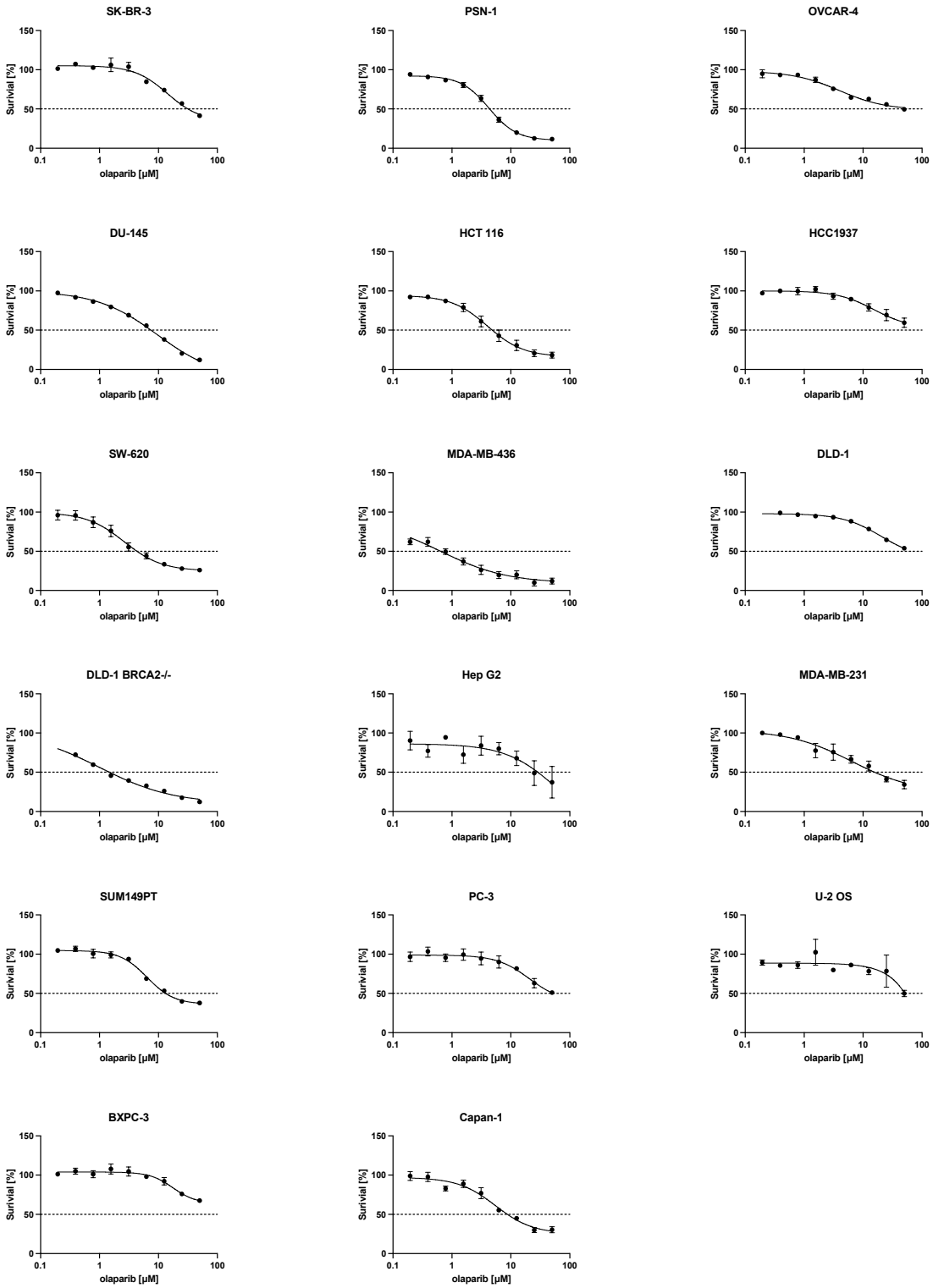

Supplementary Figure 8: 96h cellular survival assay of olaparib in the cell-panel
Different cancer cell lines were treated with olaparib. Cells were cultured for 96h and stained with SRB to analyze cell survival [%]. Survival was normalized to cells treated with vehicle (DMSO) and an “all dead control”. Inhibitor vs. response curves were fitted using GraphPad Prism non-linear regression. Error bars indicate SEM of all replicates. Number of replicates is indicated in Supplementary Table 9.

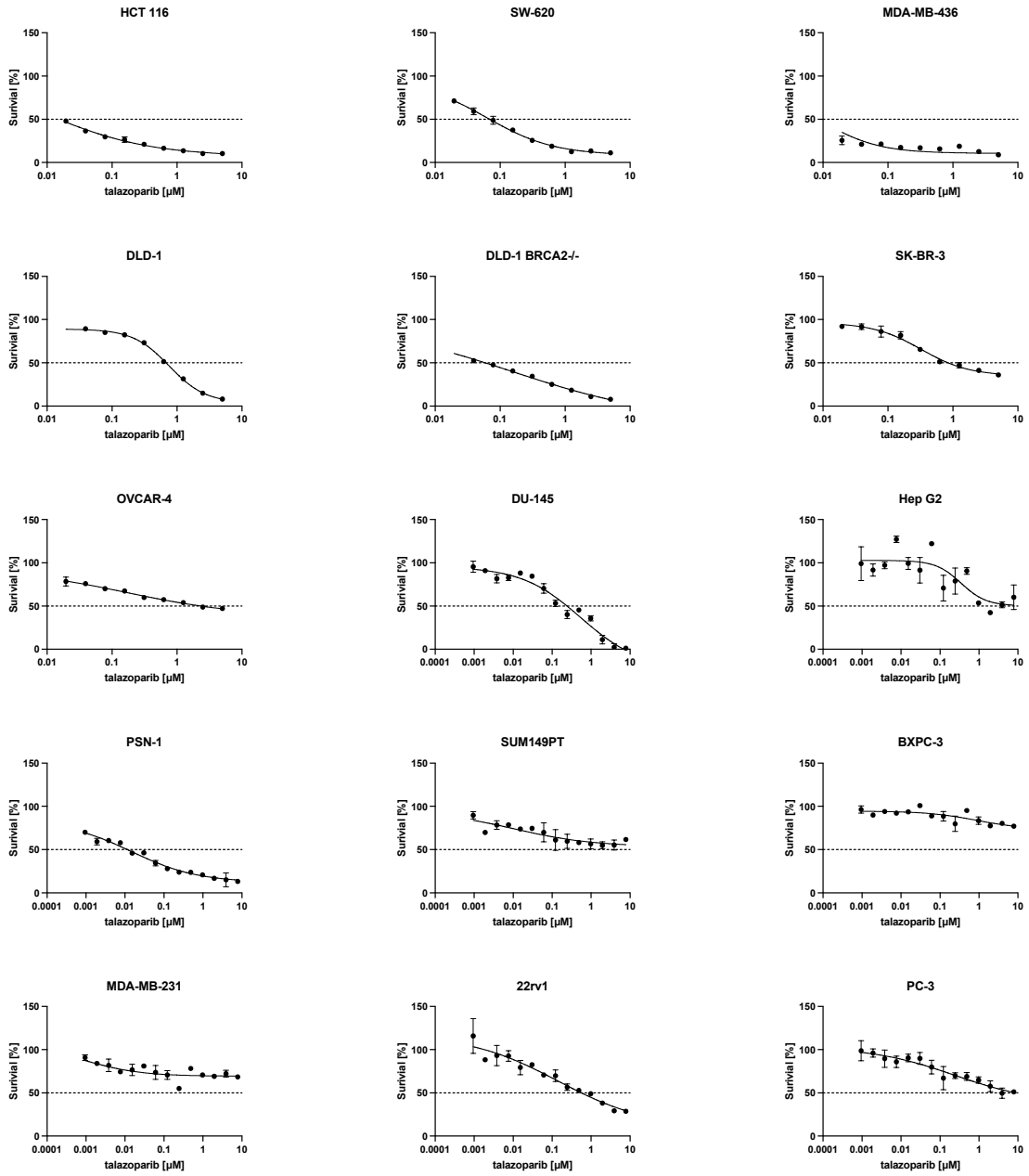

Supplementary Figure 9: 96h cellular survival assay of talazoparib in the cell-panel
Different cancer cell lines were treated with talazoparib. Cells were cultured for 96h and stained with SRB to analyze cell survival [%]. Survival was normalized to cells treated with vehicle (DMSO) and an “all dead control”. Inhibitor vs. response curves were fitted using GraphPad Prism non-linear regression. Error bars indicate SEM of all replicates. Number of replicates is indicated in Supplementary Table 9.

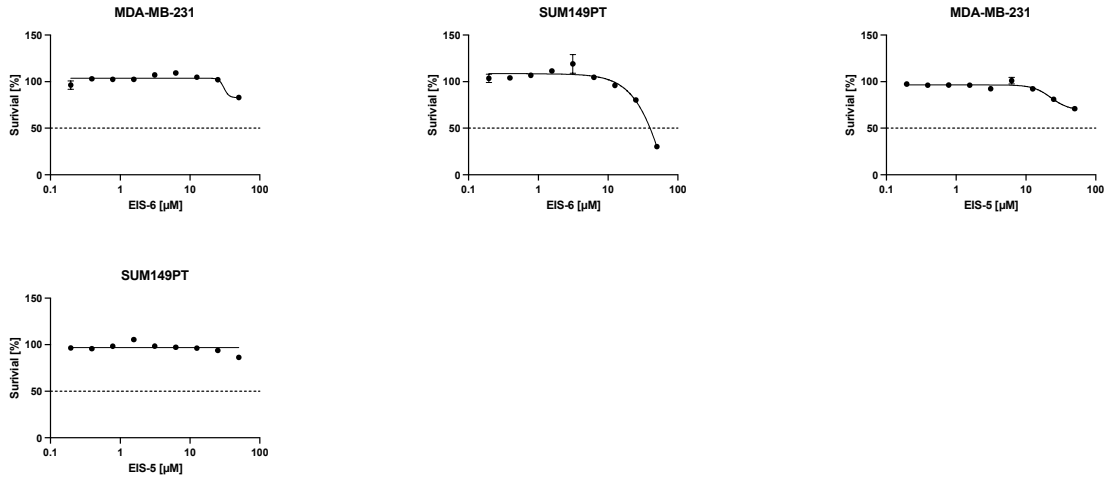

Supplementary Figure 10: 96h cellular survival assay of inactive ALC1i in the cell-panel
Different cancer cell lines were treated with inactive ALC1i (EIS-5 and EIS-6). Cells were cultured for 96h and stained with SRB to analyze cell survival [%]. Survival was normalized to cells treated with vehicle (DMSO) and an “all dead control”. Inhibitor vs. response curves were fitted using GraphPad Prism non-linear regression. Error bars indicate SEM of all replicates. Number of replicates is indicated in Supplementary Table 9.

7.1.3. 11days cell survival assay

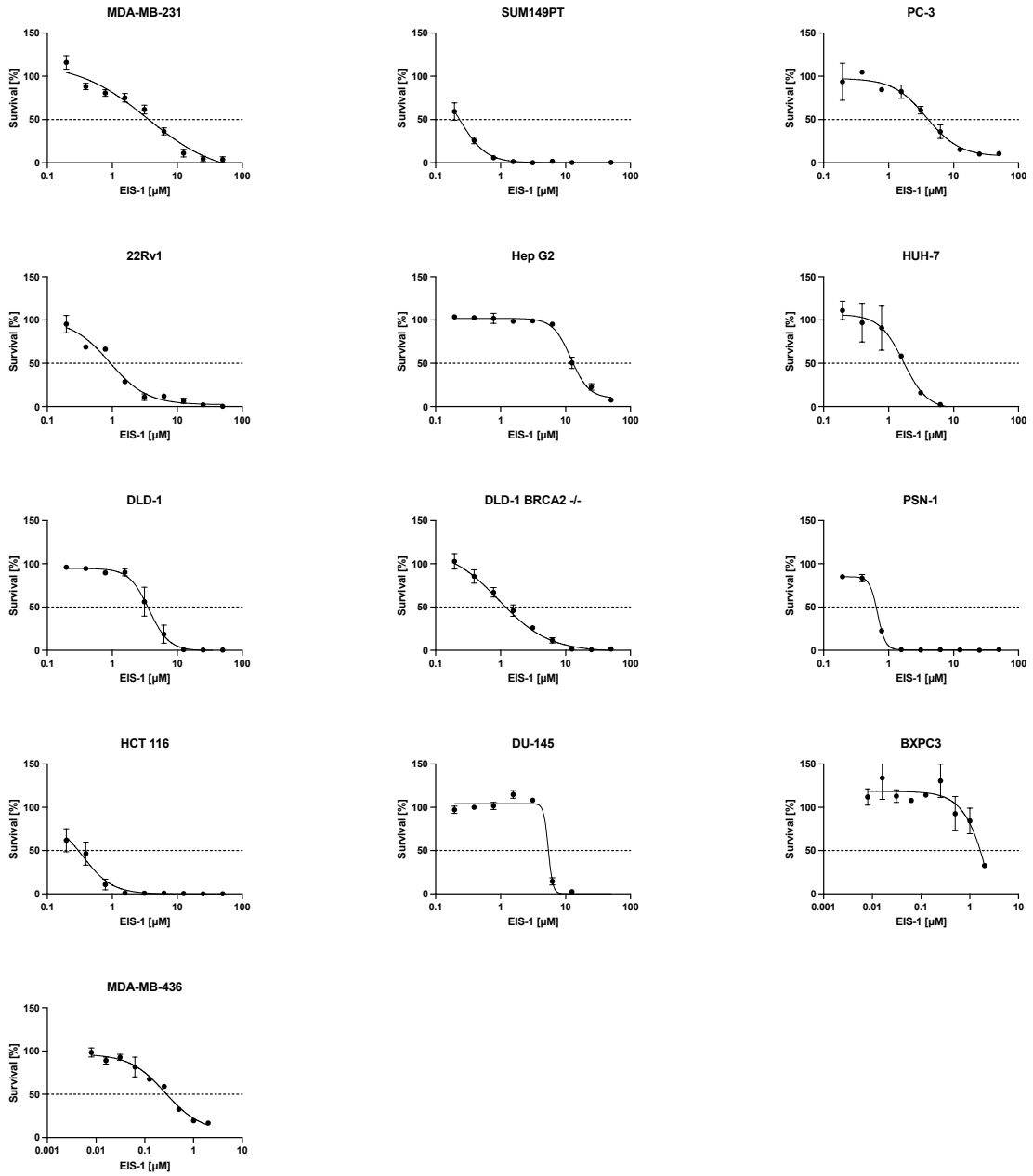

Supplementary Figure 11: 11-day cellular survival assay of EIS-1 in the cell-panel
Different cancer cell lines were treated with EIS-1. Cells were cultured for 11 days and stained with SRB to analyze cell survival [%]. Survival was normalized to cells treated with vehicle (DMSO) and an “all dead control”. Inhibitor vs. response curves were fitted using GraphPad Prism non-linear regression. Error bars indicate SEM of all replicates. Number of replicates is indicated in Supplementary Table 10.

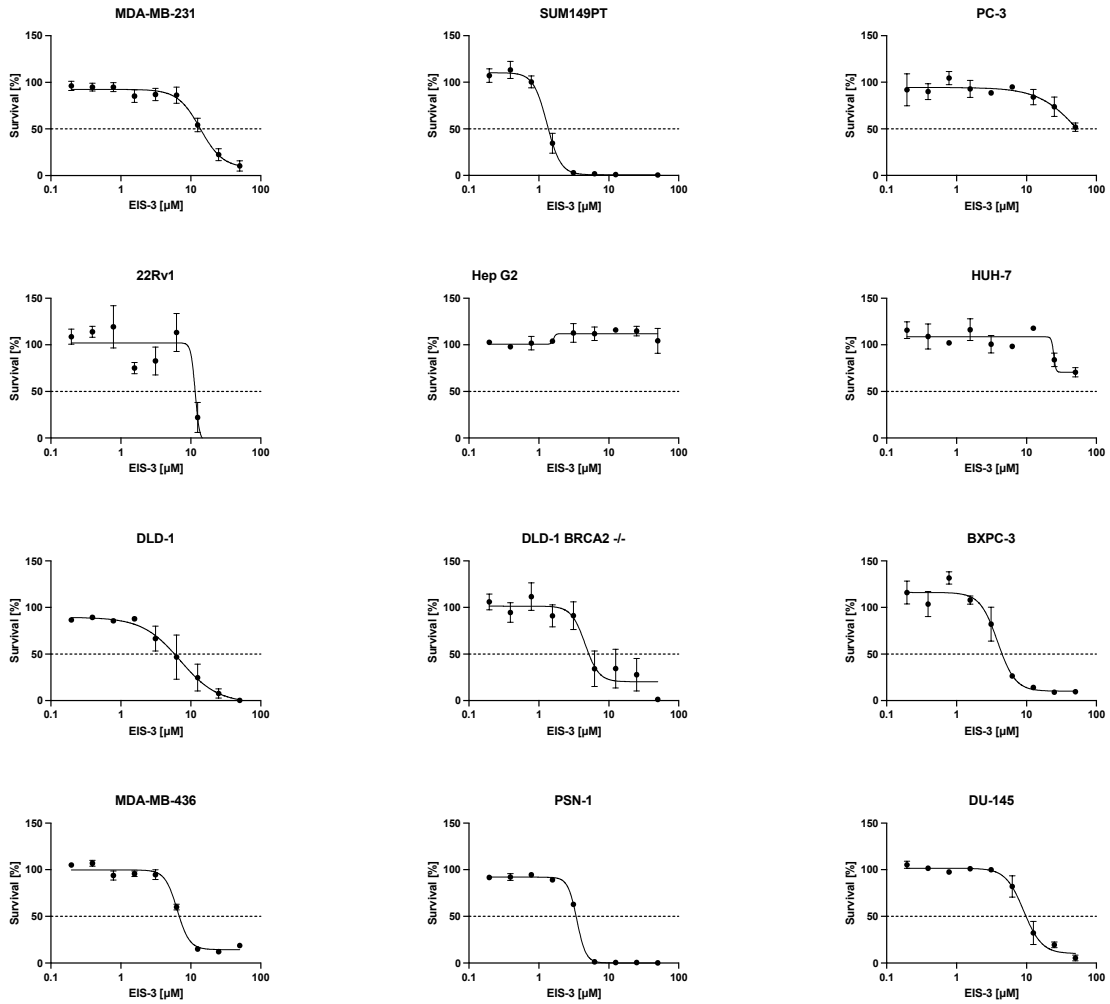

Supplementary Figure 12: 11-day cellular survival assay of EIS-3 in the cell-panel
Different cancer cell lines were treated with EIS-3. Cells were cultured for 11 days and stained with SRB to analyze cell survival [%]. Survival was normalized to cells treated with vehicle (DMSO) and an “all dead control”. Inhibitor vs. response curves were fitted using GraphPad Prism non-linear regression. Error bars indicate SEM of all replicates. Number of replicates is indicated in Supplementary Table 10.

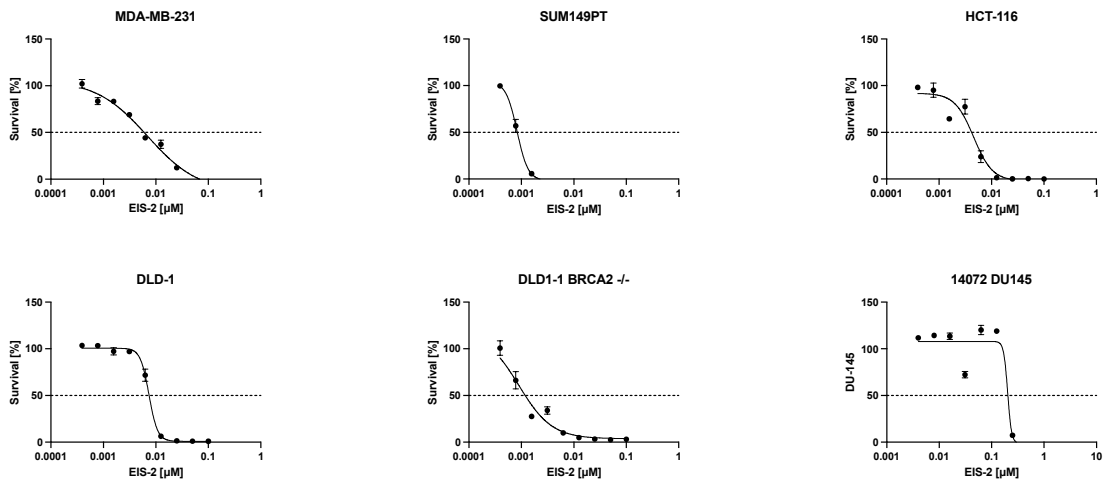

Supplementary Figure 13: 11-day cellular survival assay of EIS-2 in the cell-panel
Different cancer cell lines were treated with EIS-2. Cells were cultured for 11 days and stained with SRB to analyze cell survival [%]. Survival was normalized to cells treated with vehicle (DMSO) and an “all dead control”. Inhibitor vs. response curves were fitted using GraphPad Prism non-linear regression. Error bars indicate SEM of all replicates. Number of replicates is indicated in Supplementary Table 10.

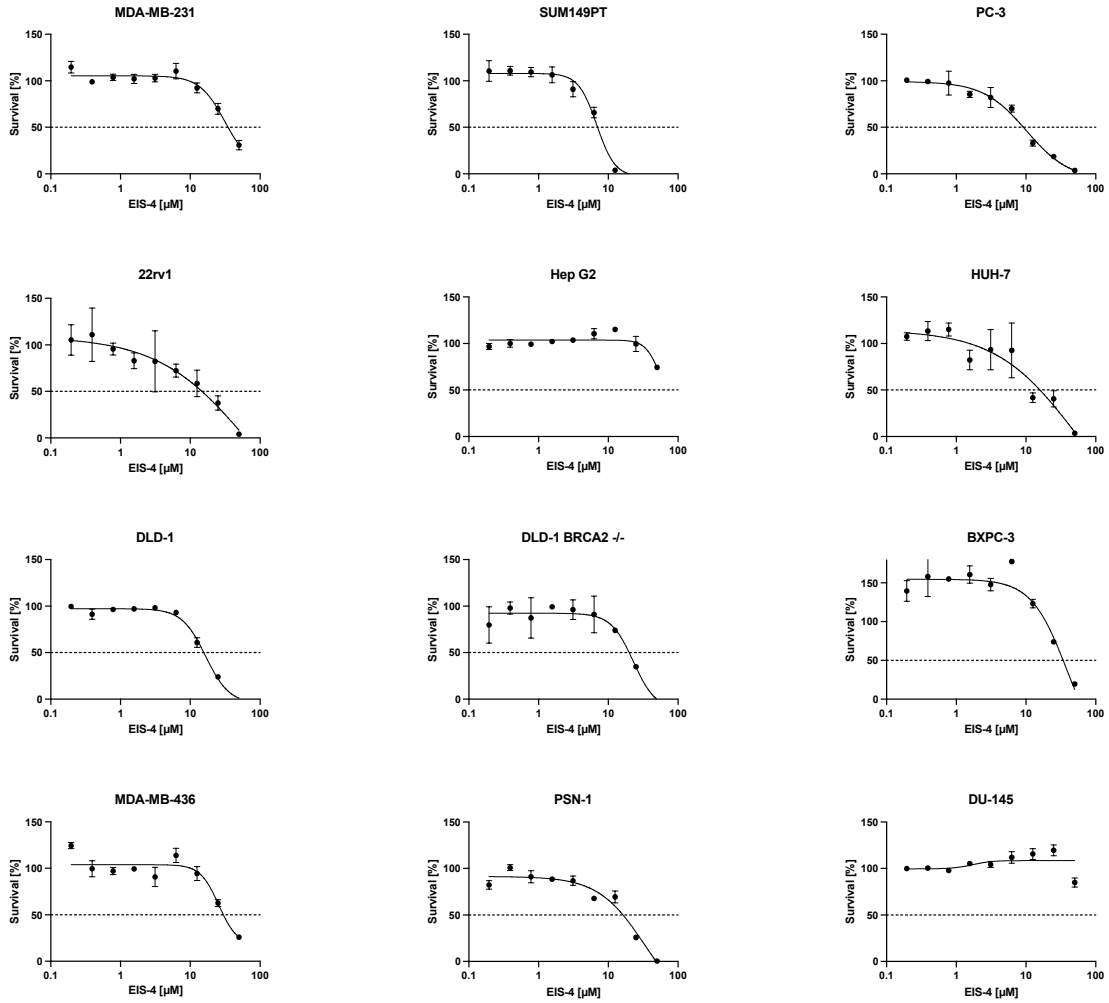

Supplementary Figure 14: 11-day cellular survival assay of EIS-4 in the cell-panel
Different cancer cell lines were treated with EIS-4. Cells were cultured for 11 days and stained with SRB to analyze cell survival [%]. Survival was normalized to cells treated with vehicle (DMSO) and an “all dead control”. Inhibitor vs. response curves were fitted using GraphPad Prism non-linear regression. Error bars indicate SEM of all replicates. Number of replicates is indicated in Supplementary Table 10.

7.1.4. γH2AX and cleaved PARP1 Western Blot

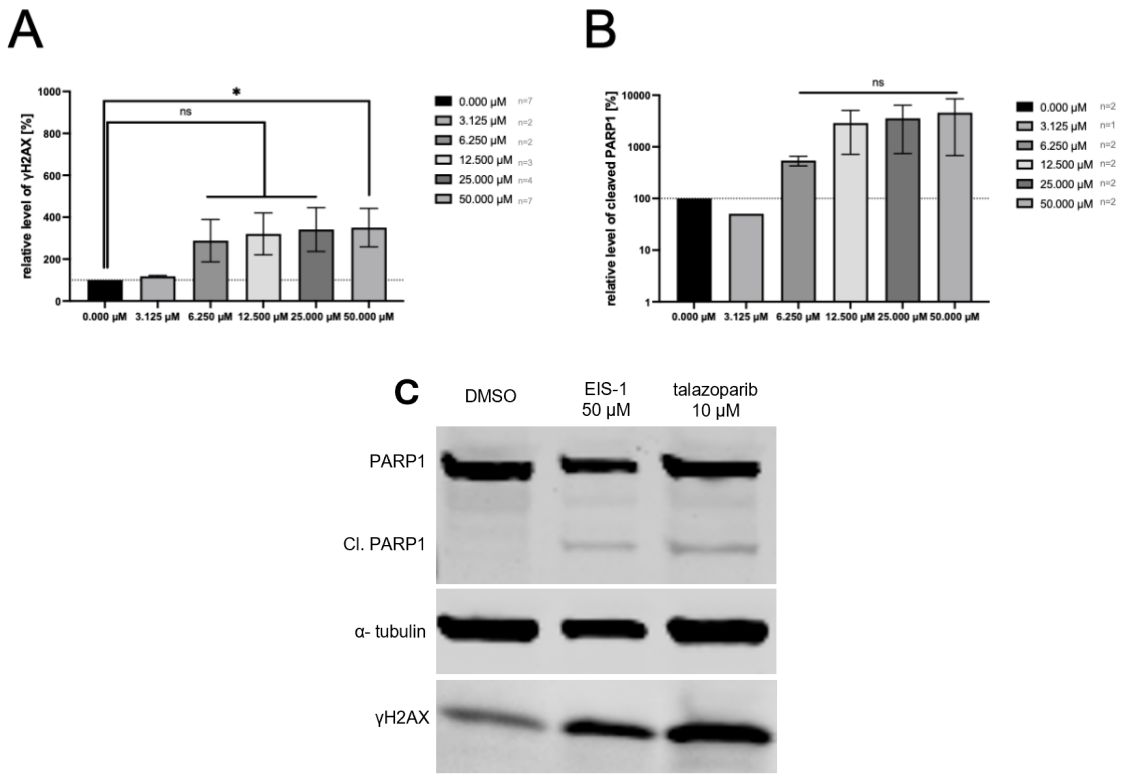

Supplementary Figure 15: γH2AX and PARP1 protein expression in PSN-1 cells under EIS-1 treatment

PSN-1 cells were treated with increasing concentrations of EIS-1 or DMSO for 48 h. For Immunodetection, the following antibodies were used. 1 °AB: Anti-PARP1 (Santa Cruz, 8007), Anti- γH2AX (Abcam, AB11174), Anti-alpha tubulin (sigma, T9026); 2 °AB (Licor): IRDye 800CW Goat anti-Rabbit 925-32211, IRDye 680RD Donkey anti-Mouse 925-68072. The protein quantity was assessed by analyzing the bands using FIJI (Image J). The protein amounts were normalized to a-tubulin. A) Bar graphs represent γH2AX levels in different treatment groups, normalized to the DMSO control. B) Bar graphs represent PARP1 and cleaved PARP1 levels in different treatment groups, normalized to the DMSO control. Error bars indicate the SEM of biological replicates n (indicated in grey). A Welch's-test was used for statistical analysis. C) Control experiment showing PSN-1 cells treated with EIS-1 vs. talazoparib.

7.1.5. γH2AX FACS

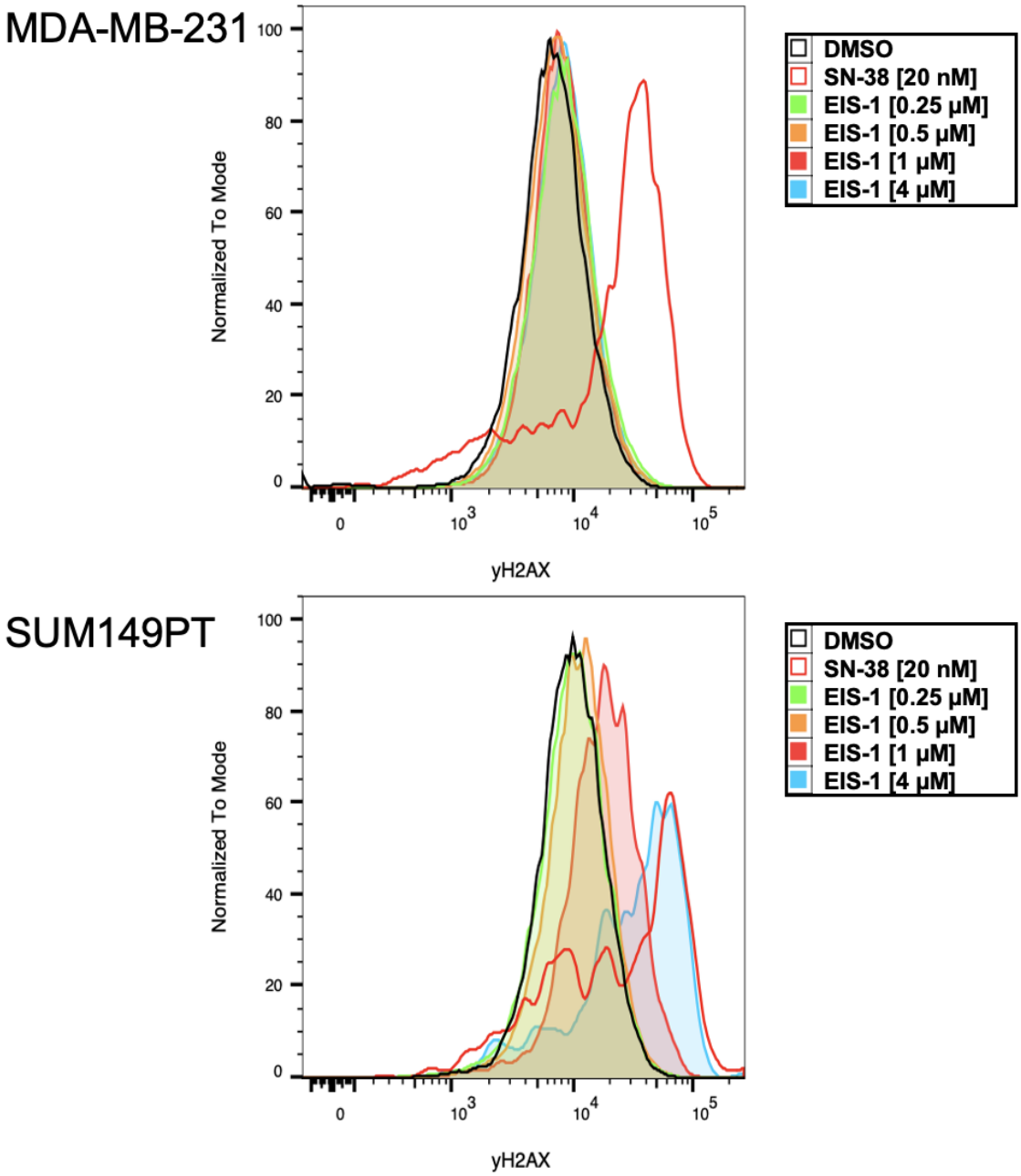

Supplementary Figure 16: γH2AX expression under EIS-1 treatment, FACS analysis (replicate 2) (modified from Dr. Markus Lechner, Eisbach Bio GmbH)
SUM149PT and MDA-MB-231 cells were treated with a titration of EIS-1 (green, orange, red, blue), SN-38 (red) or DMSO (black) for 120 h. Cells were fixed with formaldehyde, permeabilized with methanol and stained with a live/dead stain (Thermo Fischer) and γH2AX primary antibody (Abcam). A 488 nm secondary AB was used (Invitrogen). Levels of γH2AX were quantified using FlowJow 10.9.0. The data represents the second biological replicate.

7.1.6. Annexin V staining

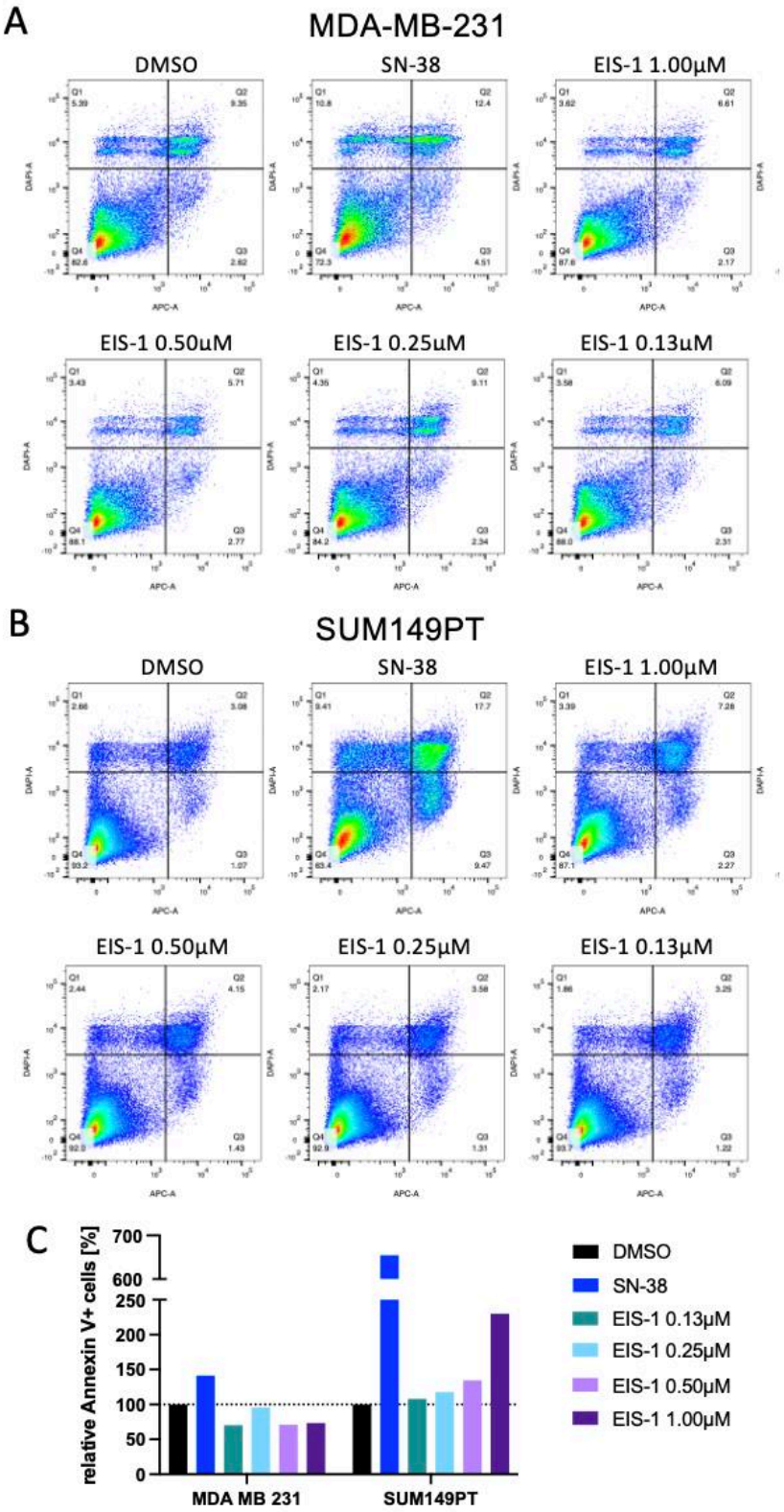

Supplementary Figure 17: Annexin V staining of MDA-MB-231 and SUM149PT cells (modified from Dr. Markus Lechner, Eisbach Bio GmbH)

MDA-MB-231 (A) and SUM149PT (B) cells were treated with EIS-1, SN-38 or vehicle (DMSO) for 48 h. Cells were stained with Annexin V. A, B) The dot plot diagrams represent the different levels of Annexin V (x-Axis) vs. DAPI (y-Axis). Dead cells are

represented in the upper left square (Q1). Healthy cells are represented in the lower left square (Q4). Cells undergoing apoptosis are represented in the lower right square (DAPI negative, Annexin V positive) (Q3). Annexin V and DAPI positive cells represent cells in late apoptosis in the upper right square (Q2). C) Total levels of Annexin V positive cells were quantified using FlowJow 10.9.0. and plotted as a bar graph diagram using GraphPad Prism. Data represents one biological replicate.

7.1.7. γH2AX and RAD51 foci formation

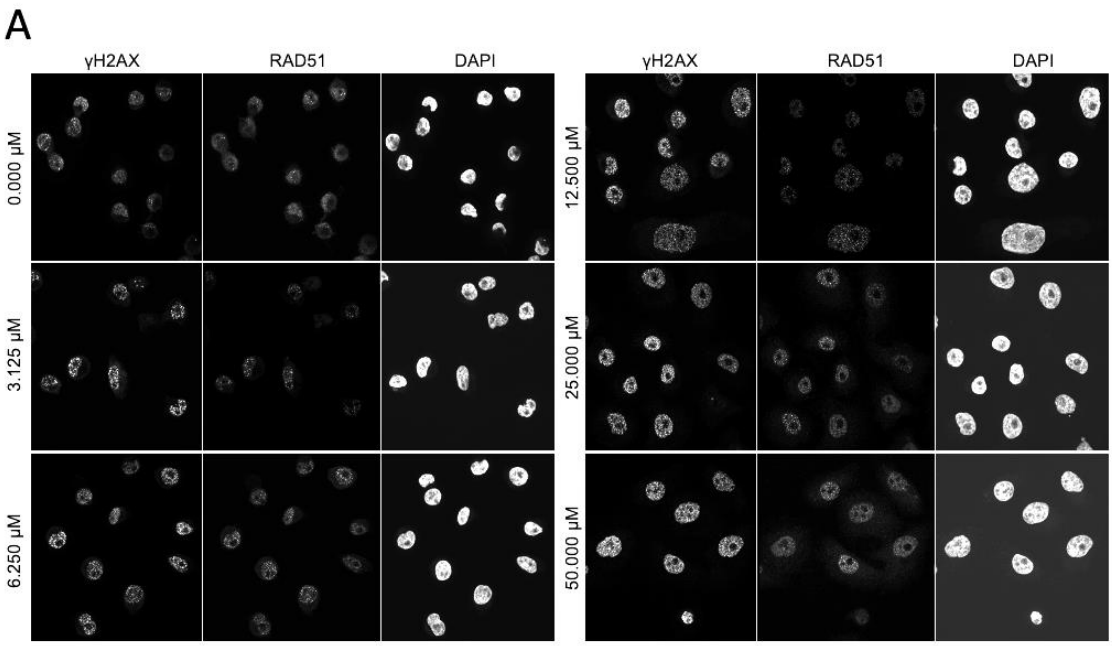

Supplementary Figure 18: γH2AX and RAD51 foci formation under EIS-1 treatment in PSN-1 cells

PSN-1 cells were treated with EIS-1 for 24 h, fixed and stained with primary antibodies anti-γH2AX (Novus) (left) and anti-RAD51 (Sigma) (middle), secondary antibodies Goat anti-Rabbit IgG Alexa Fluor™ 488 (Invitrogen) and sheep IgG anti-mouse IgG-Cy3 (Dianova), and counterstained with DAPI (right). Z-images were stacked using Fiji (ImageJ).

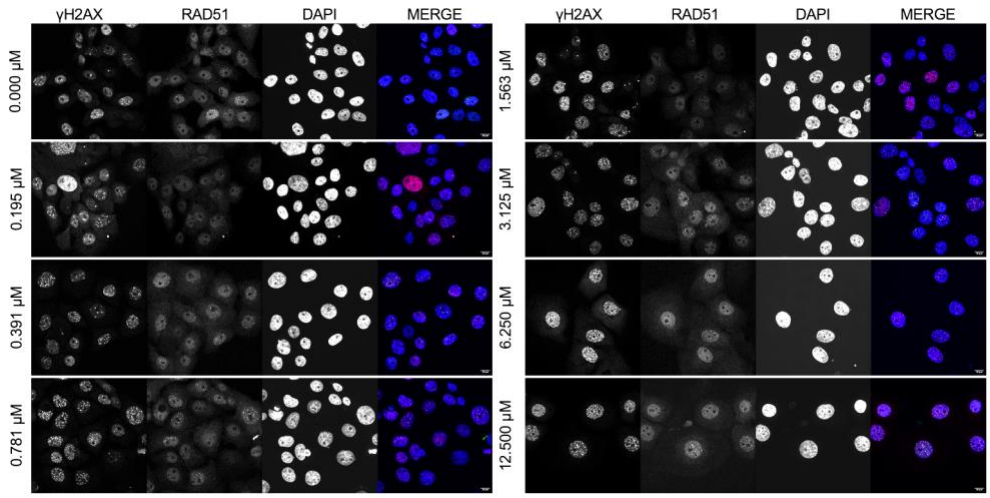

Supplementary Figure 19: Images of γH2AX and RAD51 foci formation in SUM149PT cells under EIS-1 treatment

γH2AX and RAD51 foci formation in HR-deficient SUM149PT cells under ALC1i treatment. Representative images of nuclear foci formation by immunofluorescence following 24 h treatment with different concentrations of EIS-1. Single color channel images (γH2AX on the left, RAD51 in the middle, DAPI on the right) and a merge of all the channels in color are shown. Z-images were stacked using Fiji (ImageJ).

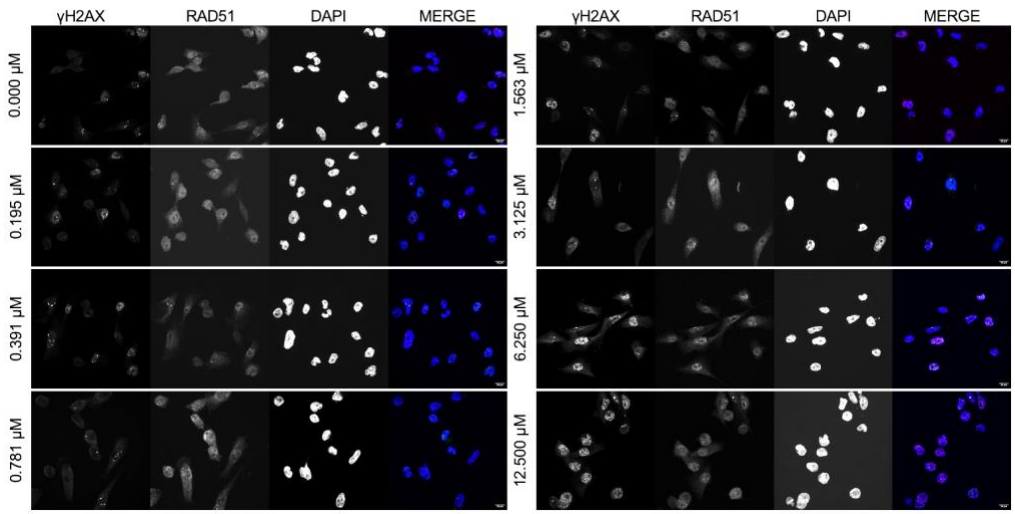

Supplementary Figure 20: Images of γH2AX and RAD51 foci formation in MDA-MB-231 cells under EIS-1 treatment

Cells were treated with EIS-1 for 24 h, fixed and stained with primary antibodies anti-γH2AX (Novus) and anti-RAD51 (Sigma), secondary antibodies Goat anti-Rabbit IgG Alexa Fluor™ 488 (Invitrogen) and sheep IgG anti-mouse IgG-Cy3 (Dianova), and counterstained with DAPI. Z-images were stacked using Fiji (ImageJ). Representative IF-images of individual channels (γH2AX : left, RAD51: middle-left, DAPI: middle-right and merged channels: right) are shown.

7.1.8. LCI recruitment assay

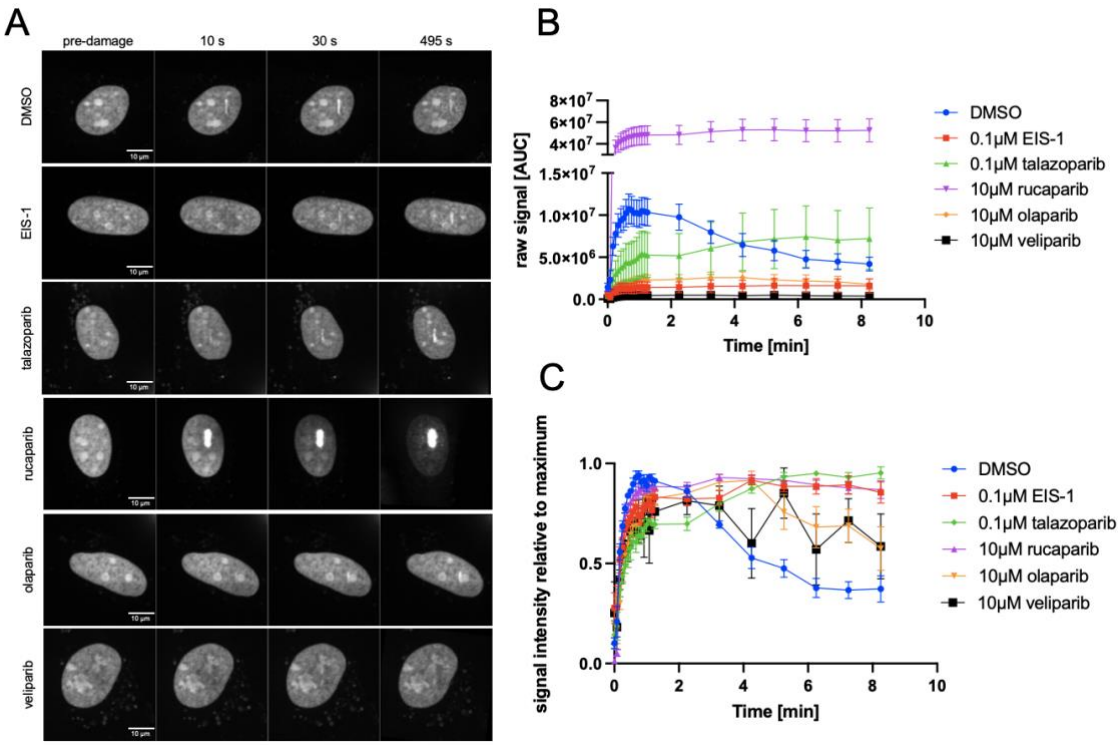

Supplementary Figure 21: Diverse effects of ALC1i and PARPi on recruitment dynamics of PARP1-GFP

U-2 OS cells were transiently transfected with PARP1-GFP. DNA damage was induced in the nucleus using a 355 nm laser with a reduced laser power of 5 %. Cells were treated with ALC1i or PARPi for 1h. PARP1-GFP recruitment to the DNA lesion was observed over time. Images of cells at t0 (before the damage; 0 s), t1 (right after the damage; 10 s), t2 (30 s)and t3 (end of the assay; 495 s) are shown in A. For visualization of diverse signal intensities, raw signal as area under the curve (AUC) is shown in B. Signal intensity relative to the maximum signal is shown in C. Curves were fitted using GraphPad Prism. The data includes one biological replicate. Error bars indicate the SEM of 4-11 nuclei per condition.

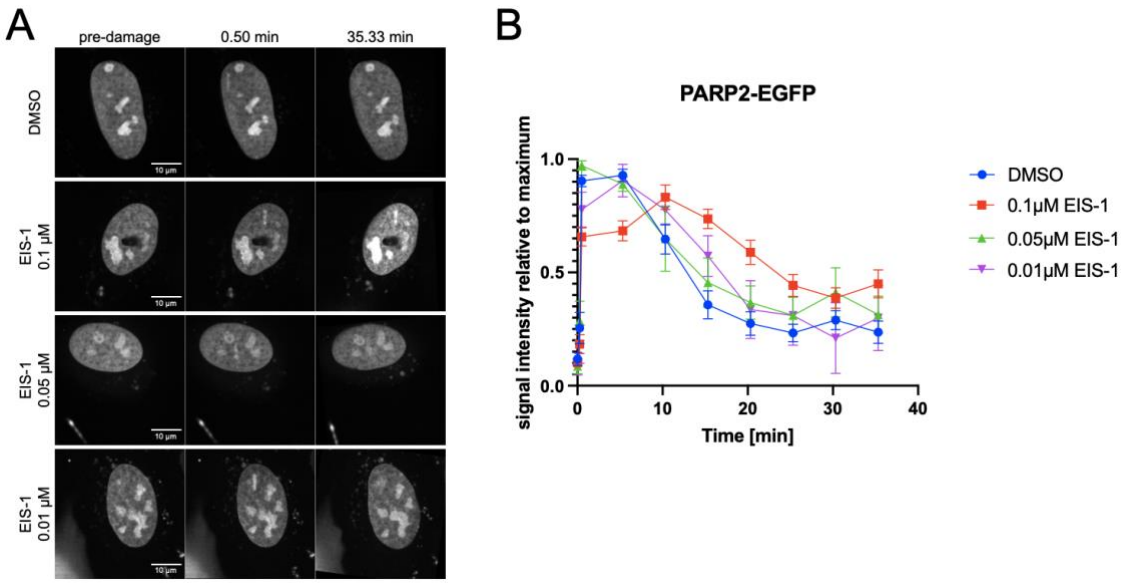

Supplementary Figure 22: Dose-response of EIS-1 in PARP2-GFP retention
U-2 OS cells were transiently transfected with PARP2-GFP. DNA damage was induced in the nucleus using a 355 nm laser with a laser power of 10 %. Cells were treated with different concentrations of EIS-1 for 1h. Protein retention at the DNA lesion was observed over time. Images of cells at t0 (before the damage; 0 min), t1 (right after the damage; 0.5 min) and t2 (end of the assay; 35.33 min) are shown in A. Signal intensity relative to the maximum signal is shown in B. Curves were fitted using GraphPad Prism. The data includes 1-3 biological replicate. Error bars indicate the SEM of 6-39 nuclei per condition.

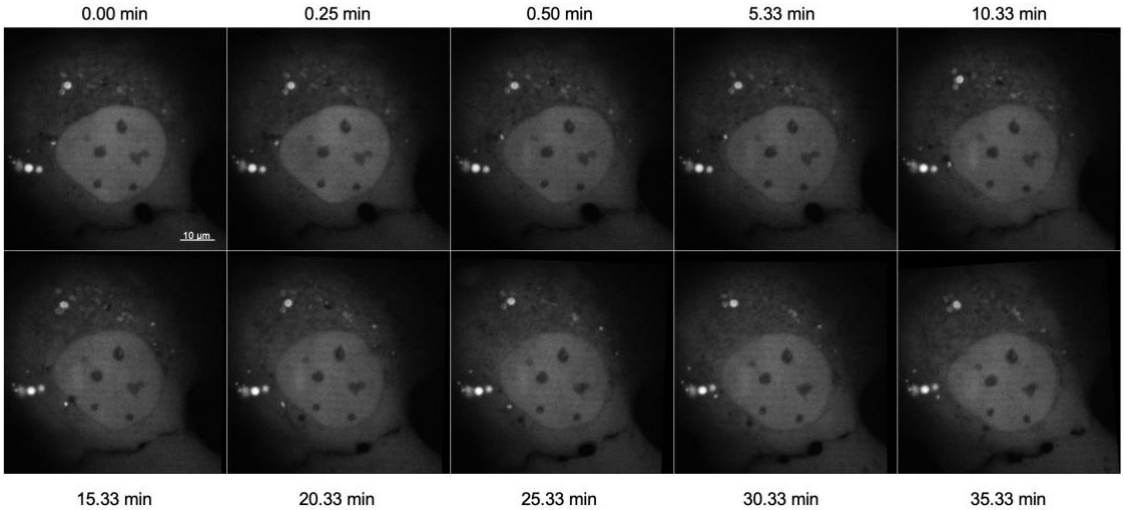

Supplementary Figure 23: PARP3-GFP dynamics at DNA damage sites
U-2 OS cells were transiently transfected with PARP3-GFP. DNA damage was induced in the nucleus using a 355 nm laser with a laser power of 10 %. Representative images show PARP3-GFP protein retention at the DNA lesion was observed over time.

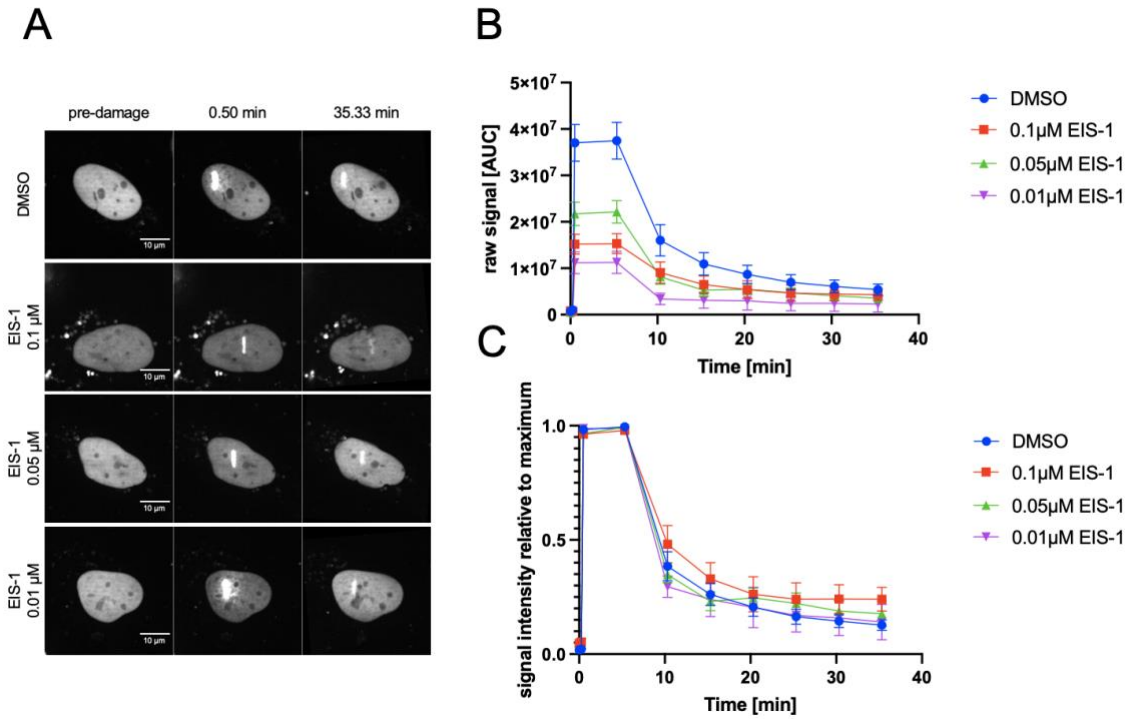

Supplementary Figure 24: Effects of EIS-1 on retention dynamics of EGFP-ALC1

U-2 OS cells were transiently transfected with EGFP-ALC1. DNA damage was induced in the nucleus using a 355 nm laser with a laser power of 10 %. Cells were treated with a titration of EIS-1 for 1h. EGFP-ALC1 retention at the DNA lesion was observed over time. Images of cells at t0 (before the damage; 0 min), t1 (right after the damage; 0.5 min) and t2 (end of the assay; 35.33 min) are shown in A. For visualization of diverse signal intensities, raw signal by area under the curve (AUC) is shown in B. Signal intensity relative to the maximum signal is shown in C. Curves were fitted using GraphPad Prism. The data includes one biological replicate. Error bars indicate the SEM of 9-14 nuclei per condition.

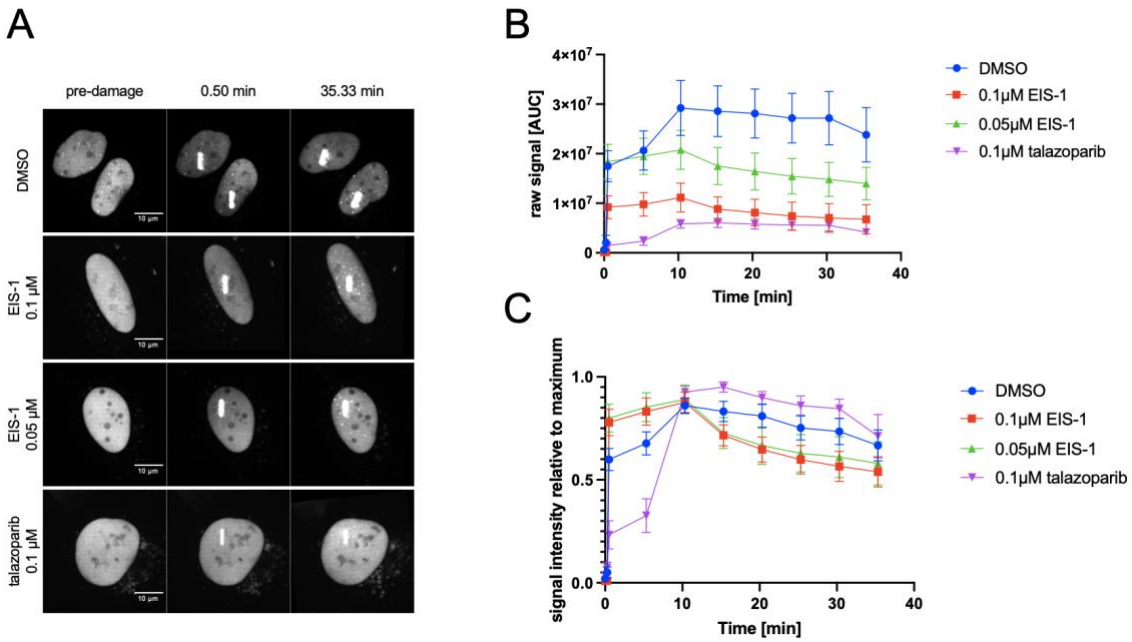

Supplementary Figure 25: Effects of EIS-1 and talazoparib on retention dynamics of XRCC1-YFP

U-2 OS cells were transiently transfected with XRCC1-YFP. DNA damage was induced in the nucleus using a 355 nm laser with a laser power of 10 %. Cells were treated with different concentrations of EIS-1 or talazoparib for 1h. XRCC1-YFP retention at the DNA lesion was observed over time. Images of cells at t0 (before the damage; 0 min), t1 (right after the damage; 0.5 min) and t2 (end of the assay; 35.33 min) are shown in A. For visualization of diverse signal intensities, raw signal as area under the curve (AUC) is shown in B. Signal intensity relative to the maximum signal is shown in C. Curves were fitted using GraphPad Prism. The data includes 1-2 biological replicates. Error bars indicate the SEM of 7-17 nuclei per condition.

7.1.9. Resistant cells

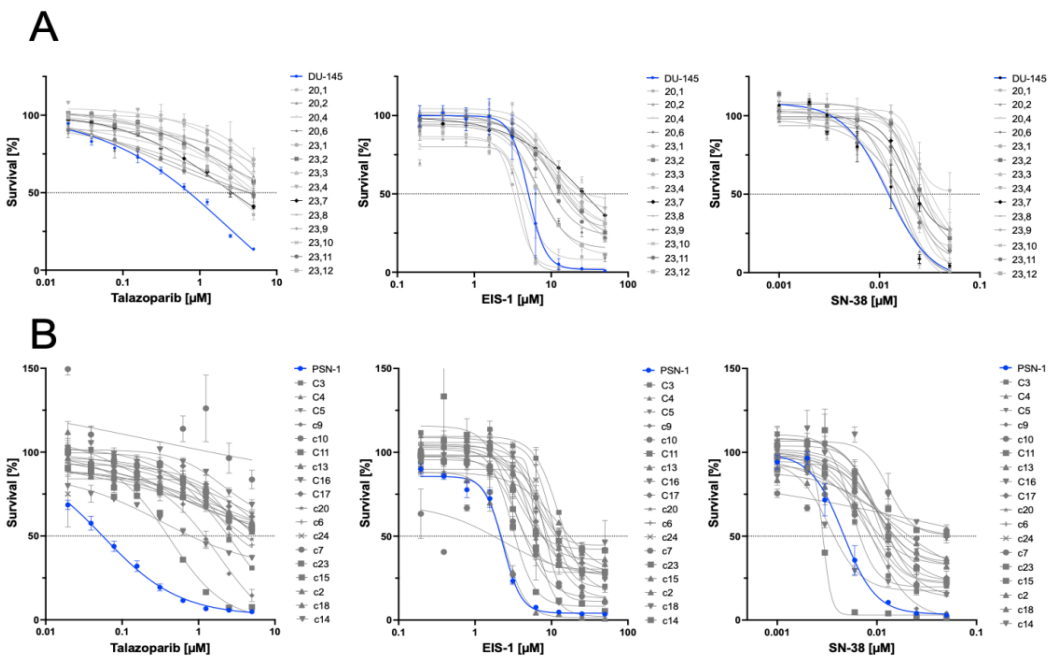

Supplementary Figure 26: Survival of talazoparib-resistant monoclonal cell lines Talazoparib-resistant DU-145 (A) and PSN-1 (B) monoclonal cell lines (grey) were tested versus their parental cell line (blue) in the 96h SRB-survival readout. Cells were treated with talazoparib, EIS-1 or SN-38. Inhibitor vs. response curves were fitted using GraphPad Prism. Error bars indicate SEM of 2 technical replicates. Due to solubility limits of the compounds, the highest assay concentration reached for EIS-1 was 50 µM and talazoparib, 5 µM. EC50 values above the solubility limit were marked with the value of the highest dose possible. IC50 values, SEM, EC50 and number of replicates are indicated in Supplementary Table 23, Supplementary Table 24.

7.1.10. Correlation ALC1 protein with ALC1i sensitivity

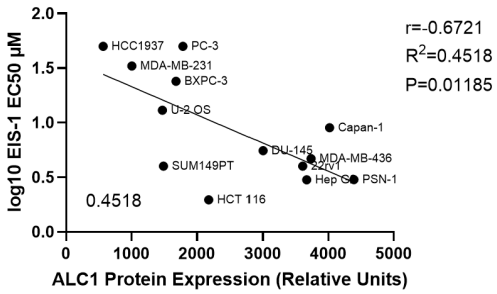

Supplementary Figure 27: Correlation between ALC1 protein expression and EIS-1 sensitivity. A Pearson correlation analysis was performed to evaluate the relationship between baseline ALC1 protein levels, quantified from the Western blot analysis shown in Figure 24A, and drug sensitivity expressed as $\log_{10}$-transformed EIS-1 EC_{50} values (µM). The analysis revealed a statistically significant strong inverse correlation ($r = -0.6721$, $R^2 = 0.4518$, $P = 0.0119$), demonstrating that higher ALC1 expression significantly correlates with increased sensitivity (lower EC_{50}) to the compound. In the scatter plot, the solid black line represents the simple linear regression best-fit, while the shaded region indicates the 95% confidence intervals.

7.2. Supplementary Tables

Supplementary Table 1: List of ALC1i

ALC1i	Chemical Compound Cluster
EIS-1	Cluster A
EIS-2	Cluster A
EIS-3	Cluster B
EIS-4	Cluster C
EIS-5	Cluster A
EIS-6	Cluster C

Supplementary Table 2: References to Table 1 (Mechanisms and rationale for drug combinations with ALC1i)

Drug	References (Effect on DDR)	References (Impact on Cell Cycle)	References (Additional Information)
PARPi	(Juhász et al., 2020; Kanev et al., 2023)	(Jelinic & Levine, 2014; Kruglov et al., 2020)	(Blessing et al., 2020; Juhász et al., 2020)
TOP1i	(J. Liu et al., 2019; Pommier et al., 2014; Tubbs & Nussenzweig, 2017)	(Maurya et al., 2011)	(Murai, Zhang, et al., 2014)
TOP2i	(for Biotechnology Information, 2023a; Nitiss, 2009)	(for Biotechnology Information, 2023a)	(Bowman et al., 2001; Murai, Zhang, et al., 2014)
ATMi	(Mimitou & Symington, 2009; H. Tang & Poon, 2011; You et al., 2009)	(Barnum & O'Connell, 2014; Faulhaber et al., 2021; O'Connor, 2015; H. Tang & Poon, 2011)	(Löser et al., 2010; Mak et al., 2020; Williamson et al., 2010)
ATRi	(Bradbury et al., 2022; H.-J. Kim et al., 2016)	(Barnum & O'Connell, 2014; Bradbury et al., 2022; Faulhaber et al., 2021; O'Connor, 2015)	(Barnieh et al., 2021; Hewitt et al., 2021; Ooka et al., 2018)
BRDi	(Pérez-Salvia & Esteller, 2016)	n.d.	(H.-Y. Peng et al., 2021)
Alkylating Agent	(Teus et al., 2009)	(Nakayama et al., 2020; Tomasz, 1995)	(Nakayama et al., 2020; Teus et al., 2009)
Taxane	(Alexandre et al., 2007; Jordan & Wilson, 1998; Re & Af, 1993; Schiff & Horwitz, 1980)	(Jordan et al., 1993; Schiff & Horwitz, 1980)	(Alexandre et al., 2007)
VEGFRi, FGFRi	(Ferrarelli, 2019)	(Nakahara et al., 2022)	(Ivy et al., 2016; Lai et al., 2020)
Wee1i	(Di Rorà et al., 2020)	(Barnum & O'Connell, 2014; Di Rorà et al., 2020; O'Connor, 2015)	(for Biotechnology Information, 2023b)
Thymidylate Synthase Inhibitor	(Curtin et al., 1991; Peters et al., 2000; Wyatt & Wilson, 2008)	(Shah & Schwartz, 2001)	(Gottifredi & Prives, 2005; Kastan & Bartek, 2004)

Supplementary Table 3: HR-related genes (K. B. Kim et al., 2021; G. Peng et al., 2014; Toh & Ngeow, 2021; Yamamoto & Hirasawa, 2021)

53BP1	CDKN2B	FGF23	KDM5C	PARP2	RMI2	TP53I3
AADAT	CDKN2C	FGF3	KDM6A	PARP3	RMI2 b	TP63
ADM	CEBPA	FGF4	KDR	PARP4	RNF43	TRAF2
AHSA1	CENPA	FGF5	KEAP1	PARPBP	ROS1	TRAF7
ALDH3B1	CENPE	FGF6	KEL	PAX5	RPA1	TRAPPC13
ALDH6A1	CENPJ	FGF9	KIT	PAXX	RPA1 b	TSC1
ALG8	CHAF1A	FGFR1	KLF4	PBRM1	RPA2	TSC2
ANLN	CHEK1	FGFR2	KLHL6	PCNA	RPA3	TSHR
ARID1a	CHEK2	FGFR3	KMT2A	PD-1	RPA4	TTK
ARID1b	CIC	FGFR4	KMT2B	PD-L2	RPS6KA4	TYRO3
ARSD	COL2A1	FH	KMT2C	PDGFB	RPS6KB1	U2AF1
ASF1B	COP1	FLCN	KMT2D	PDGFRA	RPS6KB2	VEGFA
ASPM	CREBBP	FLT1	KNSTRN	PDGFRB	RPTOR	VHL
ATM	CRKL	FLT3	KRAS	PDK1	RSPO1	VTCN1
ATP10B	CRLF2	FLT4	LATS1	PER1	RSPO2	WRN
ATR	CSF1R	FOXA1	LATS2	PGD	RUNX1	WT1
ATRIP b	CSF3R	FOXL2	LCK	PGR	RUNX1T1	XIAP
ATRX	CTCF	FOXO1	LIG4	PHF6	RYBP	XPO1
AURKB	CTLA4	FOXP1	LMO1	PHOX2B	SDC4	XRCC2
BAP1	CTNNA1	FRS2	LRP1B	PIK3C2B	SDHA	XRCC3
BARD1	CTNNB1	FTO	LYN	PIK3C2G	SDHAF2	XRCC4
BBOX1	CUL3	FUBP1	MAD2L2	PIK3C3	SDHB	XRCC5
BIRC2	CUL4A	FYN	MAGOH	PIK3CA	SDHC	XRCC6
BIRC3	CUL4B	GABRA6	MALT1	PIK3CB	SDHD	YAP1
BLM	CUX1	GADD45A	MAP2K1	PIK3CD	SESN1	YES1
BMPR1A	CXCR4	GATA1	MAP2K2	PIK3CG	SETBP1	ZFHX3
BRAF	CYLD	GATA2	MAP2K4	PIK3R1	SETD2	ZNF217
BRCA1	CYP2C19	GATA3	MAP2K7	PIK3R2	SF3B1	ZNF703
BRCA1 (FANCS)	DAXX	GATA4	MAP3K1	PIK3R3	SGK1	ZRSR2
BRCA2	DCLRE1C	GATA6	MAP3K13	PIM1	SH2B3	
BRCA2 (FANCD1)	DCUN1D1	GEN1	MAP3K14	PLCG1	SH2D1A	
BRD4	DDB1	GID4	MAP3K4	PLCG2	SHLD1	
BRI3BP	DDR1	GLI1	MAPK1	PLK2	SHLD2	
BRIP1	DDR2	GNA11	MAPK3	PMAIP1	SHPRH	
BRIP1 (FANCJ)	DDX3X	GNA13	MAPK8	PML	SHQ1	
BRIP1 b	DICER1	GNAQ	MAX	PMS1	SLC34A2	
BTG1	DIS3	GNAS	MCL1	PMS2	SLIT2	
BTG2	DLL3	GPS2	MDC1	PNKP	SLX4	
BTK	DMC1 b	GRIN2A	MDM2	PNRC1	SMAD2	
BUB1	DNA2	GRM3	MDM4	POLA1	SMAD3	
C10orf119	DNAJB1	GSK3B	MED12	POLD1	SMAD4	
C10orf73	DNMT1	H1-2	MEF2B	POLE	SMARCA2	
C11orf82	DNMT3A	H2AX	MEN1	POLQ	SMARCA4	
C13orf3	DNMT3B	H2BC5	MERTK	PPARG	SMARCAD1	
C14orf145	DOT1L	H3-3A	MET	PPM1D	SMARCB1	
C15orf42	E2F3	H3-3B	MGA	PPP1R3A	SMARCD1	
C16orf59	EED	H3-4	MGMT	PPP2R1A	SMC1A	
C16orf68	EGFL7	H3-5	MITF	PPP2R2A	SMC3	
C17orf41	EGFR	H3C1	MLH1	PPP4R4	SMC5	

C1orf112	EIF1AX	H3C10	MLH3	PPP6C	SMC6	
C1orf54	EIF4A2	H3C11	MPL	PRC1	SMO	
C1QTNF6	EIF4E	H3C12	MRE11	PRDM1	SNCAIP	
C20orf19	ELF3	H3C13	MRE11A	PREX2	SOCS1	
C20orf82	ELOC	H3C2	MSH2	PRG4	SOS1	
C4orf34	EML4	H3C3	MSH3	PRKAR1A	SOX10	
C5orf38	EMSY	H3C4	MSH6	PRKCI	SOX17	
C6orf48	ENO1	H3C6	MST1	PRKDC	SOX2	
CALR	EP300	H3C7	MST1R	PRKN	SOX9	
CARD11	EPCAM	H3C8	MTAP	PTCH1	SPEN	
CASP8	EPHA2	HDAC2	MTOR	PTEN	SPOP	
CBFB	EPHA3	HDAC9	MUTYH	PTK2	SRC	
CBL	EPHA5	HELQ	MXD4	PTPN11	SRSF2	
CBLB	EPHA7	HERC2	MYB	PTPRB	SSBP1	
CCDC138	EPHB1	HFM1	MYC	PTPRD	STAG2	
CCDC92	ERBB2	HGF	MYCL	PTPRS	STAT3	
CCN6	ERBB3	HLA-A	MYCN	PTPRT	STAT4	
CCNA2	ERBB4	HNF1A	MYD88	QKI	STAT5A	
CCNB1	ERCC1	HOXB13	MYOD1	RAB35	STAT5B	
CCNB1IP1	ERCC2	HRAS	NBN	RAC1	STK11	
CCND1	ERCC3	HSD3B1	NBN	RAD21	STK19	
CCND2	ERCC4	HSP90AA1	NCOA3	RAD50	STK40	
CCND3	ERCC5	HSP90AB1	NCOR1	RAD51	SUFU	
CCNE1	ERCC6	ICOSLG	NEGR1	RAD51AP1	SUZ12	
CD274 (PD-L1)	ERG	ID3	NF1	RAD51B	SYK	
CD276	ERRFI1	IDH1	NF2	RAD51C	TBC1D4	
CD68	ESR1	IDH2	NFE2L2	RAD51D	TBX3	
CD74	ETV1	IFNGR1	NFKBIA	RAD52	TCF3	
CD79A	ETV4	IGF1	NHEJ1	RAD54L	TCF7L2	
CD79B	ETV5	IGF1R	NKX2-1	RAF1	TEK	
CD8A	ETV6	IGF2	NKX3-1	RARA	TENT5C	
CDC20	EWSR1	IKBKE	NOTCH1	RASA1	TERC	
CDC27	EXO1	IKZF1	NOTCH2	RB1	TERT	
CDC6	EZH2	IL10	NOTCH3	RBM10	TET1	
CDC7	EZR	IL7R	NOTCH4	RECQL4	TET2	
CDC73	FADD	INHA	NPM1	REL	TFE3	
CDCA2	FANCA	INHBA	NRAS	RET	TGFB1	
CDCA3	FANCC	INO80	NSD1	REV3L	TGFBR1	
CDCA5	FANCD2	INPP4A	NSD3	RFC1	TGFBR2	
CDCA7	FANCE	INPP4B	NT5C2	RFC2	TMEM127	
CDCA8	FANCF	INSR	NTRK1	RFC3	TMPRSS2	
CDH1	FANCG	IRF2	NTRK2	RFC4	TNF	
CDK12	FANCI	IRF4	NTRK3	RFC5	TNFAIP3	
CDK2	FANCL	IRS1	NUP93	RHEB	TNFRSF14	
CDK4	FANCM	IRS2	NUTM1	RHOA	TOP1	
CDK6	FAS	JAK1	PAK1	RICTOR	TOP2A	
CDK8	FAT1	JAK2	PAK3	RIF1	TOP3A	
CDKN1A	FBXW7	JAK3	PAK5	RIF1 b	TOP3A b	
CDKN1B	FGF10	JUN	PALB2	RIT1	TOPBP1	
CDKN1C	FGF14	KAT6A	PALB2	RMI1	TP53	
CDKN2A	FGF19	KDM5A	PARP1	RMI1 b	TP53BP1	

Supplementary Table 4: Deleterious mutations in Eisbach cell-panel (DepMap: The Cancer Dependency Map Project at Broad Institute)

HCT 116	22rv1	DU-145	DLD-1	BXPC-3	Capan-1	SUM149PT	SW-620	PC-3
ATRX	BARD1	BRD4	BRCA2	BRAF	BRCA2	BRCA1	PRKDC	TP53
CDH1	CUX1	CIC	CTLA4	FCGBP	PTK2			
CDKN2A	DCLRE1C	CREBBP	DCLRE1C	FCGBP				
CTNNB1	EP300	FANCI	ERCC4					
EP300	FANCE	FAT1	ETV4					
EPHA5	FOXP1	FLT1	HDAC2					
FANCA	GPS2	FOXA1	MSH6					
FLT3	IL7R	KMT2C	NT5C2					
FLT4	JAK1	NF2	PLCG2					
GATA2	MEN1	PIK3C2B	RNF43					
HDAC9	MSH3	STK11	SHPRH					
HNF1A	NKX3-1	SUZ12						
KDM5A	PIK3CG							
KMT2B	SPEN							
KMT2C	TP53							
LATS1	TP53BP1							
MDM4	XRCC2							
MET	ZFHX3							
MSH3								
NCOR1								
NOTCH1								
PIK3CD								
PIK3R3								
POLD1								
PPM1D								
PPP4R4								
PREX2								
PTPRS								
PTPRT								
SHPRH								
SMC3								
TFE3								
ZRSR2								

Supplementary Table 5: Cell-panel

Cell Line	From (Company + ID)	Cell Culture Media	Supplement/Additives (end conc.):	Splitting Ratio
MDA-MB-231	ATCC (HTB-26)	DMEM	10 % FBS, L-Glutamine 2 mM (for Sigma)	1to4
MDA-MB-436	ATCC (HTB-130)	DMEM	10 % FBS, 10 µg/mL Insulin, L-Glutamine 2 mM (for Sigma)	1to4
SUM149PT	1)Dr. John Martens/ Erasmus University Medical Center, NL 2) BIOIVT – Elevating Science	Ham's F12	5 % FBS, 5 µg/mL Insulin, 1 µg/mL Hydrocortisone, 10 mM HEPES	1to5
U-2 OS	from Prof. Dr. Andreas Ladurner, Department of Physiological chemistry, LMU	DMEM	10 % FBS, L-Glutamine 2 mM	1to10
BxPC-3	ATCC (CRL-1687)	RPMI-1640	10% FBS	1to4
DLD-1	Horizon (HD PAR-008)	RPMI-1640	10% FBS	1to10
DLD-1 BRCA2 $^{-/-}$	Horizon (HD 105-007)	RPMI-1640	10% FBS	1to5
Capan-1	ATCC (HTB-79)	RPMI-1640	20% FBS	1to3
HCC 1937	ATCC (CRL-2336)	RPMI-1640	10% FBS	1to2
Huh-7	from Prof. Dr. Oliver T. Keppler lab, LMU	DMEM	10 % FBS, L-Glutamine 2 mM	1to20
HCT 116	Sigma Aldrich (91091005)	McCoy's 5A	10% FBS	1to20
SW-620	Sigma Aldrich (87051203)	DMEM	10 % FBS, L-Glutamine 2 mM	1to10
PC-3	Sigma Aldrich (90112714)	DMEM	10 % FBS, L-Glutamine 2 mM	1to4
22Rv1	Sigma Aldrich (5092802)	RPMI-1640 (w/o phenol red)	10 % FBS	1to4
PSN-1	Xin Zhang (Eisbach Bio, UK-Essen, Jens Sieveke lab)	RPMI	10 % FBS	1to16
Hep G2	Sigma Aldrich (85011430)	DMEM	10 % FBS, L-Glutamine 2 mM	1to10
DU-145	ATCC (HTB-81)	MEM	10 % FBS, 1 mM sodium pyruvate	1to10
SK-BR-3	from Prof. Dr. Elfride Nößner Lab, Helmholtz center Munich	DMEM	10 % FBS, L-Glutamine 2 mM	1to4
Ovcar-4	Merck (SCC258) from Prof. Dr. Peter Murray (immunoregulation group IMP)	DMEM	10 % FBS, L-Glutamine 2 mM	1to4

Supplementary Table 6: Chemotherapeutics and FDA and investigational drugs

Compound	Type of Inhibitor	Supplier	ID	Information
Mitomycin C	alkylating agent	Selleckchem	50-07-7	
AZ32	ATMi	Hycultec/MedChem Express	HY-112305	
AZD-0156	ATMi	Hycultec/MedChem Express	HY-100016	
AZD1390	ATMi	Hycultec/MedChem Express	HY-109566	
Ceralasertib	ATRi	Hycultec/MedChem Express	HY-19323	
Elimusertib	ATRi	Hycultec/MedChem Express	HY-101566	
BAY-299	BRDi	Hycultec/MedChem Express	HY-107424	
Lenvatinib	FGFRi	Hycultec/MedChem Express	HY-10981	
AZD5305	PARPi	Hycultec/MedChem Express	HY-132167	
niraparib	PARPi	Hycultec/MedChem Express	HY-10619	
olaparib	PARPi	Hycultec/MedChem Express	HY-10162	Solubility limit in cell-assay 50 µM
pamiparib	PARPi	Hycultec/MedChem Express	HY-104044	
rucaparib	PARPi	Hycultec/MedChem Express	HY-10617A	
talazoparib	PARPi	Hycultec/MedChem Express	HY-16106	Solubility limit in cell-assay 5-10 µM
veliparib	PARPi	Hycultec/MedChem Express	HY-10129	
Paclitaxel	taxane	Hycultec/MedChem Express	HY-B0015	
SN38	TOP1i	Hycultec/MedChem Express	HY-13704	
Topotecan	TOP1i	Hycultec/MedChem Express	HY-13768	
Teniposide	TOP2i	Hycultec/MedChem Express	HY-13761	
5-Fluorouracil	thymidylate synthase (TS) inhibitor	Hycultec/MedChem Express	HY-90006	
Adavosertib	Wee1i	Hycultec/MedChem Express	HY-10993	

Supplementary Table 7: Antibodies

Antibodies (primary)	Supplier	Catalog Number	Source	Dilution
ALC1	Department of Physiological Chemistry, LMU	-	rabbit	WB: 1to2000
Monoclonal anti-α-tubulin antibody produced in mouse clone DM1A	Sigma	T9026	mouse	WB: 1to50000
Anti-gH2AX (rabbit)	Abcam	ab11174	rabbit	WB: 1to2500, FACS: 1to500
PARP1(and cleavedPARP1)	SantaCruz	Sc8007	mouse	WB: 1to500
RAD51	Sigma	PC130	rabbit	IF: 1to200; WB: 1to2500
γH2AX	Novus	NB100-74435	mouse	IF: 1to500
Antibodies (secondary)	**Vendor**	**Catalog Number**	**Source**	**Dilution**
IRDye 800CW goat anti-rabbit 925-32211	Li-Cor	925-32211	goat anti-rabbit	WB: 1to15000
IRDye 680RD donkey anti-mouse 925-68072	Li-Cor	925-68072	donkey anti-mouse	WB: 1to15000
Goat anti-Rabbit IgG (H+L) Alexa Fluor™ 488	Invitrogen	a11034	goat anti-rabbit	IF: 1to1500; FACS: 1to3000
sheep IgG anti-mouse IgG (H+L)-Cy3, MinX Hu, Bo, Ho	Dianova	515-165-062	sheep anti-mouse	IF: 1to500

Supplementary Table 8: Plasmids used for LCI-assay

Insert	Plasmid Name	Reference
EGFP-ALC1	pEGFP-C1_hsCHD1L(hs1-989)	Sellou et al. 2016
PARP1-GFP	pEGFP-N1_hsPARP1(hs1-1014)-GSGSGS-EGFP	Eisbach Bio GmbH
PARP2-GFP	pEGFP-N1_hsPARP2(hs1-583)-GSGSGS-EGFP	Eisbach Bio GmbH
PARP3-GFP	pEGFP-N1_hsPARP3(hs1-533)-GSGSGS-EGFP	Eisbach Bio GmbH
XRCC1-YFP	pEYFP-N1_hsXRCCY(hs1-633(Q399R))-EYFP	Blessing et al. 2020

Supplementary Table 9: IC50 values, SEM, and estimated EC50 values of the 96h survival assay

Compound	Cell Line	IC50 (Prism)	SEM	Technical Replicates	Biological Replicates	EC50 [µM]
EIS-4	22rv1	53.019	32.811	2	3	25.000
EIS-4	BXPC-3	26.089	4.676	2	5	30.000
EIS-4	Capan-1	25.874	6.507	2	2	>50
EIS-4	DLD-1	23.906	2.826	2	2	22.000
EIS-4	DLD-1 BRCA2 -/-	27.701	5.314	2	2	22.000
EIS-4	DU-145	39.545	15.993	2	2	34.000
EIS-4	HCC1937	33.375	18.003	2	4	24.000
EIS-4	HCT 116	31.165	2.758	2	2	25.000
EIS-4	Hep G2	25.045	6.962	2	2	25.000
EIS-4	MDA-MB-231	33.602	17.382	2	4	>50
EIS-4	MDA-MB-436	27.529	2.841	2	4	33.000
EIS-4	PC-3	41.648	16.678	2	4	35.000
EIS-4	PSN-1	20.296	1.862	2	2	22.000
EIS-4	SUM149PT	14.942	0.888	2	3	13.500
EIS-4	SW-620	66.001	637.093	2	2	>50
EIS-4	U-2 OS	26.381	10.801	2	2	30.000
EIS-5	MDA-MB-231	22.806	3.571	2	1	>50
EIS-5	SUM149PT	131.820		2	1	>50
EIS-3	22RV1	9.139	2.470	2	3	7.500
EIS-3	BXPC-3	6.125	0.439	2	3	6.125
EIS-3	Capan-1	40.333	59.564	2	1	38.000
EIS-3	DLD-1	15.698	8.990	2	3	10.000
EIS-3	DLD-1 BRCA2 -/-	27.606	41.724	2	3	11.000
EIS-3	DU-145	11.379	1.266	2	6	11.000
EIS-3	HCC1937	49.415	75.419	2	2	26.000
EIS-3	HCT 116	6.712	0.304	2	3	7.000
EIS-3	Hep G2	26.227	2410.511	2	1	26.227
EIS-3	MDA-MB-231	29.295	6.327	2	6	38.000
EIS-3	MDA-MB-436	7.231	0.307	2	3	7.231
EIS-3	Ovcar-4	19.696	2.386	2	2	24.000
EIS-3	PC-3	12.736	2.994	2	3	14.000
EIS-3	PSN-1	7.706	0.354	2	7	7.706
EIS-3	SK-BR-3	29.263	19550.508	2	1	>50
EIS-3	SUM149PT	1.960	0.120	2	8	2.000
EIS-1	22Rv1	2.538	1.283	2	5	4.000
EIS-1	BXPC-3	12.770	3.484	2	3	24.000
EIS-1	Capan-1	7.876	0.943	2	2	9.000
EIS-1	DLD-1	7.501	0.575	2	3	7.501
EIS-1	DLD-1 BRCA2 -/-	4.363	0.328	2	3	4.363
EIS-1	DU-145	5.563	0.342	2	7	5.563
EIS-1	HCC1937	7.607	0.865	2	2	>50
EIS-1	HCT 116	1.966	0.108	2	5	1.966
EIS-1	Hep G2	2.545	0.406	2	3	3.000
EIS-1	HUH-7	15.775	1.556	2	1	18.000

Compound	Cell Line	IC50 (Prism)	SEM	Technical Replicates	Biological Replicates	EC50 [µM]
EIS-1	MDA-MB-231	535.648	3352.609	2	9	33.000
EIS-1	MDA-MB-436	4.694	1.900	2	2	4.694
EIS-1	Ovcar-4	5.602	1.731	2	2	>50
EIS-1	PC-3	12.406	2.874	2	8	50.000
EIS-1	PSN-1	3.011	0.216	2	9	3.011
EIS-1	SK-BR-3	10.956	2.011	2	1	20.000
EIS-1	SUM149PT	2.577	0.647	2	8	4.000
EIS-1	SW-620	7.334	8.520	2	2	7.334
EIS-1	U-2 OS	7.819	2.000	2	2	13.000
EIS-6	MDA-MB-231	30.657	6563.783	2	1	>50
EIS-6	SUM149PT	77.930	193.551	2	1	40.000
EIS-2	22RV1	0.017	0.009	2	1	0.017
EIS-2	BXPC-3	0.277	0.103	2	1	0.300
EIS-2	Capan-1	0.266	0.027	2	1	0.300
EIS-2	DLD-1	0.089	0.009	2	2	0.095
EIS-2	DLD-1 BRCA2 -/-	0.030	0.007	2	2	0.030
EIS-2	DU-145	0.081	0.010	2	5	0.080
EIS-2	HCT 116	0.019	0.004	2	4	0.019
EIS-2	Hep G2	0.027	0.005	2	1	0.048
EIS-2	HUH-7	0.051	0.008	2	1	0.070
EIS-2	MDA-MB-231	0.165	0.060	2	6	0.200
EIS-2	Ovcar-4	0.133	0.048	2	2	1.000
EIS-2	PC-3	0.109	0.042	2	1	0.150
EIS-2	PSN-1	0.036	0.004	2	7	0.036
EIS-2	SK-BR-3	0.227	0.010	2	1	0.300
EIS-2	SUM149PT	0.011	0.008	2	6	0.014
EIS-2	U-2 OS	26.143	500.764	2	1	0.360
olaparib	BXPC-3	17.578	4.645	2	1	>50
olaparib	Capan-1	5.477	1.142	2	1	9.000
olaparib	DLD-1	20.474	4.612	2	1	>50
olaparib	DLD-1 BRCA2 -/-	0.996	0.841	2	1	1.500
olaparib	DU-145	9.615	1.281	2	4	8.000
olaparib	HCC1937	15.296	7.967	2	2	>50
olaparib	HCT 116	4.007	0.682	2	4	5.000
olaparib	Hep G2	58.212	351.846	2	1	30.000
olaparib	MDA-MB-231	6.509	4.137	2	1	16.000
olaparib	MDA-MB-436	0.650	0.824	2	2	0.600
olaparib	Ovcar-4	3.949	0.803	2	2	50.000
olaparib	PC-3	20.559	11.428	2	1	50.000
olaparib	PSN-1	4.239	0.295	2	7	4.400
olaparib	SK-BR-3	14.213	3.718	2	1	30.000
olaparib	SUM149PT	6.426	0.582	2	1	14.000
olaparib	SW-620	2.621	0.470	2	2	4.000
olaparib	U-2 OS	920.024	173261.197	2	1	50.000
talazoparib	22RV1	0.105	0.076	2	1	0.600
talazoparib	BXPC-3	1.521	1.276	2	1	>10

Compound	Cell Line	IC50 (Prism)	SEM	Technical Replicates	Biological Replicates	EC50 [µM]
talazoparib	Hep G2	0.508	0.261	2	1	3.400
talazoparib	MDA-MB-231	n.d.	0.000	2	1	>10
talazoparib	PC-3	4.353	16.637	2	1	8.000
talazoparib	SUM149PT	0.006	0.046	2	1	>10
talazoparib	DLD-1	0.759	0.091	2	1	0.625
talazoparib	DLD-1 BRCA2 -/-	0.156	0.297	2	1	0.060
talazoparib	DU-145	0.689	0.176	2	4	0.360
talazoparib	HCT 116	0.010	0.046	2	3	0.020
talazoparib	MDA-MB-436	0.009	0.104	2	1	0.020
talazoparib	Ovcar-4	0.167	0.243	2	2	2.500
talazoparib	PSN-1	0.036	0.038	2	5	0.034
talazoparib	SK-BR-3	0.856	0.060	2	1	1.200
talazoparib	SW-620	0.322	0.034	2	1	0.078

Supplementary Table 10: IC50 values, SEM, and estimated EC50 values of the 11-day survival assay

Compound	Cell Line	IC50 (Prism)	SEM	Technical Replicates	Biological Replicates	EC50 [µM]
EIS-4	22rv1	68.247	485.870	2	1	16.000
EIS-4	BXPC-3	38.473	58.370	2	1	37.000
EIS-4	DLD-1	16.562	1.181	2	1	17.000
EIS-4	DLD-1 BRCA2 -/-	22.926	6.440	2	1	21.000
EIS-4	DU-145	1.514	18840.476	2	3	>50
EIS-4	Hep G2	55.371	1464.761	2	1	>50
EIS-4	HUH-7	50.060	225.658	2	1	17.000
EIS-4	MDA-MB-231	31.478	12.825	2	4	36.000
EIS-4	MDA-MB-436	25.524	5.967	2	1	34.000
EIS-4	PC-3	10.156	2.262	2	1	9.700
EIS-4	PSN-1	33.198	28.353	2	1	17.000
EIS-4	SUM149PT	6.851	0.495	2	5	7.800
EIS-3	22rv1	11.550	88.674	2	1	12.000
EIS-3	BXPC-3	3.867	0.459	2	1	4.900
EIS-3	DLD-1	6.991	2.021	2	2	6.200
EIS-3	DLD-1 BRCA2 -/-	4.579	0.955	2	2	5.500
EIS-3	DU-145	9.131	0.830	2	3	11.000
EIS-3	Hep G2	1.615	58661.570	2	1	>50
EIS-3	HUH-7	24.463	1015777.885	2	1	>50
EIS-3	MDA-MB-231	13.639	1.851	2	4	14.000
EIS-3	MDA-MB-436	6.387	0.273	2	1	7.400
EIS-3	PC-3	57.027	225.939	2	1	>50
EIS-3	PSN-1	3.495	0.157	2	1	3.700
EIS-3	SUM149PT	1.307	0.082	2	7	1.400
EIS-1	22rv1	0.908	0.190	2	1	1.000
EIS-1	BXPC-3	3.544	23.389	2	1	1.800

Compound	Cell Line	IC50 (Prism)	SEM	Technical Replicates	Biological Replicates	EC50 [µM]
EIS-1	DLD-1	3.673	0.350	2	2	3.800
EIS-1	DLD-1 BRCA2 -/-	0.937	0.298	2	2	1.300
EIS-1	DU-145	5.433	3.765	2	3	6.200
EIS-1	HCT-116	0.357	0.207	2	1	0.340
EIS-1	Hep G2	12.068	0.655	2	1	13.000
EIS-1	HUH-7	1.686	0.257	2	1	1.900
EIS-1	MDA-MB-231	3.490	0.985	2	4	3.900
EIS-1	MDA-MB-436	0.261	0.058	2	1	0.320
EIS-1	PC-3	3.822	0.693	2	1	4.500
EIS-1	PSN-1	0.675	0.072	2	1	0.710
EIS-1	SUM149PT	0.137	0.020	2	6	0.160
EIS-2	DLD-1	0.074	0.002	2	1	0.086
EIS-2	DLD-1 BRCA2 -/-	0.009	0.006	2	1	0.013
EIS-2	DU-145	0.202	0.104	4	1	0.210
EIS-2	HCT-116	0.005	0.001	2	1	0.005
EIS-2	MDA-MB-231	0.007	0.001	2	1	0.007
EIS-2	SUM149PT	0.001	0.000	2	1	0.001
olaparib	DU-145	4.739	0.337	2	3	4.800
olaparib	MDA-MB-231	1.120	0.700	2	1	1.000
olaparib	PSN-1	0.917	0.137	2	1	0.900
olaparib	SUM149PT	0.004	0.009	2	1	0.006
talazoparib	DLD-1	4156.213	16164730.938	2	1	0.100
talazoparib	DLD-1 BRCA2 -/-	0.003	0.002	2	1	0.003
talazoparib	DU-145	0.046	0.021	2	3	0.051
talazoparib	MDA-MB-231	0.003	0.001	2	1	0.003
talazoparib	PSN-1	0.002	0.018	2	1	<0.008
talazoparib	SUM149PT	0.000	0.004	2	1	<0.0004

Due to solubility limits of the compounds, the highest assay concentrations reached for ALC1i and olaparib were 50 µM and 5-10 µM for talazoparib.

Supplementary Table 11: IR-induced Foci formation, Raw Data (FociCounter)

Cell Line	Foci	Condition	Fraction <5 Foci	Fraction ≥5 Foci	SD Fraction <5	SD Fraction ≥5
BXPC-3	γH2AX	2h 0Gy	0.54	0.46	1.39	1.27
BXPC-3	γH2AX	2h 1Gy	0.17	0.83	0.45	1.97
DLD-1	γH2AX	2h 0Gy	0.59	0.41	0.21	0.19
DLD-1	γH2AX	2h 1Gy	0.20	0.80	0.13	0.11
DLD-1 BRCA2-/-	γH2AX	2h 0Gy	0.59	0.41	0.21	0.11
DLD-1 BRCA2-/-	γH2AX	2h 1Gy	0.25	0.75	0.03	0.14
DU-145	γH2AX	2h 0Gy	0.62	0.38	0.06	0.07
DU-145	γH2AX	2h 1Gy	0.31	0.69	0.34	0.09
HCT 116	γH2AX	2h 0Gy	0.58	0.42	0.01	0.16
HCT 116	γH2AX	2h 1Gy	0.23	0.77	0.23	0.02
MDA-MB-231	γH2AX	2h 0Gy	0.66	0.34	0.11	0.15
MDA-MB-231	γH2AX	2h 1Gy	0.18	0.82	0.06	0.01
MDA-MB-436	γH2AX	2h 0Gy	0.69	0.31	0.63	0.23
MDA-MB-436	γH2AX	2h 1Gy	0.47	0.53	0.23	0.09
PC-3	γH2AX	2h 0Gy	0.71	0.29	0.11	0.11
PC-3	γH2AX	2h 1Gy	0.44	0.56	0.35	0.13
PSN-1	γH2AX	2h 0Gy	0.72	0.28	0.21	0.11
PSN-1	γH2AX	2h 1Gy	0.21	0.79	0.07	0.05
SUM149PT	γH2AX	2h 0Gy	0.80	0.20	0.12	0.12
SUM149PT	γH2AX	2h 1Gy	0.28	0.72	0.11	0.09
BXPC3	RAD51	2h 0Gy	0.91	0.09	2.61	0.03
BXPC3	RAD51	2h 1Gy	0.55	0.45	1.23	0.95
DLD-1	RAD51	2h 0Gy	0.81	0.19	0.18	0.09
DLD-1	RAD51	2h 1Gy	0.69	0.31	0.26	0.05
DLD-1 BRCA2-/-	RAD51	2h 0Gy	0.84	0.16	0.17	0.18
DLD-1 BRCA2-/-	RAD51	2h 1Gy	0.72	0.28	0.22	0.10
DU-145	RAD51	2h 0Gy	0.85	0.15	0.06	0.05
DU-145	RAD51	2h 1Gy	0.71	0.29	0.31	0.07
HCT 116	RAD51	2h 0Gy	0.83	0.17	0.12	0.04
HCT 116	RAD51	2h 1Gy	0.44	0.56	0.20	0.09
MDA-MB-231	RAD51	2h 0Gy	0.76	0.24	0.16	0.17
MDA-MB-231	RAD51	2h 1Gy	0.65	0.35	0.18	0.14
MDA-MB-436	RAD51	2h 0Gy	0.93	0.07	0.53	0.03
MDA-MB-436	RAD51	2h 1Gy	0.88	0.12	0.33	0.04
PC-3	RAD51	2h 0Gy	0.82	0.18	0.08	0.02
PC-3	RAD51	2h 1Gy	0.78	0.22	0.44	0.08
PSN-1	RAD51	2h 0Gy	0.88	0.12	0.23	0.06
PSN-1	RAD51	2h 1Gy	0.63	0.37	0.21	0.19
SUM149PT	RAD51	2h 0Gy	0.89	0.11	0.11	0.05
SUM149PT	RAD51	2h 1Gy	0.88	0.12	0.10	0.05

Supplementary Table 12: γH2AX positive foci fractions after irradiation with 1 Gy

yH2AX-Foci	Number of Replicates	Two-way ANOVA Test (multiple comparison)	p-Value
BXPC3	3	**	0.0012
DLD-1	4	**	0.0018
DLD-1 BRCA2 -/-	4	*	0.0106
DU-145	4	*	0.011
HCT 116	2	ns	0.1285
MDA-MB-231	4	****	<0.0001
MDA-MB-436	4	ns	0.1438
PC-3	4	*	0.0123
PSN-1	4	****	<0.0001
SUM149PT	4	****	<0.0001

Supplementary Table 13: RAD51 foci positive fractions after irradiation with 1Gy

RAD51-Foci	Number of Replicates	Two-way ANOVA Test (multiple comparison)	p-Value
BXPC3	3	*	0.0126
DLD-1	4	**	0.0075
DLD-1 BRCA2 -/-	4	ns	0.4409
DU-145	4	*	0.0296
HCT 116	2	**	0.0088
MDA-MB-231	4	ns	0.402
MDA-MB-436	4	ns	0.0723
PC-3	4	ns	0.6071
PSN-1	4	*	0.0134
SUM149PT	4	ns	0.9833

Supplementary Table 14: Manually assessed γH2AX foci fractions of cell lines for all timepoints

Cell Line	γH2AX Foci	Condition	Fractions of Nuclei (%)	SD	Biological Replicates
DLD-1 BRCA2 -/-	negative	0Gy,2h	16.6	2.1	3
DLD-1 BRCA2 -/-	negative	0Gy,24h	13.9	4.8	3
DLD-1 BRCA2 -/-	negative	1Gy,2h	2.2	2.4	3
DLD-1 BRCA2 -/-	negative	1Gy,24h	5	4.5	3
DLD-1 BRCA2 -/-	1-10	0Gy,2h	49.9	9.2	3
DLD-1 BRCA2 -/-	1-10	0Gy,24h	59.9	9.4	3
DLD-1 BRCA2 -/-	1-10	1Gy,2h	29.7	21.8	3
DLD-1 BRCA2 -/-	1-10	1Gy,24h	52.9	2.2	3
DLD-1 BRCA2 -/-	11-20	0Gy,2h	24.6	4.4	3
DLD-1 BRCA2 -/-	11-20	0Gy,24h	17.7	6.2	3
DLD-1 BRCA2 -/-	11-20	1Gy,2h	33.7	8.5	3
DLD-1 BRCA2 -/-	11-20	1Gy,24h	32	1.1	3
DLD-1 BRCA2 -/-	>20	0Gy,2h	11.9	8.8	3
DLD-1 BRCA2 -/-	>20	0Gy,24h	8.5	7.1	3
DLD-1 BRCA2 -/-	>20	1Gy,2h	34.4	20.2	3
DLD-1 BRCA2 -/-	>20	1Gy,24h	10.1	3.6	3
MDA-MB-436	negative	0Gy,2h	27.4	17.4	3
MDA-MB-436	negative	0Gy,24h	39	16.2	3
MDA-MB-436	negative	1Gy,2h	12.5	10.7	3
MDA-MB-436	negative	1Gy,24h	26.8	12.8	3
MDA-MB-436	1-10	0Gy,2h	50.9	0.9	3
MDA-MB-436	1-10	0Gy,24h	46.7	13.1	3
MDA-MB-436	1-10	1Gy,2h	50.8	8.3	3
MDA-MB-436	1-10	1Gy,24h	62.6	16.8	3
MDA-MB-436	11-20	0Gy,2h	19.5	15.3	3
MDA-MB-436	11-20	0Gy,24h	9.1	1.4	3
MDA-MB-436	11-20	1Gy,2h	25.4	7.5	3
MDA-MB-436	11-20	1Gy,24h	6.4	6.1	3
MDA-MB-436	>20	0Gy,2h	2.2	1.9	3
MDA-MB-436	>20	0Gy,24h	5.1	4.5	3
MDA-MB-436	>20	1Gy,2h	11.3	10.2	3
MDA-MB-436	>20	1Gy,24h	4.2	1.6	3
SUM149PT	negative	0Gy,2h	48.5	3.1	3
SUM149PT	negative	0Gy,24h	36.8	10.1	3
SUM149PT	negative	1Gy,2h	5.3	4.5	3
SUM149PT	negative	1Gy,24h	26	4.5	3
SUM149PT	1-10	0Gy,2h	35.6	6.4	3
SUM149PT	1-10	0Gy,24h	40	10.7	3
SUM149PT	1-10	1Gy,2h	34.6	6.7	3
SUM149PT	1-10	1Gy,24h	56.5	8.9	3
SUM149PT	11-20	0Gy,2h	7.8	3.5	3
SUM149PT	11-20	0Gy,24h	15.8	4.9	3
SUM149PT	11-20	1Gy,2h	45.1	2.5	3
SUM149PT	11-20	1Gy,24h	9.6	3.9	3

Cell Line	γH2AX Foci	Condition	Fractions of Nuclei (%)	SD	Biological Replicates
SUM149PT	>20	0Gy,2h	6	6.7	3
SUM149PT	>20	0Gy,24h	8.5	7.9	3
SUM149PT	>20	1Gy,2h	15.4	0.6	3
SUM149PT	>20	1Gy,24h	4.6	4	3
DU-145	negative	0Gy,2h	22.4	19.4	3
DU-145	negative	0Gy,24h	19.8	14.1	3
DU-145	negative	1Gy,2h	12.5	9.9	3
DU-145	negative	1Gy,24h	29.1	22.3	3
DU-145	1-10	0Gy,2h	48	5.5	3
DU-145	1-10	0Gy,24h	52.9	5.7	3
DU-145	1-10	1Gy,2h	29.7	13.2	3
DU-145	1-10	1Gy,24h	40.4	9.7	3
DU-145	11-20	0Gy,2h	15.4	5.4	3
DU-145	11-20	0Gy,24h	17	12.1	3
DU-145	11-20	1Gy,2h	37.4	6.5	3
DU-145	11-20	1Gy,24h	21.1	11.6	3
DU-145	>20	0Gy,2h	14.6	14.6	3
DU-145	>20	0Gy,24h	10.5	7.6	3
DU-145	>20	1Gy,2h	20.5	12.8	3
DU-145	>20	1Gy,24h	10.5	7.2	3
PC-3	negative	0Gy,2h	20.3	9.8	3
PC-3	negative	0Gy,24h	18.9	12.8	3
PC-3	negative	1Gy,2h	2.7	3.1	3
PC-3	negative	1Gy,24h	15.9	6.6	3
PC-3	1-10	0Gy,2h	54.4	12.1	3
PC-3	1-10	0Gy,24h	46.3	13.7	3
PC-3	1-10	1Gy,2h	35.5	12.5	3
PC-3	1-10	1Gy,24h	57.8	3.2	3
PC-3	11-20	0Gy,2h	14.9	4.5	3
PC-3	11-20	0Gy,24h	24.4	2.2	3
PC-3	11-20	1Gy,2h	36.2	7.3	3
PC-3	11-20	1Gy,24h	12.5	4.3	3
PC-3	>20	0Gy,2h	9.8	2.6	3
PC-3	>20	0Gy,24h	10.3	13.3	3
PC-3	>20	1Gy,2h	25.6	4	3
PC-3	>20	1Gy,24h	13.7	3.1	3
DLD-1	negative	0Gy,2h	33	11.5	3
DLD-1	negative	0Gy,24h	43.9	13.8	3
DLD-1	negative	1Gy,2h	0.9	1.6	3
DLD-1	negative	1Gy,24h	35.5	13.6	3
DLD-1	1-10	0Gy,2h	39.8	12.7	3
DLD-1	1-10	0Gy,24h	37.2	1	3
DLD-1	1-10	1Gy,2h	51.7	14.3	3
DLD-1	1-10	1Gy,24h	34.5	8.9	3
DLD-1	11-20	0Gy,2h	14.1	7.6	3
DLD-1	11-20	0Gy,24h	14.8	9.8	3

Cell Line	γH2AX Foci	Condition	Fractions of Nuclei (%)	SD	Biological Replicates
DLD-1	11-20	1Gy,2h	33.1	13.1	3
DLD-1	11-20	1Gy,24h	22.3	13.3	3
DLD-1	>20	0Gy,2h	13	19.5	3
DLD-1	>20	0Gy,24h	4.2	4.2	3
DLD-1	>20	1Gy,2h	14.3	2.5	3
DLD-1	>20	1Gy,24h	7.8	9.4	3
BX-PC-3	negative	0Gy,2h	17.5	3.5	3
BX-PC-3	negative	0Gy,24h	23.5	14.1	3
BX-PC-3	negative	1Gy,2h	2.1	3.6	3
BX-PC-3	negative	1Gy,24h	13	1.6	3
BX-PC-3	1-10	0Gy,2h	59.8	13.2	3
BX-PC-3	1-10	0Gy,24h	55.9	28	3
BX-PC-3	1-10	1Gy,2h	39	21.6	3
BX-PC-3	1-10	1Gy,24h	60.8	7	3
BX-PC-3	11-20	0Gy,2h	14.7	5.5	3
BX-PC-3	11-20	0Gy,24h	16.1	10.1	3
BX-PC-3	11-20	1Gy,2h	28.4	7.8	3
BX-PC-3	11-20	1Gy,24h	16	2.9	3
BX-PC-3	>20	0Gy,2h	8.1	7.9	3
BX-PC-3	>20	0Gy,24h	4.5	4.3	3
BX-PC-3	>20	1Gy,2h	27.2	13.6	3
BX-PC-3	>20	1Gy,24h	9.8	8.7	3
MDA-MB-231	negative	0Gy,2h	24.3	9.8	3
MDA-MB-231	negative	0Gy,24h	18.7	4.3	3
MDA-MB-231	negative	1Gy,2h	0.7	1.2	3
MDA-MB-231	negative	1Gy,24h	17.9	6.5	3
MDA-MB-231	1-10	0Gy,2h	39.8	2.9	3
MDA-MB-231	1-10	0Gy,24h	56.3	4.7	3
MDA-MB-231	1-10	1Gy,2h	39.5	11.9	3
MDA-MB-231	1-10	1Gy,24h	56.7	6.4	3
MDA-MB-231	11-20	0Gy,2h	23.3	1.6	3
MDA-MB-231	11-20	0Gy,24h	15.2	1.2	3
MDA-MB-231	11-20	1Gy,2h	42	15.8	3
MDA-MB-231	11-20	1Gy,24h	15.2	3.2	3
MDA-MB-231	>20	0Gy,2h	12.7	6.3	3
MDA-MB-231	>20	0Gy,24h	9.8	8.2	3
MDA-MB-231	>20	1Gy,2h	17.7	5.3	3
MDA-MB-231	>20	1Gy,24h	10.8	4.8	3
PSN-1	negative	0Gy,2h	35.2	6.4	3
PSN-1	negative	0Gy,24h	36.1	17.2	3
PSN-1	negative	1Gy,2h	3.7	3.1	3
PSN-1	negative	1Gy,24h	18.1	15	3
PSN-1	1-10	0Gy,2h	38.3	5.2	3
PSN-1	1-10	0Gy,24h	42.7	3.8	3
PSN-1	1-10	1Gy,2h	39.5	15.9	3
PSN-1	1-10	1Gy,24h	53.5	8.8	3

Cell Line	γH2AX Foci	Condition	Fractions of Nuclei (%)	SD	Biological Replicates
PSN-1	11-20	0Gy,2h	13.1	4.8	3
PSN-1	11-20	0Gy,24h	14.2	9.9	3
PSN-1	11-20	1Gy,2h	27.5	3.6	3
PSN-1	11-20	1Gy,24h	22.2	8.6	3
PSN-1	>20	0Gy,2h	13.5	6.2	3
PSN-1	>20	0Gy,24h	7	7.8	3
PSN-1	>20	1Gy,2h	29.5	15.4	3
PSN-1	>20	1Gy,24h	6	8.6	3
HCT 116	negative	0Gy,2h	19.5		1
HCT 116	negative	0Gy,24h	9.1		1
HCT 116	negative	1Gy,2h	2.8		1
HCT 116	negative	1Gy,24h	31.2		1
HCT 116	1-10	0Gy,2h	55.3		1
HCT 116	1-10	0Gy,24h	45.5		1
HCT 116	1-10	1Gy,2h	50.4		1
HCT 116	1-10	1Gy,24h	60.5		1
HCT 116	11-20	0Gy,2h	21.2		1
HCT 116	11-20	0Gy,24h	27.3		1
HCT 116	11-20	1Gy,2h	38.5		1
HCT 116	11-20	1Gy,24h	7.3		1
HCT 116	>20	0Gy,2h	4.2		1
HCT 116	>20	0Gy,24h	18.1		1
HCT 116	>20	1Gy,2h	8.2		1
HCT 116	>20	1Gy,24h	0.9		1

Supplementary Table 15: References to Table 17

Cell Line	Reference BRCA Deficient	Reference HR Status	Reference RAD51 Foci	Reference PARPi Sensitivity
HCT 116		(De Bernardi et al., 2021; Smeby et al., 2020)	(Gol et al., 2019; J. Huang et al., 2018)	(Corsello et al., 2019; Paviolo et al., 2020; Smeby et al., 2020)
Hep G2			(Y. Wang et al., 2015)	(Corsello et al., 2019; Guillot et al., 2014)
PSN-1			(Bakr et al., 2021; Fokas et al., 2012)	(Bakr et al., 2021; Corsello et al., 2019)
SUM149PT	(Gu et al., 2016; Póti et al., 2018)		(Gu et al., 2016; Wilkerson et al., 2016)	(Hill et al., 2014; Póti et al., 2018)
DLD-1 BRCA2 -/-	(Hucl et al., 2008; Ikegami et al., 2020)		(Hucl et al., 2008; Jimenez-Sainz et al., 2022)	(Hucl et al., 2008; X. Liu et al., 2012)
MDA-MB-436	(Y. Zhao et al., 2022)		(Johnson et al., 2013)	(Keung et al., 2020; Zhu et al., 2021)

DU-145	(Feiersinger et al., 2018)	(Dillon et al., 2022)	(Dillon et al., 2022; Mansour et al., 2018)	(Cahuzac et al., 2022)
22rv1	(Feiersinger et al., 2018; J. Li et al., 2017)		(Miao et al., 2022; Shenoy et al., 2017)	(J. Li et al., 2017; H. Zhang et al., 2022)
SW-620				
DLD-1	(DepMap: The Cancer Dependency Map Project at Broad Institute; Hucl et al., 2008)		(Hucl et al., 2008; Jimenez-Sainz et al., 2022; Schultz et al., 2003)	(X. Liu et al., 2012)
Capan-1	(Porcelli et al., 2012)	(Engelke et al., 2013)	(Tarsounas et al., 2003; Yuan et al., 1999)	(Drew et al., 2010)
U-2 OS			(Garai et al., 2012)	(Corsello et al., 2019; DepMap: The Cancer Dependency Map Project at Broad Institute)
HUH-7			(Chen et al., 2021; Palagyi et al., 2010)	(Corsello et al., 2019; DepMap: The Cancer Dependency Map Project at Broad Institute)
SK-BR-3	(Wesierska-Gadek & Heinzl, 2014)		(Hill et al., 2014; Wilkerson et al., 2016)	(Keung et al., 2020; Wesierska-Gadek & Heinzl, 2014)
BXPC-3		(Engelke et al., 2013)	(Engelke et al., 2013; Yuan et al., 1999)	(Falchi et al., 2017)
MDA-MB-231	(Drew et al., 2010)		(Hill et al., 2014)	(Drew et al., 2010)
PC-3			(Xiao et al., 2013)	(Zhou et al., 2021)
HCC1937	(Arun et al., 2015)		(Yuan et al., 1999)	(Arun et al., 2015)
Ovcar-4			(Lu et al., 2022)	(Corsello et al., 2019; DepMap: The Cancer Dependency Map Project at Broad Institute)

Supplementary Table 16: Analysis of Tail Moments in comet assay

Assay Number	Cell Line	Incubation Time	Compound	Concentration1	Tail Moment	%CV	n (cells)
13	SUM149PT	48 h	DMSO	0.00 µM	1.65677E+15	331.40	220
13	SUM149PT	48 h	EIS-1	0.25 µM	8.8204E+15	122.80	187
13	SUM149PT	48 h	EIS-1	0.50 µM	9.2572E+15	120.63	154
13	SUM149PT	48 h	EIS-1	1.00 µM	1.03835E+16	110.07	147
13	SUM149PT	48 h	EIS-1	2.50 µM	7.47728E+15	134.34	86
14	SUM149PT	48 h	DMSO	0.00 µM	3.79715E+15	235.28	429
14	SUM149PT	48 h	EIS-1	0.25 µM	5.16458E+15	176.59	229
14	SUM149PT	48 h	EIS-1	0.50 µM	4.35177E+15	216.79	208
14	SUM149PT	48 h	EIS-1	1.00 µM	8.39868E+15	105.55	130
14	SUM149PT	48 h	EIS-1	2.50 µM	1.48457E+16	83.84	105

Supplementary Table 17: Dose-response γH2AX foci formation under ALC1i treatment

Cell Line	ALC1i	Concentration	Fraction <15 Foci	SD	Fraction ≥15 Foci	SD	Biol. Replicates n	Significance	2-way-ANOVA; adjusted p-Value
SUM149PT	EIS-1	0.00 µM	0.988	0.002	0.012	0.002	5		
SUM149PT	EIS-1	0.195 µM	0.864	0.044	0.136	0.044	3	ns	0.2039
SUM149PT	EIS-1	0.391 µM	0.860	0.043	0.140	0.043	3	ns	0.1778
SUM149PT	EIS-1	0.781 µM	0.692	0.150	0.308	0.150	3	***	0.0001
SUM149PT	EIS-1	1.563 µM	0.625	n.d.	0.375	n.d.	1	**	0.0014
SUM149PT	EIS-1	3.125 µM	0.609	0.081	0.391	0.081	3	****	<0.0001
SUM149PT	EIS-1	6.250 µM	0.606	0.133	0.394	0.133	2	****	<0.0001
SUM149PT	EIS-1	12.500 µM	0.352	0.040	0.648	0.040	2	****	<0.0001
MDA-MB-231	EIS-1	0.00 µM	0.986	0.014	0.014	0.014	6		
MDA-MB-231	EIS-1	0.195 µM	0.983	0.001	0.017	0.001	3	ns	0.9997
MDA-MB-231	EIS-1	0.391 µM	0.975	0.007	0.025	0.007	3	ns	0.9527
MDA-MB-231	EIS-1	0.781 µM	0.951	0.025	0.049	0.025	2	**	0.0092
MDA-MB-231	EIS-1	1.563 µM	0.979	n.d.	0.021	n.d.	1	ns	0.9996
MDA-MB-231	EIS-1	3.125 µM	0.937	0.030	0.063	0.030	2	**	0.0014
MDA-MB-231	EIS-1	6.250 µM	0.890	0.012	0.110	0.012	2	****	<0.0001
MDA-MB-231	EIS-1	12.500 µM	0.974	0.035	0.026	0.035	2	ns	0.9802
PSN-1	EIS-1	0.000 µM	0.997	0.004	0.003	0.004	2		
PSN-1	EIS-1	3.125 µM	0.756	0.070	0.244	0.070	2	ns	0.0572
PSN-1	EIS-1	6.250 µM	0.663	0.006	0.337	0.006	2	*	0.0105
PSN-1	EIS-1	12.500 µM	0.586	0.139	0.414	0.139	2	**	0.0029
PSN-1	EIS-1	25.000 µM	0.480	n.d.	0.520	n.d.	1	**	0.0026
PSN-1	EIS-1	50.000 µM	0.603	n.d.	0.397	n.d.	1	*	0.0131

Supplementary Table 18: Dose-response RAD51 foci formation under ALC1i treatment

Cell Line	ALC1i	Concentration	Fraction <5 Foci	SD	Fraction ≥5 Foci	SD	Biol. Replicates n	Significance	2-way-ANOVA; adjusted p-Value
SUM149PT	EIS-1	0.00 µM	0.885	0.060	0.115	0.060	5		
SUM149PT	EIS-1	0.195 µM	0.854	0.086	0.146	0.086	3	ns	0.994
SUM149PT	EIS-1	0.391 µM	0.779	0.083	0.221	0.083	3	ns	0.253
SUM149PT	EIS-1	0.781 µM	0.666	0.022	0.334	0.022	3	**	0.001
SUM149PT	EIS-1	1.563 µM	0.720	n.d.	0.280	n.d.	1	ns	0.213
SUM149PT	EIS-1	3.125 µM	0.603	0.037	0.397	0.037	3	****	<0.0001
SUM149PT	EIS-1	6.250 µM	0.507	0.106	0.493	0.106	2	****	<0.0001
SUM149PT	EIS-1	12.500 µM	0.447	0.107	0.553	0.107	2	****	<0.0001
MDA-MB-231	EIS-1	0.00 µM	0.758	0.028	0.242	0.028	5		
MDA-MB-231	EIS-1	0.195 µM	0.752	0.147	0.248	0.147	3	ns	>0.9999
MDA-MB-231	EIS-1	0.391 µM	0.783	0.152	0.217	0.152	3	ns	1.000
MDA-MB-231	EIS-1	0.781 µM	0.715	0.022	0.285	0.022	3	ns	0.989
MDA-MB-231	EIS-1	1.563 µM	0.750	n.d.	0.250	n.d.	1	ns	>0.9999
MDA-MB-231	EIS-1	3.125 µM	0.728	0.048	0.272	0.048	3	ns	0.999
MDA-MB-231	EIS-1	6.250 µM	0.526	0.139	0.474	0.139	2	*	0.047
MDA-MB-231	EIS-1	12.500 µM	0.659	0.074	0.341	0.074	2	ns	0.733
PSN-1	EIS-1	0.000 µM	0.746	0.131	0.254	0.131	2		
PSN-1	EIS-1	3.125 µM	0.375	0.045	0.625	0.045	2	**	0.003
PSN-1	EIS-1	6.250 µM	0.194	0.009	0.806	0.009	2	***	0.000
PSN-1	EIS-1	12.500 µM	0.207	0.009	0.793	0.009	2	***	0.000
PSN-1	EIS-1	25.000 µM	0.267	n.d.	0.733	n.d.	1	**	0.002
PSN-1	EIS-1	50.000 µM	0.281	n.d.	0.719	n.d.	1	**	0.002

Supplementary Table 19: SUM149PT Xenograft raw data

	Vehicle, SyrSpend	125 mg/kg po	62.5 mg/kg po	31.3 mg/kg po	15.6 mg/kg po	7.81 mg/kg po	3.91 mg/kg po
Tumor Volume [mm^3] day0	266.36	287.50	275.12	247.01	253.17	258.50	249.29
number of mice on day0	11.00	6.00	6.00	6.00	6.00	6.00	6.00
StDEV day0	53.47	75.88	69.29	35.88	33.59	40.37	15.36
Tumor Volume [mm^3] day30	972.86	419.51	536.96	562.18	351.40	435.25	558.33
number of mice on day30	2.00	4.00	2.00	5.00	4.00	4.00	5.00
StDEV day30	549.83	141.83	238.49	127.99	168.76	195.29	222.48

Supplementary Table 20: EIS-1 in combination with PARPi in different cell lines

ALC1i Cluster	Assay Number	Cell Line	Compound 1	Compound 2	ZIP-Score Synergy	SEM (+/-)	MSA Score	Curve Fit
A	189	DU-145	EIS-1	talazoparib	28.98	0.74	61.83	
A	187	DU-145	EIS-1	talazoparib	26.38	2.05	51.00	
A	189	DU-145	EIS-1	niraparib	16.31	0.82	43.25	
A	187	DU-145	EIS-1	niraparib	15.63	1.32	36.58	
A	189	DU-145	EIS-1	rucaparib	16.25	2.26	36.94	
A	187	DU-145	EIS-1	rucaparib	10.77	1.28	22.81	
A	189	DU-145	EIS-1	olaparib	24.31	0.88	38.47	
A	187	DU-145	EIS-1	olaparib	16.23	1.74	30.58	flag
A	189	DU-145	EIS-1	veliparib	11.17	0.91	21.07	
A	187	DU-145	EIS-1	veliparib	16.79	2.04	26.44	flag
A	285	PSN-1	EIS-1	talazoparib	28.46	0.62	65.27	
A	225	PSN-1	EIS-1	talazoparib	13.08	n.d.	26.36	
A	171	PSN-1	EIS-1	talazoparib	21.11	0.69	42.96	
A	171	PSN-1	EIS-1	niraparib	9.63	0.71	30.00	
A	171	PSN-1	EIS-1	rucaparib	12.18	0.59	28.47	
A	165	PSN-1	EIS-1	rucaparib	8.71	0.97	26.40	
A	225	PSN-1	EIS-1	olaparib	11.61	n.d.	35.08	
A	171	PSN-1	EIS-1	olaparib	13.54	0.65	31.76	
A	165	PSN-1	EIS-1	olaparib	12.22	0.94	32.82	
A	225	PSN-1	EIS-1	veliparib	8.10	n.d.	21.86	flag
A	171	PSN-1	EIS-1	veliparib	8.47	0.88	15.80	
A	208	22rv1	EIS-1	talazoparib	10.59	0.66	20.52	flag
A	208	22rv1	EIS-1	niraparib	3.86	0.50	16.16	flag
A	208	22rv1	EIS-1	rucaparib	5.85	0.70	16.23	flag
A	208	22rv1	EIS-1	olaparib	11.21	0.74	18.27	flag
A	208	22rv1	EIS-1	veliparib	2.00	0.68	8.12	flag
A	175	BXPC-3	EIS-1	talazoparib	14.17	1.30	19.27	flag
A	175	BXPC-3	EIS-1	niraparib	7.80	1.07	12.65	
A	175	BXPC-3	EIS-1	rucaparib	4.96	1.43	8.85	
A	175	BXPC-3	EIS-1	olaparib	10.01	1.79	16.40	flag
A	175	BXPC-3	EIS-1	veliparib	4.66	2.99	5.29	flag
A	223	HCT 116	EIS-1	talazoparib	5.79	n.d.	19.86	
A	223	HCT 116	EIS-1	niraparib	4.05	0.44	14.17	
A	223	HCT 116	EIS-1	rucaparib	6.72	0.41	18.60	
A	223	HCT 116	EIS-1	olaparib	0.02	0.44	15.26	
A	223	HCT 116	EIS-1	veliparib	1.19	n.d.	8.52	
A	176	Hep G2	EIS-1	talazoparib	7.89	1.17	27.48	flag
A	176	Hep G2	EIS-1	niraparib	7.13	1.51	20.55	
A	176	Hep G2	EIS-1	rucaparib	5.67	1.72	15.88	
A	176	Hep G2	EIS-1	olaparib	7.01	1.48	17.71	flag
A	176	Hep G2	EIS-1	veliparib	8.80	1.70	18.31	flag

Supplementary Table 21: Synergy results of other combination treatments

ALC1i cluster	Assay Number	Cell Line	Compound 1	Compound 2	Drug Class	ZIP-Score Synergy	MSA	Curve Fitting
A	272	PSN-1	EIS-1	5-FU	thymidylate synthase inhibitor	-1.93	6.54	
A	258	PSN-1	EIS-1	Adavosertib	Wee1i	7.34	18.49	
A	244	PSN-1	EIS-1	AZ32	ATMi	8.95	30.45	
A	244	PSN-1	EIS-1	AZD-1056	ATMi	13.37	44.97	
A	272	PSN-1	EIS-1	AZD1390	ATMi	13.65	44.20	
A	258	PSN-1	EIS-1	BAY-299	BRDi	7.13	16.13	
A	244	PSN-1	EIS-1	Ceralasertib	ATRi	5.47	19.09	
A	272	PSN-1	EIS-1	Elimusertib	ATRi	11.58	37.66	
A	258	PSN-1	EIS-1	Lenvatinib	VEGFi, FGFi	-0.90	8.79	flag
A	289	PSN-1	EIS-1	Mitomycin C	alcylating agent	8.55	25.50	
A	194	22rv1	EIS-1	Paclitaxel	taxane	5.84	9.80	
A	194	BXPC-3	EIS-1	Paclitaxel	taxane	-7.19	3.04	flag
A	194	DU-145	EIS-1	Paclitaxel	taxane	1.68	5.30	
A	194	PC-3	EIS-1	Paclitaxel	taxane	1.45	5.09	flag
A	194	PSN-1	EIS-1	Paclitaxel	taxane	1.54	5.59	
A	194	SUM149PT	EIS-1	Paclitaxel	taxane	-3.48	10.13	flag
A	192	22rv1	EIS-1	SN-38	TOP1i	7.32	13.47	
A	192	BXPC-3	EIS-1	SN-38	TOP1i	4.71	8.18	flag
A	220	DLD-1 BRCA2 -/-	EIS-1	SN-38	TOP1i	-0.31	4.46	
A	220	DLD-1	EIS-1	SN-38	TOP1i	3.92	17.89	
A	192	DU-145	EIS-1	SN-38	TOP1i	12.70	30.41	flag
A	267	HCC1937	EIS-1	SN-38	TOP1i	6.27	9.91	flag
A	223	HCT116	EIS-1	SN-38	TOP1i	1.00	7.84	
A	198	MDA-MB-231	EIS-1	SN-38	TOP1i	7.22	9.75	flag
A	246	MDA-MB-436	EIS-1	SN-38	TOP1i	2.31	10.23	flag
A	245	MDA-MB-436	EIS-1	SN-38	TOP1i	0.58	7.04	flag
A	242	PC-3	EIS-1	SN-38	TOP1i	5.49	11.71	flag
A	192	PSN-1	EIS-1	SN-38	TOP1i	12.76	33.95	
A	164	PSN-1	EIS-1	SN-38	TOP1i	9.55	39.29	
A	192	SUM149PT	EIS-1	SN-38	TOP1i	-5.08	14.41	flag
A	245	SW-620	EIS-1	SN-38	TOP1i	0.73	15.56	
A	244	PSN-1	EIS-1	Teniposide	TOP2i	4.04	13.64	
A	244	PSN-1	EIS-1	Topotecan	TOP1i	16.01	40.97	

Supplementary Table 22: 96h survival assay results for 8-week stability assay of PARPi-resistant cells

Assay Number	Cell Line	Compound	Information	Fold Resistance (EC50) to Parental Cell Line
281	DU-145	EIS-1	2weeks after treatment	
281	DU-145, olaparib-R, clone 2	EIS-1	2weeks after treatment	1.14
281	HCT 116	EIS-1	2weeks after treatment	
281	HCT 116, olaparib-R, clone 2	EIS-1	2weeks after treatment	1.85
281	PSN-1	EIS-1	2weeks after treatment	
281	PSN-1, talazoparib-R, clone E	EIS-1	2weeks after treatment	1.95
282	DU-145	EIS-1	3weeks after treatment	
282	DU-145, olaparib-R, clone 2	EIS-1	3weeks after treatment	1.19
282	HCT 116	EIS-1	3weeks after treatment	
282	HCT 116, olaparib-R, clone 2	EIS-1	3weeks after treatment	1.96
282	PSN-1	EIS-1	3weeks after treatment	
282	PSN-1, talazoparib-R, clone E	EIS-1	3weeks after treatment	1.80
283	DU-145	EIS-1	4weeks after treatment	
283	DU-145, olaparib-R, clone 2	EIS-1	4weeks after treatment	1.82
283	HCT 116	EIS-1	4weeks after treatment	
283	HCT 116, olaparib-R, clone 2	EIS-1	4weeks after treatment	0.96
283	PSN-1	EIS-1	4weeks after treatment	
283	PSN-1, talazoparib-R, clone E	EIS-1	4weeks after treatment	1.47
284	DU-145	EIS-1	8weeks after treatment	
284	DU-145, olaparib-R, clone 2	EIS-1	8weeks after treatment	1.04
284	HCT 116	EIS-1	8weeks after treatment	
284	HCT 116, olaparib-R, clone 2	EIS-1	8weeks after treatment	1.40
284	PSN-1	EIS-1	8weeks after treatment	
284	PSN-1, talazoparib-R, clone E	EIS-1	8weeks after treatment	1.69
281	DU-145	olaparib	2weeks after treatment	
281	DU-145, olaparib-R, clone 2	olaparib	2weeks after treatment	4.67
281	HCT 116	olaparib	2weeks after treatment	
281	HCT 116, olaparib-R, clone 2	olaparib	2weeks after treatment	10.28
281	PSN-1	olaparib	2weeks after treatment	
281	PSN-1, talazoparib-R, clone E	olaparib	2weeks after treatment	13.59
282	DU-145	olaparib	3weeks after treatment	
282	DU-145, olaparib-R, clone 2	olaparib	3weeks after treatment	1.82
282	HCT 116	olaparib	3weeks after treatment	
282	HCT 116, olaparib-R, clone 2	olaparib	3weeks after treatment	5.98
282	PSN-1	olaparib	3weeks after treatment	
282	PSN-1, talazoparib-R, clone E	olaparib	3weeks after treatment	>8.17
283	DU-145	olaparib	4weeks after treatment	
283	DU-145, olaparib-R, clone 2	olaparib	4weeks after treatment	4.17
283	HCT 116	olaparib	4weeks after treatment	
283	HCT 116, olaparib-R, clone 2	olaparib	4weeks after treatment	8.20
283	PSN-1	olaparib	4weeks after treatment	
283	PSN-1, talazoparib-R, clone E	olaparib	4weeks after treatment	14.93
284	DU-145	olaparib	8weeks after treatment	
284	DU-145, olaparib-R, clone 2	olaparib	8weeks after treatment	3.20

284	HCT 116	olaparib	8weeks after treatment	
284	HCT 116, olaparib-R, clone 2	olaparib	8weeks after treatment	1.82
284	PSN-1	olaparib	8weeks after treatment	
284	PSN-1, talazoparib-R, clone E	olaparib	8weeks after treatment	0.96
281	DU-145	talazoparib	2weeks after treatment	
281	DU-145, olaparib-R, clone 2	talazoparib	2weeks after treatment	1.47
281	HCT 116	talazoparib	2weeks after treatment	
281	HCT 116, olaparib-R, clone 2	talazoparib	2weeks after treatment	128.06
281	PSN-1	talazoparib	2weeks after treatment	
281	PSN-1, talazoparib-R, clone E	talazoparib	2weeks after treatment	> 118.39
282	DU-145	talazoparib	3weeks after treatment	
282	DU-145, olaparib-R, clone 2	talazoparib	3weeks after treatment	3.93
282	HCT 116	talazoparib	3weeks after treatment	
282	HCT 116, olaparib-R, clone 2	talazoparib	3weeks after treatment	> 29.07
282	PSN-1	talazoparib	3weeks after treatment	
282	PSN-1, talazoparib-R, clone E	talazoparib	3weeks after treatment	> 125.57
283	DU-145	talazoparib	4weeks after treatment	
283	DU-145, olaparib-R, clone 2	talazoparib	4weeks after treatment	166.67
283	HCT 116	talazoparib	4weeks after treatment	
283	HCT 116, olaparib-R, clone 2	talazoparib	4weeks after treatment	1.82
283	PSN-1	talazoparib	4weeks after treatment	
283	PSN-1, talazoparib-R, clone E	talazoparib	4weeks after treatment	> 250.00
284	DU-145	talazoparib	8weeks after treatment	
284	DU-145, olaparib-R, clone 2	talazoparib	8weeks after treatment	2.22
284	HCT 116	talazoparib	8weeks after treatment	
284	HCT 116, olaparib-R, clone 2	talazoparib	8weeks after treatment	3.40
284	PSN-1	talazoparib	8weeks after treatment	
284	PSN-1, talazoparib-R, clone E	talazoparib	8weeks after treatment	153.15

Supplementary Table 23: 96h survival assay results for talazoparib-resistant DU-145 cells

Assay number	Cell Line	Compound	Fold Resistance (EC50) to Parental Cell Line
306	DU-145	EIS-1	1.00
306	DU-145, talazoparib, clone 20.1	EIS-1	0.69
306	DU-145, talazoparib, clone 20.2	EIS-1	0.82
306	DU-145, talazoparib, clone 20.4	EIS-1	0.91
306	DU-145, talazoparib, clone 20.6	EIS-1	1.31
306	DU-145, talazoparib, clone 23.1	EIS-1	3.59
306	DU-145, talazoparib, clone 23.2	EIS-1	3.00
306	DU-145, talazoparib, clone 23.3	EIS-1	3.19
306	DU-145, talazoparib, clone 23.4	EIS-1	4.19
306	DU-145, talazoparib, clone 23.7	EIS-1	5.61
306	DU-145, talazoparib, clone 23.8	EIS-1	5.59
306	DU-145, talazoparib, clone 23.9	EIS-1	2.60
306	DU-145, talazoparib, clone 23.10	EIS-1	3.08
306	DU-145, talazoparib, clone 23.11	EIS-1	2.00

Assay number	Cell Line	Compound	Fold Resistance (EC50) to Parental Cell Line
306	DU-145, talazoparib, clone 23.12	EIS-1	1.38
306	DU-145	olaparib	1.00
306	DU-145, talazoparib, clone 20.1	olaparib	1.56
306	DU-145, talazoparib, clone 20.2	olaparib	1.56
306	DU-145, talazoparib, clone 20.4	olaparib	2.06
306	DU-145, talazoparib, clone 20.6	olaparib	1.70
306	DU-145, talazoparib, clone 23.1	olaparib	2.50
306	DU-145, talazoparib, clone 23.2	olaparib	1.56
306	DU-145, talazoparib, clone 23.3	olaparib	1.63
306	DU-145, talazoparib, clone 23.4	olaparib	3.13
306	DU-145, talazoparib, clone 23.7	olaparib	0.63
306	DU-145, talazoparib, clone 23.8	olaparib	1.25
306	DU-145, talazoparib, clone 23.9	olaparib	1.50
306	DU-145, talazoparib, clone 23.10	olaparib	2.56
306	DU-145, talazoparib, clone 23.11	olaparib	1.15
306	DU-145, talazoparib, clone 23.12	olaparib	1.44
306	DU-145	SN-38	1.00
306	DU-145, talazoparib, clone 20.1	SN-38	1.15
306	DU-145, talazoparib, clone 20.2	SN-38	1.36
306	DU-145, talazoparib, clone 20.4	SN-38	1.50
306	DU-145, talazoparib, clone 20.6	SN-38	1.23
306	DU-145, talazoparib, clone 23.1	SN-38	2.42
306	DU-145, talazoparib, clone 23.2	SN-38	2.26
306	DU-145, talazoparib, clone 23.3	SN-38	1.79
306	DU-145, talazoparib, clone 23.4	SN-38	4.18
306	DU-145, talazoparib, clone 23.7	SN-38	1.58
306	DU-145, talazoparib, clone 23.8	SN-38	2.52
306	DU-145, talazoparib, clone 23.9	SN-38	1.49
306	DU-145, talazoparib, clone 23.10	SN-38	2.26
306	DU-145, talazoparib, clone 23.11	SN-38	1.64
306	DU-145, talazoparib, clone 23.12	SN-38	1.80
306	DU-145	talazoparib	1.00
306	DU-145, talazoparib, clone 20.1	talazoparib	3.80
306	DU-145, talazoparib, clone 20.2	talazoparib	7.04
306	DU-145, talazoparib, clone 20.4	talazoparib	7.04
306	DU-145, talazoparib, clone 20.6	talazoparib	7.04
306	DU-145, talazoparib, clone 23.1	talazoparib	7.04
306	DU-145, talazoparib, clone 23.2	talazoparib	7.04
306	DU-145, talazoparib, clone 23.3	talazoparib	7.04
306	DU-145, talazoparib, clone 23.4	talazoparib	7.04
306	DU-145, talazoparib, clone 23.7	talazoparib	3.66
306	DU-145, talazoparib, clone 23.8	talazoparib	7.04
306	DU-145, talazoparib, clone 23.9	talazoparib	8.02
306	DU-145, talazoparib, clone 23.10	talazoparib	7.04
306	DU-145, talazoparib, clone 23.11	talazoparib	7.04
306	DU-145, talazoparib, clone 23.12	talazoparib	7.04

Supplementary Table 24: 96h survival assay results for talazoparib-resistant PSN-1 cell lines

Assay number	Cell Line	Compound	Fold Resistance (EC50) to Parental Cell Line
255, 263, 273, 295, 296	PSN-1	EIS-1	1.000
255, 263, 273	PSN-1 talazoparib resistant clone E	EIS-1	4.517
295	PSN-1, talazoparib, clone 10	EIS-1	1.532
295	PSN-1, talazoparib, clone 11	EIS-1	1.535
295	PSN-1, talazoparib, clone 13	EIS-1	2.764
296	PSN-1, talazoparib, clone 14	EIS-1	1.185
296	PSN-1, talazoparib, clone 15	EIS-1	0.924
295	PSN-1, talazoparib, clone 16	EIS-1	4.990
295	PSN-1, talazoparib, clone 17	EIS-1	3.071
296	PSN-1, talazoparib, clone 18	EIS-1	2.231
296	PSN-1, talazoparib, clone 2	EIS-1	6.526
296	PSN-1, talazoparib, clone 20	EIS-1	3.206
296	PSN-1, talazoparib, clone 23	EIS-1	2.687
296	PSN-1, talazoparib, clone 24	EIS-1	4.606
295	PSN-1, talazoparib, clone 3	EIS-1	4.784
295	PSN-1, talazoparib, clone 4	EIS-1	2.835
295	PSN-1, talazoparib, clone 5	EIS-1	3.839
296	PSN-1, talazoparib, clone 6	EIS-1	4.222
296	PSN-1, talazoparib, clone 7	EIS-1	0.867
295	PSN-1, talazoparib, clone 9	EIS-1	2.321
255, 263, 273, 295, 296	PSN-1	olaparib	1.000
255, 263, 273	PSN-1 talazoparib resistant clone E	olaparib	10.627
295	PSN-1, talazoparib, clone 10	olaparib	9.157
295	PSN-1, talazoparib, clone 11	olaparib	9.639
295	PSN-1, talazoparib, clone 13	olaparib	9.639
296	PSN-1, talazoparib, clone 14	olaparib	1.928
296	PSN-1, talazoparib, clone 15	olaparib	5.784
295	PSN-1, talazoparib, clone 16	olaparib	9.157
295	PSN-1, talazoparib, clone 17	olaparib	12.049
296	PSN-1, talazoparib, clone 18	olaparib	9.157
296	PSN-1, talazoparib, clone 2	olaparib	5.784
296	PSN-1, talazoparib, clone 20	olaparib	5.061
296	PSN-1, talazoparib, clone 23	olaparib	9.880
296	PSN-1, talazoparib, clone 24	olaparib	12.049
295	PSN-1, talazoparib, clone 3	olaparib	8.916
295	PSN-1, talazoparib, clone 4	olaparib	5.302
295	PSN-1, talazoparib, clone 5	olaparib	5.543
296	PSN-1, talazoparib, clone 6	olaparib	5.302
296	PSN-1, talazoparib, clone 7	olaparib	6.747
295	PSN-1, talazoparib, clone 9	olaparib	4.338
263, 295, 296	PSN-1	SN-38	1.000
263	PSN-1 talazoparib resistant clone E	SN-38	1.555
295	PSN-1, talazoparib, clone 10	SN-38	2.254
295	PSN-1, talazoparib, clone 11	SN-38	2.649
295	PSN-1, talazoparib, clone 13	SN-38	4.909

Assay number	Cell Line	Compound	Fold Resistance (EC50) to Parental Cell Line
296	PSN-1, talazoparib, clone 14	SN-38	0.895
296	PSN-1, talazoparib, clone 15	SN-38	0.729
295	PSN-1, talazoparib, clone 16	SN-38	13.910
295	PSN-1, talazoparib, clone 17	SN-38	2.933
296	PSN-1, talazoparib, clone 18	SN-38	3.027
296	PSN-1, talazoparib, clone 2	SN-38	6.273
296	PSN-1, talazoparib, clone 20	SN-38	2.400
296	PSN-1, talazoparib, clone 23	SN-38	13.637
296	PSN-1, talazoparib, clone 24	SN-38	4.091
295	PSN-1, talazoparib, clone 3	SN-38	1.615
295	PSN-1, talazoparib, clone 4	SN-38	2.931
295	PSN-1, talazoparib, clone 5	SN-38	2.487
296	PSN-1, talazoparib, clone 6	SN-38	2.973
296	PSN-1, talazoparib, clone 7	SN-38	13.637
295	PSN-1, talazoparib, clone 9	SN-38	2.411
255, 263, 273, 295, 296	PSN-1	talazoparib	1.000
255, 263, 273	PSN-1 talazoparib resistant clone E	talazoparib	92.687
295	PSN-1, talazoparib, clone 10	talazoparib	92.687
295	PSN-1, talazoparib, clone 11	talazoparib	92.687
295	PSN-1, talazoparib, clone 13	talazoparib	92.687
296	PSN-1, talazoparib, clone 14	talazoparib	14.274
296	PSN-1, talazoparib, clone 15	talazoparib	7.836
295	PSN-1, talazoparib, clone 16	talazoparib	92.687
295	PSN-1, talazoparib, clone 17	talazoparib	92.687
296	PSN-1, talazoparib, clone 18	talazoparib	92.687
296	PSN-1, talazoparib, clone 2	talazoparib	92.687
296	PSN-1, talazoparib, clone 20	talazoparib	77.486
296	PSN-1, talazoparib, clone 23	talazoparib	92.687
296	PSN-1, talazoparib, clone 24	talazoparib	92.687
295	PSN-1, talazoparib, clone 3	talazoparib	48.197
295	PSN-1, talazoparib, clone 4	talazoparib	92.687
295	PSN-1, talazoparib, clone 5	talazoparib	92.687
296	PSN-1, talazoparib, clone 6	talazoparib	55.612
296	PSN-1, talazoparib, clone 7	talazoparib	92.687
295	PSN-1, talazoparib, clone 9	talazoparib	24.099

Supplementary Table 25: Fold Change in EC50 compared to parental cell lines

PSN-1 Clone	talazoparib	EIS-1	SN-38
clone E	92.7	4.5	1.6
clone 2	92.7	6.5	6.3
clone 16	92.7	5.0	13.9
clone 24	92.7	4.6	4.1
clone 5	92.7	3.8	2.5
clone 17	92.7	3.1	2.9
clone 4	92.7	2.8	2.9
clone 13	92.7	2.8	4.9
clone 23	92.7	2.7	13.6
clone 18	92.7	2.2	3.0
clone 11	92.7	1.5	2.6
clone 10	92.7	1.5	2.3
clone 7	92.7	0.9	13.6
clone 20	77.5	3.2	2.4
clone 6	55.6	4.2	3.0
clone 3	48.2	4.8	1.6
clone 9	24.1	2.3	2.4
clone 14	14.3	1.2	0.9
clone 15	7.8	0.9	0.7
PSN-1	1.0	1.0	1.0
DU-145 clone	**talazoparib**	**EIS-1**	**SN-38**
clone 23.9	8.0	2.6	1.5
clone 23.8	7.0	5.6	2.5
clone 23.4	7.0	4.2	4.2
clone 23.1	7.0	3.6	2.4
clone 23.3	7.0	3.2	1.8
clone 23.10	7.0	3.1	2.3
clone 23.2	7.0	3.0	2.3
clone 23.11	7.0	2.0	1.6
clone 23.12	7.0	1.4	1.8
clone 20.6	7.0	1.3	1.2
clone 20.4	7.0	0.9	1.5
clone 20.2	7.0	0.8	1.4
clone 20.1	3.8	0.7	1.2
clone 23.7	3.7	5.6	1.6
DU-145	1.0	1.0	1.0

8. Appendix B:

8.1. Use of AI Tools for writing assistance

In the preparation of this thesis, AI programs such as ChatGPT and Grammarly were utilized for specific tasks, including checking grammar and spelling as well as suggesting synonyms and alternative wording for the text.

8.2. Macros

The macros used in this thesis can be found on GitHub under the following link:

https://github.com/KatharinaSahiri/Image_Processing_EisbachBio

- Image processing Z-project.ijm
- Z-project pixel normalization.py
- Image Analysis for Peak Detection and Area Calculation
- Stackreg_extract single-nuclei.ijm

The Toolkit options used in the FociCounter are shown in Supplementary Figure 28.

Macro Toolkit options:

OPT_CELL_MODEL_ENABLED=1
OPT_CELL_MODEL_SPLIT_AREA=30000
OPT_CELL_MODEL_MIN_AREA=4000
OPT_CELL_MODEL_SPLIT_CIRCULARITY=0.72
OPT_CELL_MODEL_FILTER_AREA=60000
OPT_CELL_MODEL_FILTER_CIRCULARITY=0.504
OPT_CELL_MODEL_SPLIT_AR=1.8
OPT_FLOATING_POINT=.
OPT_DECIMAL_PLACES=6
OPT_SKIP_WAIT_FOR_USER=1
OPT_SHIFT_COLORS=
OPT_SHIFT_X=
OPT_SHIFT_Y=
OPT_BRUSH_WIDTH=2
OPT_BRUSH_FILL=0
OPT_BRUSH_ARROW=0
OPT_BRUSH_ARROW_ANGLE=30
OPT_BRUSH_ARROW_LENGTH=10
OPT_BRUSH_ARROW_BOTH=0
OPT_FONT_SIZE=42
OPT_FONT_NAME=SansSerif
OPT_MONTAGE_ROI_COLOR=Cyan
OPT_MONTAGE_TIME_ORIT=Upper Left
OPT_MONTAGE_EVENT_ORIT=Upper Left
OPT_MONTAGE_SCALE_COLOR=White
OPT_MONTAGE_SCALE_WIDTH=10
OPT_MONTAGE_SCALE_HEIGHT=0.25
OPT_MONTAGE_SCALE_ORIT=Lower Right
OPT_MONTAGE_PADDING_COLOR=White
OPT_MONTAGE_PADDING_WIDTH=10
OPT_FOCI_THRESHOLD_METHOD=Huang
OPT_FOCI_CHAN_SELECT=Blue
OPT_FOCI_CHAN_MASK=White
OPT_FOCI_CHAN_MEASURE=Red
OPT_FOCI_FIND_MAXIMA_BIG=6000
OPT_FOCI_FIND_MAXIMA_SMALL=6000
OPT_FOCI_CHAN_MEASURE_2=Green
OPT_FOCI_FIND_MAXIMA_BIG_2=5000
OPT_FOCI_FIND_MAXIMA_SMALL_2=5000
OPT_FOCI_PRE_MEDIAN=0
OPT_FOCI_PRE_MAX=0
OPT_CROSSING_WIDTH=1.5
OPT_CROSSING_GROW=0.5
OPT_CROSSING_LENGTH=5
OPT_CROSSING_DELETE_SLICE=2
OPT_CROSSING_THRESHOLD_METHOD=Huang
OPT_CROSSING_CHAN_CORE=Blue
OPT_CROSSING_CHAN_SELECT=Red
OPT_BACKROI_TITLE=
OPT_BACKROI=
OPT_GUI_PIN_WINDOWS=1
OPT_GUI_ARRANGE_WINDOWS=1
OPT_USER_VALENTINA_BLOB_CHAN_CORE=b
OPT_USER_VALENTINA_BLOB_CHAN_MEASURE=g
OPT_USER_VALENTINA_BLOB_METHOD=Intermodes
OPT_USER_VALENTINA_BLOB_AREA_PER_BLOB=1
OPT_USER_TIAGO_LINEAPROX_SMOOTH=3
OPT_USER_TIAGO_LINEAPROX_AREA_MIN=1.2
OPT_USER_TIAGO_LINEAPROX_AREA_MAX=8
OPT_USER_TIAGO_LINEAPROX_MINOR=1.8
OPT_USER_TIAGO_LINEAPROX_MAX_SLICE=10

Supplementary Figure 28: Macro-Toolkit options for FociCounter (*FOCI Counter* | *BIC Macro Toolkit* | *Image Analysis* | *Service* | *Bioimaging Centre*, 2017)

Attributions

Supplementary Table 26: Attributions to Results

Method	Name	Attribution
IR-induced γH2AX and RAD51 foci formation of Eisbach-cell panel lines	Iris Baur and Claudia Böhland, Anna Friedl lab, LMU	Irradiation of cells and preparation of microscopy slides
γH2AX detection and Annexin V staining in FACS	Dr. Markus Lechner, Eisbach Bio GmbH	Support with cell staining and FACS
Cell cycle analysis in FACS	Dr. Markus Lechner, Eisbach Bio GmbH	Support with cell staining and FACS
γH2AX and RAD51 foci formation assay	Lucas Kalczynski, Eisbach Bio GmbH	Assistance with preparation of microscopy slides
γH2AX and cleaved PARPi protein levels in Western Blot	Frederick Zwicker	Assistance with Western Blot and antibody staining
Live-cell recruitment assay	Dr. Adrian Schomburg, Wiliam Menzer	Design of a python script to analyze protein dynamics as AUC
In vivo studies	Dana Matzek, William Menzer, Dr. Markus Lechner, Dr. Adrian Schomburg (Eisbach Bio GmbH)	Tumor cell implantation, dosing and tumor size measurements

Acknowledgements

I extend my sincere gratitude to my supervisor at the LMU, PD Dr. Anna Friedl, from the Department of Radiation Oncology. She provided great insights into the field of DNA damage repair, treatment strategies and professional knowhow in the field of oncology. Dr. Friedl's unwavering support has been a guiding force across every aspect of my doctoral journey. Her mentorship, constructive feedback, and commitment to academic excellence have been indispensable to my personal and professional development.

Next, I would like to thank my Doktorvater, Prof. Andreas Ladurner, Head of Physiological Chemistry at the LMU, for his invaluable support throughout my research. His expertise in Chromatin Biology and commitment to academic excellence have greatly shaped my scientific journey. I am grateful to him for generously taking on the role of my Doktorvater.

My appreciation extends to my supervisor at Eisbach Bio GmbH, Dr. Adrian Schomburg, CEO, whose guidance, and encouragement was fundamental to my professional growth. Dr. Schomburg's valuable insights and mentorship have played a pivotal role in shaping my skilled knowhow.

Special appreciation is extended to my colleagues Dr. Gunnar Knobloch, Dr. Corinna Lieleg, Dr. Markus Lechner, William Menzer, Dr. Xin Zhang, Lucas Kalczynski, Frederick Zwicker, Dana Matzek and the entire Eisbach Team. Their collaborative spirit, shared knowledge in protein science, biochemistry, and chromatin biology, and the creation of a supportive working environment have been essential to my research success.

I would like to acknowledge Anna Friedl's Team, particularly Iris Baur and Claudia Böhland, for their crucial role in supporting me during the cell line characterization through the foci formation assay.

I am incredibly grateful to my family for their unwavering support and guidance on my academic journey. To my dad, Martin Sahiri, and my uncle, Dr. Thomas Sahiri, I extend my heartfelt thanks for their invaluable mentorship across all domains in the biotech industry. To my mom, Babette Sahiri, who has been a constant source of strength and support, demonstrating the power of teamwork and resilience. To my brother, Philipp Sahiri, and my partner, Anton Zollbrecht, I'm immensely grateful for their unwavering support through every peak and valley of my career. To my entire family and friends, thank you for your enduring support. Your unwavering faith in my abilities has been a constant source of inspiration and motivation. I couldn't have reached this milestone without each of you by my side.

Affidavit

Affidavit

Sahiri, Katharina Arien

Surname, first name

I hereby declare that the submitted thesis entitled:

Targeting ALC1 for Synthetic Lethality in Cancer: A Superior Alternative to PARP Inhibitors

is my own work. I have only used the sources indicated and have not made unauthorized use of services of a third party. Where the work of others has been quoted or reproduced, the source is always given.
I further declare that the dissertation presented here has not been submitted in the same or similar form to any other institution for the purpose of obtaining an academic degree.

Munich, 13.01.2025 — Katharina Arien Sahiri

place, date — Signature doctoral candidate

Confirmation of Congruency

LMU LUDWIG-MAXIMILIANS-UNIVERSITÄT MÜNCHEN | Promotionsbüro Medizinische Fakultät | MMRS

Confirmation of congruency between printed and electronic version of the doctoral thesis

Sahiri, Katharina Arien

Surname, first name

I hereby declare that the submitted thesis entitled:

Targeting ALC1 for Synthetic Lethality in Cancer: A Superior Alternative to PARP Inhibitors

is congruent with the printed version both in content and format.

Munich, 13.01.2025

place, date

Katharina Arien Sahiri

Signature doctoral candidate

Confirmation of the publication of data from Eisbach Bio GmbH

Eisbach Bio GmbH
Am Klopferspitz 19
82152 Planegg-Martinsried
Germany

Dr. Adrian Schomburg
Chief Executive Officer
Tel.: +49 17621046886
adrian@eisbach.bio

Confirmation for the publication of data from Eisbach Bio GmbH in the doctoral thesis titled “Targeting ALC1 for Synthetic Lethality in Cancer: A Superior Alternative to PARP Inhibitors” authored by Katharina Sahiri.

Sincerely,
Dr. Adrian Schomburg, CEO, Eisbach Bio GmbH

Dr. Adrian Schomburg

Planegg, 24.01.25

place, date

List of Publications

Sahiri, K., Blessing, C., Schomburg, A., & Ladurner, A. (2022). *Method to evaluate the capability of compounds on the trapping of proteins* (Patent No. WO/2022/117781). Zwicker Schnappauf & Partner Patentanwälte PartG mbB. https://patentscope.wipo.int/search/de/detail.jsf?docId=WO2022117781&_cid=P11-LM977Z-71903-1

Menzer, W. M., Sahiri, K., Schomburg, A., Ladurner, A., & Sennhenn, P. (2022). Use of ALC1 inhibitors and synergy with PARPI (Patent No. WO/2023/213833). Zwicker Schnappauf & Partner Patentanwälte PartG mbB. https://patentscope.wipo.int/search/en/detail.jsf?docId=WO2023213833&_cid=P12-M2SZCT-38262-1

Menzer, W. M., Sahiri, K., & Schomburg, A. (2025). Inhibitors for use in treating cancer by potentiating the effects of FDA approved cancer drugs (Patent No. EP23205931.1, EP23207212.4 & EP 24185254.0). Zwicker Schnappauf & Partner Patentanwälte PartG mbB.

Menzer, W. M., Sahiri, K., Zhang, X., Schomburg, A., Ladurner, A., & Sieveke, J. (2025). ALC1 inhibitors ALC1i-1 and ALC1i-2 for use in treating pancreatic cancer by potentiating the effect of irinotecan (Patent No. EP23207219.9). Zwicker Schnappauf & Partner Patentanwälte PartG mbB.